# Development of Dynamic Phasors for the Modelling of Aircraft Electrical Power Systems

**By**

**Tao Yang, MEng (Hons)**

Thesis submitted to the University of Nottingham for the degree of Doctor of Philosophy, May 2013

# Acknowledgements

Firstly, I would like to express my deepest gratitude to my supervisors, Prof. Greg Asher and Dr. Serhiy Bozhko, for their invaluable advice and expert guidance throughout the course of this research. My special thanks also go to Prof. Patrick Wheeler for his assistance and helpful discussion. I would also like to thank Prof. Dave Thomas for acting as my internal examiner and Dr. Patrick Norman, from the University of Strathclyde, for acting as my external examiner.

Special thanks are extended to Mr. Jean-Marc Le Peuvédic from Dassault Aviation for his valuable advice and helpful discussion during my PhD studies. My sincere thanks also go to Dr. Elisabetta Lavopa for testing the CRU model experimentally.

I would like to express my heartfelt gratitude to the University of Nottingham for funding my PhD study through the Dean of Engineering Scholarship. Special thanks are given to Dr. Tahar Hamiti and his family, Puvan Arumugam, Dr. Hui Jiang, Dr. Chao Ji, Jiří Dušek, Christopher Brunson, Dr. Ralph Feldman, Elisa Rispetto, Dr. Marco Degano, Dr. Xi Lin, Yusuke Zushi, Prof. Hitoshi Kino and his family, Dr. Tao Wu, Dr. Chintan Patel, Xiang Wang, Shuai Shao, Tracy Xu, Guan and all other friends I have met here during this journey. You have made my life more pleasant, joyful and always sunny in the UK. I do appreciate the help and friendship from you and I will cherish our friendship lifelong.

I would like to express the earnest appreciation to my parents, my sister. Although thousands miles away, you give me the most valuable strength and courage to go through this journey.

With much love, I would like to thank my wife, Dr. Fang Xu, for her love, understanding and encouragement during this journey.

Tao Yang

Nottingham
Summer 2013

# Abstract

As the More-Electric Aircraft (MEA) has been identified as a major trend of future aircraft, the on-board Electrical Power System (EPS) will see significant increased numbers of Power Electronic Converters (PECs) and motor drive systems. In order to study the behaviour and performance of the EPS in MEA, extensive simulation studies need to be done during the system design process. This in return, gives the need to have computationally efficient and accurate models to reduce the design period. In this thesis, the Dynamic Phasor (DP) is used for modelling EPS in the MEA. The DP technique is a general averaging method and naturally a frequency-domain analysis tool. Compared with other averaging models, which is only efficient under balanced conditions, the DP model maintains efficiency under both balanced and unbalanced conditions. The DP technique has been widely used in modelling the constant, single frequency EPS. In this thesis, the DP technique is extended to modelling time-varying frequency EPS. The application of DP in modelling a multi-generator, multi-frequency system is for the first time, developed in this thesis. The developed theory allows a wider application of the DPs. The developed DP model covers key elements in MEA electrical power systems, including the synchronous generator, control, transmission lines, uncontrolled rectifiers, PWM converters and 18-pulse autotransformer rectifier units. The DP model library developed based on this thesis allows the flexibility to study various EPS's by integrating elements from the library. A twin-generator aircraft EPS, which is based on the More Open Electrical Technology (MOET) large aircraft EPS architecture, is used to demonstrate the application of DP models. Comparing the DP model with the ABC model (models in three-phase coordinates) and the DQ0 model (models in a synchronous dq frame), the efficiency and the accuracy of the DP model are demonstrated under both balanced and unbalanced conditions.

# Contents

# List of Figures

# List of Tables

# List of Abbreviations

| | |
|---|---|
| AC | Alternating Current |
| APU | Auxiliary Power Unit |
| ATRU | Auto-Transformer Rectifier Unit |
| AVM | Average-Value Modelling |
| BAT | Back-up Battery |
| CIU | Controlled Inverter Unit |
| CRU | Controlled Rectifier Unit |
| CSD | Constant Speed Drive |
| DB | Diode Bridge |
| DP | Dynamic Phasor |
| DC | Direct Current |
| ECS | Environmental Control System |
| EEPDC | Emergency Electrical Power Distribution Centre |
| EHA | Electro-Hydrostatic Actuator |
| EMA | Electro-Mechanical Actuator |
| EMC | Electro-Magnetic Compatibility |
| EPS | Electrical Power System |
| FACTS | Flexible AC Transmission System |
| GCU | Generator Control Unit |
| HVDC | High-Voltage Direct Current |
| MCU | Motor Control Unit |
| MEA | More-Electric Aircraft |
| MOET | More Open Electrical Technology |
| PEC | Power Electronic Converter |
| PEPDC | Primary Electrical Power Distribution Centre |
| PLL | Phase-Lock Loop |
| PMSM | Permanent Magnet Synchronous Machine |

| | |
|---|---|
| PWM | Pulse-Width Modulation |
| SG | Synchronous Generator |
| STATCOM | Static Synchronous Compensator |
| TCSC | Thyristor Controlled Series Capacitor |
| UPFC | Unified Power Flow Controller |
| USSC | Unified Series-Shunt Compensator |
| WIPS | Wing-Icing Protection System |

# Chapter 1

# Development of More-Electric Aircraft

## 1.1 Introduction

Air travel has become an inevitable part of today's world. Going through turbulent times with rising fuel price, the industry has been re-engineering itself to survive and counter the impact [1]. Given the fact that fuel prices are unlikely to remain stable in the years to come, governments worldwide are urging the industry to develop more efficient and cleaner solutions. The total contribution of aircraft emissions to total anthropogenic carbon dioxide ($CO_2$) emission was considered to be about 2% in 1990 and this figure is estimated to increase to 3% by 2050 [2, 3]. With more and more concern about aircraft $CO_2$ emission, airlines are under pressure to reduce their carbon emissions by governments concerned about global warming.

Research on alternative fuels has been on-going for decades, but none have the energy density of aviation fuel, which is essential since minimizing the gross weight of aircraft is critical for efficient operations. Synthetic fuels have been demonstrated on aircraft and are mentioned as an alternative. However, producing these fuels is far more energy intensive than common aviation fuel. Alternatives to fossil fuels are more practical with other forms of transportation; hence, the airline industry must focus on increasing efficiency [1].

Increasingly moving towards More-Electric Aircraft (MEA) is one of the few existing solutions available for the development of more efficient and environment friendly aircraft. The MEA has become a dominant trend for the

next-generation aircraft. Many functions which are conventionally driven by hydraulic, pneumatic and mechanical power will be replaced by electrical systems in the MEA, to improve the efficiency and safety of aircraft systems operation [4-6]. Compared with conventional aircraft, the MEA offers significant cost benefits with lower recurring costs due to fewer parts, integration of key sub-systems, and multi-use of components. It also reduces the overall cost of operation and ownership because its more-electric architecture helps reduce fuel consumption per passenger per mile, increase overall aircraft performance and energy usage.

## 1.2 Conventional Power Systems in Aircraft

Conventional aircraft architectures used for civil aircraft embody a combination of systems dependent on mechanical, hydraulic, pneumatic, and electrical sources. In a conventional architecture, the fuel is converted into power by the engine. Most of power is used as propulsive power to keep the aircraft in the sky and the remainder is converted in to four main forms of non-propulsive power: pneumatic power, mechanical power, hydraulic power and electrical power, as shown in Figure 1-1.

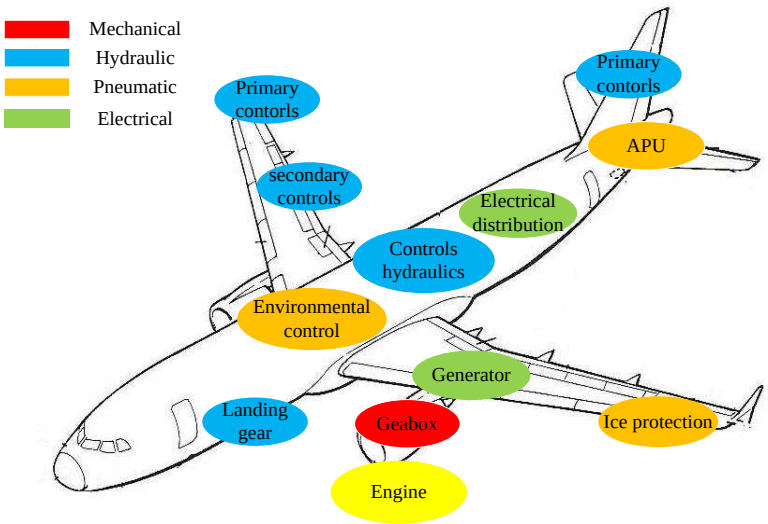


Figure 1-1 Schematic conventional aircraft power distribution systems [7]

- **Pneumatic Power**

The modern turbofan engine is a very effective hot gas generator and this has led to the use of engine bleed air for a number of aircraft systems. In the engine, the external air is processed by a multi-stage axial compressor, driven by the turbine before entering the combustion chamber. As shown in Figure 1-2, the air is commonly bled at two different stages of the compressor, a low pressure port at an intermediate stage and a high pressure port at a final stage. The low pressure bleeding port is normally open and the high pressure port is open when the pressure coming from the intermediate stage is not adequate or a considerable amount of air is necessary. A low flow rate can be extracted from the engine, between 2% and 8% of the total flow rate processed. Compressed air can also be extracted from a gas turbine Auxiliary Power Unit (APU), which allows operation of all pneumatic system when the aircraft is on the ground with engines off, in particular the Environmental Control System (ECS) and engine starting.

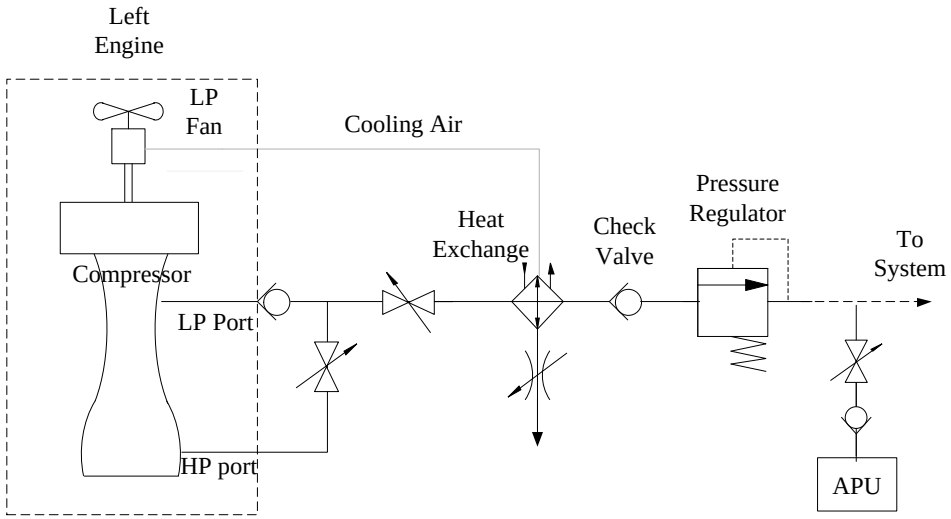


Figure 1-2 Typical bleed air system in aircraft – left hand side

The main uses of pneumatic power are environmental control and ice protection. The pneumatic system has advantages of simple design and high reliability. However, the bleed air reduces the efficiency of the engine since the process of heat exchanging leads to a lower thermal and energy efficiency.

- **Hydraulic Power**

Hydraulic systems made their appearance on aircraft in the early 1930s when the retractable undercarriage was introduced [7]. In conventional hydraulic systems, there are normally two aircraft-wide hydraulic circuits installed on the aircraft, each of which is pressurized by centralised hydraulic pumps driven directly by the engine through a gear box. The hydraulic pumps deliver power to hydraulic actuators local to the flight surface through the hydraulic pipes. When the actuator receives a control demand from the pilot, the electrical hydraulic servo valve is moved to allow the hydraulic fluid to enter the actuator, making the piston within the actuator move in either direction. In this way, the actuator is pressurised such that the associated control surface is moved to satisfy the demand. The hydraulic system today remains the main power source for both primary and secondary flight controls, for landing gear deployment, for retraction and braking, for engine actuation and for numerous ancillaries [7, 8]. Hydraulic systems have a high power density and are very robust. Their drawbacks are the heavy and inflexible infrastructure (piping) and the potential leakage of dangerous and corrosive fluid.

- **Mechanical Power**

The mechanical power in the aircraft is transferred, by means of mechanical gearboxes, from the engine to central hydraulic pumps, from the engine to local pumps for engine equipment and other mechanically driven subsystems, and also from the engine to the main electrical generator. The drawbacks of the mechanical system are the use of a heavy gearbox and its associated maintenance cost. In order to reduce friction of the bearings within the gearbox, extra oil pumps are used to make the oil circulate through rotating bearings within the mechanical system.

- **Electrical Power**

Electrical systems have made significant advances over the years with the development of power electronics and electrical drive systems. The use of electrical power structure in a conventional aircraft has been illustrated by an

electrical power system structure shown in Figure 1-3. Each generator delivers 115VAC/400Hz electrical power to the main AC bus and controlled by its own Generator Control Unit (GCU). To generate the constant frequency AC power from the aircraft engine running at variable speeds, a Constant Speed Drive (CSD) is employed. The CSD in effect acts as an automatic gearbox which maintains the generator shaft speed constant with a variable engine speed as its input. This complex hydro-mechanical equipment needs to be correctly maintained in terms of oil charge level and oil cleanliness to ensure high reliabilities [7]. The 115VAC power is transformed to 28VDC power using Transformer Rectifier Units (TRUs). TRUs consist of a multiphase transformer and an n-pulse diode rectifier, where n=12 or 18, to reduce the ripple on the DC-link and to achieve the power quality requirements. The electrical loads supplied by the 28V DC bus are the avionics, cabin electronics and the back-up batteries. Other AC electrical loads, such as lighting, galley loads, entertainment system and auxiliary hydraulic pumps are directly fed by the AC bus.

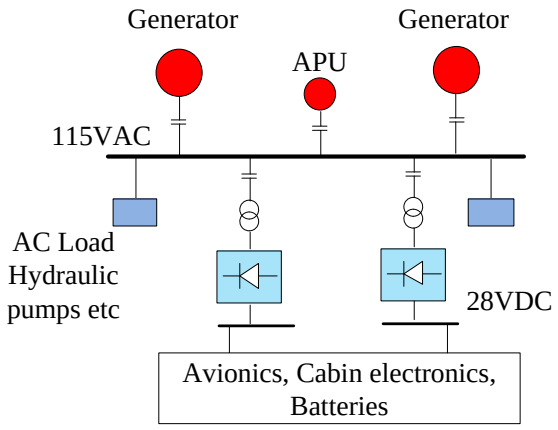


Figure 1-3 Conventional aircraft electrical system architecture

The Figure 1-4 shows the estimated power distribution of the Boeing 737 system. It is estimated that the propulsion thrust generates around 40MW for the flying power and the total 'non-thrust' power consumes around 1.7MW, of which the electrical power system consumes approximately 12% of the total 'non-thrust' power. The electrical power system thus plays a minor role on conventional aircraft. Since the electrical power system has many advantages, such as high efficiency, low maintenance, the application of advanced

diagnostics technology, the evolution of the use of more electric power has become a key technology trend which will dominate the design of the next generation commercial aircraft.

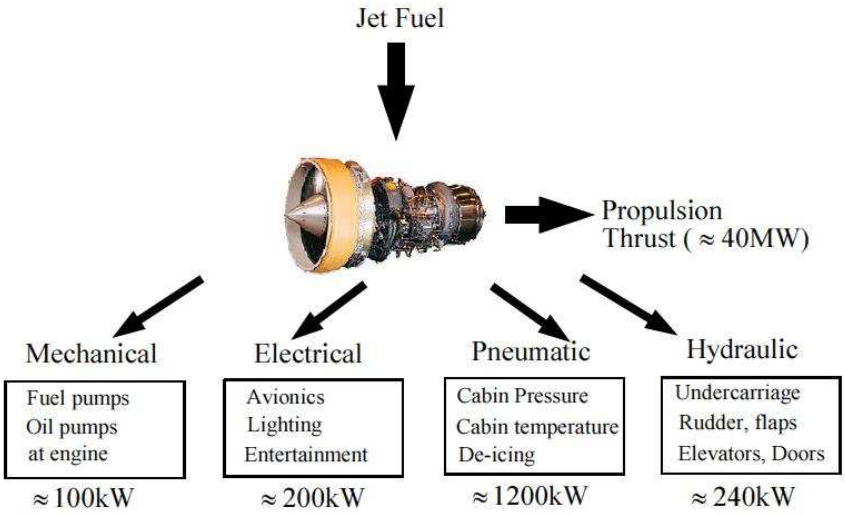


Figure 1-4 The estimated power distribution on Boeing 737 [9]

# 1.3 More-electric Aircraft Power Systems

The More-Electric Aircraft (MEA) concept is based on utilizing electrical power to drive aircraft subsystems which historically have been driven by a combination of hydraulic, electric, pneumatic and mechanical power. Increasing use of electric power is seen as the direction of technologies for aircraft power systems due to the advancement of power electronics, fault tolerant electrical power distribution systems, electrical drives as well as the control theory.

## 1.3.1 Evolution of the Aircraft Electrical Power Systems

While the performance of the conventional hybrid non-propulsive power system has improved over time, it still represents a major factor in aircraft maintenance downtimes and failures. Towards the end of 1970s, the idea of the use of a single electrical type of secondary power arose and the United States

Air Force and NASA started a development and demonstration program called MEA. This program aimed to reduce or eliminate centralized hydraulic, mechanical and pneumatic power systems, replacing them with an electrically-based system to improve the efficiency, reliability, maintainability and flexibility, and to reduce the operation and support cost of the aircraft. The requirement of electrical power will rise dramatically in the future aircraft with the advent of more new electrical loads such as the environmental control system, electrical actuation, landing gears etc., in accordance with the MEA concept. The on-board electrical power evolution trend over past few years for the main civil aircraft is shown in Table 1-1.

Table 1-1 On-board electrical power generation

| Aircraft | Electrical power |
|---|---|
| A300 | 2×90kVA (1× Engine*) + 90kVA APU |
| A310 | 2×90kVA (1× Engine) + 90kVA APU |
| A320 | 2×90kVA (1× Engine) + 90kVA APU |
| A330 | 2×115kVA (1× Engine) + 115kVA APU |
| A340 | 4×75kVA (1× Engine) + 115kVA APU |
| A380 | 4×150kVA (1× Engine) + 2×120kVA APU |
| B737 | 2×90kVA (1× Engine) + 90kVA APU |
| B747 | 4×90kVA (1× Engine) + 2×90kVA APU |
| B767 | 2×120kVA (1× Engine) + 120kVA APU |
| B777 | 2×120kVA (1× Engine) + 120kVA APU |
| B787 | 4×250kVA (2× Engine) + 2×225kVA APU |
| * n× Engine means one engine is driving n generators | |

Numerous projects and initiatives have been funded by the Europe Union (EU) to explore the application of the MEA concept both to military and civil aircraft. In 2000, the Magnetostrictive Equipment and Systems for More-Electric Aircraft (MESA) project was launched. This project aimed to reduce the power take-up and the weight of on-board aircraft systems through the development of magnetostrictive motors and actuators. Launched in early 2002,

the four-year Power Optimised Aircraft (POA) project aimed to qualitatively and quantitatively validate the ability of next generation aircraft equipment systems to enable the reduction in consumption of non-propulsive power [10]. In 2006 the More Open Electrical Technologies (MOET) project was launched. This project aimed to establish a new industrial standard for electrical design system of commercial aircraft, a standard which is applicable to business and regional aircraft, and rotorcraft as well. To create this new standard, MOET launched significant changes in power management and use, in conjunction with the reducing aircraft emissions and improving the operational capacity [11, 12]. The EU CleanSky project aims to demonstrate and validate the technology breakthroughs that are necessary to make major steps towards the environmental goals set by the European Technology Platform for Aeronautics & Air Transport to be reached in 2020 [13].

In the MEA, many functions which used to be driven by hydraulic, pneumatic and mechanical power will be driven by electrical power. This will not only increase the efficiency, but also improve the flexibility and availability of the aircraft system. The prominent features for the future aircraft are described as follows:

**(a) Bleedless Engine**

In the conventional aircraft, the bleed air is extracted from the engine and used for the ECS, cabin pressurisation and wing anti-icing systems. Figure 1-5 illustrates the difference between conventional power extraction using bleed air on the left versus a more-electric version on the right. These architectures broadly represent the difference between the Boeing 767 (B767, left, conventional aircraft) and the Boeing 787 (B787, right, More-electric aircraft).

The pneumatic power extracted from bleed air off the engine has been dominant for the past few decades. Even though it is convenient to extract bleed air from the engine, it is not without penalties. The bleed air reduces the efficiency of the engine since the process of heat exchanging leads to a lower thermal and energy efficiency. As the pressure ratios and bypass ratios increase

on modern engines, tapping bleed air off the engine compressor becomes extremely wasteful, dramatically reduces the engine efficiency and increases the fuel consumption [7].

In order achieve high efficiency, the bleedless engine has been seen as the trend for future aircraft engines. In B787, the only bleed air taken from the engine is low pressure fan air used to perform an anti-icing function for the engine cowl. As shown in Figure 1-5, the ECS, cabin pressurisation and wing anti-icing systems are supplied by electrical power. Compared with conventional aircraft, the increased electrical power generation is 500kVA per channel instead of 120kVA in the conventional aircraft.

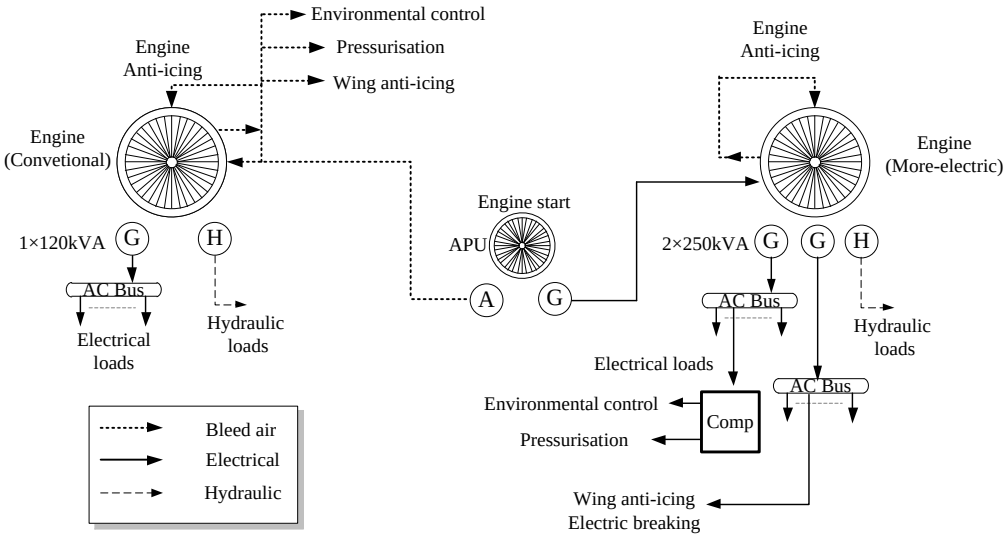


Figure 1-5 Comparison of conventional and more-electric power system [7]

**(b) Variable frequency generators**

The CSD used in the conventional aircraft is a complex hydro-mechanical device that is not highly reliable and reduces the efficiency [7]. The trend is that the CSD will be removed from the system. The generator will be driven by the accessory gearbox and produce AC outputs at a variable frequency proportional to the engine speed. There are considerable benefits of the VF system including higher efficiency, simpler engine design etc. This concept has

been used in the B787 and A380. In B787, each generator drives two 250kVA generators with variable frequencies. In A380, there are four 150kVA VF generators.

### (c) More Electrical Loads

In future aircraft, a large increase in electrical on-board loads will arise in the EPS. The main more-electric loads include the ECS, the wing anti-icing system, Electro-Mechanical Actuators (EMAs) or Electro-Hydrostatic Actuators (EHAs) in flight control systems, etc. The ECS is one of the largest consumers of the electrical power, since there is no engine bleed air available. The air for the ECS and pressurization systems is pressurised by electrical means. In the B787, the ECS contains four large electrically driven compressors and the total power drawn is in the region of 500kVA. Non-availability of bleed air also means that the wing anti-icing system has to be provided by electrical heating mats embedded in the wing leading edge. In the B787, the wing anti-icing system is driven electrically and requires in the order of 100kVA of electrical power. The EHA uses the three-phase AC power to feed power drive electronics which in turn drive a variable speed pump together with a constant displacement local hydraulic pump. The EMA is a more-electric version of EHA since it replaces the hydraulic power actuation in the EHA with an electric motor.

### (d) Higher Voltages

The move towards MEA means an increase in electrical power demand. However, the resulting levels of electrical power cannot be efficiently transported at the conventional voltage level. Continuing use of low voltages will result in unsustainable voltage drops as well as increased conductor size and weight. Use of higher level voltages thus becomes the trend for future aircraft. In Boeing 787, the main HVAC bus is set at 230VAC and the main DC bus uses ±270V.

## 1.3.2 Boeing 787 Electrical Power System Architecture

The Boeing 787 is a big step toward the MEA. Virtually everything that has conventionally been powered by bleed air from the engine is powered electrically. As shown in Figure 1-6, the only bleed system on B787 is the anti-icing system for the engine cowl.

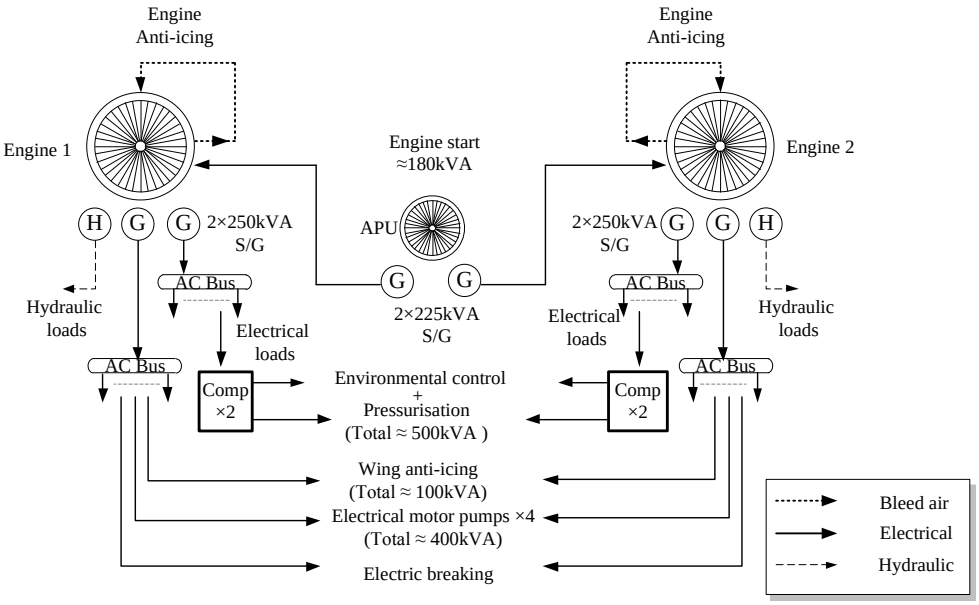


Figure 1-6 Boeing 787 electrical power system

The B787 is equipped with two engines each driving two 250kVA variable-frequency generators. This enables elimination of the CSD and greatly reduces the complexity of the generator. In addition, the B787 uses the engine generator as the starter motor and this enables the elimination the pneumatic starter from the engine. Compared with conventional APUs, the B787 APU replaces the pneumatic load compressor with a starter generator. This results in significantly improved start reliability and power availability. The use of starter generators reduces maintenance requirements and increases reliability due to the simpler design and lower part counts. In terms of inflight start reliability, the B787 APU is expected to be approximately four times more reliable than conventional APUs with a pneumatic load compressor [14]. As there is no air feeding the ECS, cabin pressurisation and wing anti-ice systems are driven electrically. In the B787, four large electrically driven compressors are used to

pressurise the air needed for the ECS with a total power in the region of 500kVA. The wing anti-icing function has been provided by electrical heating mats embedded in the wing leading edge with electrical power requirement in the order of 100kVA. Some of the aircraft hydraulic engine driven pumps are replaced by electrically driven pumps with total power requirement at 400kVA. This reduces the weight and improves the flexibility of the aircraft system. Another innovative application of the more-electric system architecture in the B787 is the move from hydraulically actuated brakes to the electric ones. These electric brakes significantly reduce the complexity of the braking system and eliminate the potential delays associated with leaking brake hydraulic fluid, leaking valves, and other hydraulic failure [14]. The locations of the main electrical equipment and the primary electrical distribution panels are shown in Figure 1-7. There are four main primary distribution panels, two in the forward electrical equipment bay and two others in the aft electrical equipment bay. The high levels of power involved and associated power dissipation generates a large amount of heat and the primary distribution panels are liquid cooled.

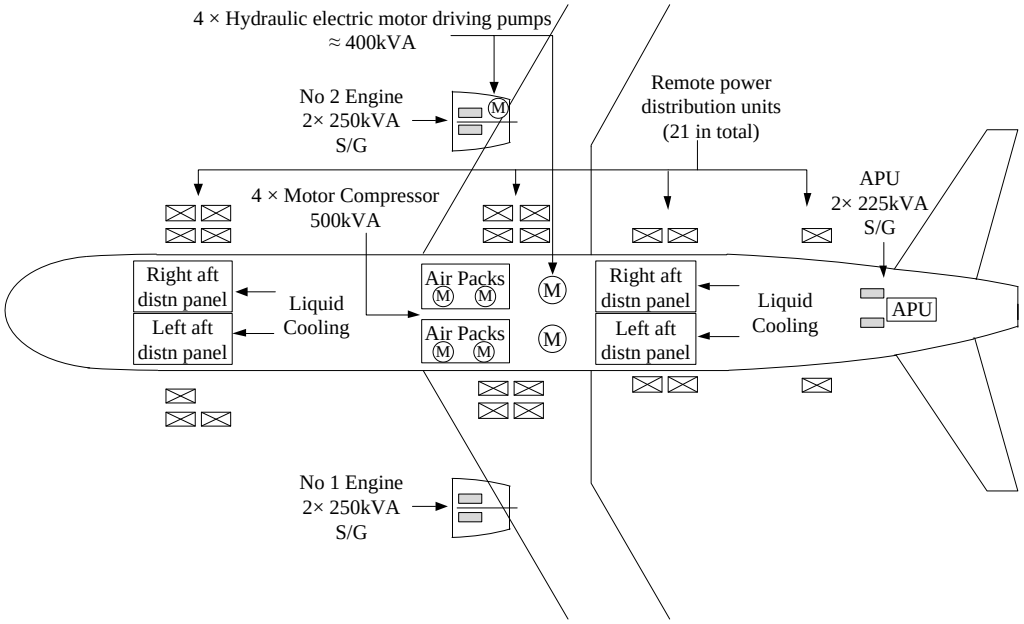


Figure 1-7 Boeing 787 electrical power distribution system

### 1.3.3 Electric System Architectures

As the amount of electrical power in the future aircraft will be higher than that in conventional aircraft, the electric system will also involve different architectures. The power converters will be widely used in the future aircraft. As a result, the main bus will not necessary be the HVAC bus. Delivering power through the main HVDC bus is an option for the future aircraft since it has the advantage of using less cable compared with AC systems and reactive power is not required. A Hybrid system with both HVAC and HVDC buses is also a choice.

Figure 1-8 shows the MOET aircraft electrical power system architecture [15]. Under this structure, each engine is driving VF generators which supply power to a 230V HVAC bus. The HVAC bus feeds the ±270V HVDC bus through an Auto-Transformer Rectifier Unit (ATRU). In the MOET architecture, the loads that are conventionally driven by pneumatic, mechanical and hydraulic power, are replaced by electrical systems. However, the conventional 115VAC, 28VDC subsystems are still being used for the legacy equipment, lighting, galley and avionics etc.

Figure 1-9 shows a possible MEA DC power system layout. The AC power from the two main starter/generators is transformed to DC power through bi-directional AC/DC converters. The flight control actuation system, the ECS and the actuators are driven electrically through DC/AC converters. The main advantage for the DC system includes less cable weight as it only requires two cables instead of three cables. It also decouples the generator frequency from that of the main distribution system [16]. Furthermore, DC distribution readily permits the paralleling of multiple generators onto a single bus [17] and enables the application of variable-frequency power to be more convenient. The choice of DC power distribution, however, is also associated with some issues, for example: the safety aspect requires safe isolation of power buses carrying fault currents [18]; the demanding protection requirements under fault

condition [19]; the transient voltage disturbance issues during regeneration [20]. DC power system architectures for aircraft are an important area of study.

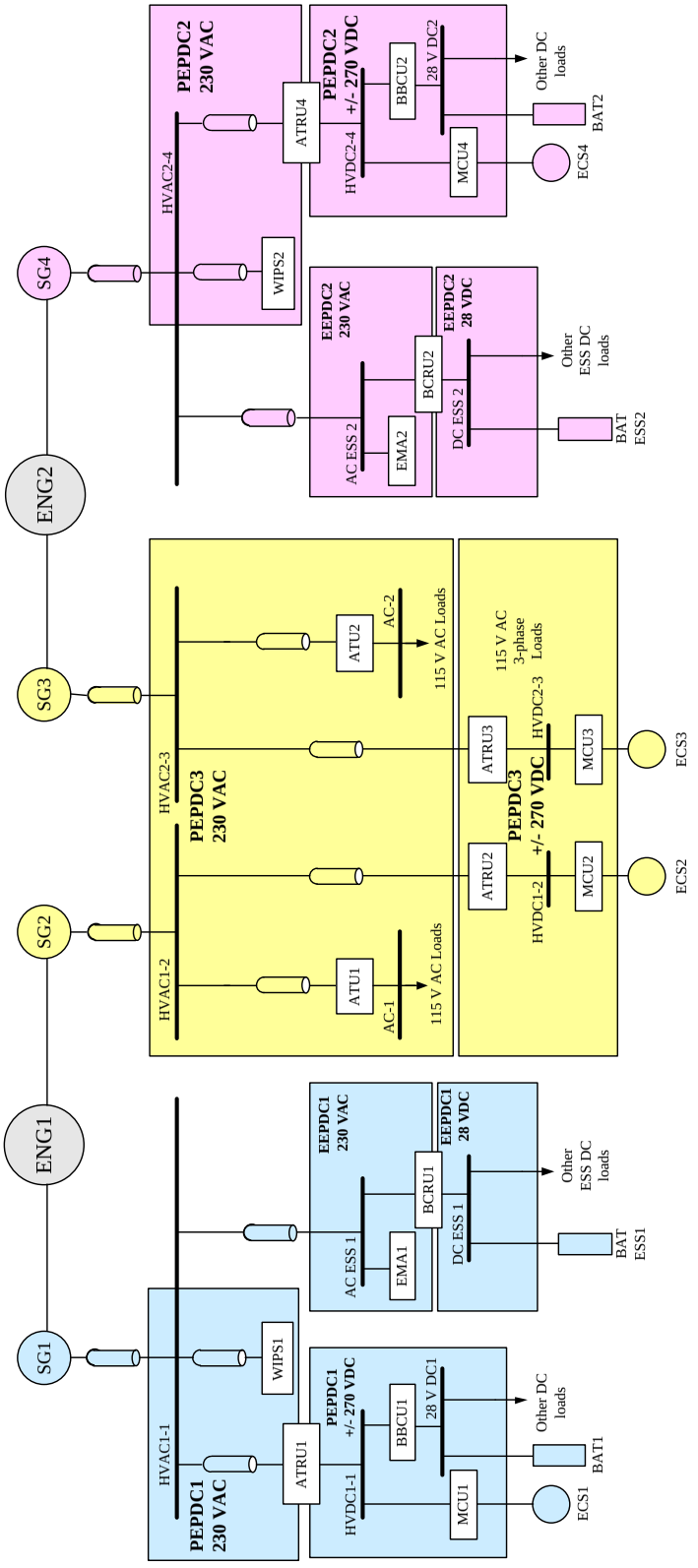


Figure 1-8 MOET aircraft electrical power system architecture

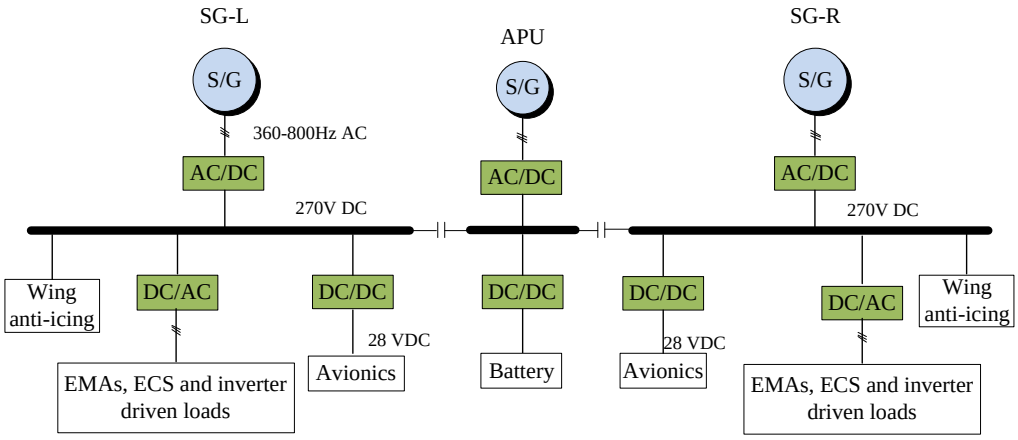


Figure 1-9 MEA DC power system layout

# 1.4 Modelling of Power Systems

No matter which EPS scheme is chosen, the use of a large number of Power Electronic Converters (PEC) will be inevitable. These PECs and their control systems will lead to significant challenges for EPSs designers. In order to ensure system stability, availability and power quality issues, the modelling and simulation of the EPS is required.

## 1.4.1 Multi-level Modelling Paradigm

Modelling of the electrical power system element has been studied for decades. The model required for EPS studies is always dependent on its application. Figure 1-10 categorises the EPS model into four different levels: architecture level, functional level, behavioural level and component level [21]. The complexity of the model increases from the top architecture-level models to the bottom component-level models.

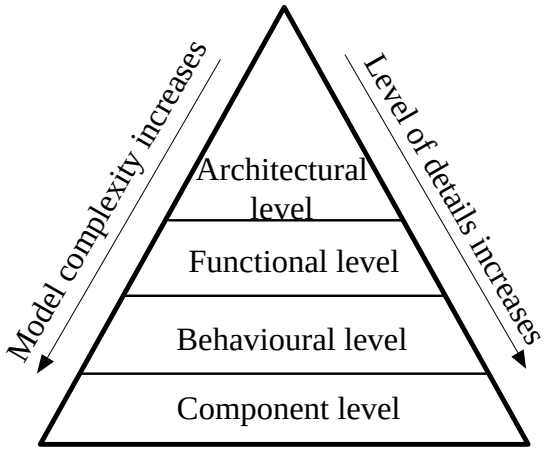


Figure 1-10 The multi-level modelling paradigm [22]

**(a) Component level**

The bottom component layer aims to model behaviour of components within a subsystem, especially critical components. Component models cover high frequencies, electromagnetic field and electromagnetic compatibility (EMC) behaviour, and perhaps thermal and mechanical stressing. The modelling bandwidth of component models can be up to in MHz region if required.

**(b) Behavioural level**

The model in the "behavioural" layer uses lumped-parameter subsystem models and the modelling frequencies can be up to hundreds of kHz. Models in this level cover the converter switching behaviour and the impact of harmonics. The nonlinearities and the dynamics of the subsystem up to the switching frequency are preserved in the behavioural model.

**(c) Functional level**

The next level is generally known as the functional level where system components are modelled to handle the main system dynamics up to 150Hz and the error should be less than 5% in respect of the behaviour model accuracy [22]. The functional-level model is targeted at the study of overall power system performance, stability, transient response to loading and start-up, and aims to model the power system either in its entirety or in sections

sufficiently large to obtain a holistic generator-to-load dynamic overview. Since the model complexity of the functional model is reduced, the computation time of the functional model is aimed at that approaching the real simulated time. The model developed in this thesis will be targeted at this level and a model library suitable for the simulation study of the future MEA power system will be established.

**(d) Architecture level**

The top architectural layer computes steady state power flow and is used for weight, cost and cabling studies [23]. The model in this level also allows event modelling such as bus configuration and step of loading, and reliability, stability and availability studies. The architectural models are the simpler ones and are representative only of steady state power consumptions.

## 1.4.2 Studies of Functional Models

Modelling and simulation of EPS are essential steps that enable design and verification of numerous electrical energy systems including modern electric grid and its components, distributed energy resources, as well as electrical systems of ships, aircraft, vehicles and industrial automation. With the increase use of power electronic devices, it is impractical to simulate and study such a complex system with detailed component-level device models or behavioural device models. As these models include high bandwidth components, from kHz to MHz, very small simulation steps and a huge amount of computer memory are required. This leads to significant simulation time and makes the large-scale EPS simulation at these two lower levels impractical. In addition, these two lower-level models are discontinuous and therefore are difficult to use for extracting the small-signal characteristics of various modules for system-level analysis [24]. The above challenges have led to development of average modelling techniques; these can be categorised at the functional level.

The Average-Value Modelling (AVM) method removes the effect of the switching behaviour of the power electronic device using the dynamic average values of the variables. Due to fact that the switching frequency of the electronic power converters is much higher than the system dynamics, the system-level study can be conducted with the dynamic average value defined over the length of a switching interval, instead of looking at the instantaneous values of currents and voltages that contain ripples due to switching behaviour of PECs. The dynamic average value of a time-domain variable x(t) is defined as

$$\bar{x} = \frac{1}{T_s} \int_{t-T_s}^{t} x(t)dt \tag{1-1}$$

where $T_s$ is the switching period. For the DC/DC converters, x(t) may represent the input or output voltage v(t) and current i(t). The AVM of PWM DC/DC converters can be given in either an analytical or equivalent circuit form using the definition (1-1). Theoretically, these two forms of models are equivalent for any given converter topology. As shown in Figure 1-11, the left side shows a switched cell commonly used in a DC/DC converter; the right side shows its equivalent circuit. In the average model, the switch pair, an IGBT and a diode, is replaced with dependent sources which are functions of the duty cycle and the averaged values of the cell's terminal variables [25, 26].

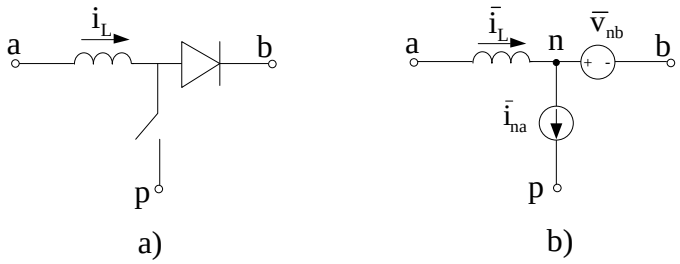


Figure 1-11 Switched-inductor cell and its averaged circuit model

In the analytical AVM for the PWM DC/DC converter, the state equations for each topology within a switching interval $T_s$ are firstly obtained. Using (1-1), the final average model is then derived from the weighted sum of the state-space equations for different subintervals.

This concept of averaging has also been extended to modelling AC/DC and DC/AC converters. However, instead of directly averaging of the AC variables using (1-1), the AC side variables are transformed to a synchronous rotating reference frame, referred to as the dq frame [27]. In the dq frame, the three-phase AC variables are transformed so as to be composed of a DC (constant) term and high-frequency ripples with the same switching interval. Because the variables have the DC component that is constant in the steady state, these variables can be used for averaging using (1-1). Compared with original signals, the DC-like averaged signals allow the variable-step solver to choose bigger simulation steps under the same tolerance condition.

Instead of deriving the AVM model by averaging variables after the dq transformation, the calculation of AVM models of AC/DC or DC/AC converters can use the converse process, i.e. pre-processing the AC variables and then using the dq transformation. This method neglects all the switching higher harmonics and only considers the fundamental component of the AC variables and the switching functions. The variables on the AC and DC sides are related through the fundamental components of the switching functions. The application of the dq transformation on these fundamental components gives the AVM model of the AC/DC or DC/AC converters. This method will give the same result as that obtained from the first one and is more applicable in the modelling of an EPS. In this thesis, it will be referred as the DQ0 modelling technique. The DQ0 modelling technique is based on the fact that the DC component in the d and q axis is only derived from the fundamental components of the AC variables. The DC component of the DC-side variables is also only dependent on the fundamental components of the AC-side variables and the switching functions. The DQ0 model has been successfully used in the modelling of MOET aircraft EPS [9, 22, 28-30]. There the DQ0 model has been proved to be an effective way to study a large-scale EPS with high accuracy and computation efficiency, especially under balanced conditions where the DQ0 model simulates more than 1000 times faster than the corresponding behavioural model. It is, so far, one of the most efficient models in EPS studies [9]. In this thesis, the DQ0 model is used for comparison

studies. The efficiency of the DQ0 model, however, decreases dramatically when the system is under unbalanced conditions. This is due to the negative sequence present in the system. In the DQ0 model this negative sequence will become the second harmonic in the d- and q-axis variables. Since the dq variables are no longer constant in the steady state, the simulation speed becomes much slower and is comparable to simulating with non-transformed AC variables.

An alternative approach that can address this problem is to use dynamic phasors (DP) modelling, also referred to as the general averaging model [31]. The DPs essentially are time-varying Fourier series coefficients. This method can model not only the fundamental component but also higher harmonics in the system. Considering the significant harmonic components, the DP model is capable of retaining the dominant dynamic features of an EPS and is ideally suited for functional non-switching EPS modelling. Under balanced conditions, the DP variables are complex DC quantities which allow big steps during the simulation process and make the DP model very efficient. Under unbalanced conditions, the three complex DP variables (one per phase) are still DC valued and will result in much better computational performance compared with the DQ0 approach. This thesis will thoroughly discuss the application of the DP concept in modelling electrical power systems. The concept of the DP and its benefits will be fully discussed in the next chapter.

### 1.4.3 Software

The software chosen in this research is Dymola, standing for dynamic modelling laboratory. This software uses the open Modelica modelling language which allows users to freely create their own model libraries or modify the ready-made model libraries.

Dymola provides a number of different integration algorithms for the simulation of dynamic systems, including LSODAR, DASSL, Radau IIa etc. These algorithms can be categorised into variable step size and fixed step size

integration algorithms. For the variable step size algorithms, the solver estimates the local error at every step. The integration step size is chosen in such a way that the local error is smaller than the desired maximum local error, defined via the relative and absolute tolerances. That is:

$$\left|\text{error}_{\text{local}}\right| < \text{tolerance}_{\text{relative}} \times |x| + \text{tolerance}_{\text{absolute}} \tag{1-2}$$

This implies that, if smaller tolerances are defined, a smaller step sizes will be used. In other words, a variable (or adaptive) step size implies that the algorithm adapts the step size to meet a local error criterion based on the tolerance [32].

Modelica is an object oriented modelling language for component-oriented modelling of complex systems. This language is developed under open source license since 1996 by the non-profit Modelica Association, based at Linköping University, Sweden. Now this language is widely used in automotive, aerospace, robotics and other applications. Many free Modelica model libraries for different physical domains are also available. The Dymola/Modelica standard library contains a large collection of components to model analogue and digital electronics, electrical machines, thermal and rotational mechanical systems, as well as input/output control blocks.

In contrast to data flow-oriented languages with directed inputs and outputs, such as the widely known Matlab/Simulink tool, Modelica employs an equation-based modelling technique and all the variables are treated equally. This avoids algebraic loop issues. The equation-based modelling concept also results in a faster modelling process and a significantly increased re-usability, since the interconnection between models is easier and simpler than that of the signal-flow based modelling. There is no need to explicitly define the interface equations and predefine the input and output signals.

In Modelica, each model can contain several sub-models at different modelling levels. This means one system architecture only has to be built once and can be

simulated at different levels of accuracy and at different speeds depending on the purpose of the study. Results can be compared and validated between different levels of modelling [33].

## 1.5 Aim of Thesis and Thesis Structure

The aim of the thesis is to develop functional DP models suitable for the future MEA electrical power systems studies. Specific objectives of the DP model in functional modelling layer are summarized as follows:

- Deriving the functional DP models to maximize the computational efficiency but meet the accuracy criteria, under both balanced and unbalanced conditions.
- Developing a library of DP models common to a large number of aircraft electrical power system architectures in Dymola/Modelica software package.

In order to accomplish the research objectives mentioned above, this thesis is organized into seven chapters. The structure of the thesis will be outlined as follows:

**Chapter 1** is the introduction to the thesis which shows the motivation of this research. The trend of moving from conventional aircraft to more-electric aircraft is explained. Different modelling techniques are reviewed and the multi-level modelling concept is introduced in this chapter. Models in the functional level are introduced and the move to the DP model is explained. The thesis layout is also outlined.

**In Chapter 2**, the DP concept and other different phasors, including the traditional phasor and the frequency-shift phasor, are introduced. In addition, the DP concept, for the first time, is extended to modelling the time-varying frequency system and a practical implementation is proposed. The proposed

theory in this chapter allows a wider application of DPs in EPS modelling studies. Through discussion of different phasors, the advantage of the DP is demonstrated. The potential of the DP modelling technique is demonstrated through comparing ABC (three-phase models), DQ0 (models in dq frame) and DP models, using a generator-load system under balanced and unbalanced conditions.

In **Chapter 3**, the DP model of uncontrolled rectifiers is developed. The DP model is developed using the vector theory and Taylor expansion. The method proposed in this chapter is the key through the entire thesis. The algebraic relations between the magnitudes of the AC-side voltage and current vectors, and the DC-link voltage and current serve as the basis for developing the DP model. The DP model capability of handling higher harmonics is demonstrated using the $6^{th}$ harmonic component on the DC-link voltage. The unbalanced operation condition is handled with the DP model by viewing the negative sequence as a disturbance and the operation point is selected according to the positive sequence. This creative idea enables the DP model handling the unbalanced case conveniently. The DP model of the uncontrolled rectifier is validated through experiment. In this chapter, the DP modelling technique is also extended to modelling multi-pulse rectifiers. An 18-pulse ATRU is used to demonstrate this capability and the performance of the DP ATRU model under both balanced and unbalanced operation conditions is shown.

In **Chapter 4,** the DP model for controlled PWM rectifiers is developed. The model is validated experimentally under balanced, lightly unbalanced and open-circuit fault conditions. The validation of the DP model under line-to-line fault conditions is accomplished by comparing with the ABC model through simulations. Experiments could not be done due to the high current during short circuits. The computation efficiency of the DP model is also illustrated.

In **Chapter 5**, the DP technique is extended to modelling a multi-generator, multi-frequency system. The DP modelling technique is for the first time applied to model multi-frequency EPS's. A common reference frame or master

frame is chosen and all the DP variables are transformed into the master frame. A twin-generator system with generators rotating at different speed is studied. The simulation results from ABC, DQ0 and DP models are compared. The accuracy and the efficiency of DP model are demonstrated.

In **Chapter 6**, the modelling issues associated with the complex aircraft electrical power system is discussed in detail. The large MOET aircraft power system architecture is described. A twin-generator aircraft power system, which is a representative of the MOET aircraft power system architecture, is simulated using the ABC, DQ0 and DP models. It is the first time the DP modelling technique has been used in modelling the entire aircraft EPS. Case studies based on such a system are presented, including a start-up operation, the loss of one generator and the impact of a line-to-line fault on the system. The computation time comparison is carried out.

**Chapter 7** gives the conclusion of this thesis. The research work and contributions are summarised. Future work based this thesis is discussed. The publications from this research work are listed.

# Chapter 2

# Introduction of Dynamic Phasors

## 2.1 Background

The Dynamic Phasor (DP) modelling technique was firstly introduced in the 1990s [31]. The DPs are in nature some Fourier coefficients and the modelling technique based on DPs is essentially a frequency-domain analysis method. Compared with other time-domain modelling techniques, the DP models offer a number of advantages over conventional methods. This is due to the fact that the oscillating waveforms of AC circuits become constant or slowly-varying in the DP domain and different frequency components can be handled separately with convenience. This property of DPs allows large step sizes in numerical simulations, and makes simulation potentially faster than conventional time-domain models under both balanced and unbalanced conditions.

The DP modelling technique was firstly used in modelling series resonant converters [31], where the converter switching functions were represented with DPs of fundamental components of switching functions. Since then, the DP technique has been widely implemented in modelling electronic converters as well as electromagnetic machines.

The DP models for AC machines have been well developed during the past few years. These include induction machines [34], synchronous machines [35-37], double-fed induction machines [38, 39]. All these DP models are derived by transforming the time-domain linear machine models, either in the three-phase

frame (ABC models) or in a synchronous rotating frame (DQ0 models), into the DP domain. The DP models are called "DP-ABC" model or "DP-DQ0" model depending on whether three-phase or DQ0 variables are represented as DPs. Such transformations can be derived using the properties of DPs and are mathematically straightforward as illustrated in the references and in this chapter.

The DP concept has also been comprehensively applied to model power electronic devices especially in Flexible AC Transmission Systems (FACTS). A DP model for Unified Power Flow Controllers (UPFC) has been reported in [40], where the DP model is developed based on the corresponding DQ0 model with the active power and reactive power controlled through DP-domain controllers. Similarly, the DP models for Static Synchronous Compensators (STATCOM) were studied in [41-43] and some new control techniques based on the DP concept have been proposed in [41]. The DP models for thyristor-based HVDC transmission systems with Equi-distant Pulse Control (EPC) can also be found in [44] and [45]. By transforming the DPs of three-phase variables into sequence components and implementing superposition theory, the authors of [44] and [45] developed a DP model for this type of thyristor-based EPC controlled converter. The DP models of other power electronic devices include Thyristor Controlled Series Capacitors (TCSC) [46-48], DC-DC converters [49] and Unified Series-Shunt Compensators (USSC) [50]. These DP models, by representing the switching functions with DPs, illustrate good performance and high efficiency compared with behavioural models.

All the above DP models are based on the assumption that the fundamental frequency of the system is constant. However, this is not true in many practical situations. In addition, though the DP model for these controlled power electronic devices have been well developed under balanced conditions based on non-switching averaging models, the DP models which are suitable for unbalanced conditions still require further studies and investigation. The behaviour of such controlled power electronic devices, under balanced and unbalanced conditions, is dependent on the control technique. Thus the

mapping of different control structures into DPs is of high importance. For example, the controller of an active filter in STATCOM [41] is based on the frame-invariant active power and reactive power control and this is different from the controller of traditional controlled rectifier units (CRUs), which use active and reactive components of input currents for the control and require orientation on the voltage vector at the connection point. These two different control structures require different DP models, even though both of them are PWM-controlled IGBT converters. This will be further discussed and a DP model of CRU suitable for both balanced and unbalanced conditions will be developed in the Chapter 4.

Furthermore, all the above reported DP models are focusing on the controlled power electronic devices and there is no reference dealing with modelling three-phase or multi-phase uncontrolled rectifier using dynamic phasors. The switching behaviour of uncontrolled rectifiers is exclusively dependent on the power system conditions. The averaging modelling technique has been widely used to study this type of converters [51-53] and the DP model will be developed using the averaging models. This will be discussed in the Chapter 3.

In this chapter, firstly the DP concept will be introduced, illustrated and discussed through some simple examples. The benefits from DP models will then be demonstrated by comparing four different types of models, i.e. ABC, DQ0, DP-ABC and DP-DQ0 models. Furthermore, the DP concept will be extended to modelling systems with time-varying fundamental frequencies. Finally a chapter summary is given.

## 2.2 Dynamic Phasors

The DP concept is based on the generalized averaging theory [31]. The DPs essentially are some time-varying Fourier coefficients. For a time-domain quasi-periodic waveform $x(\tau)$, defining a time-moving window $\tau \in (t-T, t]$, as shown in Figure 2-1, and viewing the waveforms in this window to be periodic,

the Fourier expansion of the waveform in this interval can be represented by the following Fourier series:

$$x(\tau) = \sum_{k=-\infty}^{\infty} X_k(t) e^{jk\omega_s \tau} \tag{2-1}$$

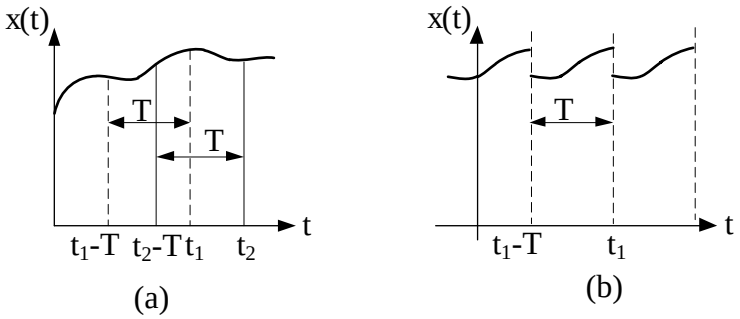


Figure 2-1 (a) Defined moving window at time $t_1$ and $t_2$, (b) equivalent periodic signal at time $t_1$

where $\omega_s=2\pi/T$ and T is the length of the window. Though the window length T can be an arbitrary value, it is common that the fundamental period of the signal is chosen to avoid the DPs spreading over the entire frequency axis. $X_k(t)$ is the $k^{th}$ Fourier coefficient in a complex form and is referred to as a "dynamic phasor". It is defined as follows:

$$X_k(t) = \frac{1}{T} \int_{t-T}^{t} x(\tau) e^{-jk\omega_s \tau} d\tau = \langle x \rangle_k \tag{2-2}$$

where k can be any integer and is called the DP index. The triangular pair '‹ ›' is used as the DP calculation symbols for any time-domain variables. In contrast to the traditional Fourier coefficients, these Fourier coefficients are time-varying as the integration interval (window) slides with time. The selected set of DPs, or K with $k \in K$, defines the approximation accuracy of the waveform. For example, for DC-like variables and signals the index set only includes the component k=0, and for purely sinusoidal waveforms, with the window length equal to one period gives k=1. The waveforms with fundamental and higher harmonics, for example, the 3rd harmonic, the index set can be chosen at K={1,3}. This is illustrated in the following table.

Table 2-1 DPs for some common functions

| DP index | Constant $A_0$ | $A_1\cos(\omega t+\varphi_1)$ | $A_1\sin(\omega t+\varphi_1)$ $+A_3\sin(\omega t+\varphi_3)$ |
|---|---|---|---|
| k=0 | $\mathbf{A_0}$ | 0 | 0 |
| k=1 | 0 | $0.5\,\mathbf{A_1}e^{-J\varphi 1}$ | $0.5j\,\mathbf{A_1}e^{-J\varphi 1}$ |
| k=3 | 0 | 0 | $0.5j\,\mathbf{A_3}e^{-J\varphi 3}$ |

According to (2-2), a DP calculator is proposed as follows:

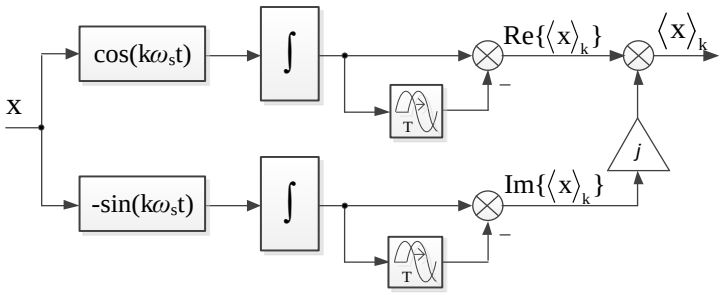


Figure 2-2 DP calculator

This can be implemented on a computer and used to obtain the DP when the variable x exists as a function of time. As will be seen later, if the modelling is done solely in term of DPs, this calculator would not be needed.

The case where the fundamental frequency $\omega_s$ is time-varying will also need to be considered in the analysis of electrical power systems, e.g. when a generator is speeding up. In this case, the definition of DPs in (2-2) needs to be modified and this will be discussed in section 2.5.

A key factor in developing DP models is the relation between the derivatives of the variable x(t) and the derivatives of $k^{th}$ Fourier coefficients given as:

$$\left\langle \frac{dx}{dt} \right\rangle_k = \frac{d\langle x\rangle_k}{dt} + jk\omega_s \langle x\rangle_k \tag{2-3}$$

**Proof:**

The derivative of the DP ‹x›$_k$ can be written as:

$$\frac{d\langle x\rangle_k}{dt}=\frac{d\left(\frac{1}{T}\int_{t-T}^{t}xe^{-jk\omega_s t}dt\right)}{dt}=\frac{1}{T}xe^{-jk\omega_s t}\Big|_{t-T}^{t} \tag{2-4}$$

Considering the fact that

$$\begin{aligned}\left\langle\frac{dx}{dt}\right\rangle_k&=\frac{1}{T}\int_{t-T}^{t}\frac{dx}{dt}e^{-jk\omega_s t}dt\\&=\left(\frac{1}{T}xe^{-jk\omega_s t}\,|_{t-T}^{t}+jk\omega_s\frac{1}{T}\int_{t-T}^{t}xe^{-jk\omega_s t}dt\right)\end{aligned} \tag{2-5}$$

It is seen that on the right side of (2-5), the first term is equal to $\frac{d\langle x\rangle_k}{dt}$ and the second term is $jk\omega_s\langle x\rangle_k$. Thus the combination of (2-4) and (2-5) comes to (2-3).

Another important property of DPs is that the k$^{th}$ phasors of a product of two time-domain variables can be obtained via the convolution of corresponding dynamic phasors:

$$\langle xy\rangle_k=\sum_i\langle x\rangle_{k-i}\langle y\rangle_i \tag{2-6}$$

The proof of (2-6) relies on the fact that:

$$\langle xy\rangle_k=\frac{1}{T}\int_{t-T}^{t}xye^{-jk\omega_s t}dt \tag{2-7}$$

$$y=\sum_i\langle y\rangle_i e^{ji\omega_s t} \tag{2-8}$$

Substituting (2-8) to (2-7) yields:

$$\langle xy\rangle_k=\frac{1}{T}\int_{t-T}^{t}xe^{-jk\omega_s t}\sum_i\langle y\rangle_i e^{ji\omega_s t}dt \tag{2-9}$$

Exchanging the order of sum and integration gives

$$\langle xy\rangle_k=\sum_i\langle y\rangle_i\frac{1}{T}\int_{t-T}^{t}xe^{-jk\omega_s t}e^{ji\omega_s t}dt=\sum_i\langle x\rangle_{k-i}\langle y\rangle_i \tag{2-10}$$

The derivative property (2-3) and the convolution property (2-6) play a key

role when transforming the time-domain models into the DP domain. Algebraic manipulations in this paper will also exploit the following conjugate property:

$$\langle x \rangle_k^* = \left( \frac{1}{T} \int_{t-T}^{t} x e^{-jk\omega t} dt \right)^* = \frac{1}{T} \int_{t-T}^{t} x e^{jk\omega t} dt = \langle x \rangle_{-k} \tag{2-11}$$

# 2.3 Comparison of Different Phasors

## 2.3.1 Steady-state Phasors

The phasor representation of steady-state, constant-frequency sinusoidal signals has been used for decades in analysing the steady-state behaviour of voltages and currents in a linear network [54]. Let us briefly review the traditional phasor concept through the steady-state solution of an RL circuit shown in Figure 2-3. The transient behaviour of the circuit can be described by the equation

$$v = Ri + L\frac{di}{dt} \tag{2-12}$$

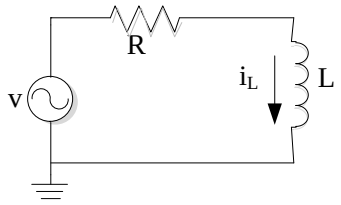


Figure 2-3 An RL circuit

where v is a sinusoidal function defined as $v = v_a \cos(\omega_0 t)$. The traditional phasor representation assumes that the sinusoidal motions are of constant frequency and constant amplitude. The corresponding phasor representation of the RL circuit can be written as

$$V(\omega_0) = [R + j\omega_0 L] I(\omega_0) \tag{2-13}$$

where $V(\omega_0)$ and $I(\omega_0)$ represent the phasors which are constant complex numbers. It can be noticed that, in the phasor model, the differential operator in

(2-12) becomes $j\omega_0$ and the phasor relationships become algebraic linear functions. This reduces the complexity and order of the model and allows fast analysis and simulation for power system studies. However, the steady-state or quasi-stationary assumption limits the application of such phasors to transient studies in power systems.

### 2.3.2 Frequency-shift Phasors

Due to the limitation of traditional phasors, a time-varying phasor was proposed in [54-57] . The band limited signals can be represented by their analytic signals defined as:

$$x_a(t) = x(t) + j\hat{x}(t) \tag{2-14}$$

where $\hat{x}(t)$ is the Hilbert transformation of time-domain signal x(t) and can be obtained by the convolution:

$$\hat{x}(t) = \frac{1}{\pi t} * x(t) = \frac{1}{\pi}\int_{-\infty}^{\infty} \frac{x(\tau)}{t-\tau} d\tau \tag{2-15}$$

The Fourier transformation of $\hat{x}(t)$ is given by:

$$\hat{X}(\omega) = \{-j\,\mathrm{sgn}(\omega)\}X(\omega) \tag{2-16}$$

Combining (2-14) and (2-16) yields the Fourier transformation of the analytic signal $x_a(t)$ as:

$$X_a(\omega) = X(\omega) + \mathrm{sgn}(\omega)X(\omega) = \begin{cases} 2X(\omega) & \omega > 0 \\ X(\omega) & \omega = 0 \\ 0 & \omega < 0 \end{cases} \tag{2-17}$$

The spectrum of the band limited signal x(t) and the spectrum of its analytic signal $x_a(t)$ are shown below:

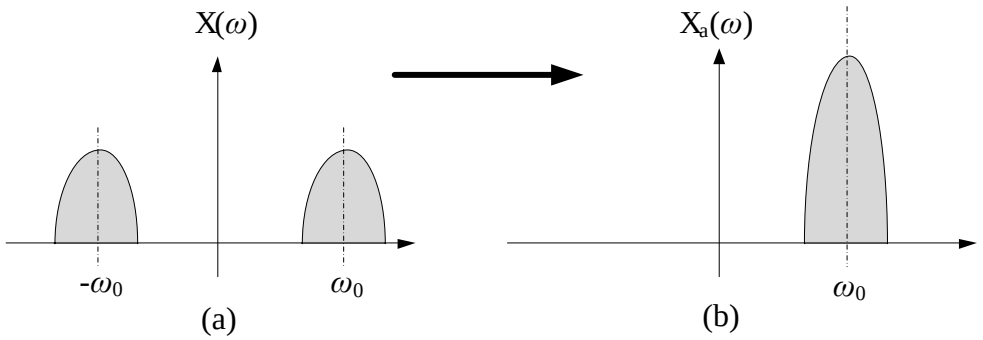


Figure 2-4 (a) the spectrum of a band limited signal (b) the spectrum of its analytic signal

The frequency-shift phasor is now defined as:

$$x_b(t) = x_a(t)e^{-j\omega_0 t} \tag{2-18}$$

The frequency-shift phasor $x_b(t)$, compared with the traditional phasor, is a time-varying complex number which includes all the information of the original signal x(t).

The time-domain signal can be calculated from the frequency-shift phasor as:

$$x(t) = \Re e\left\{x_b(t)e^{j\omega_0 t}\right\} \tag{2-19}$$

The spectrum of $x_b(t)$ is shown in Figure 2-5.

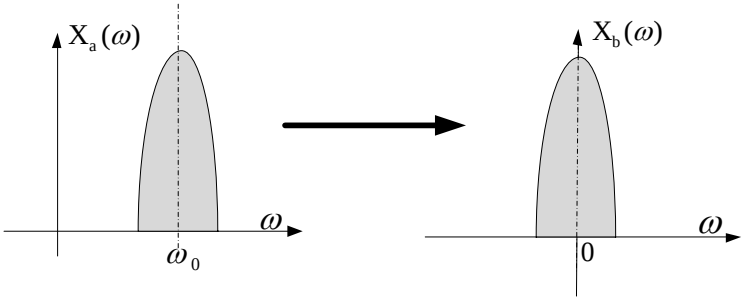


Figure 2-5 Spectrum of frequency-shift phasors $x_b(t)$

As can be seen in Figure 2-5, the spectrum of the frequency-shift phasor is the same as that of the analytic signal but shifted by an angular frequency $-\omega_0$, i.e. $X_b(\omega)=X_a(\omega-\omega_0)$. From the point of view of simulation performance, the shift in the spectrum to the "base band" makes the simulation of power system transients more efficient when compared with time-domain modelling

techniques. However, this type of phasor is constrained to the band-limited signal and is not suitable for studying power systems with wider range of frequency components.

When using the frequency-shift phasor to represent non-band-limited signals, the frequency shift applied to the analytic signal is, from (2-18), only $-\omega_0$. Though the base band spectrum $X_b(\omega)$ spreads around $\omega=0$, other higher harmonics will exist in the system and condense around system harmonic frequencies. For example a 3rd harmonic of x(t) will reduce to a second harmonic in the phasor model, as illustrated in Figure 2-6. The existing higher harmonics will deteriorate the performance of the phasors model and slow down the simulation process.

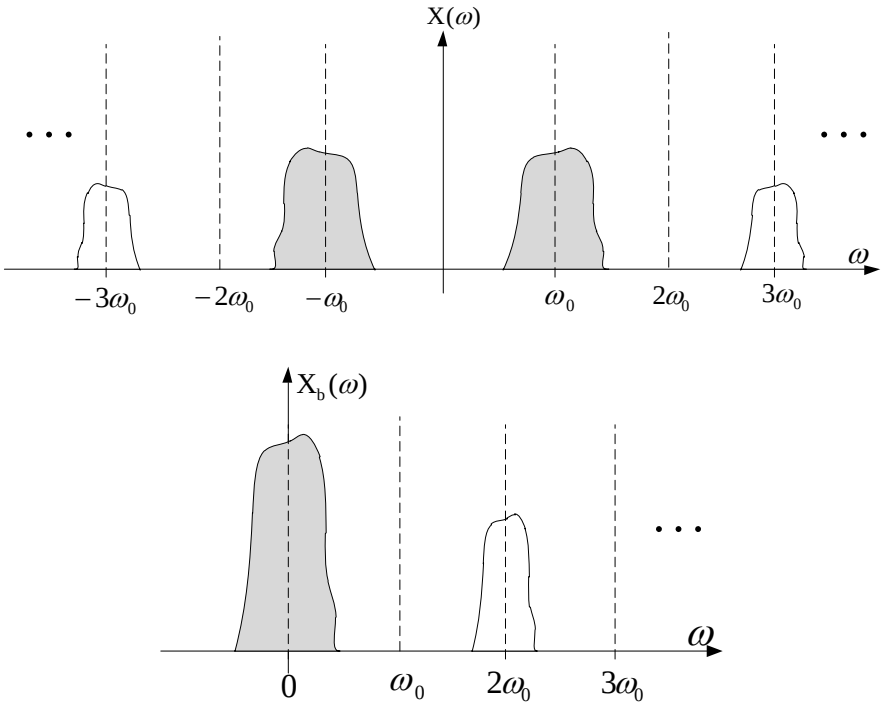


Figure 2-6 Frequency-shift phasors of non-band-pass signals

## 2.3.3 Dynamic Phasors

The DP concept, which has been introduced in section 2.2, is an extension of the frequency-shift phasor. Writing the equation (2-1) in the frequency domain gives

$$X(\omega) = \sum_{k=-\infty}^{+\infty} X_k(j\omega - jk\omega_0) \tag{2-20}$$

As seen in (2-20), instead of shifting the spectrum by $-\omega_0$, the DP concept is to shift all the band limited components about $k\omega_0$ by $-k\omega_0$. This makes all the harmonics become base band components, as illustrated in Figure 2-7.

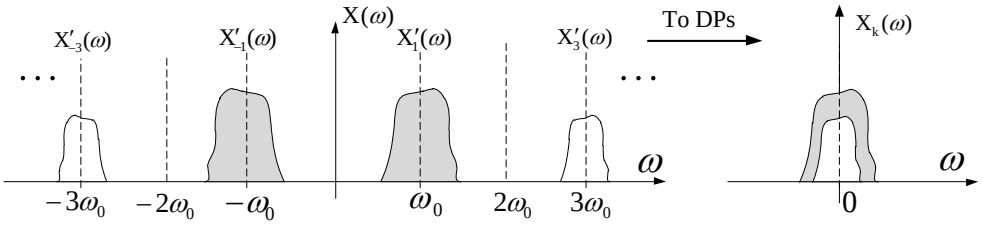


Figure 2-7 Illustrative spectrum of dynamic phasors for signals with higher harmonics

This property allows the DP to handle power system with harmonics more effectively. The use of power electronic devices gives rise to other higher harmonics in the system. Shifting all these harmonics to base-band signals gives the DP great potential for the modelling of electrical power systems.

## 2.4 Introduction to Dynamic Phasor Modelling: A Simple Example

The electrical component models in the DP domain are building blocks for a DP-based network simulation. In this section, we start from DP models of basic electrical elements, i.e. resistors, inductors and capacitors in order to explain this DP concept. The DP model of a RLC circuit will be simulated to show how to implement the DP models. After that, some examples will be given to reveal the application of DPs in modelling of EPS systems.

## 2.4.1 Dynamic Phasor Model of RLC Components

The DP models of RLC components are based on their time-domain voltage dynamic equations. Using the DP definition and properties, the DP transformation can be achieved conveniently.

**(i) Resistance element**

The time-domain voltage equation for a resistor can be expressed by:

$$v = Ri \tag{2-21}$$

Calculating the DPs on both sides of (2-21) using the definition in (2-2) gives

$$\langle v \rangle_k = \frac{1}{T}\int_{t-T}^{t} v(\tau)e^{-jk\omega_s\tau}d\tau = \frac{1}{T}\int_{t-T}^{t} Ri(\tau)e^{-jk\omega_s\tau}d\tau = \langle Ri \rangle_k \tag{2-22}$$

If the resistance R is constant and time invariant, it can be moved out from the integration symbol and we obtain the DP form as:

$$\langle v \rangle_k = R\langle i \rangle_k \tag{2-23}$$

**(ii) Inductance element**

The time-domain voltage equation for an inductor is written as

$$v = L\frac{di}{dt} \tag{2-24}$$

The DP form of (2-24) can be obtained by employing the DP definition (2-2) and the differential property (2-3). The result is:

$$\langle v \rangle_k = \left\langle L\frac{di}{dt} \right\rangle_k = L\frac{d\langle i \rangle_k}{dt} + j\omega L\langle i \rangle_k \tag{2-25}$$

**(iii) Capacitance element**

The DP model for a capacitor can be derived the same way as that for the inductor and is written as:

$$\langle i \rangle_k = C\frac{d\langle v \rangle_k}{dt} + j\omega C\langle v \rangle_k \tag{2-26}$$

The DP model of RLC components suggests an equivalent circuit representation of the RLC circuit as shown in Figure 2-8 (b).

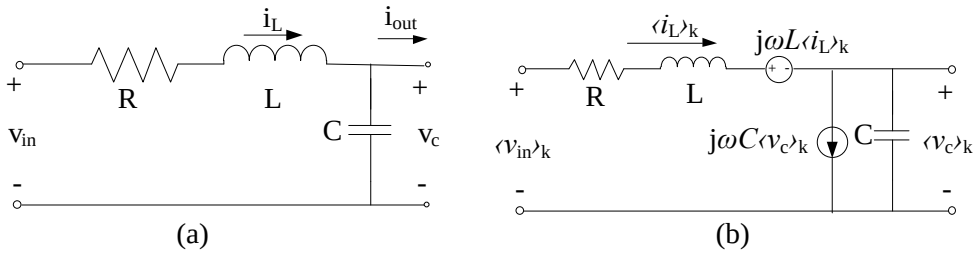


Figure 2-8 Transformation of RLC circuits from time domain to DP domain.(a) time-domain model; (b) DP model

## 2.4.2 RLC Circuit Simulation with Dynamic Phasors

This simple example is used to illustrate the potential benefits which can be derived from DP models. The simulation scheme is shown in Figure 2-8, with $v_{in}$=230V at 60Hz, R=1Ω, L=0.05H, C=2×10-4F, $i_L(0)$=0 and $v_C(0)$=0. The DP model of RLC circuit in the state-space form is

$$
\begin{aligned}
\langle v_{in}\rangle_0 &= R\langle i_L\rangle_0 + L\frac{d\langle i_L\rangle_0}{dt} + \langle v_c\rangle_0 \\
\langle v_{in}\rangle_k^R &= R\langle i_L\rangle_k^R + L\frac{d\langle i_L\rangle_k^R}{dt} - k\omega L\langle i_L\rangle_k^I + \langle v_c\rangle_k^R \\
\langle v_{in}\rangle_k^I &= R\langle i_L\rangle_k^I + L\frac{d\langle i_L\rangle_k^I}{dt} + k\omega L\langle i_L\rangle_k^R + \langle v_C\rangle_k^I \\
C\frac{d\langle v_c\rangle_0}{dt} &= \langle i_L\rangle_0 - \langle i_{out}\rangle_0 \\
C\frac{d\langle v_c\rangle_k^R}{dt} &= \langle i_L\rangle_k^R - \langle i_{out}\rangle_k^R - k\omega C\langle v_c\rangle_k^I \\
C\frac{d\langle v_c\rangle_k^I}{dt} &= \langle i_L\rangle_k^I - \langle i_{out}\rangle_k^I + k\omega C\langle v_c\rangle_k^R \\
k &= 1,2,3.....
\end{aligned}
\tag{2-27}
$$

The DP with k=0 corresponds to the existence of a DC input or non-zero initial conditions. If the input voltage and all variables are sinusoidal, then the DP index k=1. If the input voltage has higher harmonics, the DP index k=2,3,4… will be included depending on the accuracy required. For the sinusoidal case

here, the DPs with index k=0,2,3… are equal to zero, and the DP model becomes a 4th-order system. Though the RLC circuit order of DP model is higher than the time-domain model, which is 2nd order, the variables in the DP models fluctuate much slower, as shown in Figure 2-9. In the time domain, $i_L$ and $v_c$ are sinusoidal with frequency f=60Hz. In Figure 2-9, the sinusoidal waveforms are reconstructed from the DPs using equation (2-1) and are identical to those obtained from a conventional time-domain simulation. However, the real and imaginary parts of DP variables, $\langle i_L \rangle_1$ and $\langle v_c \rangle_1$, fluctuate at a much slower frequency. This allows the solver to use bigger simulation steps and enables an accelerated simulation process.

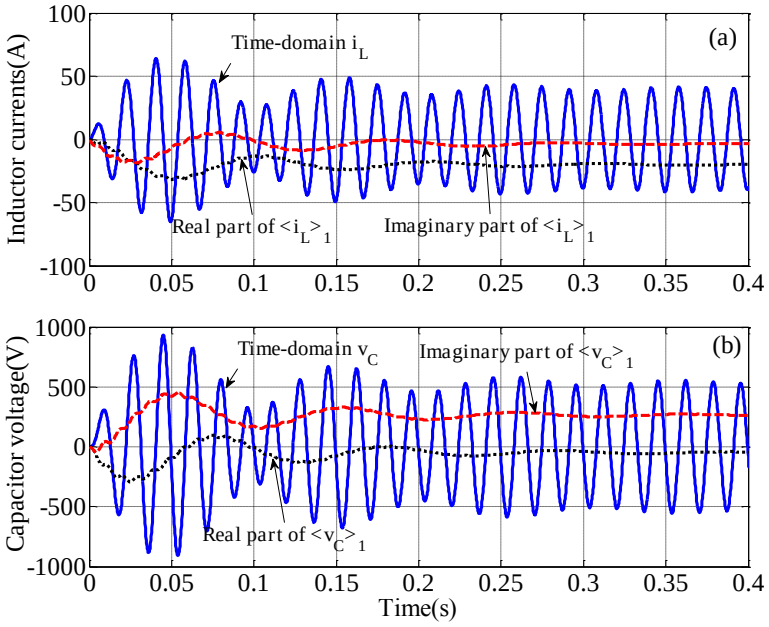


Figure 2-9 Comparison of simulation results of the RLC circuit from different models, (a) currents $i_L$, (b) voltage $v_C$

## 2.4.3 Comparison of Different Modelling Techniques

The previous section illustrated that the DPs have potential for acceleration simulation studies in the modelling of power systems. This section will illustrate the accuracy and computational efficiency of different modelling

techniques using an example system with phase imbalance. These models include:

1) Standard three-phase domain modelling (ABC)
2) DQ0 modelling using EPS components library reported in [9] (DQ0)
3) Dynamic phasor (DP) model based on three-phase system equations (DP-ABC)
4) DP model based on EPS DQ0 equations (DP-DQ0)

We use an example three-phase EPS as depicted in Figure 2-10. The voltage source is a synchronous generator with the rated voltage $V_{phase}$=230V and f=400Hz. Simulations were run on Intel(R) i7 CPU 960 at 3.20GHz with 24.0GB of RAM using Modelica/Dymola v.7.4 software. The Dassl algorithm was chosen as the solver and the tolerance was set at $10^{-4}$. To evaluate the computation efficiency of these modelling techniques, the CPU time taken for the simulation process has been used. The simulation accuracy has been evaluated by comparing the simulation results in the Figure 2-11 and Figure 2-12. The errors of the DP model are less than 5% compared with ABC models under balanced conditions. The errors under unbalanced conditions are slightly higher but still less than 10%. The accuracy of DP models is dependent on the DP index chosen. The higher order of DP index, the more accurate the model will be.

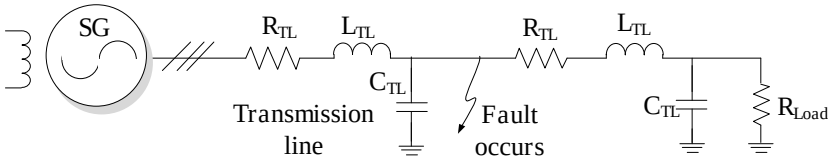


Figure 2-10 Simulation EPS scheme for modelling technique comparison studies

A line-to-line fault between phase A and phase B is applied to the system at t=0.2s. The fault is simulated by connecting phase A and phase B with a 1mΩ resistor. The current flowing through the resistive load, $R_{Load}$, is chosen for comparative studies. In order to compare the results more conveniently, the results from all models are transformed to the time-domain ABC frame and

drawn in the same figure, as shown in Figure 2-11. The currents for all the modelling techniques are well-matched under both balanced and unbalanced conditions. Even during the transient period from balanced to unbalanced conditions, the errors of the DQ0 model and the DP model are less than 10% when compared with ABC benchmark model.

Figure 2-12 depicts the load currents from different models before and after the line fault occurs. It can be noticed that before the fault occurs, the load currents in the DQ0, DP-ABC and DP-DQ0 models are all DC-like. However, during the fault conditions, the current in the DQ0 model, $i_d$, starts to fluctuate at a frequency of 800Hz because of the negative sequence in the system under unbalanced conditions. The negative sequence when transformed in to DQ frame, become the second harmonic in d and q axes. This will be further discussed in Chapter 3. On the other hand, the DP variable $\langle i_a \rangle_1$ and $\langle i_d \rangle_{1,2}$ are still DC-like after a short-transient period with much slower fluctuations.

The computation times are presented in Figure 2-13. It shows that ABC model nearly keeps the same simulation speed before and after the fault occurs. This is understandable as the reconfiguration will not change the complexity of the system and the fundamental in the system keeps at 400Hz without change. It also can be noticed that the DQ0 model is the fastest model before the fault occurs; however after the fault occurs, this model becomes the slowest one. As has mentioned before, under balanced conditions, the variables in the DQ0 models are DC-like, which enables the solver to evolve with large simulation steps. However, under unbalanced conditions, the second harmonic (f=800Hz) appears in the d and q axes in the DQ0 model. In this case, the solver is obliged to choose smaller simulation steps and the simulation process is hence decreased dramatically.

From Figure 2-13, it is important to realise that, under balanced conditions, though the DP variables are DC-like, the system order is higher than that of the DQ0 model. This makes the DP model slower than the DQ0 model. However, the slowly fluctuation DP variables under unbalanced condition enables the

solver to implement larger simulation steps under fault conditions, which makes the total simulation time of DP models shorter than that of the DQ0 model.

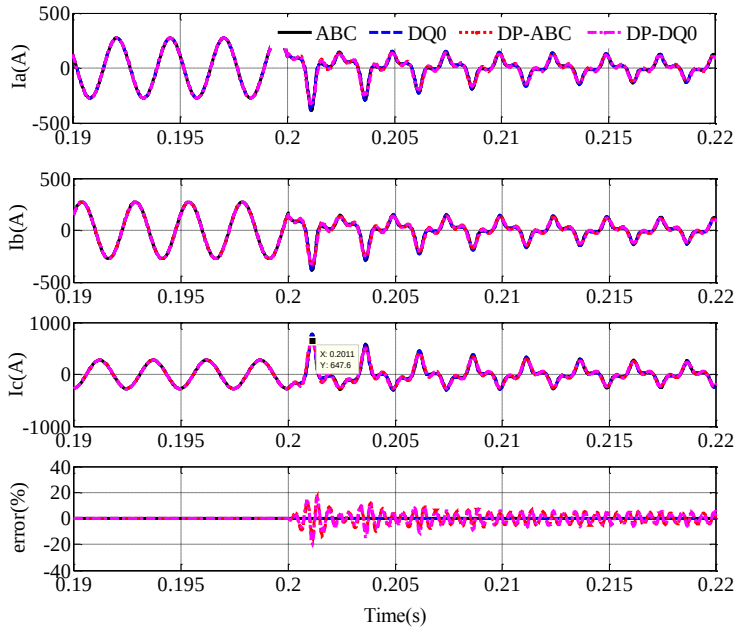


Figure 2-11 Phase currents flowing through resistor comparison among four modelling methods, with Line-to-Line fault occurs at t=0.2s

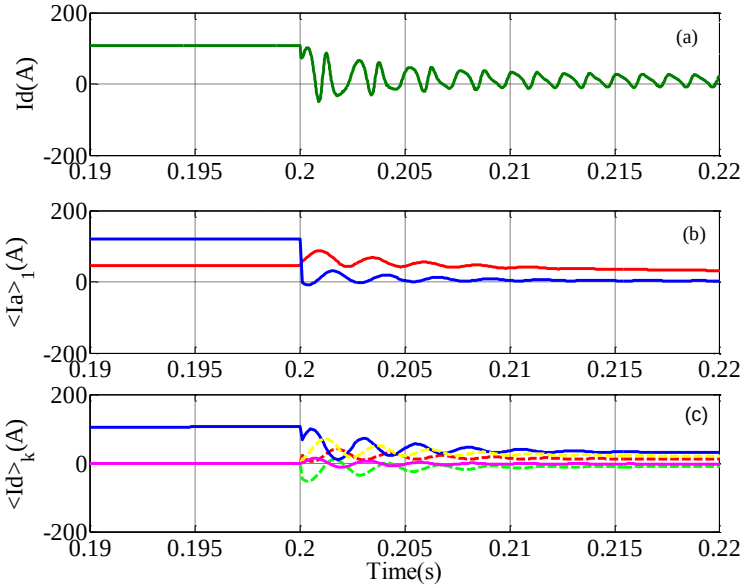


Figure 2-12 Phase A current of the resistive load in different models in different domains

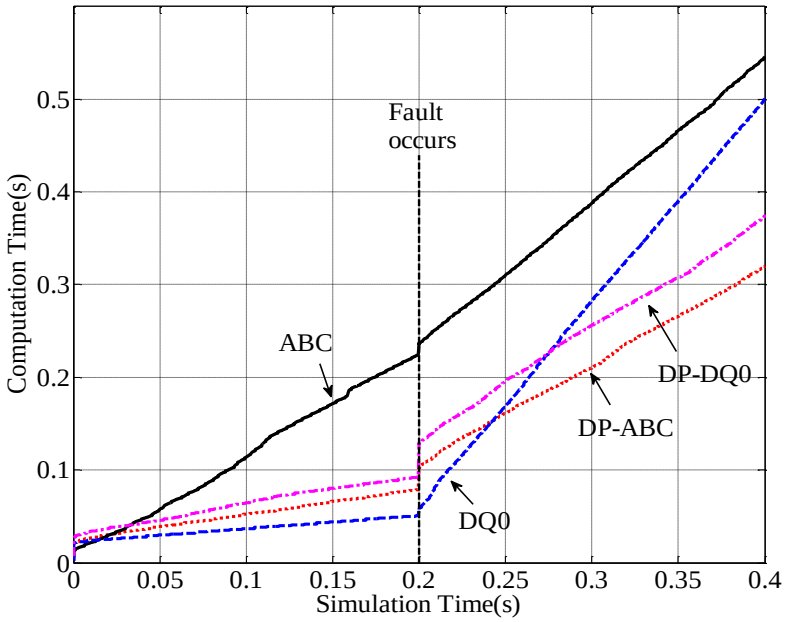


Figure 2-13 Computation time comparison among four modelling methods, with Line-to-Line fault occurs at t=0.2s

The comparison of the four modelling methods, ABC, DQ0, DP-ABC and DP-DQ0, through this example EPS, illustrates the potential application of DPs in modelling the EPS for acceleration simulation studies, especially for the system under fault condition. With an increase in system complexity, the benefits from DPs will increase simultaneously. This will be further revealed in the following chapters of this thesis.

## 2.5 DPs of Varying Frequency Waveforms

So far, all the phasors are with constant frequencies. The application of DPs in modelling time-varying frequency system has been touched on in [31]. There, the author chooses the sliding window with phase angle $\theta(t)=2\pi$ for the time-varying frequency signals. The theory developed in [31] is difficult for application and there is no further development in this area ever since. In this section, the author proposes another methodology that makes the application of DPs in modelling time-varying EPS conveniently.

### 2.5.1 Phase-Based Dynamic Phasors

As briefly discussed in section 2.2, the analysis based on (2-3) is valid if $\omega_s$ is constant. In the case where the frequency $\omega_s$ is time varying, the selection of the sliding window in the DP definition should be reconsidered. The main concern of DPs of time-variant frequency waveforms is to derive the differential of a DP when $\omega_s$ varies. For a waveform with a time-varying frequency, it is convenient to define the DP using the phase angle $\theta$ instead of the angular speed $\omega_s$ as was used in (2-2). Using the phase angle $\theta$, the DP definition becomes:

$$\langle x \rangle_k = \frac{1}{2\pi} \int_{\theta-2\pi}^{\theta} x(t(\theta)) e^{-jk\theta} d\theta \qquad k = 0,1,2,\ldots \tag{2-28}$$

where

$$\theta(t) = \int_0^t \omega_s(\tau) d\tau \tag{2-29}$$

This approach was reported in [31] but not used since [31] derived the derivative property as:

$$\begin{aligned} \left\langle \frac{dx(t)}{dt} \right\rangle_k = {} & \frac{d\langle x(t) \rangle_k}{dt} - \frac{1}{2\pi} x\{t - T(t)\} e^{-jk\theta\{t-T(t)\}} \omega\{t - T(t)\} \dot{T}(t) \\ & - \frac{1}{2\pi} \int_{\theta-2\pi}^{\theta} x(t) e^{-jk\theta(t)} \left\{ \frac{\dot{\omega}(t)}{\omega(t)} - jk\omega(t) \right\} d\theta \end{aligned} \tag{2-30}$$

The proof of (2-30) is given in the Appendix I. As can be seen above, when the frequency is constant, i.e. $\dot{\omega}(t)=0$ and $\dot{T}(t)=0$, (2-30) will reduce to (2-3). However, for the case when $\dot{\omega}(t)\neq 0$, the equation (2-30) is complicated and this makes the implementation difficult. In particular, the two terms x(t-T(t)) and $\omega$(t-T(t)) will require the solver to store all the results during the T(t) period. Each simulation step will involve a search process of x(t-T(t)) and $\omega$(t-T(t)) to derive the DP differentials in (2-30) and thus the simulation process will slow down dramatically.

In this thesis, the author introduces an alternative approach to derive a simple formula for the DP of the differential term and this is:

$$\left\langle \frac{\mathrm{dx}}{\mathrm{dt}} \right\rangle_{\mathrm{k}} = \frac{\mathrm{d}\left\langle \mathrm{x} \right\rangle_{\mathrm{k}}}{\mathrm{dt}} + \mathrm{jk}\omega(\mathrm{t})\left\langle \mathrm{x} \right\rangle_{\mathrm{k}} \tag{2-31}$$

**Proof:**

According to the definition in (2-28), the differential of DP $\langle x \rangle_k$ can be expressed as:

$$\frac{\mathrm{d}\left\langle \mathrm{x} \right\rangle_{\mathrm{k}}}{\mathrm{dt}} = \frac{\mathrm{d}\left\langle \mathrm{x} \right\rangle_{\mathrm{k}}}{\mathrm{d}\theta}\frac{\mathrm{d}\theta}{\mathrm{dt}} = \omega(\mathrm{t})\frac{1}{2\pi}\mathrm{x}\{\mathrm{t}(\theta)\}\mathrm{e}^{-\mathrm{jk}\theta}\Big|_{\theta-2\pi}^{\theta} \tag{2-32}$$

On the other hand, the DP form of a differential term $dx/dt$ can be given as:

$$\begin{aligned}\left\langle \frac{\mathrm{dx}}{\mathrm{dt}} \right\rangle_{\mathrm{k}} &= \frac{1}{2\pi}\int_{\theta-2\pi}^{\theta}\frac{\mathrm{dx}(\mathrm{t}(\theta))}{\mathrm{dt}}\mathrm{e}^{-\mathrm{jk}\theta}\mathrm{d}\theta \\ &= \frac{1}{2\pi}\int_{\theta-2\pi}^{\theta}\frac{\mathrm{dx}(\mathrm{t}(\theta))}{\mathrm{d}\theta}\frac{\mathrm{d}\theta}{\mathrm{dt}}\mathrm{e}^{-\mathrm{jk}\theta}\mathrm{d}\theta\end{aligned} \tag{2-33}$$

Since $d\theta/dt=\omega(\mathrm{t})$, (2-33) can be written as:

$$\left\langle \frac{\mathrm{dx}}{\mathrm{dt}} \right\rangle_{\mathrm{k}} = \frac{1}{2\pi}\int_{\theta-2\pi}^{\theta}\omega(\mathrm{t})\mathrm{e}^{-\mathrm{jk}\theta}\mathrm{dx}(\mathrm{t}(\theta)) \tag{2-34}$$

Exchanging the integration terms in (2-34) yields:

$$\left\langle \frac{\mathrm{dx}}{\mathrm{dt}} \right\rangle_{\mathrm{k}} = \frac{1}{2\pi}\mathrm{x}(\mathrm{t}(\theta))\omega(\mathrm{t})\mathrm{e}^{-\mathrm{jk}\theta}\Big|_{\theta-2\pi}^{\theta} + \mathrm{jk}\omega(\mathrm{t})\frac{1}{2\pi}\int_{\theta-2\pi}^{\theta}\mathrm{x}(\tau(\theta))\mathrm{e}^{-\mathrm{jk}\theta}\mathrm{d}\theta \tag{2-35}$$

The first term, from (2-32) is equal to $d\langle x\rangle_k/\mathrm{dt}$. The second term, from (2-28) is equal to $jk\omega(t)\langle x\rangle_k$.

Compared with (2-30) proposed in [31], the derivative property derived here is much simpler and convenient for application. Comparing the two equations and recalling the DP definition yields:

$$-\frac{1}{2\pi}\mathrm{x}\{\mathrm{t}-\mathrm{T}(\mathrm{t})\}\mathrm{e}^{-\mathrm{jk}\theta\{\mathrm{t}-\mathrm{T}(\mathrm{t})\}}\omega\{\mathrm{t}-\mathrm{T}(\mathrm{t})\}\dot{\mathrm{T}}(\mathrm{t}) + \left\langle \mathrm{jk}\omega(\mathrm{t}) - \frac{\dot{\omega}(\mathrm{t})}{\omega(\mathrm{t})} \right\rangle_{\mathrm{k}} = \mathrm{jk}\omega(\mathrm{t})\left\langle \mathrm{x} \right\rangle_{\mathrm{k}} \tag{2-36}$$

The inverse transformation of this phase-base DP is

$$x(t) = \sum_{-\infty}^{\infty} X_k(t) e^{jk\theta(t)} \tag{2-37}$$

## 2.5.2 Application of Phase-Based DPs

The validation of the proposed phase-based DPs will be validated in this sector, using the simulation scheme as in Figure 2-10. However, the SG is replaced with an ideal AC source with the frequency ramps up from 50Hz to 400Hz during 25ms from t=0.3s.

The phase-based DP model of an RLC circuit is shown in Figure 2-14.

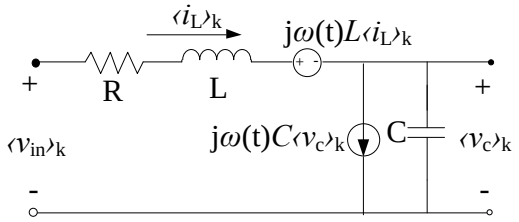


Figure 2-14 Phase based DP model of an RLC circuit

Comparing Figure 2-14 with the DP model of the RLC circuit shown in Figure 2-8, the only difference is that the constant angular speed $\omega$ becomes a time-varying variable $\omega(t)$ in Figure 2-14. This property conveniently modifies the DP concept for modelling the time-variant frequency system.

The load currents from DP models are transformed to the time-domain and compared with results from ABC models, as shown in Figure 2-15. The results from phase-based DP model and ABC are identical during the constant-frequency period and frequency ramping-up period.

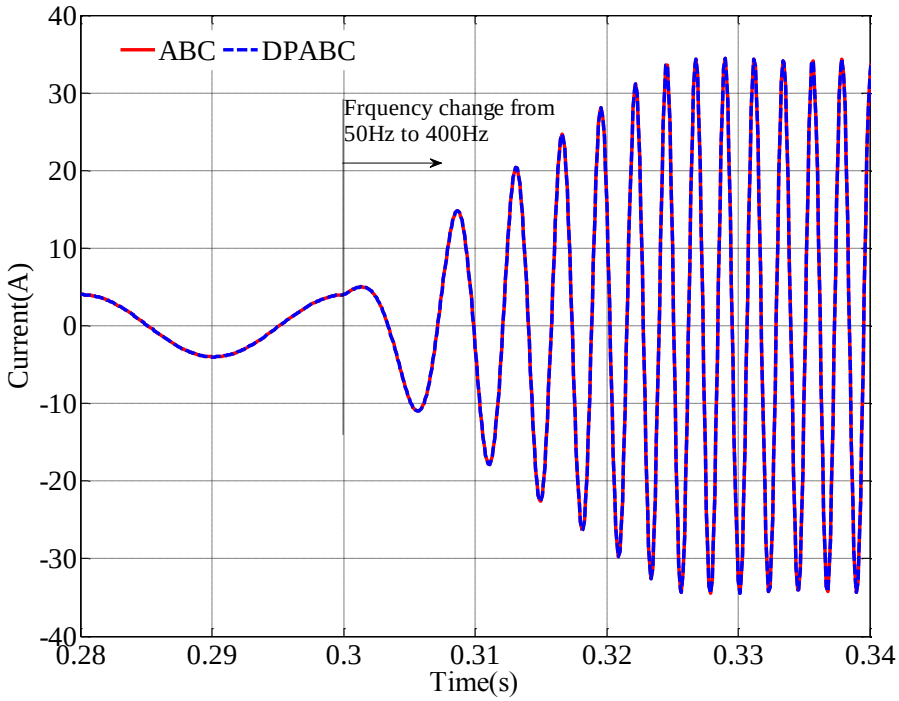


Figure 2-15 Phase A currents flowing through resistor comparison between DP model and ABC model with frequency ramping up from 50Hz to 400Hz during 25ms

## 2.6 Chapter Summary

In this chapter, the DP concept has been introduced. The DPs are essentially some Fourier coefficients. Compared with traditional phasors and frequency-shift phasors, DPs can be used for modelling systems with higher harmonics and for transient response studies. The DC-like DP variables allows the solver to apply larger steps during the simulations. This is the key advantage of DP models compared with the DQ0 model, the performance of which deteriorates under unbalanced conditions. The phase-based DP concept, which is based on phase angle $\theta$ instead of angular speed $\omega$ in DPs, is proposed for modelling time-varying frequency systems. The derivative property revealed in this thesis makes this type of DP more convenient for application and the phase-based DP models can be conveniently modified from the ω-based DP. For that reason, in following chapters of the thesis, the term 'DP' will refer to phase-based DPs.

# Chapter 3

# Dynamic Phasor Models of Uncontrolled Rectifiers

## 3.1 Introduction

The MEA concept leads to a wide use of electrical power in the aircraft and makes the AC/DC power converter an integral part of the EPS. Conventionally, AC/DC power conversion is performed through three-phase uncontrolled converters. A majority of the power electronics applications such as switching DC power supplies, AC motor drives, DC servo drives, and so on, use such uncontrolled rectifiers [58]. The diode rectifiers have the advantage of high reliability, low cost and relatively high efficiency. However, the main drawback of these rectifiers is that they inject significant current harmonics into the power network.

In order to meet the aircraft power quality requirement, for example standard ISO-1540, the multi-pulse uncontrolled rectifier is a preferred option for the aircraft electrical power system. Multi-pulse diode rectifiers have long been used in the passenger aeroplanes to produce 28V DC from 400Hz AC input [59]. Even with the development of Pulse-Width Modulated (PWM) AC/DC converters, multi-pulse rectifiers are still the dominant technology in commercial jet aeroplanes due to their better reliability and relatively compact size. The multi-pulse uncontrolled rectifier is normally fed by a phase-shift transformer, typically an autotransformer. The whole unit is called an “Auto-Transformer Rectifier Unit” (ATRU). The

advantages of the ATRU are simple circuit structure, low cost, high reliability and relatively high efficiency and compact size. The drawback of the ATRU is that the total weight of the ATRU can be relatively high due to the use of the transformer.

In the MEA electrical power system, the ATRU usually acts as an interface between the AC source and a large DC bus instead of individual DC loads. Although the ATRU is a mature technology in the aviation industry, its presence in the MEA power system has raised concerns such as the optimization of the input current distortion and dynamic interactions with the rest of the power system especially if the EPS has many speed-regulated motor drive systems. Such concerns are attributed to the increased loading which results in increased harmonics on the AC distribution system. The work of this chapter is motivated by the simulation study of the MEA electrical power system and the study of dynamic interactions between individual subsystems. Since the switching behaviour in the ATRU arises exclusively from the multi-pulse rectifier, the development of a functional model for the ATRU comes down to the development of functional models for the multi-phase converters.

The modelling of rectifiers has been of particular interest to the power engineering community for a long time [60]. The detailed device simulation approach, which is based on the non-linear diode model, has been widely used in the software such as MATLAB/Simulink, SABER etc. The main challenge of using these detailed models is the increased computational complexity which leads to a longer simulation time especially when the overall system contains many rectifiers.

Apart from the detailed modelling techniques, several approaches for modelling uncontrolled rectifiers have been reported in previous works. These are the dynamic average modelling method [51, 61, 62], the impedance mapping method [59, 63, 64] and the DQ0 modelling method [65]. Three dynamic average models of the three-phase rectifier have been reported recently. These are classical Average-Value Model (AVM) [27, 52], improved AVM [66] and parametric AVM [53, 67]. In the classical AVM, the DC current is assumed to be constant. The improved AVM, instead of assuming a constant DC current, considered a

linearly varying DC current during the switching intervals. However, these two models are both developed for balanced operation and thus are not suitable for unbalanced system studies. In the parametric AVM, the rectifier is considered as an algebraic block such that the relationships between the AC terminals and DC link are modelled with parametric functions. Though the parametric AVM model can handle balanced and unbalanced situations, the derivation of parameters involves extensive simulations beforehand and different systems will have different parameters. The DQ0 model of the diode bridge involves the transformation of the switching function from the ABC frame to the synchronous DQ0 frame. This modelling technique has been used in modelling a 12-pulse ATRU and shown to be effective under both balanced and unbalanced conditions [65].

The impedance mapping method provides a useful tool to predict the input impedance of the AC/DC converters for stability studies. The basic idea is to map the voltage and current of the AC and DC sides into the frequency domain and obtain the input impedance of the converter. However, the impedance models are in analytical form which is not suitable for simulation studies of the entire electrical power system.

This chapter presents a switching model and a DP-based functional model of the uncontrolled rectifier. The switching model is used as the benchmark model and the diodes are modelled with controlled ideal switches. The relationship between the voltage vector and the DC-link voltage, and the current vector and the DC-link current, are used for deriving the DP model. Considering that the operation point of DBs is determined by the positive sequence, the negative sequence under unbalanced conditions has been viewed as a disturbance in the DP model. Together with the DP model for the phase-shift transformer, the DP model for the ATRU is presented as well. Compared with the DQ0 model, both the $2^{nd}$ and $6^{th}$ harmonic on the DC-link voltage are included in the DP system. This enables the DP model to cover the AC imbalanced voltage and DC ripple voltage for both continuous and discontinuous operation.

This chapter will be organized as follows. Firstly, the switching model and DP model of three-phase rectifiers will be introduced and validated with experimental results under both balanced and unbalanced conditions. Based on the developed DP model of three-phase rectifiers, a DP model for the multi-pulse rectifier will be established. After that, the switching model and DP model of the ATRU will be given and tested under balanced and unbalanced conditions. The efficiency and performance of the DP model for the ATRU will be demonstrated through comparing with switching models at the end of this chapter.

# 3.2 Benchmark Model of the Diode Bridge

A three-phase Diode Bridge (DB) rectifier is shown in Figure 3-1. In general, it is supplemented by an output DC filter $L_fC_f$ and a front-end inductance $L_s$ representing a long feeding cable, or leakage inductances in the transformer. The DC load is represented as an equivalent resistance $R_L$.

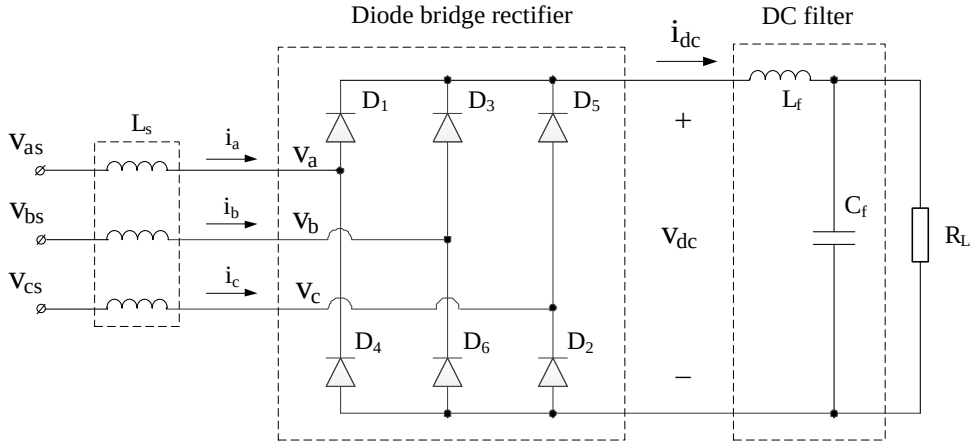


Figure 3-1 Three-phase diode bridge rectifiers simulation scheme

The benchmark model is established in the software Dymola 2012. The diode is modelled as an ideal switch controlled by the forward voltage and conducting current, as shown in Figure 3-2. In the model, the ideal switch is controlled by the voltage $v_{ak}$ and current $i_{ak}$. When the diode is forward biased ($v_{ak}>0$), it starts to conduct with a small forward voltage $V_f$ across it and conduction resistance $R_{on}$. It

turns off when the conducting current $i_{ak}$ becomes zero. Apart from the diode, the other electrical elements are derived from the standard library in Dymola 2012.

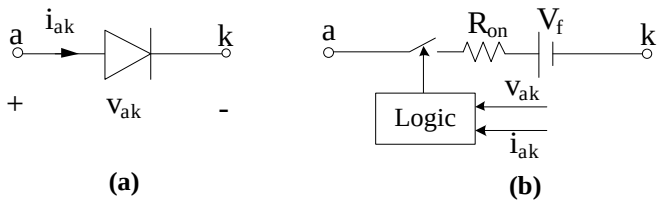


Figure 3-2 Switching model of diodes in the benchmark model, (a) diagram of a diode (b) switching model of diodes

# 3.3 DQ0 Model of the Diode Bridge

The main idea for the non-switching model is to represent the converter switching behaviour with the fundamental components. For a three-phase diode bridge, a non-switching model for a three-phase diode bridge in the DQ0 frame has been developed in [65] and is briefly described in this section.

The non-switching DB model is well developed and documented [58, 68]. Under the symmetrical balanced supply, the terminal voltages can be represented as:

$$\mathbf{V}_{abc} = \begin{bmatrix} v_a \\ v_b \\ v_c \end{bmatrix} = V_m \begin{bmatrix} \sin(\omega t + \varphi) \\ \sin(\omega t + \varphi - 2\pi/3) \\ \sin(\omega t + \varphi + 2\pi/3) \end{bmatrix} \tag{3-1}$$

where $V_m$ is the voltage magnitude, $\omega$ is the supply electrical frequency and $\varphi$ is the initial phase angle. For an ideal six-pulse rectifier shown in Figure 3-1, the switching functions can be described as in Figure 3-3.

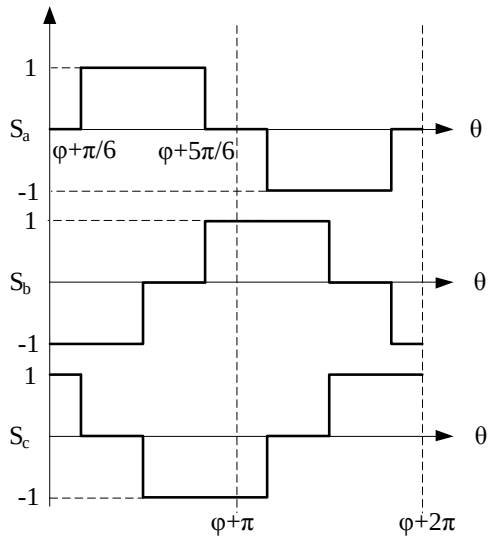


Figure 3-3 Switching functions of a diode bridge under ideal operation conditions

The fundamental component of the diode switching function is then given as [58]:

$$\mathbf{S}_{abc} = \begin{bmatrix} S_a \\ S_b \\ S_c \end{bmatrix} = \frac{2\sqrt{3}}{\pi} \begin{bmatrix} \sin(\omega t + \varphi) \\ \sin(\omega t + \varphi - 2\pi/3) \\ \sin(\omega t + \varphi + 2\pi/3) \end{bmatrix} \tag{3-2}$$

Using (3-2), the voltage relationship between the AC and DC terminals of the diode bridge is [65]:

$$v_{dc} = \mathbf{S}_{abc}^{T} \mathbf{V}_{abc} \tag{3-3}$$

$$\mathbf{I}_{abc} = \mathbf{S}_{abc} i_{dc} \tag{3-4}$$

where $\boldsymbol{I}_{abc}=[i_a \quad i_b \quad i_c]^T$, $v_{dc}$ and $i_{dc}$ are the rectifier output DC voltage and current respectively. The effect of $L_s$ on the AC side causes an overlap angle $\mu$ and results in a commutation voltage drop. This drop can be represented as a variable resistance $r_\mu$ depending on the system frequency [27]. Since the commutation voltage drop has been moved on to the DC side, the switching signals for 3-phase bridge rectifier can be applied without considering the effect of overlap angle, as shown in Figure 3-4. From (3-1), (3-2) and (3-4), the fundamental component of switching functions and input currents can be seen to be in phase.

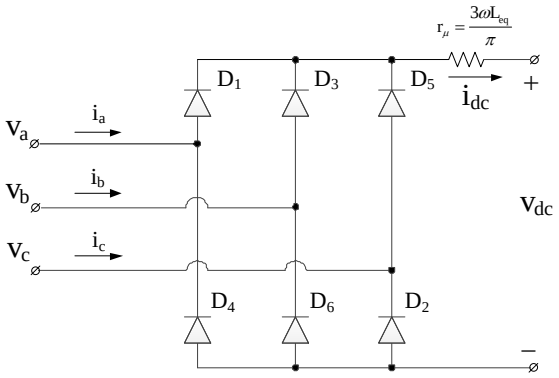


Figure 3-4 Three-phase diode rectifier with overlap angle resistance

The voltage vector is defined as:

$$\vec{v} = 2/3\left(v_a + v_b e^{j2\pi/3} + v_c e^{-j2\pi/3}\right) \tag{3-5}$$

Substituting the three-phase voltage in (3-1) into (3-5) yields:

$$\vec{v} = V_m e^{j\varphi} e^{j\omega t} \tag{3-6}$$

Equation (3-6) shows that the voltage vector defined in (3-5) rotates with an angular speed $\omega$ with an initial angle $\varphi$ at t=0. The magnitude is equal to the peak value of the phase voltage. Defining a synchronous rotating frame dq rotating at $\omega$ rad/s with $\theta$=0 at t=0 the voltage vector in this frame can be expressed as:

$$\vec{v}e^{-j\omega t} = v_d + jv_q = V_m e^{j\varphi} \tag{3-7}$$

The vector of fundamental currents can be defined in the same way. These vectors are depicted in a complex plane as in Figure 3-5.

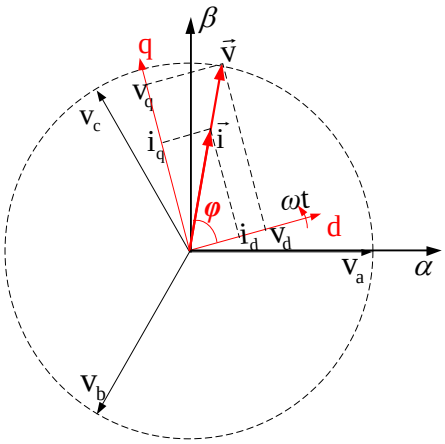


Figure 3-5 Voltage and current vectors in the complex plane

Combining (3-6) and (3-7) and separating the real and imaginary parts yields the three-phase variables and the components in the dq frame:

$$\mathbf{f}_{dq} = \mathbf{T}\mathbf{f}_{abc} \tag{3-8}$$

where **T** is the transformation matrix:

$$\mathbf{T} = \frac{2}{3}\begin{bmatrix} \cos\omega t & \cos(\omega t - 2\pi/3) & \cos(\omega t + 2\pi/3) \\ -\sin\omega t & -\sin(\omega t - 2\pi/3) & -\sin(\omega t + 2\pi/3) \end{bmatrix} \tag{3-9}$$

Combining (3-3) and (3-9) yields:

$$v_{dc} = \frac{3\sqrt{3}}{\pi}|\vec{v}| = \frac{3\sqrt{3}}{\pi}\sqrt{v_d^2 + v_q^2} \tag{3-10}$$

$$|\vec{i}| = \sqrt{i_d^2 + i_q^2} = \frac{2\sqrt{3}}{\pi} i_{dc} \tag{3-11}$$

With the assumption that the front-end inductance, $L_s$, is relatively small, the input fundamental current can be considered to be in phase with the input voltage. Its d and q components are express as:

$$i_d = |\vec{i}|\cos\varphi; \quad i_q = |\vec{i}|\sin\varphi \tag{3-12}$$

where

$$\varphi = \tan^{-1}\left(\frac{v_q}{v_d}\right) \tag{3-13}$$

The presence of $L_s$ will make the voltage and current vector out of phase and (3-13) will give some discrepancy. However, in this thesis, this effect has been neglected due to the relatively small inductance in the system. The DC-link voltage in (3-10) will reduce due to the commutation (commutation angle $<60^o$) and this effect can be taken into account by introducing an additional resistor $r_u$ at the DC output with [58]:

$$r_u = 6fL_s \tag{3-14}$$

where f is the line frequency.

From (3-10) to (3-14), the 6-pulse rectifier can be represented by Figure 3-6.

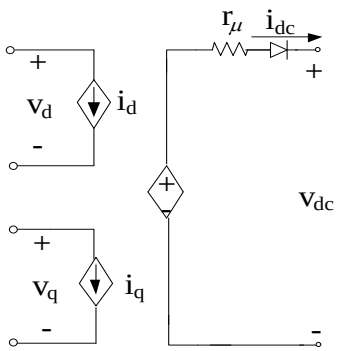


Figure 3-6 The diode bridge equivalent circuit in the dq frame

Equations (3-10)-(3-14) comprise the relations between the DB input voltage/current expressed through their dq components and the output DC voltage/current. These equations will be employed for the development of the DB model in the DP domain.

# 3.4 Dynamic Phasor Model of Diode Bridges

The requirement for the DP-based functional model is time-efficiency with good accuracy (<5% error compared with the benchmark model), under both balanced and unbalanced conditions including line faults. The DP model is based on the relationship between the voltage vector and DC-link voltage, and the current vector and DC-link current. The challenge is to map these relations into DPs. This task, being mathematically straightforward for balanced conditions, turns into a complex problem when unbalance or line fault occurs. The solution of this task is proposed in the following sections. The proposed DP is based on the relationship between the AC-side voltage vector and the DC-link voltage, and the AC-side current vector and the DC-link current. It is also important to point out that the DC-link side of the DP model is interfaced with time-domain models. The main consideration of this time-domain interface is to avoid modelling a single diode in DP, which is cumbersome to derive. It will also allow the DP model a wider application to be combined with other time-domain model based software. The transformation from the DP domain to the time domain on the DC side is

convenient and will not affect the simulation time. This will be shown in the following sections of this chapter.

This section explains the mapping of these relationships into the DP domain in the following order. Firstly, we express the time-domain vectors with the DPs of three-phase variables; secondly, the DC-link voltage and current are mapped into DPs; the developed DP model is validated by comparing results from experiments.

### 3.4.1 Dynamic Phasor of Vectors

The voltage and current vectors play a key role for developing the DQ0 model of three-phase rectifiers. This is also true for developing DP models. The AC terminal voltage can be represented by the set of phase components:

$$v_i = V_i \cos(\omega t + \varphi_i), \quad i = a,b,c \tag{3-15}$$

where $V_i$ (i=a,b,c) is the phase voltage magnitude, and $\varphi_i$ (i=a,b,c) is the phase angle. Using the Euler formula [69] , the equation (3-15) can be rewritten as:

$$v_i = \frac{V_i e^{j\varphi_i} e^{j\omega t} + V_i e^{-j\varphi_i} e^{-j\omega t}}{2}, \quad i = a,b,c \tag{3-16}$$

Recalling Table 2-1, the DP conjugate property (2-11) gives:

$$\langle v_i \rangle_1 = \frac{1}{2} V_i e^{j\varphi_i}, \quad \langle v_i \rangle_{-1} = \langle v_i \rangle_1^* = \frac{1}{2} V_i e^{-j\varphi_i}, \ i = a,b,c \tag{3-17}$$

Combining the vector definition (3-5), (3-16) and (3-17) results in:

$$\begin{aligned} \vec{v} = & \frac{2}{3} e^{j\omega t} \left\{ \langle v_a \rangle_1 + \langle v_b \rangle_1 e^{j2\pi/3} + \langle v_c \rangle_1 e^{-j2\pi/3} \right\} \\ & + \frac{2}{3} e^{-j\omega t} \left\{ \langle v_a \rangle_1^* + \langle v_b \rangle_1^* e^{j2\pi/3} + \langle v_c \rangle_1^* e^{-j2\pi/3} \right\} \end{aligned} \tag{3-18}$$

This equation illustrates that the time-domain voltage vectors can be calculated through three-phase DPs. The two terms on the right-hand side define the positive and negative sequences of the AC voltage vector. The latter will appear under unbalanced conditions. Expressing the vector in the synchronous dq frame given in (3-7), equation (3-18) becomes:

$$\begin{aligned}\vec{v}e^{-j\omega t} &= v_d + jv_q \\ &= \frac{2}{3}\left\{\langle v_a\rangle_1 + \langle v_b\rangle_1 e^{j2\pi/3} + \langle v_c\rangle_1 e^{-j2\pi/3}\right\} + \frac{2}{3}e^{-2j\omega t}\left\{\langle v_a\rangle_1^* + \langle v_b\rangle_1^* e^{j2\pi/3} + \langle v_c\rangle_1^* e^{-j2\pi/3}\right\}\end{aligned} \tag{3-19}$$

The first term on the right side of (3-19) arises from the positive sequence with no harmonics. The real and imaginary part represents the DC components of $v_d$ and $v_q$. The second term arises from the negative sequence and represents the second harmonic of $v_d$ and $v_q$. Defining:

$$V_{d0} = \frac{2}{3}\Re e\left\{\langle v_a\rangle_1 + \langle v_b\rangle_1 e^{j2\pi/3} + \langle v_c\rangle_1 e^{-j2\pi/3}\right\} \tag{3-20}$$

$$V_{q0} = \frac{2}{3}\Im m\left\{\langle v_a\rangle_1 + \langle v_b\rangle_1 e^{j2\pi/3} + \langle v_c\rangle_1 e^{-j2\pi/3}\right\} \tag{3-21}$$

$$V_{d2} = \frac{2}{3}\Re e\left\{\langle v_a\rangle_1^* + \langle v_b\rangle_1^* e^{j2\pi/3} + \langle v_c\rangle_1^* e^{-j2\pi/3}\right\} \tag{3-22}$$

$$V_{q2} = \frac{2}{3}\Im m\left\{\langle v_a\rangle_1^* + \langle v_b\rangle_1^* e^{j2\pi/3} + \langle v_c\rangle_1^* e^{-j2\pi/3}\right\} \tag{3-23}$$

the vector in dq frame in (3-19) can be expressed as

$$\vec{v}e^{-j\omega t} = v_d + jv_q = \left\{V_{d0} + jV_{q0}\right\} + e^{-2j\omega t}\left\{V_{d2} + jV_{q2}\right\} \tag{3-24}$$

Expansion of the above equation gives:

$$v_d = \mathrm{Re}\left(\vec{v}_{dq}\right) = V_{d0} + V_{d2}\cos 2\omega t + V_{q2}\sin 2\omega t \tag{3-25}$$

$$v_q = \mathrm{Im}\left(\vec{v}_{dq}\right) = V_{q0} + V_{q2}\cos 2\omega t - V_{d2}\sin 2\omega t \tag{3-26}$$

From the two equations above, it can be concluded that the DPs $\langle v_d\rangle_k$ and $\langle v_q\rangle_k$ cover the zero and 2nd harmonics (i.e. the DP index set K={0,2}) in order to represent the supply voltage in the dq frame under both balanced and unbalanced conditions. The dynamic phasors for the voltage dq-frame components are given in Table 3-1, together with the dynamic phasors for the input current $\vec{i}$, derived in a similar manner.

Table 3-1 Dynamic phasors for voltage and current vectors in a synchronously rotating frame

| Variable | Dynamic phasors | |
|---|---|---|
| | k=0 | k=2 |
| $v_d$ | $\langle v_d \rangle_0 = V_{d0}$ | $\langle v_d \rangle_2 = (V_{d2} - jV_{q2})/2$ |
| $v_q$ | $\langle v_q \rangle_0 = V_{q0}$ | $\langle v_q \rangle_2 = (V_{q2} + jV_{d2})/2$ |
| $i_d$ | $\langle i_d \rangle_0 = I_{d0}$ | $\langle i_d \rangle_2 = (I_{d2} - jI_{q2})/2$ |
| $i_q$ | $\langle i_q \rangle_0 = I_{q0}$ | $\langle i_q \rangle_2 = (I_{q2} + jI_{d2})/2$ |

## 3.4.2 DC-link Voltages in DP Domain

In this section, we will transform the DB voltage relation (3-10) into the DP domain. In Section 3.4.1, the DPs of $v_d$ and $v_q$ have been derived. However, the calculation of the DPs of $v_{dc}$ is not easy due to the non-linearity of the square root function in the vector magnitude function (3-10). This function makes the direct application of the DP properties non-analytic. However, with the help of the Taylor expansion, it is possible to express $v_{dc}$ with a polynomial function of $v_d$ and $v_q$. Together with the DP convolution property (2-6), the DP of $v_{dc}$ can be derived.

We re-write the DC-link voltage function (3-10):

$$f_1(v_d, v_q) = v_{dc} = \frac{3\sqrt{3}}{\pi}\sqrt{v_d^2 + v_q^2} \tag{3-27}$$

Approximating the DC-link voltage in (3-27) by the Taylor series requires the selection of an operational point for the expansion. With the assumption that the switching behaviour of the DB is mainly determined by the positive sequence and the negative sequence is treated as a disturbance, the operating point can defined as $\{V_{d0}, V_{q0}\}$.The Taylor expansion of (3-27) is given as:

$$v_{dc} = k_0 + \frac{k_1}{1!}(v_d - V_{d0}) + \frac{k_2}{1!}(v_q - V_{q0}) + \frac{k_3}{2!}(v_d - V_{d0})^2 + \frac{k_4}{2!}(v_q - V_{q0})^2 + \frac{k_5}{2!}(v_d - V_{d0})(v_q - V_{q0}) + \dots \tag{3-28}$$

where $k_i$ (i=0,1,…) are the Taylor expansion coefficients. They are constant and

dependent on the selected operation point $\{V_{d0}, V_{q0}\}$. The calculation of these coefficients is given in Appendix II. Section 3.4.8 will discuss the errors introduced in the assumption that one sequence (the negative sequence in this case) acts as a disturbance.

Though traditionally only the first-order terms are considered, in this study we find that a second order approximation and the truncation of the third and higher order terms in (3-28) provides enough accuracy. This will be demonstrated by a comparative simulation in following sections.

From the Taylor expansion of $v_{dc}$ in (3-28), under balanced conditions where $v_d = V_{d0}$ and $v_q = V_{q0}$, the DC-voltage $v_{dc}$ will be constant and equal to $k_0$ which is associated with the positive sequence of the input voltages. Under unbalanced conditions, the negative sequence will appear and disturb the diode switching function in (3-2). With the operation point $\{V_{d0}, V_{q0}\}$, the impact of the negative sequence is considered as a disturbance. The resulting disturbance to $v_{dc}$ will be effectively represented in (3-27), through the AC-side voltage $v_d$ and $v_q$ in (3-25) and (3-26) which are fluctuating under unbalanced conditions.

Since the DP index set for $v_d$ and $v_q$ is K={0,2}, the same set should be applied for $v_{dc}$ as it is a polynomial algebraic function of $v_d$ and $v_q$, shown in (3-28). Employing the convolution property to the truncated Taylor series, the dynamic phasors of DC-link voltage $v_{dc}$ are derived as follows:

$$\left\langle v_{dc} \right\rangle_0 = k_0 + k_3 \left\langle v_d \right\rangle_2 \left\langle v_d \right\rangle_2^* + k_4 \left\langle v_q \right\rangle_2 \left\langle v_q \right\rangle_2^* + k_5 \left( \left\langle v_d \right\rangle_2 \left\langle v_q \right\rangle_2^* + \left\langle v_d \right\rangle_2^* \left\langle v_q \right\rangle_2 \right) \tag{3-29a}$$

$$\left\langle v_{dc} \right\rangle_2 = k_1 \left\langle v_d \right\rangle_2 + k_2 \left\langle v_q \right\rangle_2 \tag{3-29b}$$

where the dynamic phasors $\langle v_d \rangle_0$, $\langle v_d \rangle_2$, $\langle v_q \rangle_0$ and $\langle v_q \rangle_2$ are given in the Table 3-1. Hence, the dynamic phasors for DC-link voltage are fully defined.

## 3.4.3 Accounting for the DC-Link Voltage Ripple

The converter output voltage calculated with (3-29) exhibits a DC component

under balanced conditions, and includes the 2nd harmonic under unbalance conditions. For functional-level simulation studies this may be sufficient. However, under balanced conditions, a six-pulse DB exhibits the 6th harmonic on the DC side[58]. This section demonstrates how this component can be mapped into the DP model if required.

Under balanced conditions, the 6th harmonic in the DC voltage is due to the 5th and 7th harmonic in the switching function [70] that can be given as:

$$S_{a5,7} = -\frac{2\sqrt{3}}{5\pi}\cos(5\omega t + 5\varphi) + \frac{2\sqrt{3}}{7\pi}\cos(7\omega t + 7\varphi) \tag{3-30a}$$

$$S_{b5,7} = -\frac{2\sqrt{3}}{5\pi}\cos(5\omega t + 5\varphi + \frac{2\pi}{3}) + \frac{2\sqrt{3}}{7\pi}\cos(7\omega t + 7\varphi - \frac{2\pi}{3}) \tag{3-30b}$$

$$S_{c5,7} = -\frac{2\sqrt{3}}{5\pi}\cos(5\omega t + 5\varphi - \frac{2\pi}{3}) + \frac{2\sqrt{3}}{7\pi}\cos(7\omega t + 7\varphi + \frac{2\pi}{3}) \tag{3-30c}$$

Substituting these switching functions into (3-3) and (3-4), the magnitude and phase angle of the 6th harmonic in the DC voltage is:

$$v_{dc6} = -\frac{3\sqrt{3}}{5\pi}\sqrt{V_{d0}^2 + V_{q0}^2} + \frac{3\sqrt{3}}{7\pi}\sqrt{V_{d0}^2 + V_{q0}^2} \tag{3-31}$$

$$\varphi_{dc6} = 6\tan^{-1}\left(\frac{V_{q0}}{V_{d0}}\right) \tag{3-32}$$

The corresponding DP for this 6th harmonic can be given in the same as any other sinusoidal waveform and it is written as:

$$\langle v_{dc}\rangle_6 = \frac{1}{2} v_{dc6} e^{j\varphi_{dc6}} \tag{3-33}$$

This extra DP can be added to the previously derived set (3-29) to represent the DC-link voltage in the DP domain. The time-domain value of the DC-link voltage can be calculated using the DP definition and is given as:

$$v_{dc}(t) = \sum_k \langle v_{dc}\rangle_k e^{jk\omega t} = 2\left\{\Re e\left(\langle v_{dc}\rangle_k\right)\cos k\omega t - \Im m\left(\langle v_{dc}\rangle_k\right)\sin k\omega t\right\} \tag{3-34}$$

where k={0,2,6}. Hence, the DC-link voltage in (3-34) includes the DC

component as well as the 2nd and the 6th harmonics. Under balanced conditions, the 2nd harmonic is absent. However under unbalanced or line fault conditions, it becomes the dominant harmonic component.

### 3.4.4 Rectifier AC Currents

This section addresses the mapping of the rectifier current relation into the DP domain. The linear relationship between the magnitude of the current vector $\left|\vec{i}\right|$ and the DC-link current $i_{dc}$ was given in (3-11) and can be transformed into the DP domain as follows:

$$\left\langle \left|\vec{i}\right| \right\rangle_k = \frac{2\sqrt{3}}{\pi} \left\langle i_{dc} \right\rangle_k \tag{3-35}$$

The AC currents of the rectifier are dependent on the DC load current which is determined jointly by the DC-link voltage $v_{dc}$ and the load itself. In the proposed model, a DP/time-domain interface will be used in the DC-link side, and the calculated DC current (time-domain value) is converted into the DP, as shown in Figure 3-7.

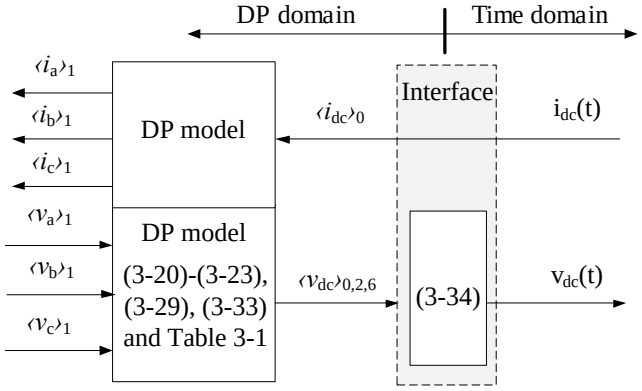


Figure 3-7 Interface of DP model to the time-domain model on the DC-link side

The DP index for $\langle i_{dc} \rangle_k$ for linear loads could of course chosen according to $\langle v_{dc} \rangle_k$, i.e. k={0,2,6}.However, using the following equation

$$\left\langle i_{dc} \right\rangle_0 = i_{dc}(t) \tag{3-36}$$

will allow us to avoid calculating of $\langle i_{dc} \rangle_{2,6}$ with the DP definition (2-1) and thus

no cumbersome calculation of $\int_{t-T}^{t} xe^{-jk\omega t}dt$ is needed. With (3-36), all the DC-link current information will be included in $\langle i_{dc}\rangle_0$. The fluctuation of $i_{dc}$ will be reflected to the fundamental DPs $\langle i_{a,b,c}\rangle_1$ through $\langle i_{dc}\rangle_0$ and this will be illustrated later in this section. From (3-35), the same DP index k=0 will apply to $\langle|\vec{i}|\rangle_k$. The DP for the d- and q-axis components of AC currents can be derived using (3-12) as follows:

$$\langle i_d \rangle_k = \sum_{m=0}^{k} \langle |\vec{i}| \rangle_m \langle \cos\varphi \rangle_{k-m} \tag{3-37a}$$

$$\langle i_q \rangle_k = \sum_{n=0}^{k} \langle |\vec{i}| \rangle_n \langle \sin\varphi \rangle_{k-n} \tag{3-37b}$$

The main challenge in calculating (3-37) is to calculate the DPs for the non-linear functions, $\sin\varphi$ and $\cos\varphi$. As in the previous section, the approximation is executed by a Taylor series. The non-linear terms are expressed via the voltage components in d and q axes:

$$\cos\varphi = f_2(v_d, v_q) = \frac{v_d}{\sqrt{v_d^2 + v_q^2}} \tag{3-38a}$$

$$\sin\varphi = f_3(v_d, v_q) = \frac{v_q}{\sqrt{v_d^2 + v_q^2}} \tag{3-38b}$$

Selecting the operation point $\{V_{d0}, V_{q0}\}$, the equation (3-38) can be approximated by a Taylor series with respect to $v_d$ and $v_q$. Using the convolution property of DP and truncating the harmonics higher than the 3rd order, the DP transformation of (3-38) is derived as:

$$\langle \cos\varphi \rangle_0 = h_0 + h_3 \langle v_d \rangle_2 \langle v_d \rangle_2^* + h_4 \langle v_q \rangle_2 \langle v_q \rangle_2^* + h_5 \left\{ \langle v_d \rangle_2 \langle v_q \rangle_2^* + \langle v_d \rangle_2^* \langle v_q \rangle_2 \right\} \tag{3-39a}$$

$$\langle \cos\varphi \rangle_2 = h_1 \langle v_d \rangle_2 + h_2 \langle v_q \rangle_2 \tag{3-39b}$$

$$\langle \sin\varphi \rangle_0 = g_0 + g_3 \langle v_d \rangle_2 \langle v_d \rangle_2^* + g_4 \langle v_q \rangle_2 \langle v_q \rangle_2^* + g_5 \left\{ \langle v_d \rangle_2 \langle v_q \rangle_2^* + \langle v_d \rangle_2^* \langle v_q \rangle_2 \right\} \tag{3-39c}$$

$$\langle \sin\varphi \rangle_2 = g_1 \langle v_d \rangle_2 + g_2 \langle v_q \rangle_2 \tag{3-39d}$$

### 3.4.5 DQ0 to ABC Transformation in Dynamic Phasors

The previous sections have established the DP model of a diode bridge using the d and q components of voltage and current vectors. If the three-phase AC variables are modelled as DPs, then the DPs in d and q axes have to be transformed into ABC frame. Implementing the DP convolution property to the ABC/DQ0 transformation given by (3-9) and (3-10) yields:

$$\begin{bmatrix} \langle i_a \rangle_1 \\ \langle i_b \rangle_1 \\ \langle i_c \rangle_1 \end{bmatrix} = \langle \mathbf{T}^{-1} \rangle_1 \begin{bmatrix} \langle i_d \rangle_0 \\ \langle i_q \rangle_0 \end{bmatrix} + \langle \mathbf{T}^{-1} \rangle_1^* \begin{bmatrix} \langle i_d \rangle_2 \\ \langle i_q \rangle_2 \end{bmatrix} \tag{3-40}$$

where $\mathbf{T}^{-1}$ is the generalized inverse matrix $\mathbf{T}$:

$$\mathbf{T}^{-1} = \begin{bmatrix} \cos\omega t, & -\sin\omega t \\ \cos(\omega t - 2\pi/3), & -\sin(\omega t - 2\pi/3) \\ \cos(\omega t + 2\pi/3), & -\sin(\omega t + 2\pi/3) \end{bmatrix} \tag{3-41}$$

With Table 2-1, the DPs of Matrix $T^{-1}$ are given as:

$$\langle \mathbf{T}^{-1} \rangle_1 = \begin{bmatrix} 0.5 & 0.5\,j \\ -1/4 - j\sqrt{3}/4 & -j1/4 + \sqrt{3}/4 \\ -1/4 + j\sqrt{3}/4 & -j1/4 - \sqrt{3}/4 \end{bmatrix} \tag{3-42}$$

Using (3-41) and (3-42), the DP of input currents in ABC frame can be derived.

### 3.4.6 Model Assembly

The equations derived above build the DP-domain model of the uncontrolled rectifier as shown in Figure 3-8. The current flow shown in Figure 3-8 illustrates the mapping of $i_{dc}$ into the AC currents $\langle i_{a,b,c} \rangle_1$. With (3-36), all the information in $i_{dc}$ is reserved in the DP $\langle i_{dc} \rangle_0$. This makes $\langle i_{a,b,c} \rangle_1$ a function of the time-varying current $i_{dc}$ and allows the harmonic characteristics in the AC currents to be represented by the fundamental DPs $\langle i_{a,b,c} \rangle_1$. The DP model shown in Figure 3-8 can be used in EPS simulations with no need for the user to understand DP theory. For the user who wishes to build the entire EPS model in the DP domain, the model does not need the interface blocks (coloured in grey in Figure 3-8) since the

DP variables are already available and the DB model can be directly interfaced to the other EPS model blocks.

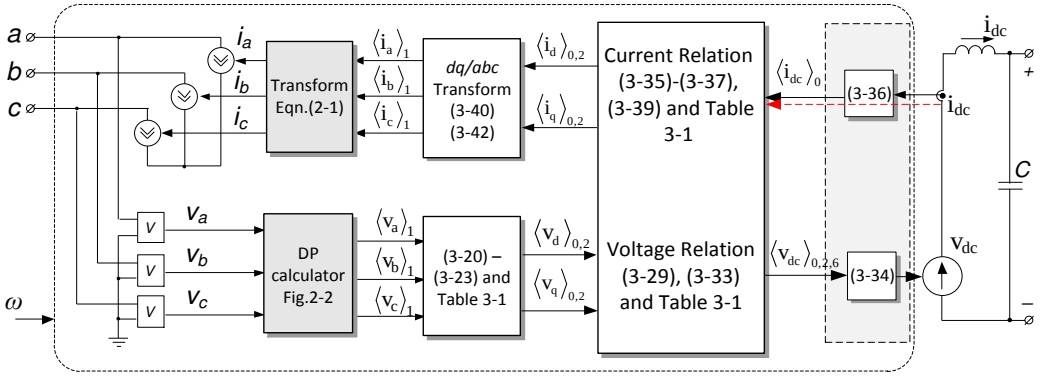


Figure 3-8 DP model of the three-phase rectifier

## 3.4.7 Model Validation

A test rig shown in Figure 3-9 was set up for the model verification. The system includes a programmable source Chroma II model 61511, a DB rectifier IRKD101-14, and filters on both DC and AC sides. The parameters are $L_s$=1mH, $R_s$=0.1Ω, C=2400μF and $L_{dc}$=120μH. The DC-link is feeding two resistive loads with $R_L$=200Ω, $R'_L$=19Ω. The model is verified in continuous and discontinuous current modes, balanced and unbalanced conditions as reported below.

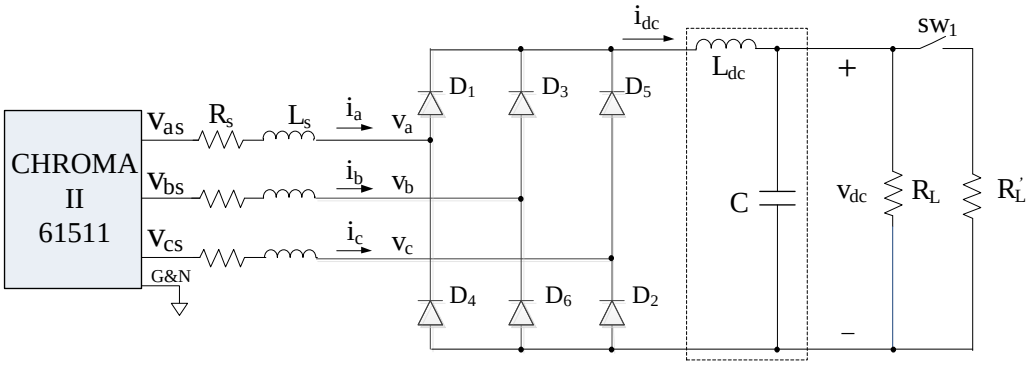


Figure 3-9 Experimental configuration

### 1) Continuous Mode

In this experiment, the balanced supply voltage is set at $v_{as}$=$v_{bs}$=$v_{cs}$=40V at 50Hz to avoid source protection triggering when applying the fault. The phase A

voltage is set to zero at t=0.2s in order to perform an unbalanced supply to the system. A continuous current mode is ensured with a heavy load on the DC-link side by switching on $sw_1$ and paralleling $R_L$ and $R'_L$. The simulation and experiment values of $v_{dc}$, $i_{abc}$ and $i_{dc}$ are compared in Figure 3-10, Figure 3-11 and Figure 3-12 respectively.

As can be seen in Figure 3-10, under the balanced condition (t<0.2s), $v_{dc}$ has the $6^{th}$ harmonic component. With the $6^{th}$ harmonic included in the DP model, the results from the experiment and DP model are matched quite well. The slight difference between experiment and the DP model results from the higher dc current harmonics (components higher than the $6^{th}$ harmonic) are charging the capacitor, as shown in Figure 3-12. After the fault occurs, the DC-link voltage fluctuates at a double frequency. In this case, the $2^{nd}$ harmonic is included in the DP model and the results from the experiment and simulation are well matched.

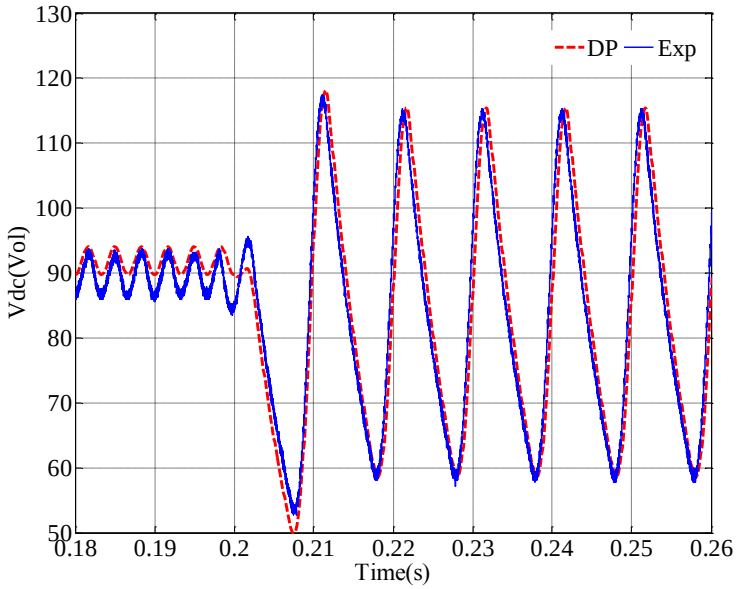


Figure 3-10 The DC-link voltage of the DB with a power supply fault occurring in phase A at t=0.2s

The DP model and experiment results for $i_{a,b,c}$ are shown in Figure 3-11 and they are well matched before and after the fault occurs. The DC-link current $i_{dc}$, as shown in Figure 3-12, changes from a Continuous Current Mode (CCM) to a Discontinuous Current Mode (DCM) after the fault occurs. It can be seen that

under CCM and DCM conditions, the DP model demonstrates good performance in both cases. The small discrepancy between the DP model and experiment results is due to the fact that the DP model is an approximation technique and harmonics higher than $6^{th}$ order is not considered in the DP model.

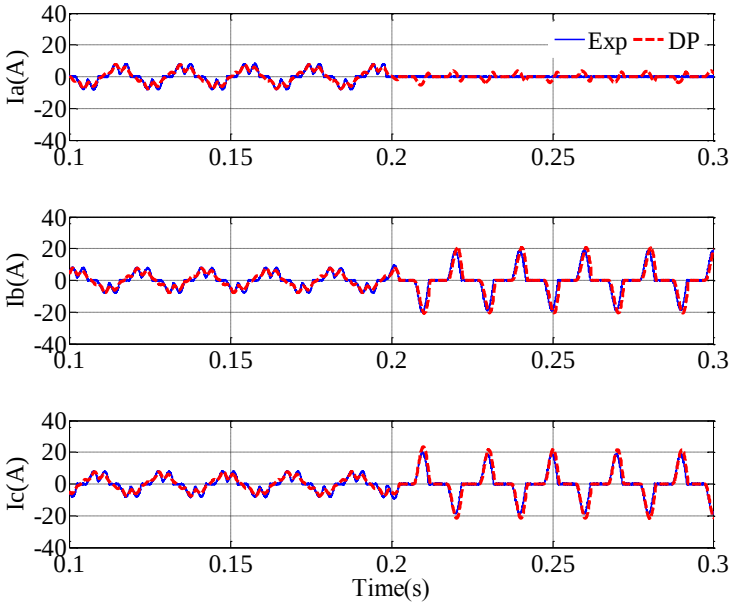


Figure 3-11 The AC side currents of the DB with a power supply occurring in phase A at t=0.2s

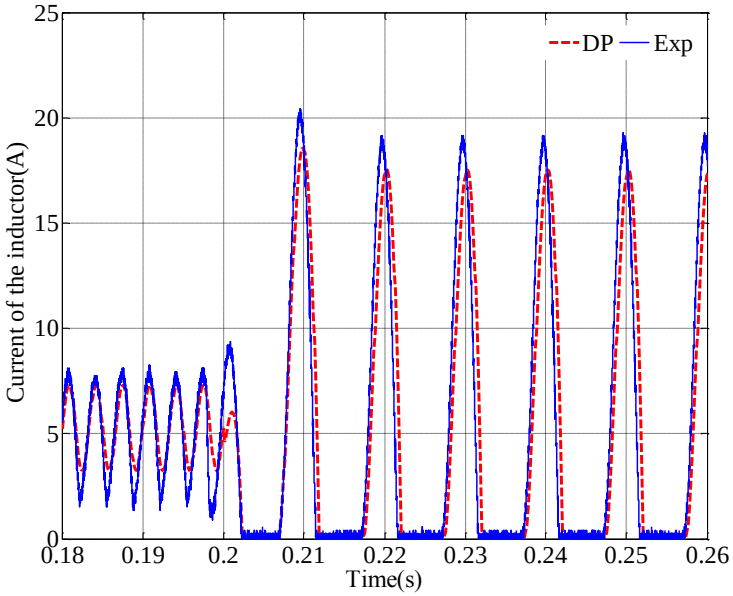


Figure 3-12 The DC-link current, $i_{dc}$, the DB with a power supply fault occurring in phase A at t=0.2s

### 2) Discontinuous Mode

In this case the switch $sw_1$ is open and a large load resistance $R_L$ results in a small load current on the DC side which makes the inductor current discontinuous. The experiment starts with balanced voltages set $v_{as}=v_{bs}=v_{cs}=80V$ at 50Hz followed the loss of phase A supply ($v_{as}=0$) at t=0.2s. The simulation and experiment values of $v_{dc}$, $i_{abc}$ and $i_{dc}$ are compared in Figure 3-13, Figure 3-14 and Figure 3-15 respectively.

As can be seen in Figure 3-13, $v_{dc}$ has a $6^{th}$ harmonic under the balanced condition and a $2^{nd}$ harmonic under the line fault condition. In both cases, the results from the DP model are well matched with experiment.

The AC side currents from the experiment and the DP model, shown in Figure 3-14, are well matched before and after the fault occur. The DC-link current $i_{dc}$, shown in Figure 3-15, indicates that the rectifier works under the DCM under both normal and faulty conditions. The results from the experiment and DP model are well matched in both cases.

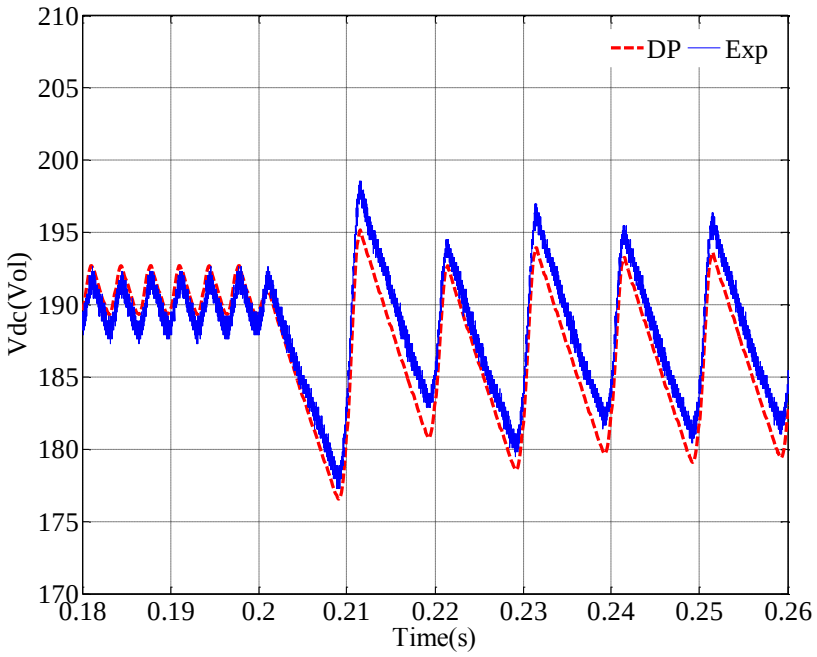


Figure 3-13 The DC-link voltage of the DB with a power supply fault occurring in phase A at t=0.2s

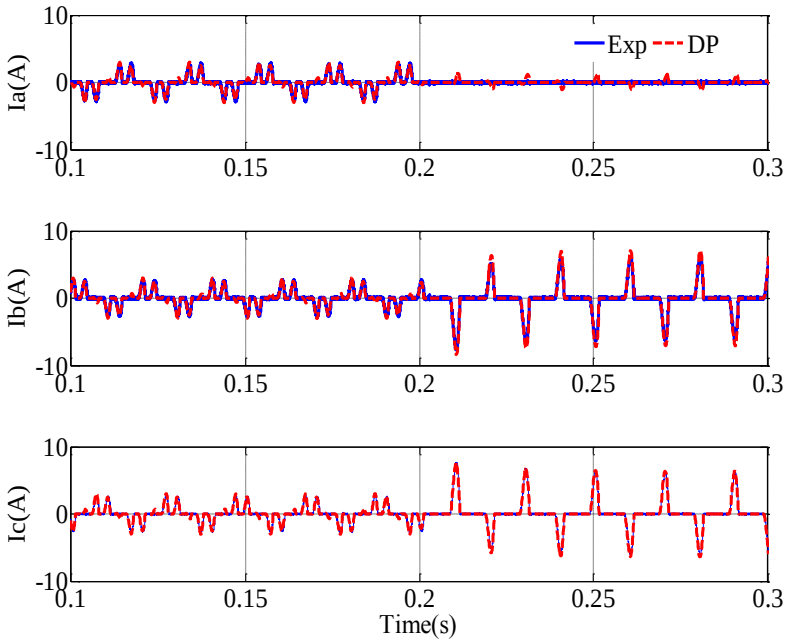


Figure 3-14 The AC side currents of the DB with a power supply fault occurring in phase A at t=0.2s

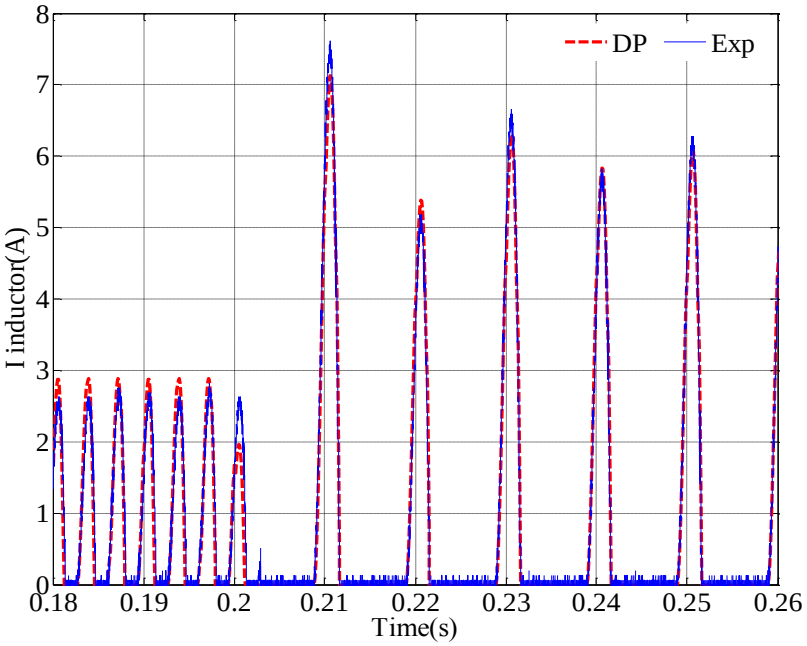


Figure 3-15 The DC-link current, $i_{dc}$, the DB with a power supply fault occurring in phase A at t=0.2s

### 3.4.8 Error Analysis

The input voltages of three-phase rectifier can be separated into positive and negative sequences. In the proposed DP model, the operation point is determined by the positive sequence and the negative sequence is treated as a disturbance. This consideration is true when the positive sequence is dominant. However, with the increase of the negative sequence, this consideration may give some discrepancy. Here, we define an unbalance factor λ. It is the magnitude ratio between the negative voltage vector and the positive voltage vector and written as:

$$\lambda = \frac{\left|\vec{V}_n\right|}{\left|\vec{V}_p\right|} \tag{3-43}$$

where $|\vec{v}_p|$ represents the magnitude of positive sequence vector and $|\vec{v}_n|$ denotes the magnitude of the negative sequence vector. Using the simulation scheme of Figure 3-8, we set the three-phase voltage source as:

$$\begin{cases} v_{as} = 80\cos(\omega t) \\ v_{bs} = V_m \sin(\omega t + \phi_b) \\ v_{cs} = 80\cos(\omega t + 2\pi/3) \end{cases} \tag{3-44}$$

The magnitude and angle of phase B are variables that can be set to any value before simulation. It can be understood that with $V_m$ changing from 0 to 80V and $\phi_b$ from 0 to 2π, the simulation condition will cover all balanced and unbalanced conditions. The dc-link voltages of the benchmark model and the DP model are compared and the error of DP model is defined as

$$\text{error} = \frac{\int_T v_{dc\_benchmark}\,dt - \int_T v_{dc\_DP}\,dt}{\int_T v_{dc\_benchmark}\,dt} \times 100\% \tag{3-45}$$

where T is the fundamental period. Other electrical variables can be chosen to calculate the error. However, in this thesis, the dc-link voltage is selected. Figure 3-16 shows the DP error (%) as a function of $V_m$ and $\phi_b$. Also shown is the corresponding unbalance factor λ. It can be seen that the DP model error is a function of $\lambda$. This is reasonable because the disturbance from the negative

sequence becomes more severe and thus the operation point will be shifted from $\{V_{d0}, V_{q0}\}$. The closer $\phi_b$ is to $5\pi/6$ and $V_m$ is to 120V, the larger λ becomes and the error approaches a maximum. In practice, if the negative sequence becomes dominant, i.e. $|\vec{v}_n|/|\vec{v}_p|>1$, the operation point can be selected using the negative sequence and the positive sequence can be viewed as a disturbance. Thus, we only have to consider the conditions with $|\vec{v}_n|/|\vec{v}_p|\in[0,1]$. For the case $|\vec{v}_n|/|\vec{v}_p|=0$, this corresponds to the balanced condition and the error is less than 2%. For the case $|\vec{v}_n|/|\vec{v}_p|=1$, this corresponds to the line-to-line fault condition and the error is less than 15%, as shown in Figure 3-17 When $V_m$=0V, corresponding to the phase-to-ground fault condition, the error is very small and is always less than 2%.

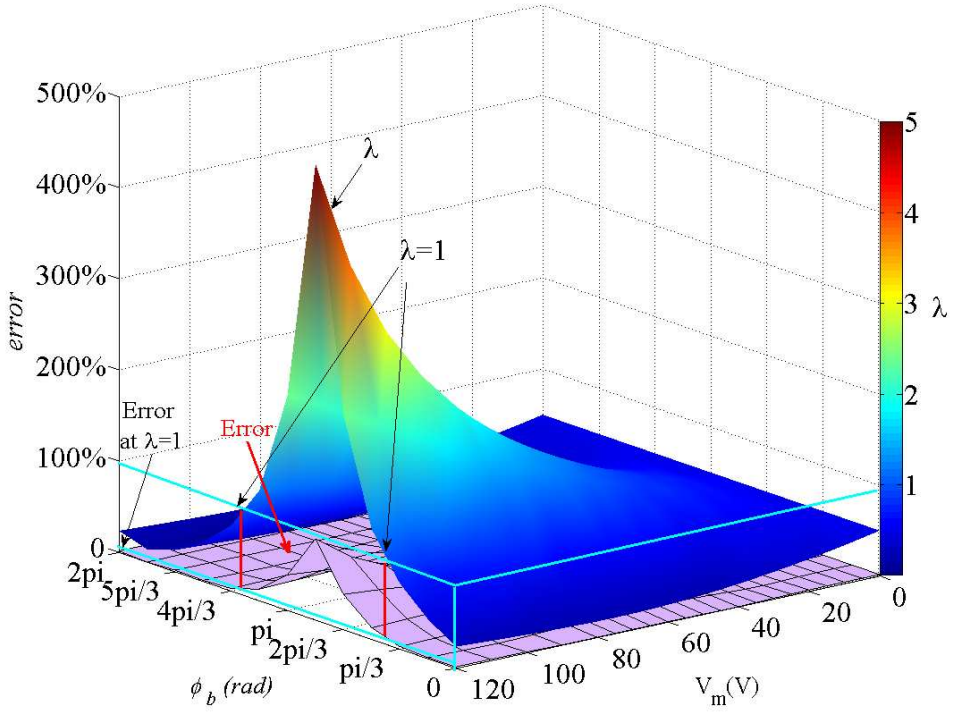


Figure 3-16 Relationship between the DP model Error and λ

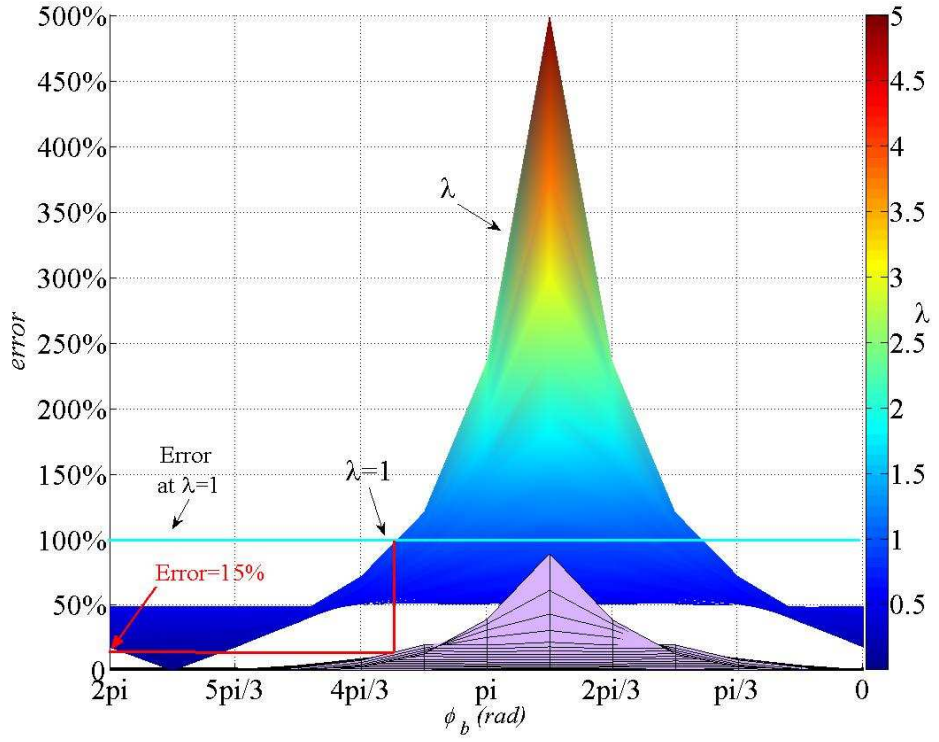


Figure 3-17 Front view of the relationship between the DP model Error and λ

# 3.5 DP Model of Auto-Transformer Rectifier Units

The multi-pulse ATRU is an essential element for supplying the main DC bus in an aircraft EPS. It essentially consists of two parts: a phase-shift transformer and a multi-pulse rectifier. Therefore, the development of DP models for ATRUs can also be separated into these two parts.

Assuming the transformer saturation can be neglected, the electrical variables on the primary and secondary side will present a linear relationship, which can be conveniently transformed into the DP domain. The DP model of the rectifier part will be developed from the DP model of the three-phase diode rectifier in Section 3.4. In this section, the DP model for an 18-pulse ATRU will be introduced. The performance and efficiency of the developed DP model is validated through comparison with benchmark model (in three-phase frame and referred to ABC

model, Section 2.1) and the DQ0 model (models in a synchronous rotating frame, Section 2.1).

### 3.5.1 Benchmark Model of ATRU

The ATRU presented in this section uses an 18-pulse differential delta connected autotransformer. The primary windings are delta connected and the secondary windings are pseudo star-connected, as shown in Figure 3-18. The three sets of secondary windings directly feed three sets of diode bridges, with their DC sides connected in parallel, as shown in Figure 3-19. The voltages on the secondary side windings are $40^{o}$ shift from each other, as shown in Figure 3-20. With this type of configuration, there is no need for an inter-phase transformer and the three sets of diode bridges are equal to a nine-phase AC/DC converter.

The design procedure for the autotransformer is presented in [71] and the parameters of ATRU are not given due to confidentiality issues. The switching model of diode bridges has been given in section 3.2.

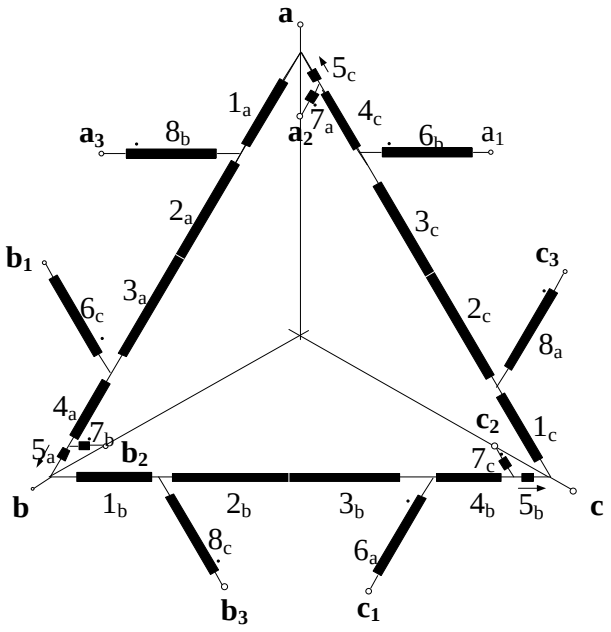


Figure 3-18 Configuration of the differential-delta autotransformer

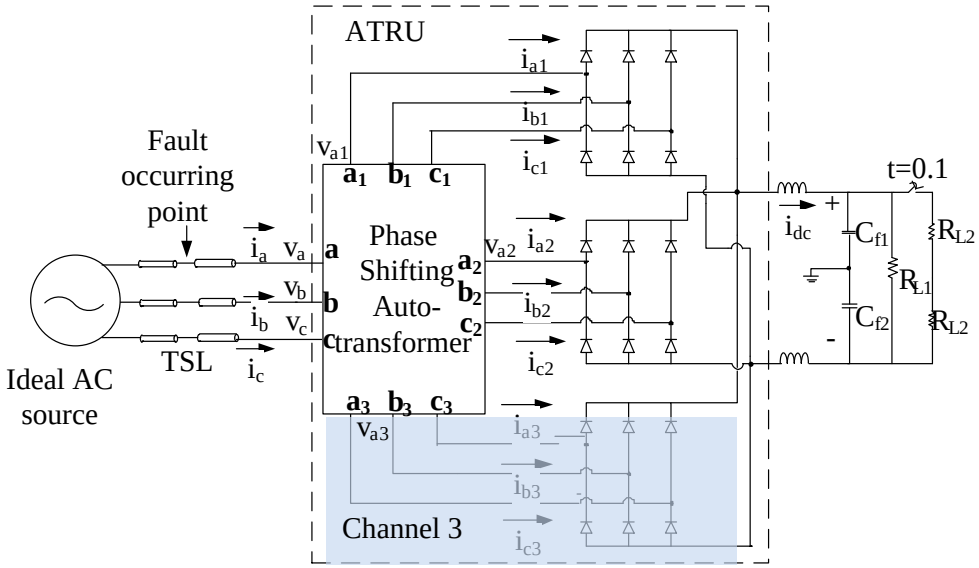


Figure 3-19 Configuration of an 18-pulse autotransformer rectifier unit

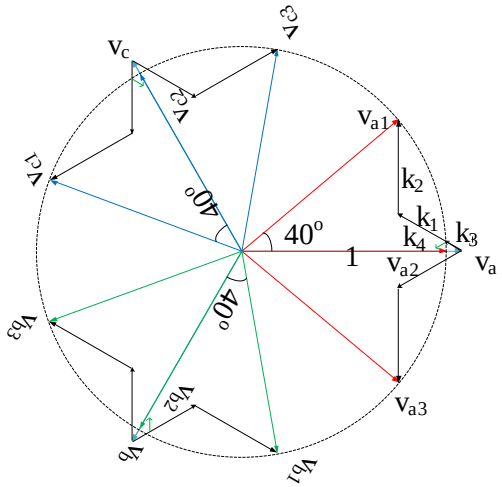


Figure 3-20 The voltage phasor diagram of the delta-type autotransformer for 18-pulse operation

## 3.5.2 DQ0 Model of the ATRU

In the DQ0 model of the ATRU, the higher switching harmonics are neglected and only the fundamental component is considered. The development of the DQ0 model consists of two steps. Firstly, we use the symmetry of the ATRU to reduce the system order, as shown in Figure 3-21. In this step the three-to-nine phase autotransformer is reduced to a three-to-three phase system. The primary side and the third channel on the secondary side of the transformer (marked in grey in

Figure 3-19), have been chosen to represent the whole system at this stage. The second step uses the ABC/DQ0 transformation to transform the derived three-to-three phase system from the ABC frame to the DQ0 frame.

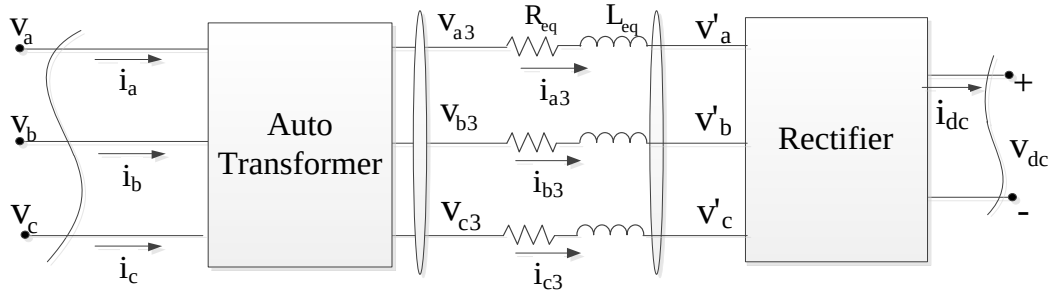


Figure 3-21 The equivalent representation of an 18-pulse ATRU

**1) Autotransformer**

The autotransformer part in Figure 3-21 represents the order-reduced autotransformer. The voltage and current relations between the output and input terminals at the transformer can be derived from the voltage phasor diagram shown in Figure 3-20 and written as:

$$\begin{bmatrix} v_{a3} \\ v_{b3} \\ v_{c3} \end{bmatrix} = \begin{bmatrix} 1-\frac{k_1}{\sqrt{3}} & \frac{k_1}{\sqrt{3}}+\frac{k_2}{\sqrt{3}} & -\frac{k_2}{\sqrt{3}} \\ -\frac{k_2}{\sqrt{3}} & 1-\frac{k_1}{\sqrt{3}} & \frac{k_1}{\sqrt{3}}+\frac{k_2}{\sqrt{3}} \\ \frac{k_1}{\sqrt{3}}+\frac{k_2}{\sqrt{3}} & -\frac{k_2}{\sqrt{3}} & 1-\frac{k_1}{\sqrt{3}} \end{bmatrix} \begin{bmatrix} v_a \\ v_b \\ v_c \end{bmatrix} \tag{3-46}$$

$$\begin{bmatrix} i_a \\ i_b \\ i_c \end{bmatrix} = 3\cdot \begin{bmatrix} 1-\frac{k_1}{\sqrt{3}} & -\frac{k_2}{\sqrt{3}} & \frac{k_1}{\sqrt{3}}+\frac{k_2}{\sqrt{3}} \\ \frac{k_1}{\sqrt{3}}+\frac{k_2}{\sqrt{3}} & 1-\frac{k_1}{\sqrt{3}} & -\frac{k_2}{\sqrt{3}} \\ -\frac{k_2}{\sqrt{3}} & \frac{k_1}{\sqrt{3}}+\frac{k_2}{\sqrt{3}} & 1-\frac{k_1}{\sqrt{3}} \end{bmatrix} \begin{bmatrix} i_{a3} \\ i_{b3} \\ i_{c3} \end{bmatrix} \tag{3-47}$$

where $k_1$ =0.3471 and $k_2$ =0.4133 are corresponding to the relative length of $1_{abc}$ and $8_{abc}$ in Figure 3-18 respectively. The coefficient '3' in the current relation is due to the fact that there are three channels on the secondary side.

Using the ABC/DQ0 transformation

$$f_{dq0} = K_s f_{abc} \tag{3-48}$$

with

$$K_s = \frac{2}{3}\begin{bmatrix} \cos\omega t & \cos(\omega t - 2/3\pi) & \cos(\omega t + 2/3\pi) \\ -\sin\omega t & -\sin(\omega t - 2/3\pi) & -\sin(\omega t + 2/3\pi) \\ 1/2 & 1/2 & 1/2 \end{bmatrix} \tag{3-49}$$

Implementing this ABC/DQ0 transformation on both sides of (3-46) and (3-47), yields the voltage and current relations in the DQ0 frame:

$$\begin{bmatrix} v_{d3} \\ v_{q3} \\ v_{03} \end{bmatrix} = \begin{bmatrix} 0.6994 & 0.5868 & 0 \\ -0.5868 & 0.6994 & 0 \\ 0 & 0 & 1 \end{bmatrix} \begin{bmatrix} v_d \\ v_q \\ v_0 \end{bmatrix} \tag{3-50}$$

$$\begin{bmatrix} i_d \\ i_q \\ i_0 \end{bmatrix} = 3 \cdot \begin{bmatrix} 0.6994 & -0.5868 & 0 \\ 0.5868 & 0.6994 & 0 \\ 0 & 0 & 1 \end{bmatrix} \begin{bmatrix} i_{d3} \\ i_{q3} \\ i_{03} \end{bmatrix} \tag{3-51}$$

**2) Rectifier**

In the ATRU, the combination of the three parallel diode bridges is essentially a nine-phase rectifier, with each leg conducting $40^o$ in the balanced condition, instead of $120^o$ for a three-phase rectifier. Thus the voltage and current on the AC and DC sides should display a similar relationship as that in the three-phase rectifier. For an ideal nine-phase rectifier, the DC-link voltage is written as:

$$v_{dc} = \frac{18}{\pi}\sin(\frac{\pi}{9})\sqrt{v_d^{'2} + v_q^{'2}} \tag{3-52}$$

where $v_d^{'}$ and $v_q^{'}$ are the d and q components of $v_{abc}^{'}$ as shown in Figure 3-20. Compared with the DC-link voltage for the three-phase rectifier in (3-10), one can identify that the only difference between equations (3-52) and (3-10) is the coefficient. since the commutation loss of a three-phase diode bridge can be represented with a loss resistor on the DC-link side [21] and the commutation

happens every π/9, instead of π/3, the commutation loss of this nine-phase rectifier becomes:

$$\Delta v_{dc} = \frac{\omega L_{s1} i_{dc}}{\pi/9} = \frac{9}{\pi}\omega L_{s1} i_{dc} \tag{3-53}$$

where $L_{s1}$ is the inductance in the front end of the rectifier and equal to $L_{eq}$ in the ATRU as shown in Figure 3-21. $i_{dc}$ is the DC-link current. Combining equations (3-52) and (3-53) gives the DC link voltage as:

$$v_{dc} = \frac{18}{\pi}\sin(\frac{\pi}{9})\sqrt{v_d^{'2} + v_q^{'2}} - \frac{9}{\pi}\omega L_{s1} i_{dc} \tag{3-54}$$

The relationship between the current vector at the AC terminals of the rectifier and DC-link currents of the rectifier part is:

$$\left|\vec{i}_3\right| = \frac{4\sin(\pi/9)}{\pi} i_{dc} \tag{3-55}$$

where $\left|\vec{i}_3\right|$ is the magnitude of the current vector for $i_{a3,b3,c3}$. The calculation of the current vector angle is the same as that for the three-phase rectifier and is given as

$$\theta_{i3} = \tan^{-1}(v_q^{'}/v_d^{'}) \tag{3-56}$$

Hence, the currents on the d and q axes are:

$$i_{3,d} = \left|\vec{i}_3\right|\cos\theta_{i3} = \frac{4\sin(\pi/9)}{\pi} i_{dc} \frac{v_d^{'}}{\sqrt{v_d^{'2} + v_q^{'2}}} \tag{3-57}$$

$$i_{3,q} = \left|\vec{i}_3\right|\sin\theta_{i3} = \frac{4\sin(\pi/9)}{\pi} i_{dc} \frac{v_q^{'}}{\sqrt{v_d^{'2} + v_q^{'2}}} \tag{3-58}$$

The Equations (3-54)-(3-58) establish the relationship between the currents on the AC and DC sides of the nine-phase rectifier.

### 3) Equivalent RL Circuit

The parameters $L_{eq}$ and $R_{eq}$ can be calculated as below:

$$L_{eq} = L_s + \frac{L_p}{N^2} \tag{3-59}$$

$$R_{eq} = R_s + \frac{R_p}{N^2} \tag{3-60}$$

Here, $L_p$ and $L_s$ are the primary and secondary leakage inductances of the transformer respectively, $R_p$ and $R_s$ are the primary and secondary winding resistances respectively. N is the turn ratio between the primary and secondary windings of the transformer.

## 3.5.3 Dynamic Phasor Model of the ATRU

The development of the DP model uses similar steps as those used in the DQ0 model.

### 1) Autotransformer

The DP model of the transformer part in Figure 3-20 can be derived by transforming the voltage and current relations in (3-46) and (3-47) to the DP domain, applying the properties of DPs. As the higher harmonics are neglected and only the fundamental components are considered in the DP model, the DP index is set at K={1}. The voltage and current relations in the DP domain can be written as:

$$\begin{bmatrix} \langle v_{a3} \rangle_1 \\ \langle v_{b3} \rangle_1 \\ \langle v_{c3} \rangle_1 \end{bmatrix} = \begin{bmatrix} 1-\frac{k_1}{\sqrt{3}} & \frac{k_1}{\sqrt{3}}+\frac{k_2}{\sqrt{3}} & -\frac{k_2}{\sqrt{3}} \\ -\frac{k_2}{\sqrt{3}} & 1-\frac{k_1}{\sqrt{3}} & \frac{k_1}{\sqrt{3}}+\frac{k_2}{\sqrt{3}} \\ \frac{k_1}{\sqrt{3}}+\frac{k_2}{\sqrt{3}} & -\frac{k_2}{\sqrt{3}} & 1-\frac{k_1}{\sqrt{3}} \end{bmatrix} \begin{bmatrix} \langle v_a \rangle_1 \\ \langle v_b \rangle_1 \\ \langle v_c \rangle_1 \end{bmatrix} \tag{3-61}$$

$$\begin{bmatrix} \langle i_a \rangle_1 \\ \langle i_b \rangle_1 \\ \langle i_c \rangle_1 \end{bmatrix} = 3 \cdot \begin{bmatrix} 1-\frac{k_1}{\sqrt{3}} & -\frac{k_2}{\sqrt{3}} & \frac{k_1}{\sqrt{3}}+\frac{k_2}{\sqrt{3}} \\ \frac{k_1}{\sqrt{3}}+\frac{k_2}{\sqrt{3}} & 1-\frac{k_1}{\sqrt{3}} & -\frac{k_2}{\sqrt{3}} \\ -\frac{k_2}{\sqrt{3}} & \frac{k_1}{\sqrt{3}}+\frac{k_2}{\sqrt{3}} & 1-\frac{k_1}{\sqrt{3}} \end{bmatrix} \begin{bmatrix} \langle i_{a3} \rangle_1 \\ \langle i_{b3} \rangle_1 \\ \langle i_{c3} \rangle_1 \end{bmatrix} \tag{3-62}$$

**2) Rectifier**

The DP model of the rectifier part can be developed in the same way as is used for the three-phase rectifier discussed in Section 3.4. Compared with the three-phase rectifier, the first higher harmonic appearing in the DC-link side of the 18-pulse ATRU will be the 18$^{th}$, rather than the 6$^{th}$. This 18$^{th}$ harmonic will not be included in the DP model due to its high order and relatively little added value in the DP model. The DP model development process for this part is the same as that used for the three-phase rectifier. With the $v_{dc}$ function (3-27) replaced by (3-54) and using the Taylor expansion, the DP expression of $v_{dc}$ for the rectifier in ATRU can be given as

$$\begin{aligned} v_{dc} = \langle v_{dc} \rangle_0 \approx\ & f_2(V'_{d0}, V'_{q0}) + \frac{\partial^2 f_2(V'_{d0}, V'_{q0})}{\partial v_d'^{\,2}} \langle v'_d \rangle_2 \langle v'_d \rangle_2^* \\ & + \frac{\partial^2 f_2(V'_{d0}, V'_{q0})}{\partial v_q'^{\,2}} \langle v'_q \rangle_2 \langle v'_q \rangle_2^* + \frac{\partial^2 f_2(V'_{d0}, V'_{q0})}{\partial v'_d \partial v'_q} \left( \langle v'_d \rangle_2 \langle v'_q \rangle_2^* + \langle v'_d \rangle_2^* \langle v'_q \rangle_2 \right) \end{aligned} \tag{3-63}$$

where

$$f_2 = \frac{18}{\pi} \sin\left(\frac{\pi}{9}\right) \sqrt{v_d'^2 + v_q'^2} \tag{3-64}$$

As has been discussed in Section 3.4.1, the DPs $\langle v'_d \rangle_k$ and $\langle v'_q \rangle_k$ (k=0,2) can be calculated with the DPs $\langle v'_{abc} \rangle_1$. Thus the $v_{dc}$ can be expressed using $\langle v'_{abc} \rangle_1$ in the DP model.

For the current relation, replacing (3-35) by (3-55), the DP currents in d and q axes can be written as:

$$\langle i'_d \rangle_k = \frac{4\sin(\pi/9)}{\pi} \langle i_{dc} \rangle_0 \left\langle \frac{v'_d}{\sqrt{v_d'^2 + v_q'^2}} \right\rangle_k, k = 0,2 \tag{3-65}$$

$$\langle i'_q \rangle_k = \frac{4\sin(\pi/9)}{\pi} \langle i_{dc} \rangle_0 \left\langle \frac{v'_q}{\sqrt{v_d'^2 + v_q'^2}} \right\rangle_k, k = 0,2 \tag{3-66}$$

With the DQ0/ABC transformation (3-42) and (3-40), the relation between $i_{dc}$ and $\langle i'_{abc} \rangle_1$ in DP model can be derived.

### 3) Equivalent RL Circuit

The DP representation for the RL has been reported in Section 2.4.2, and is rewritten below:

$$\langle v \rangle_k = L\frac{d\langle i \rangle_k}{dt} + R\langle i \rangle_k + j\omega L\langle i \rangle_k \tag{3-67}$$

Thus the DP model of ATRU can be displayed in an electrical circuit as:

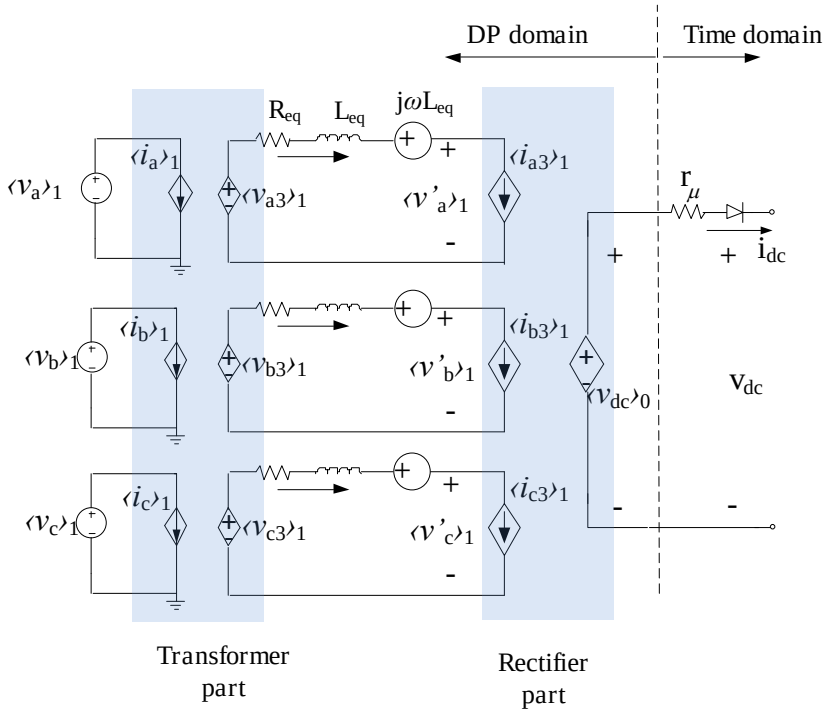


Figure 3-22 Electrical circuit representation of DP model of an 18-pulse ATRU

## 3.5.4 Model Validation

In this section, the effectiveness and performance of the developed DP ATRU model will be assessed. The simulation scheme is shown in Figure 3-18. The simulation results from three different models, i.e. ABC model, DQ0 model and DPABC model, are compared under balanced and unbalanced conditions. The consumed CPU time is tracked to evaluate the computation efficiency of these models. The evaluation of simulation accuracy is illustrated through comparing

plots of the AC currents flowing into the ATRU and voltages at the DC-link side. All the models are developed in the software Dymola.

### 1) Balanced Conditions

In this case, the three-phase voltage sources are balanced and a load step-up change is applied at t=0.1s. The system parameters are shown in Table 3-2.

Table 3-2 Parameter for ATRU system simulation

| | |
|---|---|
| **ATRU** | |
| Power rate | 150kW |
| **Transmission Line** | |
| R | 0.01Ω |
| L | 2μH |
| C | 2nF |
| **DC-link** | |
| Capacitors $C_{f1}$,$C_{f2}$ | 500μF |
| Resistor $R_{L1}$ | 10Ω |
| Resistor $R_{L2}$ | 5Ω |
| $\mathbf{R_{Fault}}$ | 1μΩ |

Figure 3-23 shows the transient response of $i_{a,b,c}$ flowing into the ATRU. Figure 3-24 illustrates the transient response of $v_{dc}$. With a step increase in the load, $i_{a,b,c}$ increase correspondingly and $v_{dc}$ reduces due to the voltage drop in the line impedance. The simulation results reveal that $i_{a,b,c}$ and $v_{dc}$ from the three different models are well matched and the results from the DQ0 and DPABC models reflect the fundamentals of those from the ABC model.

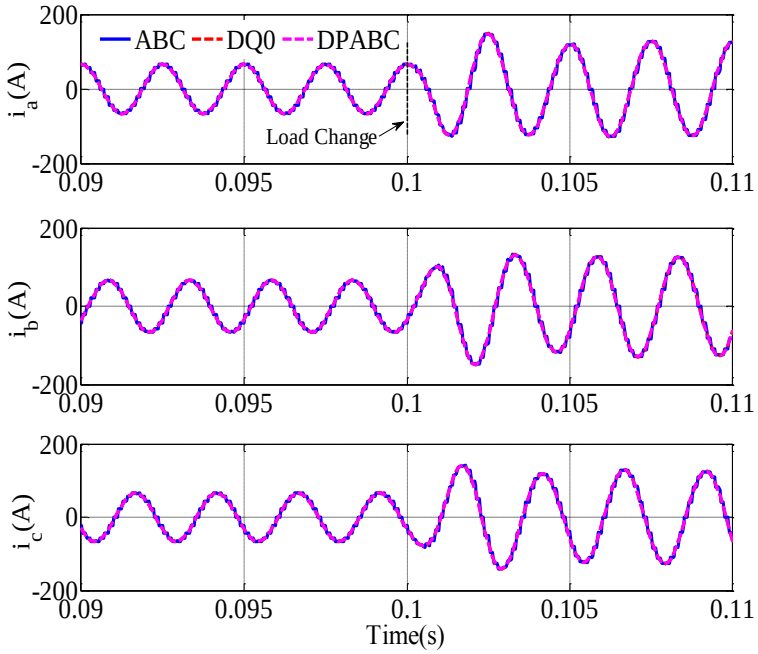


Figure 3-23 Phase currents flowing into the ATRU in the balanced condition with load change at t=0.1s

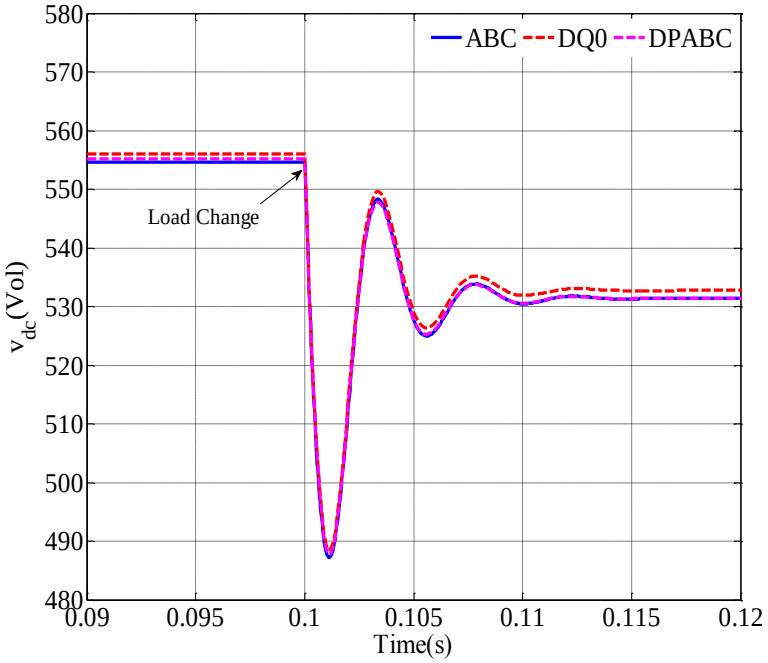


Figure 3-24 DC-link voltage of the ATRU in the balanced condition with load change at t=0.1s

### 2) Unbalanced Conditions

An unbalanced condition is simulated by implementing a line-to-line fault or a power supply fault in the transmission lines in the front end of the ATRU at t=0.15s, as shown in Figure 3-19. These two types of faults are of great concern for power system engineers. The DC-link voltage $v_{dc}$ and AC currents $i_{a,b,c}$ are selected to evaluate the accuracy of the models.

Line-to-Line Fault Conditions

A line-to-line fault occurs between phase A and phase B and the fault condition is simulated with a small resistance $R_{fault}=10^{-6}$ Ω. Figure 3-25 shows $i_{a,b,c}$ flowing into the ATRU. The ABC model and DQ0 model match very well before and after the fault occurs. Meanwhile a small discrepancy (less than 5%) can be identified between the ABC and DPABC models. As has mentioned before, the error in the DP models is a function of the unbalance factor λ. This line-to-line fault will make λ=1 at the primary side of the ATRU. However, due to the phase-shift transformer, the unbalanced factor λ is reduced in the AC terminals of the rectifier and a smaller error is derived in this case. The DC-link voltages from the different models are well matched under line-to-line fault conditions, as shown in Figure 3-26.

Figure 3-27 shows the computation time comparison for the different models. Before the line-to-line fault occurs, the DQ0 model is the fastest model of the three techniques. However, under fault conditions, this modelling technique consumes a substantial amount of computation time and loses its efficiency. This is due to the second harmonics in the d and q axis in the DQ0 models. On the other hand, the DPABC model shows its advantage in the simulations under fault conditions, with the simulation being slightly slower than the DQ0 model under balanced conditions. In addition, the efficiency of DPABC model is unaffected by the line-to-line fault. Interestingly, the simulation of ABC model during the line-to-line fault condition is faster than that in the balanced condition. It is known that the line-to-line fault at the AC side will reduce a three-phase rectifier to a single phase rectifier and thus the system order is reduced. Similarly, under line-to-line

fault conditions, the order of the 18-pulse ATRU system is also reduced and this is thought to be the reason for the simulation becoming slightly faster than that under the balanced condition.

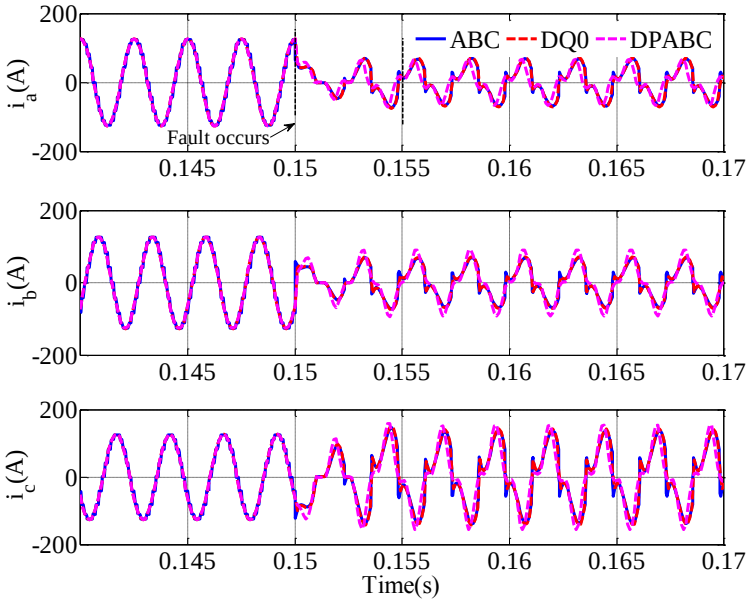


Figure 3-25 Phase currents flowing into the ATRU with line-to-line fault occurred at t=0.15s

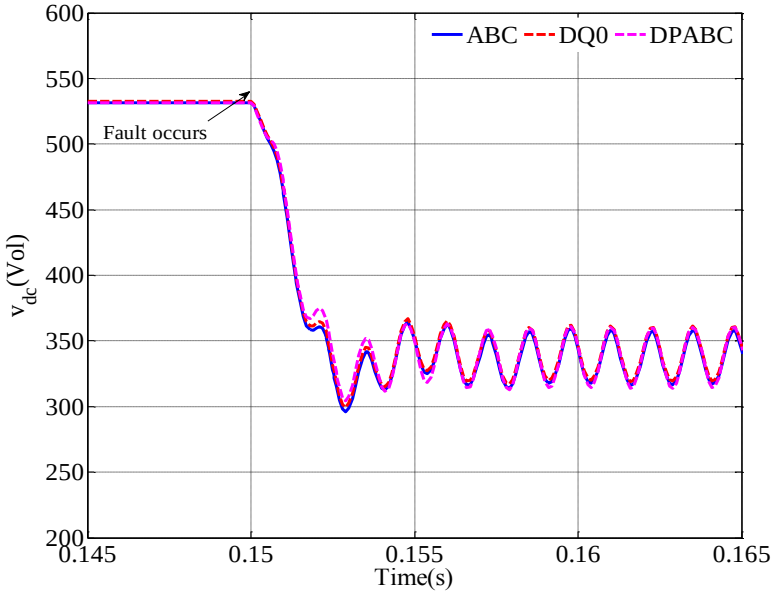


Figure 3-26 DC-link Voltage of the ATRU with line-to-line fault occurred at t=0.15s

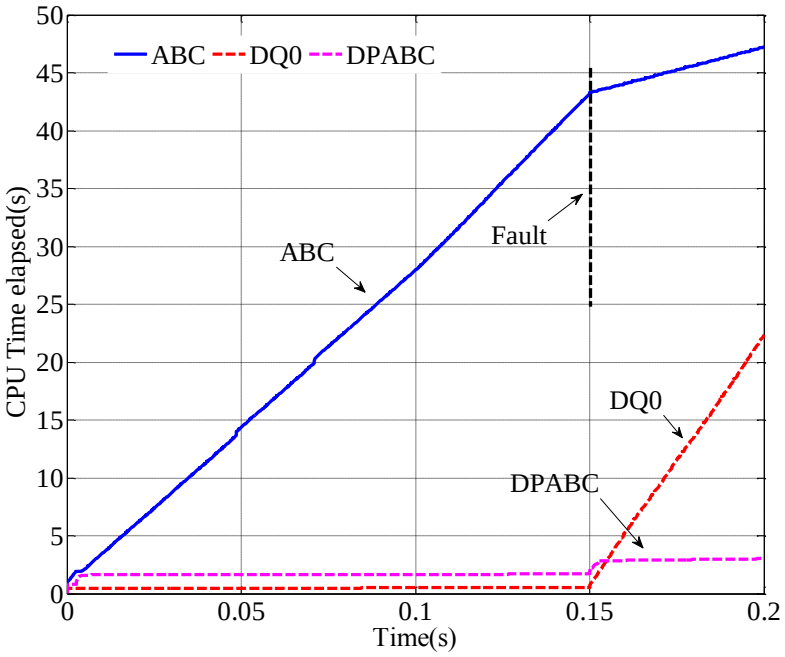


Figure 3-27 Computation time comparison between different models with line-to-line fault occurs at t=0.15s

Line-to-Ground Fault Conditions

A line-to-ground fault occurs between phase A and ground with $R_{fault}$=1μΩ. Figure 3-28 shows the $i_{a,b,c}$ flowing into ATRU. The results from the three techniques match very well under line-to-ground fault conditions. The plots of $v_{dc}$ from different models lay upon each other under line-to-ground fault conditions, as shown in Figure 3-29.

The computation time comparison between the different techniques in Figure 3-30 shows the efficiency of the DPABC model under both balanced and unbalanced conditions. The DQ0 model is the most efficient one under the balanced condition, but loses its efficiency under the line-to-ground condition. The ABC model keeps the same simulation efficiency and is the slowest one before and after the fault occurs.

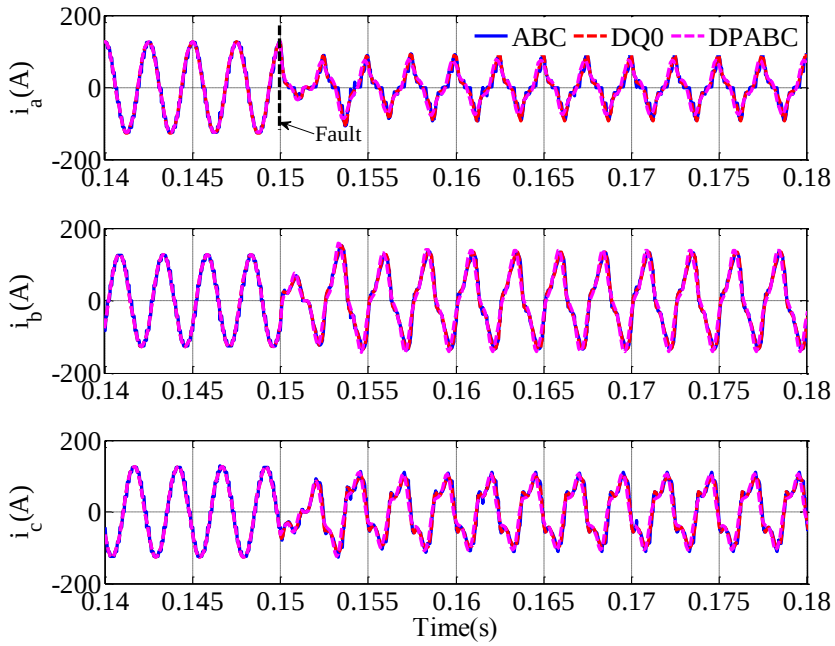


Figure 3-28 Currents flowing into ATRU with line-ground fault occurs at t=0.15s

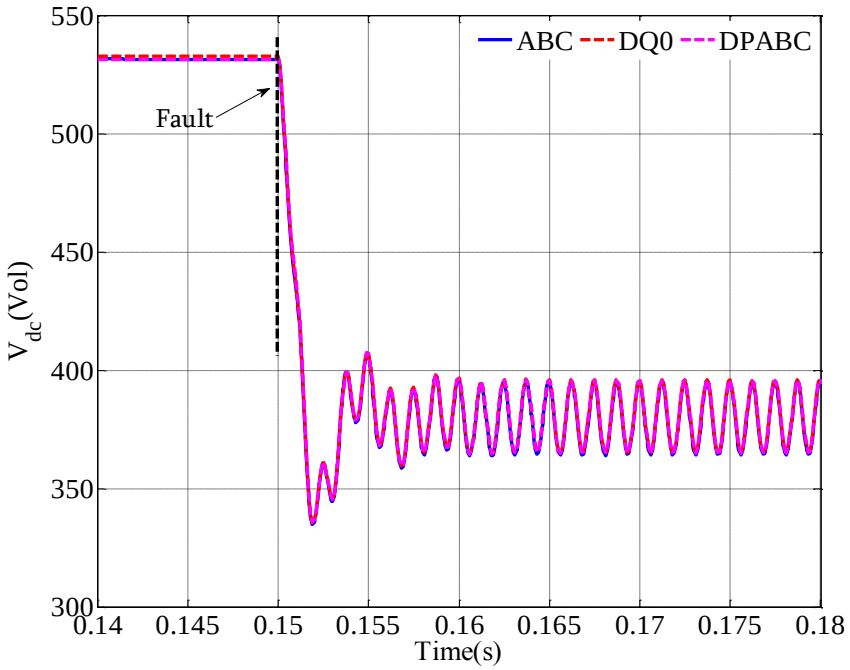


Figure 3-29 DC-link voltage comparison between different modelling techniques with line-to-ground fault occurs at t=0.15s.

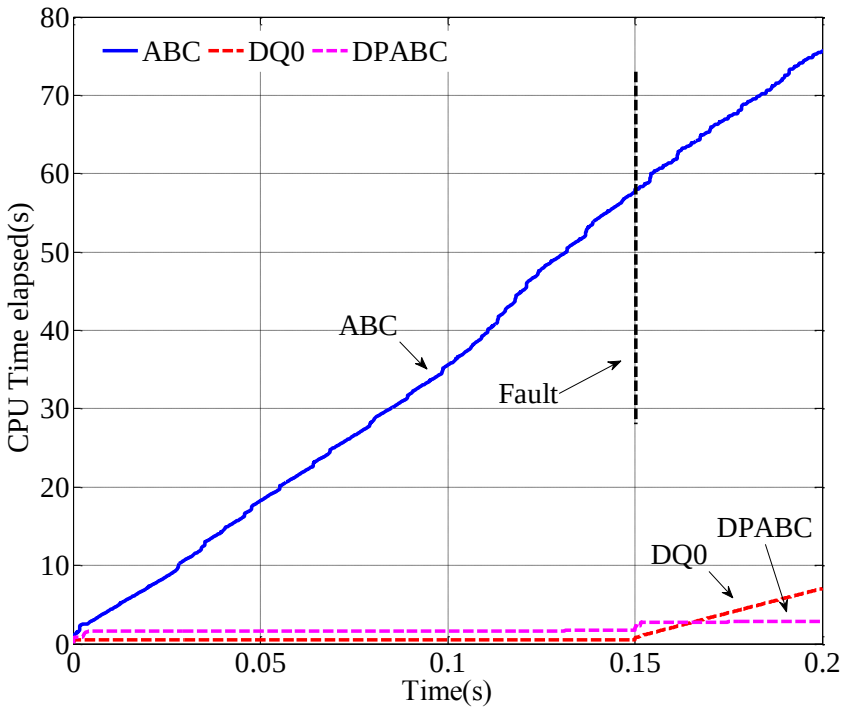


Figure 3-30 Computation time comparison between different modelling techniques with line-to-ground fault occurs at t=0.15s

# 3.6 Conclusion

In this chapter, the DP model for uncontrolled rectifiers has been introduced and developed. The algebraic relations between the magnitudes of the AC-side voltage and current vectors, and the DC-link voltage and current serve as the basis for developing the DP model. Mapping these vectors in to DP domain with corresponding three-phase DPs, the DP model can be derived. Furthermore, the higher harmonics can also be included in the DP model. In this chapter, the $6^{th}$ harmonic component on the DC-link voltage has been used to demonstrate this capability. The unbalanced operation condition has also been handled with the DP model, where the negative sequence of the supply has been viewed as a disturbance in the model and the operation point selected according to the positive sequence.

The developed DP model of diode bridges has been validated through experiment and the effectiveness of the DP model has been demonstrated. The error analysis shows the DP model error is a function of the unbalance factor λ. The error analysis illustrates that dominant sequence should be selected to calculate the operation point and the non-dominant one can be viewed as the disturbance. By doing this, the DP model error can be limited to less than 10% under line-to-line fault conditions.

Based on the DP model of the three-phase diode bridges, the DP modelling technique can be conveniently extended to modelling multi-pulse rectifiers. Neglecting the saturation of the transformers, the DP model for the ATRUs can be derived. In the case where the saturation modelling is required, the non-linearity can be written in a polynomial form which can be represented in DPs using the convolution property. This technique was used to represent the DB non-linear functions such as (3-27) and (3-28).

In this chapter, an 18-pulse ATRU has been modelled with DPs. The DP ATRU model has shown impressive performance under both balanced and unbalanced operation conditions. Compared with well-established ABC and DQ0 models, the DP model is more time-efficient for unbalanced condition simulations. The developed ATRU model has been added to the DP based modelling library for future studies of EPS architectures in MEA. A full ATRU test rig for model validation is currently under construction and will be the subject of our future publications.

# Chapter 4

# Dynamic Phasor Models of PWM Controlled Rectifiers

## 4.1 Introduction

In Chapter 3, we presented the DP modelling of uncontrolled rectifiers. In this chapter, we will extend the DP concept to modelling the Pulse-Width Modulated (PWM) Controlled Rectifier Unit (CRU). For rectifying the HVAC in aircraft EPS's, the PWM CRU has its advantages. It does not need the heavy and complex autotransformer system; the output voltage is controlled; it is inherently bi-directional and can control the active and reactive power on the AC side. With these advantages, the CRU will be increasingly used in AC distribution aircraft power systems to supply the essential electrical loads such as the flight control actuation. This chapter will focus on the development of the DP model of the CRU.

The control of the CRU uses the concept of vector control which exploits a synchronously rotating reference frame with its d axis fixed on the AC voltage vector. This technique was developed from field oriented control techniques for AC drives in the early 1980s [72]. The control objectives of the CRU are to regulate the output voltage on the DC-side, to achieve the controlled power factor operation on the AC-side, and to obtain a fast dynamic response to line and load disturbances.

The three-phase model of the CRU has been presented in [73], where the fundamental switching functions were used to derive the variable relations on the DC and AC sides. The state-average models of the CRU in the synchronous frame have been developed in [74, 75] and have demonstrated good accuracy. Based on these works, a non-switching functional DQ0 model of CRU was developed in [76] and illustrated high accuracy within MEA functional-level requirements. The model developed in [76] also demonstrates high computational efficiency under balanced conditions. However, under unbalanced and line fault conditions, the simulation speed reduces significantly due to the second harmonic in the system. This lends motivation for the development of DP models of this device.

In this chapter, the DP model of the CRU will be developed and validated with experiments under both balanced and unbalanced conditions. The DP model is developed through modelling the electrical converter and the control system separately. The DP model of an electrical converter is based on the three-phase non-switching model of CRU. The vector control of the CRU is mapped into DPs using a constant-speed rotating frame (dq frame) with its initial angle $\theta_0=0^o$. The controller is expressed using state-space equations which are transformed to the DP domain using DP properties. Projecting the current vector to the voltage vector and expressing the projections in terms of DPs, and combining this with the DP-domain controller, the DP model of the CRU control system can be derived.

The DP CRU model handles unbalanced conditions in a similar way to that of the DP model of uncontrolled rectifiers. The operation of the CRU is assumed to be determined by the positive sequence in the system. The negative sequence of the system under unbalanced conditions is viewed as a disturbance. However, the error of the DP CRU model is smaller than that of the DP uncontrolled rectifier model. This is due to the fact that, the switching behaviour of the CRU is controlled based on the voltage and current vectors and the variables on AC and DC sides are related with modulation functions. In the DP model, these two vectors are modelled in the dq frame and the angle

between these two vectors is well approximated in the DP domain under both balanced and unbalanced conditions. Thus the DP CRU model presents better accuracy compared with the DP uncontrolled rectifier during unbalanced conditions, as can be seen later in this chapter.

The structure of this chapter is as follows: firstly, the DP model of the CRU will be discussed in detail. After that, the experiment validation of the CRU is presented. The efficiency of the DP model is demonstrated through comparison with other different models, including the ABC and DQ0 models. The conclusion is given in the end of this chapter.

# 4.2 Dynamic Phasor Model of the CRU

The PWM controlled rectifier unit is well-known from previous publications [65, 77] , and the topology is shown in Figure 4-1. With the voltage vector aligned with the d axis in a synchronous rotating frame, denoted as DQ frame, the projections of the current vector onto the D and Q axes correspond to the active power and reactive power components respectively. This allows independent control of the active and reactive power flow. The voltage vector angular position $\theta$ is derived from a Phase-Locked Loop (PLL) [78].

The PLL has been widely used in distributed generation systems, Flexible AC Transmission systems (FACTs), static VAR compensators, active power filters and other systems connected to the utility [79]. A common configuration of a PLL is shown in Figure 4-2 and is called the Synchronous Reference Frame PLL (SRF-PLL) [80]. The SRF-PLL has been widely used for three-phase applications including grid synchronization and autonomous operation of PECs due to it simple structure and fast response characteristics [81]. In the SRF-PLL, the three-phase voltages are transformed to $v_d$ and $v_q$. Setting $v_q^*$ to zero, the angle $\theta^*$ is found to be the angle of the voltage vector [80].

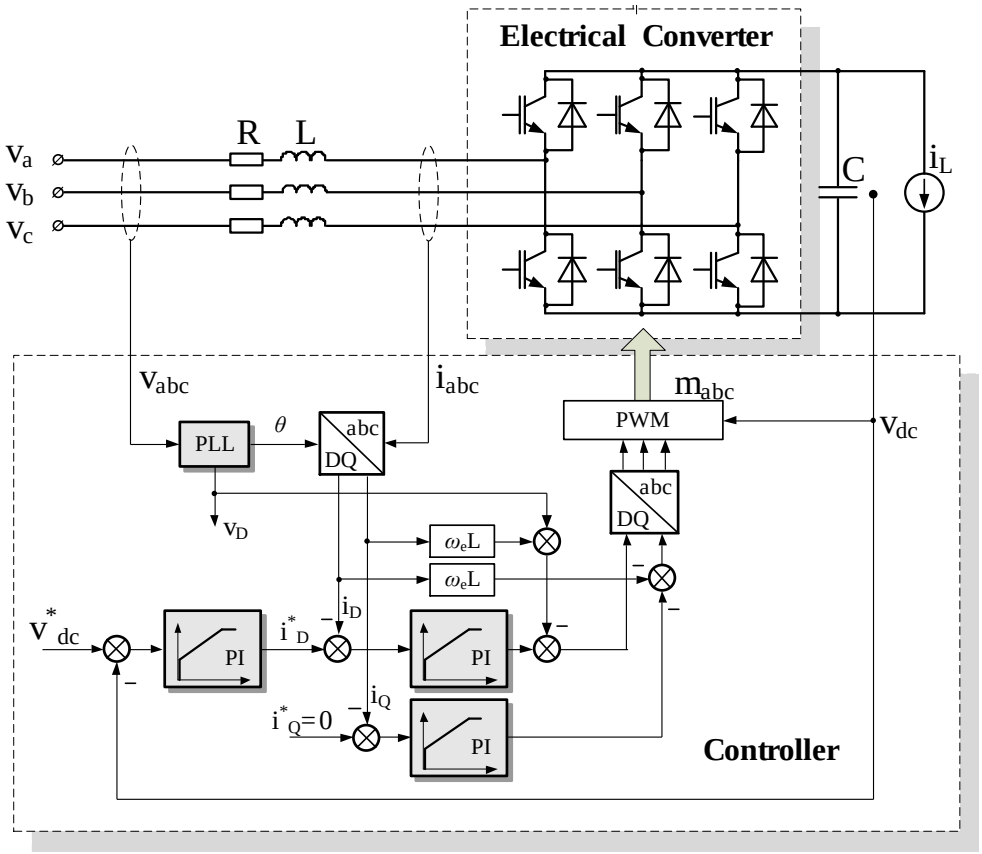


Figure 4-1 Structure of the PWM controlled rectifier

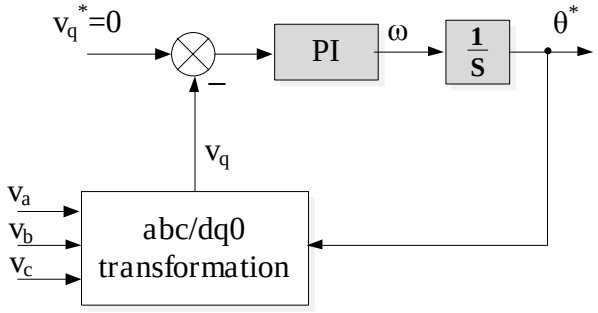


Figure 4-2 Synchronous frame PLL scheme

When estimating the phase angle of the positive sequence, this SRF-PLL suffers from double-frequency error when there is unbalance in the system. For power conditioning equipment such as active filters, VAR compensators etc. the angle of positive sequence is needed for achieving the desired goal of the system. A large number of research activities have developed PLL design, including double SRF-PLL (DSRF-PLL) [82], Double Second-Order

Generalized Integrator PLL (DSOGI-PLL) [83], SRF-PLL with Positive Sequence Filter (PSF-PLL) [84] etc. All these enhanced PLLs are basically adding some filter in front of the SRF-PLL. For example, the DSRF-PLL separates the positive and negative sequences and then applies the SRF-PLL to the positive sequence as shown in Figure 4-3.

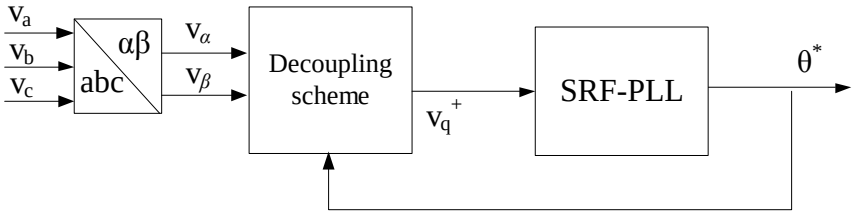


Figure 4-3 DSRF-PLL scheme

The enhanced PLLs have more complex structures than the conventional SRF-PLL and still need further investigation for aircraft applications. In this thesis, we focus on the modelling of the CRU with the conventional SRF-PLL. However, the DP modelling developed in this chapter can be conveniently extended to modelling the CRU using other enhanced PLLs. The PLL basically provides a filtered version of the angle $\text{atan}^{-1}(v_\beta/v_\alpha)$ or $atan^{-1}(v_\beta^+/v_\alpha^+)$. The time constant is in the order of milliseconds and thus in the functional DP model, the filter impact is neglected and the vector angle is used directly.

The CRU is essentially composed of two subsystems: the electrical converter and the control system, as shown in Figure 4-1. The DP model of the electrical converter is based on the non-switching models of the CRU, and the DP model of these two subsystems will be developed separately. The DP modelling of the control system needs more discussion. Firstly, the DP expression of the time-domain voltage and current vectors introduced in section 3.4.1 will be used. Secondly, the projection of the current vector to the voltage vector is mapped into DPs. Finally, the DP models of the controller are developed.

## 4.2.1 Developing the DP Representation of the Control System

### 1) Expression of Vectors in Dynamic Phasors

The DP expression of time-domain vectors has been well discussed in Chapter 3. However, in order to make this chapter self-contained, some key equations will be rewritten in this section. Here, the DPs will be represented in the dq frame. This is not the DQ frame as will be discussed later.

The voltage vector is defined as:

$$\vec{v} = 2/3\left(v_a + v_b e^{j2\pi/3} + v_c e^{-j2\pi/3}\right) \tag{4-1}$$

The current vector is defined in the same way. In the rotating dq frame, the voltage vector in (4-1) can be expressed as:

$$\vec{v}e^{-j\omega t} = v_d + jv_q = \left\{V_{d0} + jV_{q0}\right\} + e^{-2j\omega t}\left\{V_{d2} + jV_{q2}\right\} \tag{4-2}$$

The first term on the right side of (4-2) arises from the positive sequence with no harmonics and the real and imaginary part represents the DC components of $v_d$ and $v_q$ respectively. The second term arises from the negative sequence and represents the second harmonic of $v_d$ and $v_q$. Thus the DP index set for $\langle v_d \rangle_k$ and $\langle v_q \rangle_k$ should be chosen at K={0,2}. The variables $V_{d0}$, $V_{q0}$, $V_{d2}$ and $V_{q2}$ can be calculated as follows:

$$V_{d0} = \frac{2}{3}\mathrm{Re}\left[\langle v_a \rangle_1 + \langle v_b \rangle_1 e^{j2\pi/3} + \langle v_c \rangle_1 e^{-j2\pi/3}\right] \tag{4-3a}$$

$$V_{q0} = \frac{2}{3}\mathrm{Im}\left[\langle v_a \rangle_1 + \langle v_b \rangle_1 e^{j2\pi/3} + \langle v_c \rangle_1 e^{-j2\pi/3}\right] \tag{4-3b}$$

$$V_{d2} = \frac{2}{3}\mathrm{Re}\left[\langle v_a \rangle_1^* + \langle v_b \rangle_1^* e^{j2\pi/3} + \langle v_c \rangle_1^* e^{-j2\pi/3}\right] \tag{4-3c}$$

$$V_{q2} = \frac{2}{3}\mathrm{Im}\left[\langle v_a \rangle_1^* + \langle v_b \rangle_1^* e^{j2\pi/3} + \langle v_c \rangle_1^* e^{-j2\pi/3}\right] \tag{4-3d}$$

The dynamic phasors for $v_d$ and $v_q$ can be calculated using (4-2) and (4-3) together with the DP definition. The current vector can be dealt with in the same way. The DPs of vectors in the rotating dq frame are summarized in Table 4-1.

Table 4-1 Dynamic phasors for CRU input voltage and current in synchronously rotating frame

| Variable | Dynamic phasors | |
|---|---|---|
| | k=0 | k=2 |
| $v_d$ | $\langle v_d \rangle_0 = V_{d0}$ | $\langle v_d \rangle_2 = (V_{d2} - jV_{q2})/2$ |
| $v_q$ | $\langle v_q \rangle_0 = V_{q0}$ | $\langle v_q \rangle_2 = (V_{q2} + jV_{d2})/2$ |
| $i_d$ | $\langle i_d \rangle_0 = I_{d0}$ | $\langle i_d \rangle_2 = (I_{d2} - jI_{q2})/2$ |
| $i_q$ | $\langle i_q \rangle_0 = I_{q0}$ | $\langle i_q \rangle_2 = (I_{q2} + jI_{d2})/2$ |

**2) Active and Reactive Current Components**

The control structure shown in Figure 4-1 considers a rotating frame fixed on the voltage vector. Thus the active power and reactive power can be controlled by the projections of the current vector onto the real and imaginary axes respectively. Under balanced conditions, this frame rotates at a synchronous speed $\omega$. However, under unbalanced conditions, this frame rotation speed $\omega$ includes a second harmonic ripple due to the negative sequence. This rotating frame, generally elliptic, is denoted as DQ frame in this thesis and the corresponding current components are denoted as $i_D$ and $i_Q$. In the DQ frame, the D-axis is always fixed on and synchronized with the voltage vector. However, the elliptical rotation of DQ frame makes the DPs of $i_D$ and $i_Q$ mathematically complicated to derive under unbalanced conditions.

The transformation of vectors from $\alpha\beta$ frame to the DQ frame is obtained by multiplying $e^{-j\theta_v}$ with the voltage vector, i.e.

$$\vec{v}_{DQ} = \vec{v}e^{-j\theta_v} = |\vec{v}| \tag{4-4}$$

where $\theta_v$ is the voltage vector angle in $\alpha\beta$ frame as shown in Figure 4-4 and can be written as:

$$\theta_v = \tan^{-1}\left\{\frac{\Im m(\vec{v})}{\Re e(\vec{v})}\right\} = \tan^{-1}\left\{\frac{v_\beta}{v_\alpha}\right\} \tag{4-5}$$

Under balanced conditions, $\theta_v$ is with a linear function of $\omega$ and equal to $\omega t+\theta_0$. However under unbalanced conditions, $\theta_v$ fluctuates due to the negative sequence and can be express as

$$\theta_v = (\omega+\Delta\omega)t \tag{4-6}$$

where $\Delta\omega$=0 under balanced conditions. Thus the current vector in DQ frame can be written as

$$\begin{aligned}\vec{i}_{DQ} &= \vec{i}\,e^{-j\theta_v} = i_D + j i_Q \\ &= \frac{2}{3}\left\{\langle i_a\rangle_1 + \langle i_b\rangle_1 e^{j2\pi/3} + \langle i_c\rangle_1 e^{-j2\pi/3}\right\}e^{j\omega t}e^{-j\theta_v} \\ &\quad + \frac{2}{3}\left\{\langle i_a\rangle_1^* + \langle i_b\rangle_1^* e^{j2\pi/3} + \langle i_c\rangle_1^* e^{-j2\pi/3}\right\}e^{-j\omega t}e^{-j\theta_v}\end{aligned} \tag{4-7}$$

Combining (4-6) and (4-7) gives

$$\begin{aligned}i_D + j i_Q &= \frac{2}{3}\left\{\langle i_a\rangle_1 + \langle i_b\rangle_1 e^{j2\pi/3} + \langle i_c\rangle_1 e^{-j2\pi/3}\right\}e^{-j\theta_0}e^{-j\Delta\omega t} \\ &\quad + \frac{2}{3}\left\{\langle i_a\rangle_1^* + \langle i_b\rangle_1^* e^{j2\pi/3} + \langle i_c\rangle_1^* e^{-j2\pi/3}\right\}e^{-2j\omega t}e^{-j\theta_0}e^{-j\Delta\omega t}\end{aligned} \tag{4-8}$$

It can be noticed from (4-8) that the calculation of DPs of $i_D$ and $i_Q$ is not mathematically convenient due to the term $e^{-j\Delta\omega t}$. This is due to the discontinuous $atan^{-1}$ function. In addition, the DPs of the vector DQ components will fluctuate under unbalanced conditions due to the term $e^{-j\Delta\omega t}$. A sliding window with width T=2π/$\omega$ and DP index set at K={0,2} will result.

To avoid the cumbersome calculation of DPs of currents $i_D$ and $i_Q$ in the DQ frame, we choose another rotating frame denoted as the dq frame in this thesis. The dq frame is a frame rotating at the basic frequency of the AC supply $\omega$ under both balanced and unbalanced conditions. The selection of this dq frame allows us to conveniently represent the d and q components of voltage and current vectors in DPs. Under both balanced and unbalanced conditions, the DPs in the dq frame are always dc-like, as shown in Table 4-1. In reality, the DQ and dq frames have an angle difference denoted as $\phi$, as shown in Figure 4-4. In the balanced condition, this angle is constant and is determined by the initial phase angle of voltage angle $\theta_0$. However, under unbalanced conditions,

this angle $\phi$ fluctuates with time due to the time-varying rotating speed of the DQ frame.

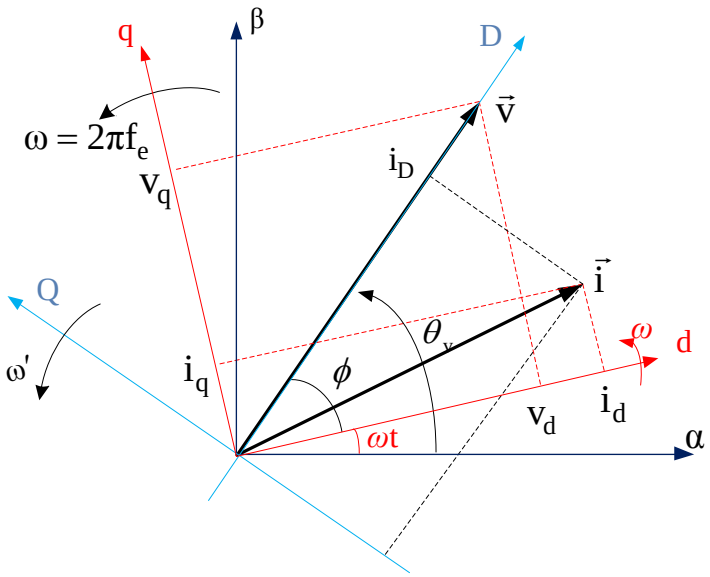


Figure 4-4 Frame considerations for development of the DP CRU model

With the chosen dq frame, the voltage and current vectors conveniently are represented in DPs and expressed in term of $\langle v_{a,b,c}\rangle_k$ and $\langle i_{a,b,c}\rangle_k$, as shown in (4-2) and (4-3) and Table 4-1. As mentioned before, the D axis is fixed onto the voltage vector, thus the components $i_D$ and $i_Q$ always represent the active and reactive power. In the DP model, these two components $i_D$ and $i_Q$ will be represented by the current component in the dq frame, $i_d$ and $i_q$ and then transformed to the DP domain. According to Figure 4-4, the relation between the input current components in the DQ and dq frames at any instant can be derived as:

$$i_D = i_d \cos\phi + i_q \sin\phi \tag{4-9a}$$

$$i_Q = -i_d \sin\phi + i_q \cos\phi \tag{4-9b}$$

Mapping (4-9) into the DP domain can be achieved using the DP convolution property. The DPs of $i_d$ and $i_q$ are needed and have already been derived in Table 4-1. The DPs for the functions $\sin\phi$ and $\cos\phi$ are also required. Under unbalanced conditions, the angle $\phi$ is time-varying and these sinusoidal functions can be expressed via the voltage dq components as:

$$\cos\phi = f_1(v_d, v_q) = v_d \Big/ \sqrt{v_d^2 + v_q^2} \tag{4-10}$$

$$\sin\phi = f_2(v_d, v_q) = v_q \Big/ \sqrt{v_d^2 + v_q^2} \tag{4-11}$$

The DP forms of (4-10) and (4-11) can be derived in the same way as that used in Section 3.3.4 and are written as:

$$\langle \cos\phi \rangle_0 = h_0 + h_3 \langle v_d \rangle_2 \langle v_d \rangle_2^* + h_4 \langle v_q \rangle_2 \langle v_q \rangle_2^* + h_5 \left\{ \langle v_d \rangle_2 \langle v_q \rangle_2^* + \langle v_d \rangle_2^* \langle v_q \rangle_2 \right\} \tag{4-12a}$$

$$\langle \cos\phi \rangle_2 = h_1 \langle v_d \rangle_2 + h_2 \langle v_q \rangle_2 \tag{4-12b}$$

$$\langle \sin\phi \rangle_0 = g_0 + g_3 \langle v_d \rangle_2 \langle v_d \rangle_2^* + g_4 \langle v_q \rangle_2 \langle v_q \rangle_2^* + g_5 \left\{ \langle v_d \rangle_2 \langle v_q \rangle_2^* + \langle v_d \rangle_2^* \langle v_q \rangle_2 \right\} \tag{4-12c}$$

$$\langle \sin\phi \rangle_2 = g_1 \langle v_d \rangle_2 + g_2 \langle v_q \rangle_2 \tag{4-12d}$$

The DP transformation of (4-9) is written as:

$$\begin{aligned} \langle i_D \rangle_0 = {} & \langle i_d \rangle_0 \langle \cos\phi \rangle_0 + \langle i_d \rangle_2^* \langle \cos\phi \rangle_2 + \langle i_d \rangle_2 \langle \cos\phi \rangle_2^* \\ & + \langle i_q \rangle_0 \langle \sin\phi \rangle_0 + \langle i_q \rangle_2^* \langle \sin\phi \rangle_2 + \langle i_q \rangle_2 \langle \sin\phi \rangle_2^* \end{aligned} \tag{4-13}$$

$$\begin{aligned} \langle i_Q \rangle_0 = {} & -\langle i_d \rangle_0 \langle \sin\varphi \rangle_0 - \langle i_d \rangle_2^* \langle \sin\varphi \rangle_2 - \langle i_d \rangle_2 \langle \sin\varphi \rangle_2^* \\ & + \langle i_q \rangle_0 \langle \cos\varphi \rangle_0 + \langle i_q \rangle_2^* \langle \cos\varphi \rangle_2 + \langle i_q \rangle_2 \langle \cos\varphi \rangle_2^* \end{aligned} \tag{4-14}$$

$$\langle i_D \rangle_2 = \langle i_d \rangle_0 \langle \cos\varphi \rangle_2 + \langle i_d \rangle_2 \langle \cos\varphi \rangle + \langle i_q \rangle_0 \langle \sin\varphi \rangle_2 + \langle i_q \rangle_2 \langle \sin\varphi \rangle_0 \tag{4-15}$$

$$\langle i_Q \rangle_2 = -\langle i_d \rangle_0 \langle \sin\varphi \rangle_2 - \langle i_d \rangle_2 \langle \sin\varphi \rangle_0 + \langle i_q \rangle_0 \langle \cos\varphi \rangle_2 + \langle i_q \rangle_2 \langle \cos\varphi \rangle_0 \tag{4-16}$$

Hence, all DPs constituting the controlled variables, i.e. $i_D$ and $i_Q$, are derived. From the basic principle of CRU control, the components $\langle i_D \rangle_2$ and $\langle i_Q \rangle_2$ should be controlled to zero. The component $\langle i_Q \rangle_0$ controls the reactive power and the component $\langle i_D \rangle_0 \langle i_D \rangle_0$ controls the active power and hence the DC-link voltage.

### 3) Dynamic Phasors for the CRU controller

In this section, we will introduce the DP model of a PI controller. However, the

DP model of any other pole-zero controllers can follow the same procedure as that used for the PI controller here.

As shown in Figure 4-1, the control structure of the CRU employs proportional-integral (PI) controllers that should be converted into the DP domain. The state-space equation for the PI controller in the time domain is:

$$\dot{x} = k_i u \tag{4-17a}$$

$$y = k_p u + x \tag{4-17b}$$

where u is the input, x is the state variable, and $k_p$ and $k_i$ are the proportional and integral gains correspondingly. This equation can be converted into dynamic phasors as:

$$\frac{d\langle x\rangle_k}{dt} = k_i \langle u\rangle_k - jk\omega\langle x\rangle_k \tag{4-18a}$$

$$\langle y\rangle_k = k_p\langle u\rangle_k + \langle x\rangle_k \tag{4-18b}$$

The selection of the DP index for the controller should be chosen the same as that for $\langle i_D\rangle_k$ and $\langle i_Q\rangle_k$ and is set at K={0,2}

**4) Modulation Index and Transformation to Three-phase Coordinates**

The CRU control output is a three-phase modulation index $m_{abc}$. However the modulation index produced by the current controller $m_{DQ}$ is in the DQ frame. The angle between the DQ frame and the static $\alpha\beta$ frame is $(\omega t+\phi)$ as shown in Figure 4-4. The relation between $m_{DQ}$ to $m_{abc}$ is:

$$\begin{bmatrix} m_a & m_b & m_c \end{bmatrix}^T = \mathbf{K}_s \begin{bmatrix} m_D & m_Q \end{bmatrix}^T \tag{4-19}$$

where the transformation matrix $\mathbf{K}_s$ is:

$$\mathbf{K}_s = \begin{bmatrix} \cos(\omega t + \phi) & -\sin(\omega t + \phi) \\ \cos(\omega t + \phi - 2\pi/3) & -\sin(\omega t + \phi - 2\pi/3) \\ \cos(\omega t + \phi + 2\pi/3) & -\sin(\omega t + \phi + 2\pi/3) \end{bmatrix} \tag{4-20}$$

As discussed in previous sections, under unbalanced conditions the voltage

vector angle $\phi$ is not constant and includes harmonics. Therefore the DPs of elements in $\mathbf{K}_s$ are not constant complex numbers as in Table 2-1. The DP of $K_s$ can be derived by two steps: firstly expanding all the elements in the matrix into a series of sinusoidal functions of $\omega t$ and $\phi$; secondly using the DP property to transform the functions derived in the first step into DPs. For example, the element $\cos(\omega t + \varphi - 2\pi/3)$ can be expanded as:

$$\cos(\omega t + \phi - 2\pi/3) = 0.5\left\{\cos\omega t(-\cos\phi + \sqrt{3}\sin\phi) + \sin\omega t(\sin\phi + \sqrt{3}\cos\phi)\right\} \tag{4-21}$$

The DPs for all the sinusoidal functions are already known according to Table 2-1 and (3-39). In addition, the DP index for $\cos\omega t$ (k=1) and $\cos\phi$ (k=0, 2) determines that the DP index set for $K_s$ should be set at K={1, 3} according to the DP convolution property. The DP transformation of (4-21) can be written as:

$$\begin{aligned}\left\langle\cos(\omega t + \phi - 2\pi/3)\right\rangle_1 = {} & 0.5\left\langle\cos\omega t\right\rangle_1\left\langle(-\cos\phi + \sqrt{3}\sin\phi)\right\rangle_0 - 0.5\left\langle\sin\omega t\right\rangle_1\left\langle(\sin\phi + \sqrt{3}\cos\phi)\right\rangle_0 \\ & + 0.5\left\langle\cos\omega t\right\rangle_1^*\left\langle(-\cos\phi + \sqrt{3}\sin\phi)\right\rangle_2 - 0.5\left\langle\sin\omega t\right\rangle_1^*\left\langle(\sin\phi + \sqrt{3}\cos\phi)\right\rangle_2\end{aligned} \tag{4-22}$$

$$\begin{aligned}\left\langle\cos(\omega t + \phi - 2\pi/3)\right\rangle_3 = {} & 0.5\left\langle\cos\omega t\right\rangle_1\left\langle(-\cos\phi + \sqrt{3}\sin\phi)\right\rangle \\ & - 0.5\left\langle\sin\omega t\right\rangle_1\left\langle(\sin\phi + \sqrt{3}\cos\phi)\right\rangle_2\end{aligned} \tag{4-23}$$

The DPs for other elements of $K_s$ can be calculated in a similar way. Since only the fundamental of the AC variables is considered, the DP index is k=1. Applying the DP convolution and conjugate properties, the DPs for (4-18) can be established as:

$$\left\langle\begin{bmatrix} m_a \\ m_b \\ m_c \end{bmatrix}\right\rangle_1 = \left\langle\mathbf{K}_s\right\rangle_1\left\langle\begin{bmatrix} m_D \\ m_Q \end{bmatrix}\right\rangle_0 + \left\langle\mathbf{K}_s\right\rangle_1^*\left\langle\begin{bmatrix} m_D \\ m_Q \end{bmatrix}\right\rangle_2 + \left\langle\mathbf{K}_s\right\rangle_3\left\langle\begin{bmatrix} m_D \\ m_Q \end{bmatrix}\right\rangle_2^* \tag{4-24}$$

Here $\langle K_s\rangle_1$ and $\langle K_s\rangle_3$ are the DP transformation of $K_s$.

### 4.2.2 Electrical Converter

The Electrical converter of the CRU will be represented with the voltage and current relations on the DC and AC sides as mathematic functions, rather than using electrical switches. This is also true for the DP models. The relationship between variables on the AC side and the DC side can be expressed as [76]:

$$\mathbf{v}_{\mathbf{abc}} = 0.5 \mathrm{v}_{\mathrm{dc}} \mathbf{M}_{\mathbf{abc}} \tag{4-25}$$

$$\mathrm{i}_{\mathrm{dc}} = 0.5 \mathbf{M}_{\mathbf{abc}}^{\mathbf{T}} \mathbf{i}_{\mathbf{abc}} \tag{4-26}$$

where $\mathbf{M}_{\mathrm{abc}}=[m_a \quad m_b \quad m_c]^T$ , $\mathbf{v}_{\mathrm{abc}}=[v_a \quad v_b \quad v_c]^{\mathrm{T}}$ and $\mathbf{i}_{\mathrm{abc}}=[i_a \quad i_b \quad i_c]^T$ Variables $\mathrm{v}_{\mathrm{dc}}$ and $\mathrm{i}_{\mathrm{dc}}$ are the dc-link voltage and current respectively. The DP transformation of (4-25) and (4-26) can be derived with the DP convolution property. Only the fundamental component is considered on the AC side (DP index k=1) and only the DC component is considered on the DC side (DP index k=0). The transformation of these equations into dynamic phasors is as follows:

$$\left\langle \mathbf{v}_{\mathbf{abc}} \right\rangle_1 = 0.5 \left\langle \mathrm{v}_{\mathrm{dc}} \right\rangle_0 \left\langle \mathbf{M}_{\mathbf{abc}} \right\rangle_1 \tag{4-27}$$

$$\left\langle \mathrm{i}_{\mathrm{dc}} \right\rangle_0 = 0.5 \left\langle \mathbf{M}_{\mathbf{abc}}^{\mathbf{T}} \right\rangle_1 \left\langle \mathbf{i}_{\mathbf{abc}} \right\rangle_1^* \tag{4-28}$$

### 4.2.3 Model Assembly

The above derived DP equations constitute the core model of the CRU. As a signal flow diagram the model is given in Figure 4-5. This model can be directly applied for simulation studies when the whole EPS is modelled in the DP domain [37]. In this case all the required inputs (supply voltages, input currents and the DC voltage) are available in DP forms, and the outputs of the model (CRU terminal voltages and the DC current) can be directly interfaced with the other DP models. The signal flow can be easily conceived through comparison of Figure 4-1 and Figure 4-5. All the 2nd order DP references $\langle i_D \rangle_2^{ref}$ and $\langle i_Q \rangle_2^{ref}$ are always set to zero in the DP model. In order to achieve the unity power factor on the AC side, $\langle i_Q \rangle_0^{ref}$ is set to zero. It can also be seen from

Figure 4-5 that the system order is increased compared with the three-phase domain model in Figure 4-1. However since the DPs are dc-like in steady state, a significant acceleration in simulation is expected even with a relatively higher order system (to be confirmed in the following sections).

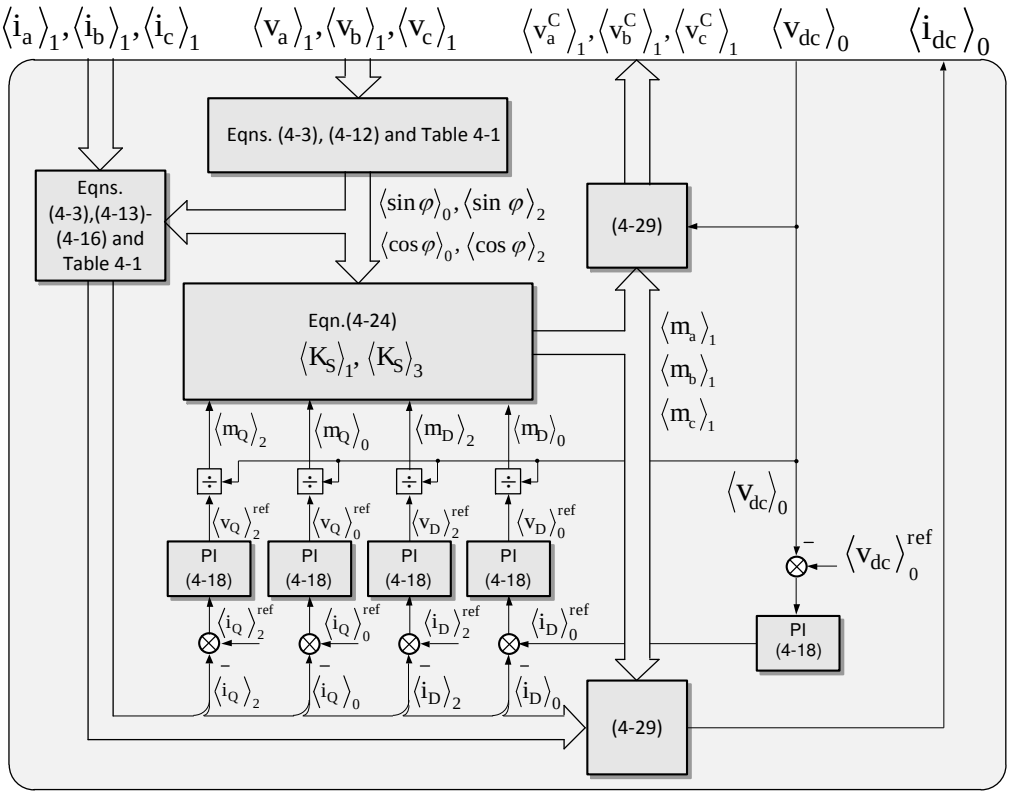


Figure 4-5 DP domain model of the active front-end rectifier

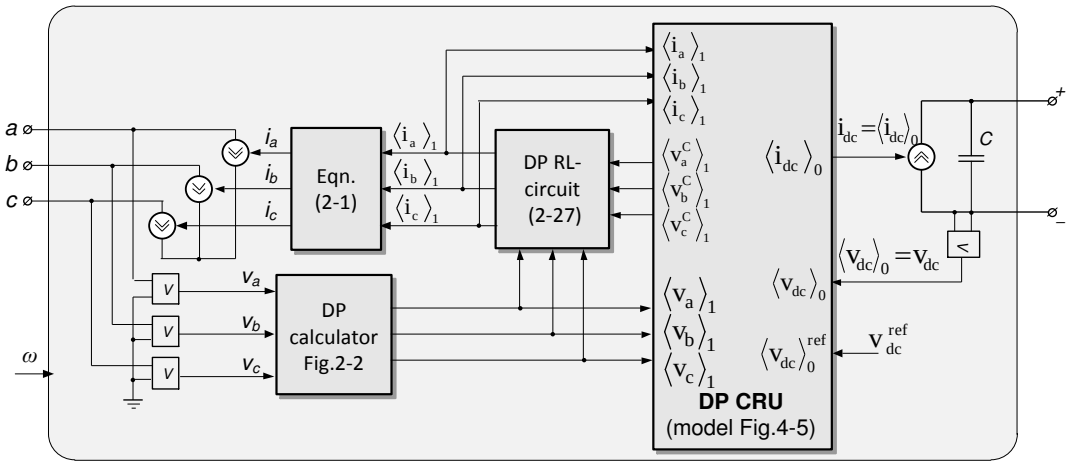


Figure 4-6 Three-phase interfacing of the DP CRU model

In order to allow a wider application of the DP CRU model, an interface between the time-domain model and the DP model is developed as well. The CRU model with the time-domain interface is shown in Figure 4-6. Apart from the DP calculators, the interface module also includes the DP-domain equations for the buffer RL circuit to link the CRU terminals.

## 4.3 Model Experiment Validation

A test rig was set up to validate the developed DP model. The CRU was supplied by a programmable AC source Chroma 61705 capable of generating balanced and unbalanced sets of three-phase voltages. The CRU control is implemented using a digital signal processor TMS320C671 connected to an FPGA board for data acquisition and sampling. The SRF-PLL is implemented. The system scheme is shown in Figure 4-7. The parameters are given in Table 4-2.

Table 4-2 Experimental system parameters

| Parameters | Values | Note |
|---|---|---|
| R | 0.1 Ω | Front-end resistance |
| L | 3 mH, | Front-end inductance |
| C | 2200 μF | DC-Link capacitor |
| $R_1$ | 200 Ω | Resistive load |
| $R_2$ | 92 Ω | Resistive load |
| $f_{sw}$ | 10 kHz | Switching frequency |
| $f_c$ | 10 kHz | Data Sampling frequency |
| $K_{pv}$ | 0.03 | Proportional gain of voltage loop |
| $K_{iv}$ | 0.6 | Integral gain of Voltage loop |
| $K_{pi}$ | 4.5 | Proportional gain of current loop |
| $K_{ii}$ | 2115 | Integral gain of current loop |
| $K_{p\_PLL}$ | 3553 | Proportional gain of PLL |
| $K_{i\_PLL}$ | 6.3e5 | Integral gain of PLL |

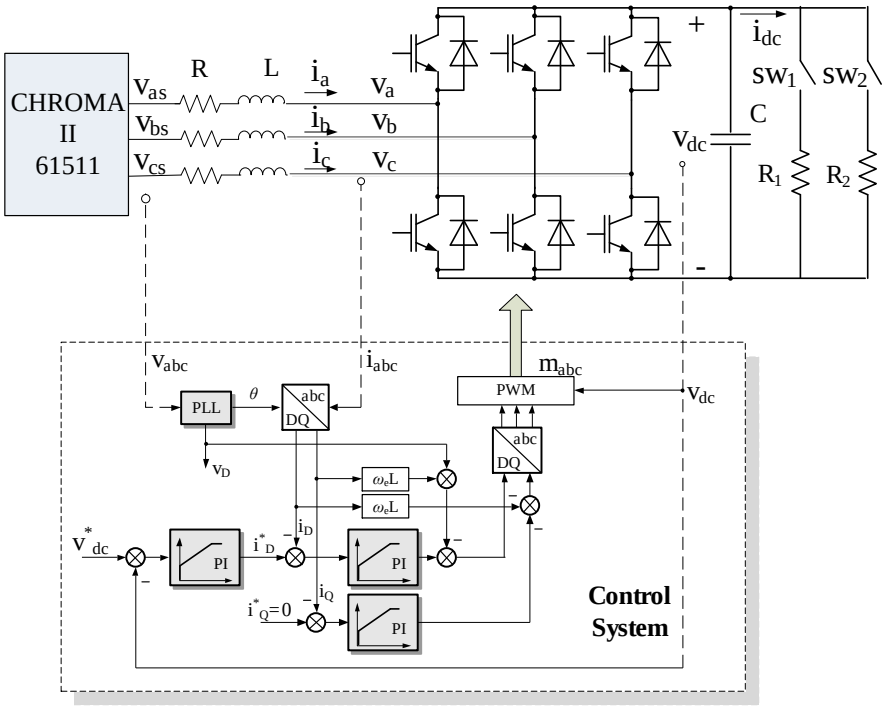


Figure 4-7 CRU validation scheme

### 4.3.1 Response to $v_{dc}$ Step under Balanced Conditions

In this experiment, the CRU is supplied by a balanced voltage source with 80Vrms at 400Hz. The CRU is loaded by $R_1$. The DC-link voltage reference changes from 200V to 270V. The simulation and experiment results of $v_{dc}$ and $i_{a,b,c}$ are compared in Figure 4-8 and Figure 4-9 respectively.

As can be seen from Figure 4-8, the $v_{dc}$ from DP model well reflects the average value of that from the experiment. Even during the transient period, the result from DP model is well matched with the experiment result. The AC currents $i_{a,b,c}$ from the DP model well represents the fundamentals of those from the experiment as shown in Figure 4-9.

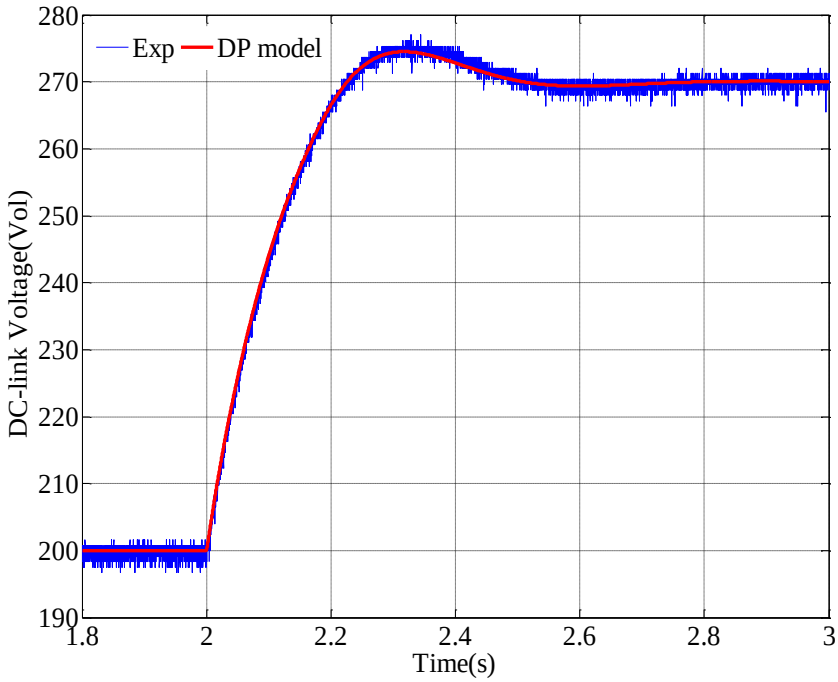


Figure 4-8 DC voltage in response to a step in voltage demand under balanced conditions

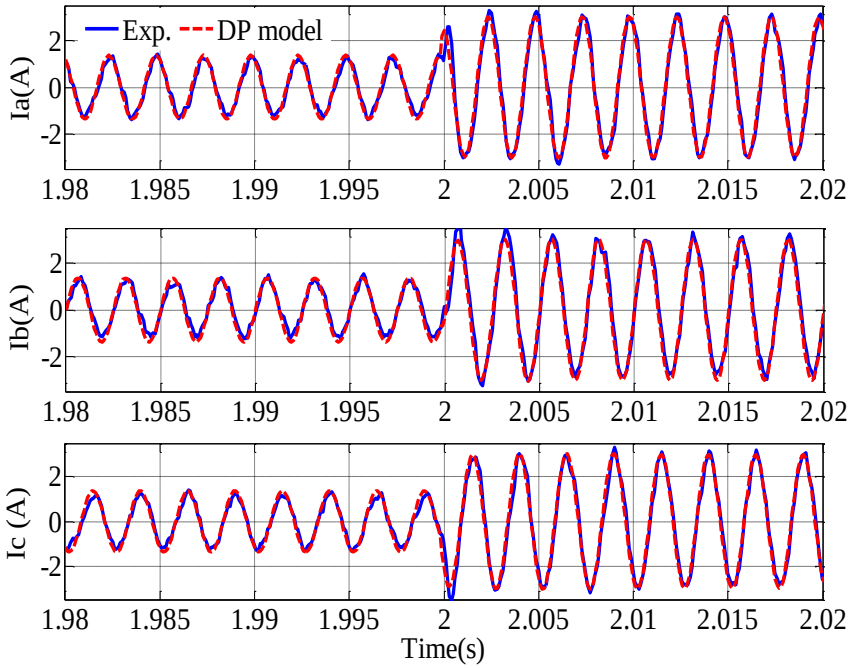


Figure 4-9 AC currents in response to a step in voltage demand under balanced conditions

### 4.3.2 Dynamic Responses under Unbalanced Conditions

In this section, the DP model was experimentally tested under conditions where the three-phase source involves a small unbalance. The imbalance was made small in order to avoid the trip of the rig. Two different cases were tested: a DC-link voltage step change and a DC-link load change.

#### 1) DC-link Voltage Step Change

In this case, A step in DC-link voltage from 250V to 270V has been applied to the CRU with the voltage source chosen at $v_a$=80V, $v_b$=90V, $v_c$=100V at 400Hz. The CRU feeds $R_1$ only. The simulation and experiment results of $v_{dc}$ and $i_{a,b,c}$ in this case are compared in Figure 4-10 and Figure 4-11 respectively. It can be seen from Figure 4-10 that $v_{dc}$ from the DP model well matches the experiment. With higher DC-link voltage, the resistive load draws more current from the converter. This results in an increase in AC current, as can be seen in Figure 4-11.

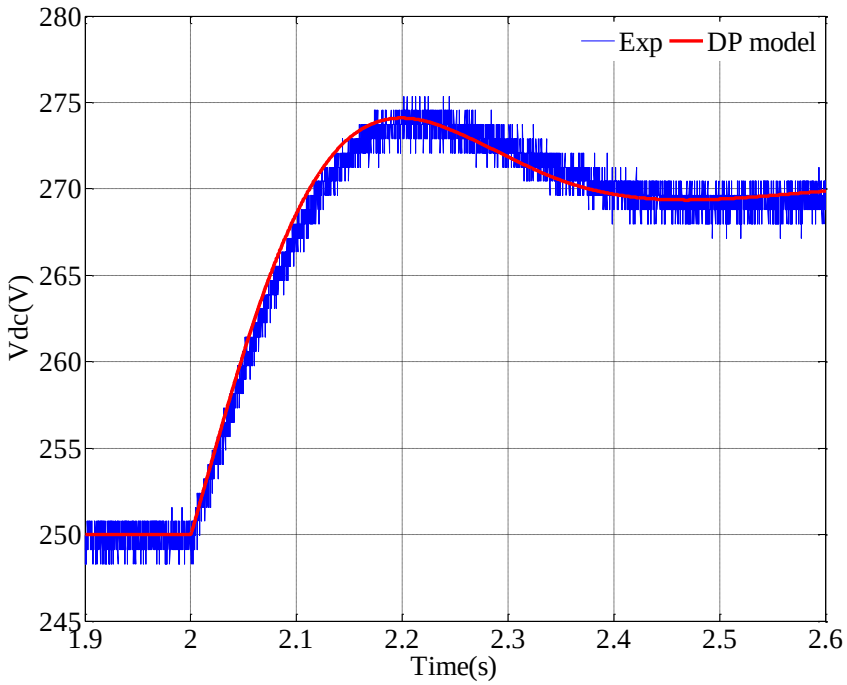


Figure 4-10 DC voltage in response to a step in voltage demand under the unbalanced supply condition

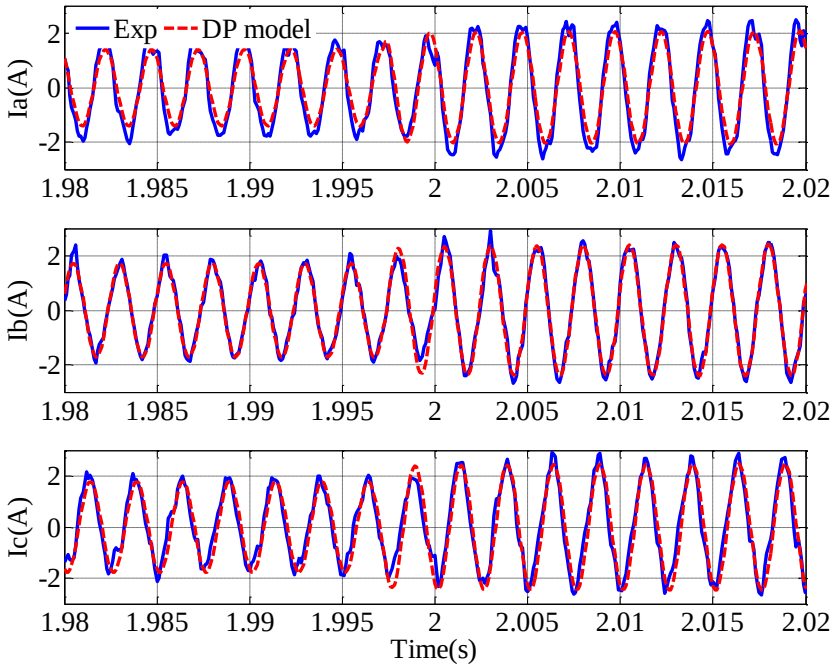


Figure 4-11 Input currents in response to a step in voltage demand under the unbalanced supply condition

### 2) Load Step Change

A step in the load ($R_{load}$ changed from $R_1$ to $R_2$) is applied to the CRU system. The supply voltage is set at $V_a$=65V, $V_b$=70V, $V_c$=60V and DC-link voltage is controlled at 185V. The experiment results are compared against the simulation results in Figure 4-12 and Figure 4-13. The response of the DC-link voltage in Figure 4-12 is from load current step due to the load change and the voltage control loop regulates the $v_{dc}$ back to 185V after. The results from the DP model well present the average value of those from experiment. In Figure 4-13, $i_{a,b,c}$ from the DP model represents the fundamentals of those from experiments. As can be seen, with the increase of the load on the DC-link side, the AC currents increase at the same time.

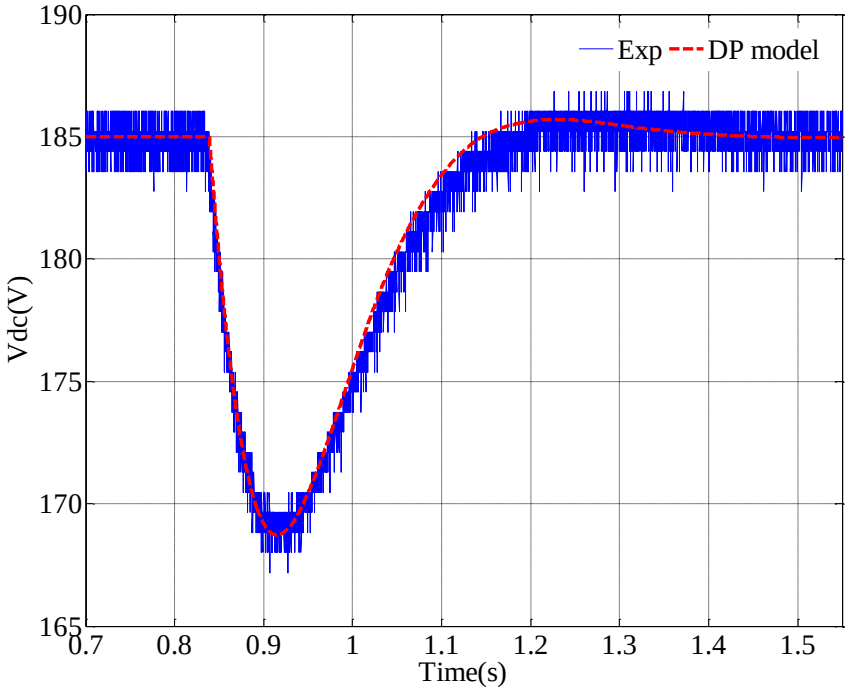


Figure 4-12 DC voltage in response to a load impact under unbalanced supply condition

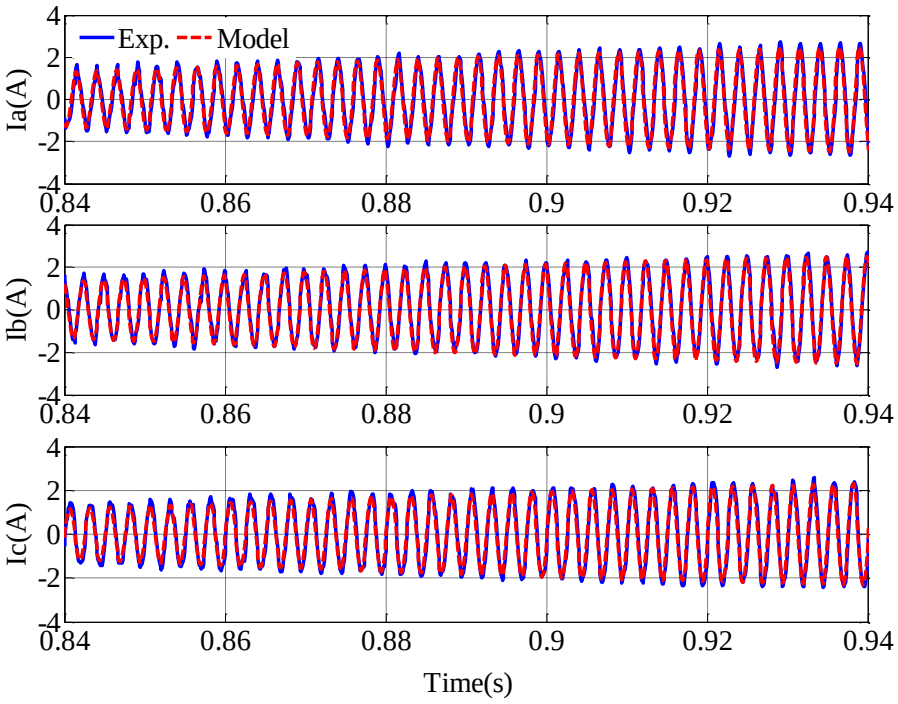


Figure 4-13 Input current in response to a load impact under unbalanced supply condition

### 4.3.3 Dynamic Responses under Line Fault Conditions

In this section, the DP model is tested under even more severe unbalanced conditions: open-circuit conditions and line-to-line fault conditions.

#### 1) Open Circuit Conditions

In this experiment, the open-circuit fault was implemented with phase C be an open circuit. Phases A and B voltages are set at 80Vrms at 400Hz. A step of the DC-link voltage demand is implemented in the CRU. The $v_{dc}$ and $i_{a,b,c}$ from the DP model and experiment are compared in Figure 4-14 and Figure 4-15. These results show that the model accurately reproduces the dynamics of DC voltage, as well as the behaviour of CRU input current under the phase loss.

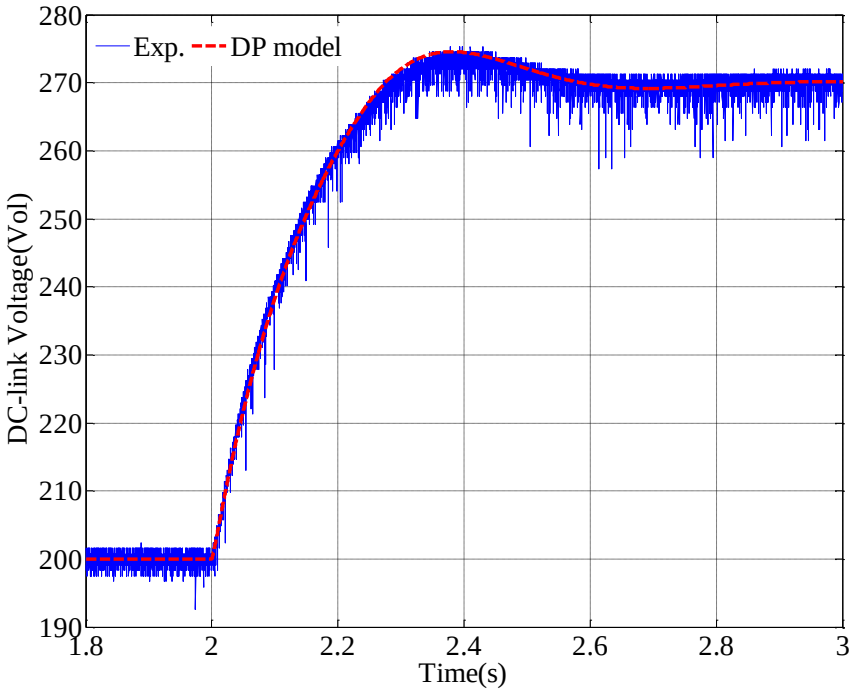


Figure 4-14 DC-link voltage in response to a step in voltage demand under open-circuit fault conditions

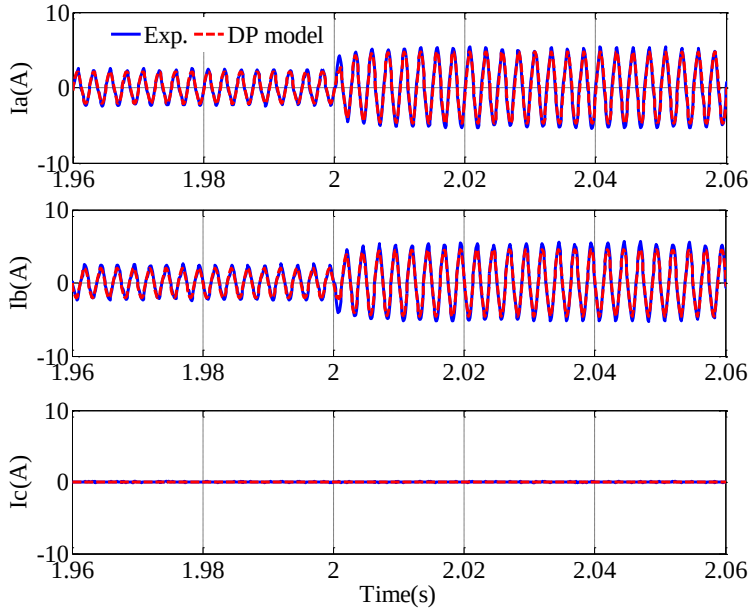


Figure 4-15 AC currents in response to a step in voltage demand under open-circuit fault conditions

### 2) Line-to-Line Fault Conditions

Due to the high current of the short circuit fault, the validation of the DP model under line-to-line fault conditions was conducted using only a benchmark simulation. The system parameters are slightly different from the experimental rig and are shown in Table 4-3.

Table 4-3 System parameters for simulation for line-to-line fault conditions

| Parameters | Values | Note |
|---|---|---|
| R | 0.1 Ω | Front-end resistance |
| L | 1.25 mH, | Front-end inductance |
| C | 2400 μF | DC-Link capacitor |
| $f_{sw}$ | 10 kHz | Switching frequency |
| $K_{pv}$ | 1.187 | Proportional gain of voltage loop |
| $K_{iv}$ | 93.25 | Integral gain of Voltage loop |
| $K_{pi}$ | 3.76 | Proportional gain of current loop |
| $K_{ii}$ | 4430 | Integral gain of current loop |
| $K_{p\_PLL}$ | 3553 | Proportional gain of PLL |
| $K_{i\_PLL}$ | 6.3e5 | Integral gain of PLL |

Table 4-4 Simulation events under line-to-line fault conditions

| **Time** | **Event** |
|---|---|
| t=0s | Simulation starts |
| t=0.1s | Line-to-line fault occurs between phase A and B |
| t=0.2s | Load current changes from 5A to 10A |
| t=0.3s | $v_{dc}$ reference changes |
| t= 0.4s | Simulation ends |

The CRU behaviour model (ABC model) is used as the benchmark. In the ABC model, the electrical converter in Figure 4-1 is modelled with controlled ideal switches. The carrier-based PWM is used and the switching signals are generated by comparing the modulation signal $m_{abc}$ and a switching-frequency triangular carrier [85]. The results from CRU behavioural models (ABC model) and DP models are compared and the events in the simulations are shown in Table 4-4.

The DC-link voltage from the ABC and the DP model is shown in Figure 4-16. It can be seen that the result from DP model well represents the average value of that from the ABC model during all the transient and steady states. In the DP model, the voltage vector angle is well approximated with DPs in the dq frame where the error of the DP model very small. The error is smaller than the corresponding case in the uncontrolled diode rectifier. The error difference of these two DP models is mainly due to difference in the switching behaviour between the CRU and the uncontrolled rectifier. In the CRU model, the switching behaviour in the converter is modelled with modulation functions (4-25) and (4-26). These functions are conveniently transformed into the DPs (4-27) and (4-28). The appropriate appoximation of the current components $i_D$ and $i_Q$ in the DP domain, under both balanced and unbalanced conditions, and the accurate DP modelling of the controllers make the DP CRU model represent the control system very well and give an accurate value of the modulation

index in DPs. Meanwhile, the switching behaviour of the uncontrolled rectifier is exclusively dependent on the condition of the circuit. The switching behaviour is assumed to be exclusively dependent on the positive sequence voltage vector under both balanced and unbalanced conditions. The impact of the votlage negative sequence is considerred as a disturbance to the system. This assumption means that the accuracy of the DP model for the uncontrolled rectifier is dependent on the severity of the unbalance, i.e. the unbalance factor λ, as shown in Chapter 3.

The AC currents flowing into the CRU are shown in Figure 4-17, Figure 4-18 and Figure 4-19. At each simulation event, one can notice that the currents from the DP model well represent the fundamental components of the currents from the ABC model. It can also be seen that during the line-to-line fault conditions, the current in the phase A is equal to that in the phase B.

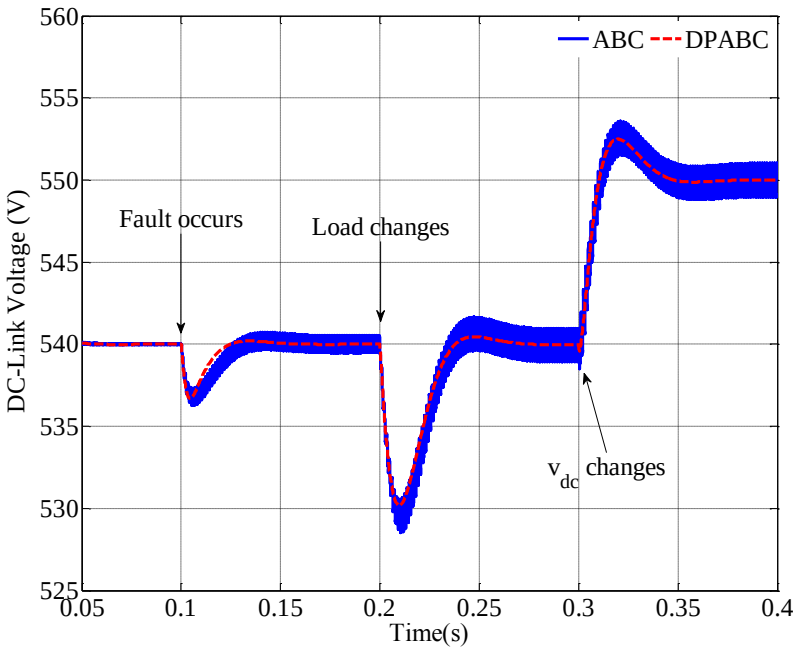


Figure 4-16 Dynamic response of $v_{dc}$ under line-to-line fault conditions; comparison between the DP model and the behavioural model

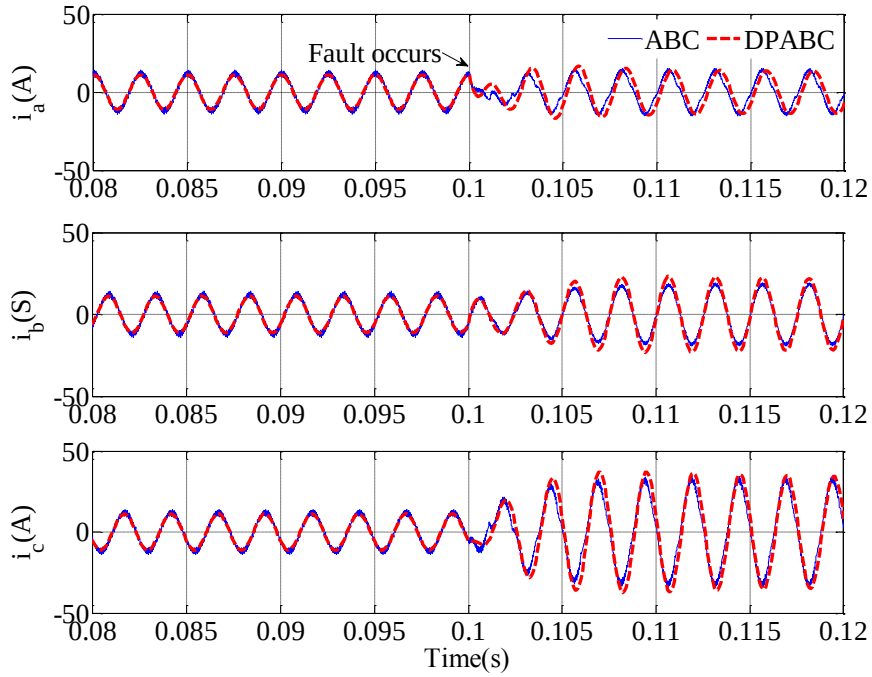


Figure 4-17 Currents flowing into CRU, $i_{abc}$ under a line-to-line fault; comparison between the DP model and the behavioural model

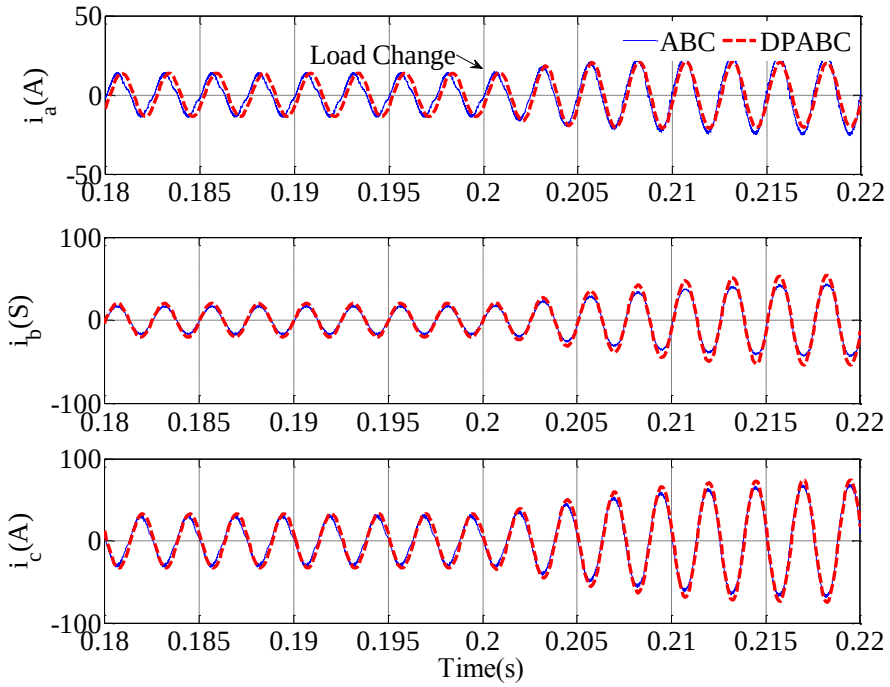


Figure 4-18 Current Flowing into CRU, $i_{abc}$ for a load change under line-to-line fault conditions; comparison between the DP model and the behavioural model

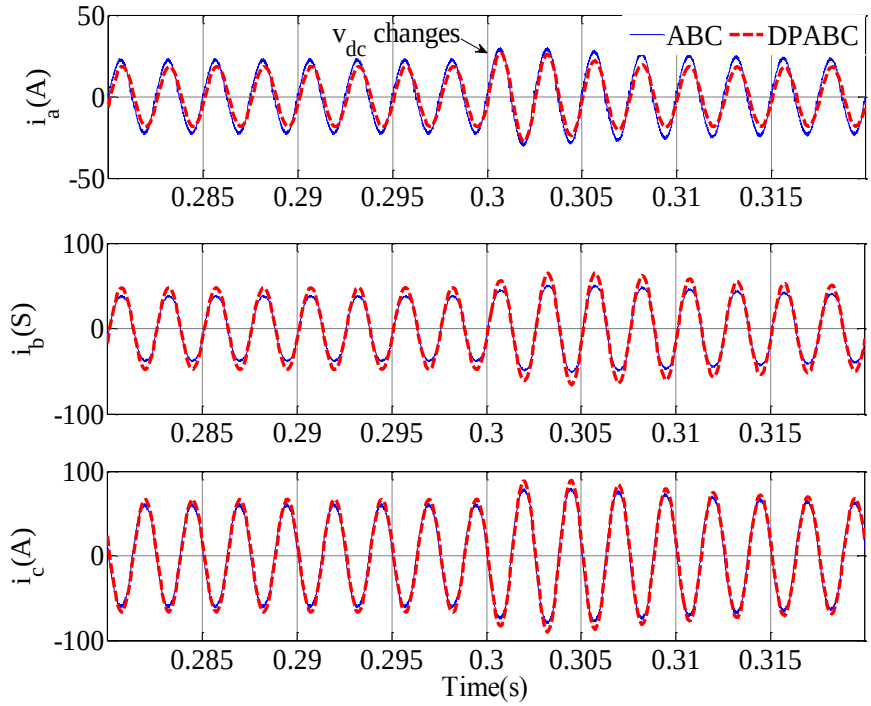


Figure 4-19 Current Flowing into CRU, $i_{abc}$ for a the $v_{dc}$ change under line-to-line fault conditions; comparison between the DP model and the behavioural model

The comparison between the results from the DP model and the ABC model simulation above validates the accuracy of the DP model under balanced, unbalanced and line-fault conditions. As the DP model addresses at the functional modelling level, the higher harmonics are neglected. The DC-link voltage from the DP model represents an average value of that from the experiment. Meanwhile, the AC currents from the DP model give the fundamentals of those from the experiment or the ABC models. Apart from the accuracy, the efficiency is also a very important aspect for functional models. However, for model efficiency studies, it is also convenient to consider the functional time domain DQ0 model of the CRU. This is now considered in the following section.

# 4.4 DQ0 Model of the CRU

The DQ0 model of CRU has been well developed in previous work [76]. It will be used here as one of the comparison models for simulation efficiency assessment of the modelling methods. In order to make this thesis self-contained, the development of the CRU model in the DQ0 frame is briefly described in this section.

In the developed DQ0 model, the voltages and currents on the AC and DC sides are related by:

$$v_{sq} = m_q \frac{v_{dc}}{2} \tag{4-29}$$

$$v_{sd} = m_d \frac{v_{dc}}{2} \tag{4-30}$$

$$i_{dc} = \frac{3}{4}\left(m_q i_q + m_d i_d\right) \tag{4-31}$$

Here, the d axis is aligned with the voltage vector of the three-phase source. The simulation scheme of DQ0 model thus can be drawn in Figure 4-20.

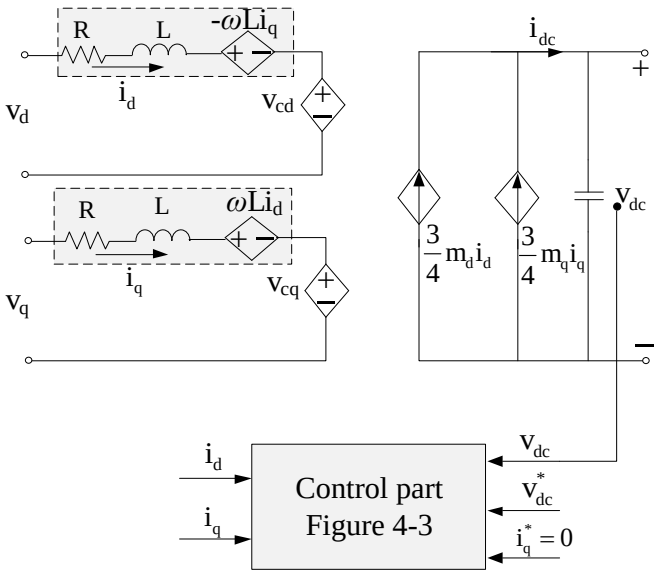


Figure 4-20 DQ0 model of the CRU

The DQ0 model can also be connected to the three-phase model using the DQ0/ABC transformation. The transformation matrix is the same as $K_s$ in (4-19).

# 4.5 Comparison of Simulation Times

## 4.5.1 Simulation Schemes

In this section the computational efficiency of the DP model is assessed. The simulation scheme is shown in Figure 4-21 and the parameters are given in Table 4-5.

Table 4-5 The set of parameters for the CRU in Figure 4-21

| Parameters | Value | Description |
|---|---|---|
| $V_s$ | 115Vrms | Phase supply voltage |
| $f_e$ | 400Hz | Frequency of the source |
| $f_{sw}$ | 10kHz | Switching frequency |
| $P_{rated}$ | 10kW | Power rate of the CRU |
| R | 0.1Ω | Resistance of the boost inductor |
| L | 1mH | The boost inductor |
| C | 2.4mF | DC-link capacitance |
| $R_t$ | 0.1Ω | Transmission line resistance |
| $L_t$ | 1μH | Transmission line inductance |
| $C_t$ | 2nF | Transmission line capacitance |
| $K_{pv}$ | 1.187 | Proportional gain of voltage loop |
| $K_{iv}$ | 93.25 | Integral gain of Voltage loop |
| $K_{pi}$ | 3.76 | Proportional gain of current loop |
| $K_{ii}$ | 4430 | Integral gain of current loop |
| $R_f$ | 1mΩ | Fault resistance |
| $K_{p\_PLL}$ | 3553 | Proportional gain of PLL |
| $K_{i\_PLL}$ | 6.3e5 | Integral gain of PLL |

The computation times consumed by five different models under balanced and unbalanced conditions are monitored during the simulation processes.

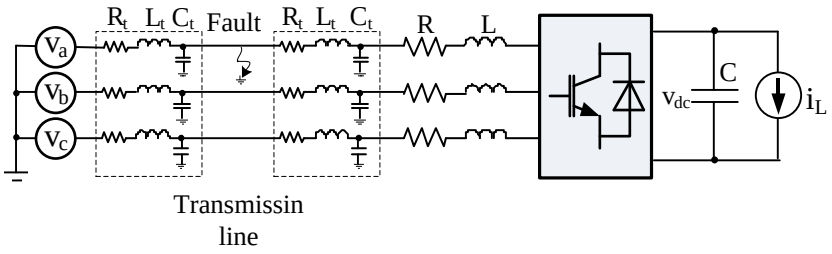


Figure 4-21 Circuit diagram of EPS for computation time comparison

The five different models are used for computation time comparative studies:

(a) Three-phase model with switching behaviour in the CRU. It is a behavioural model and is illustrated in Figure 4-22 (a) and is referred to as ABC model in the text below.

(b) DQ0 model, in which the all AC variables are represented in terms of the synchronously rotating frame orientated on the supply voltage vector. This model is given in Figure 4-22 (b). There are no three-phase variables in this model.

(c) DQ0 model with ABC interface. The functional DQ0 CRU model is used but with the three-phase interface as shown in Figure 4-22 I. The AC system is seen by the user as a three-phase system and the DQ0/ABC transformation is not visible. This model is referred to as DQ0/int model in this section.

(d) DP model, where all the elements are in DPs, as shown in Figure 4-22 (d). This model does not include three-phase time-domain variables. In the text below this model is referred to as DPABC model.

(e) DP model with ABC interface. The DP CRU model is used with the three-phase interface as shown in Figure 4-6. The AC system is seen by the user as a three-phase system and the DP formulation is not visible. This model is shown in Figure 4-22 I and is noted as the DP/int model.

It is important to point out that in these five models, only the ABC model includes switching behaviour and is at the behaviour modelling level. The other four models are all at the functional modelling level.

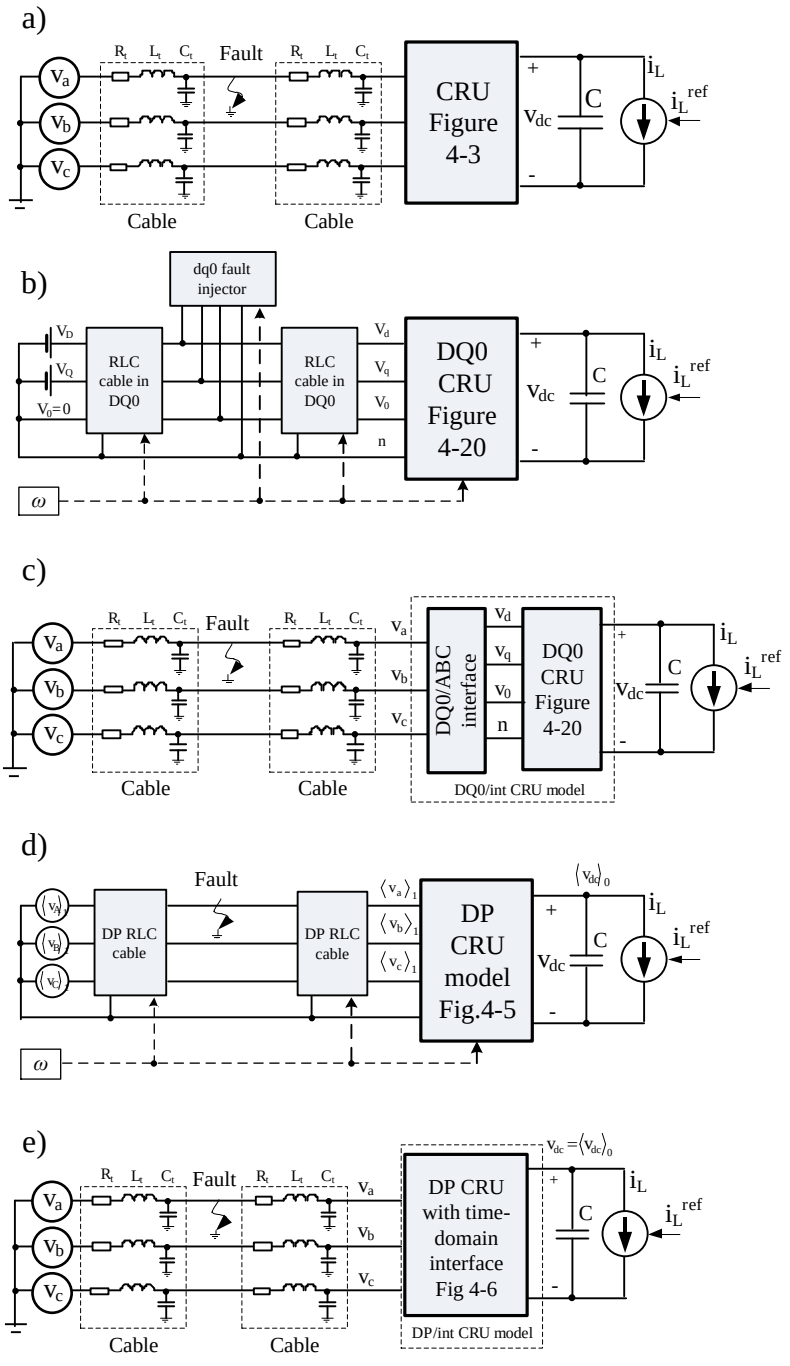


Figure 4-22 Five different models for computation time comparative studies a) ABC model, b) DQ0 model, c)DP model, d) DQ0/int model, e) DP/int model

The simulation scenario is set at 1s of EPS operation including a step of DC load current $i_L$ from 5A to 10A occurring at t=0.2s and a line-to-ground fault occurring at t=0.5s. The fault is implemented by using a 0.1mΩ resistor in the ABC model. In the DQ0 model, the fault is modelled using an inductance matrix as shown in Appendix III. The simulation results are discussed below. All the models are established in Modelica/Dymola 2012 environment.

### 4.5.2 Simulation Results

The transient of $v_{dc}$ due to the load change under the balanced conditions from different models is shown in Figure 4-23. It can be seen that the results from the five different models are well matched in this case.

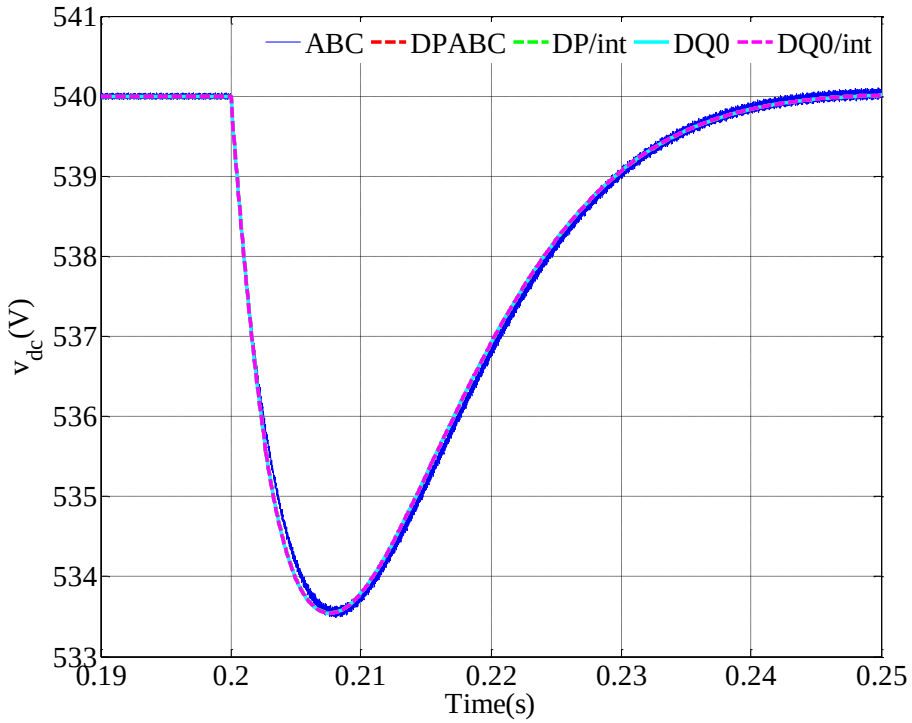


Figure 4-23 Models comparison: DC-link voltage transient due to a step change in the DC load under balanced conditions

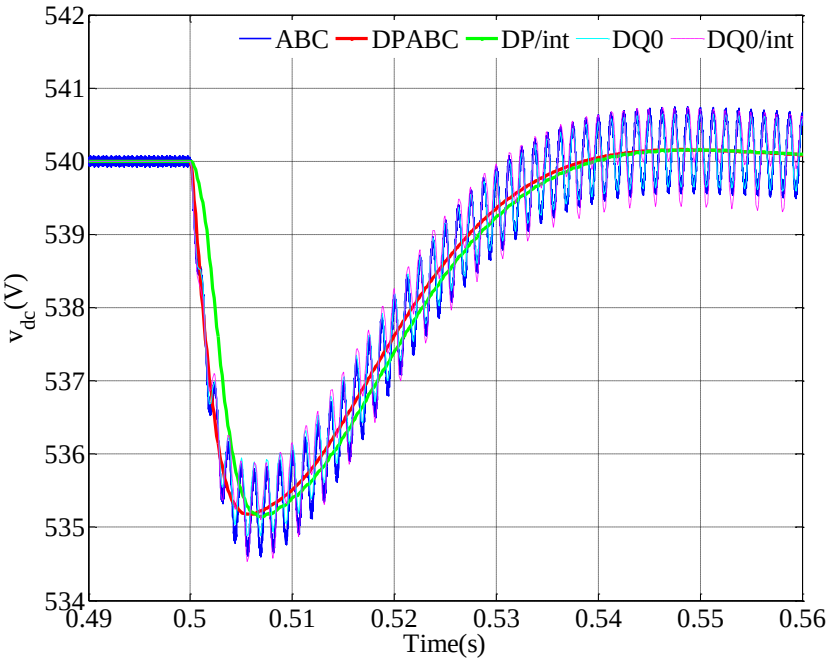


Figure 4-24 Models comparison: DC-link voltage transient due to a step change in DC load under unbalanced conditions

The transient of $v_{dc}$ after the fault occurs is shown in Figure 4-24. After the line-to-ground fault, $v_{dc}$ includes a small 800Hz ripple in the ABC, DQ0 and DQ0/int models. This is due to the negative sequence in the system under line-to-ground fault conditions. Results from the DP and DP/int models represent the DC component of $v_{dc}$ and agree with the average value of $v_{dc}$ of the ABC model.

The computation times taken by different models are shown in Figure 4-25. All the functional models are faster than the ABC model. This is due to the neglect of the higher harmonics in the functional models. Under balanced conditions, the DQ0, DQ0/int models are slightly faster than the DP and DP/int models. However, after the fault occurs, the DQ0 and DQ0/int models become much slower compared with the simulation under balanced conditions. This is due to the second harmonic in the DQ0 systems. On the other hand, the DP and DP/int models still keep the same simulation speed and there is virtually no difference in the curve slopes

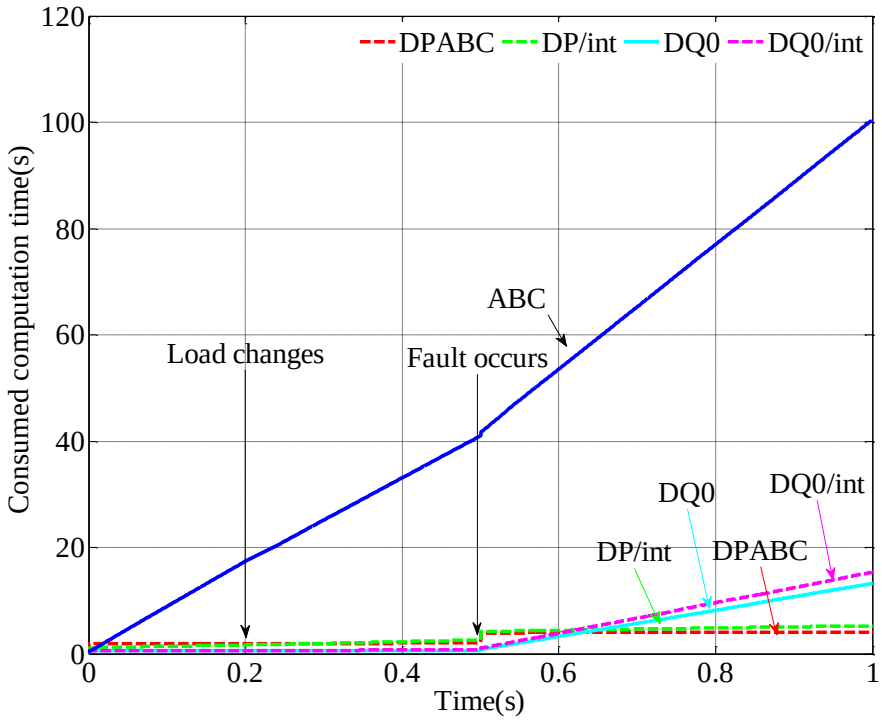


Figure 4-25 Consumed computation time by different models

The acceleration index of the functional models is shown in Table 4-5. It can be seen that the DQ0 model is 1635 time faster than the ABC model neglecting the initialization time. The DP model is 262 times faster than the ABC model in this case. Under unbalanced conditions, the DP model is 28 times faster than the ABC model.

Table 4-6 CPU time taken for balanced scenario simulation
(The initialization time is ignored)

| **Model** | **ABC** | **DQ0** | **DP** | **DQ0/int** | **DP/int** |
|---|---|---|---|---|---|
| **Balanced conditions (0-0.5s)** | | | | | |
| CPU time(s) | 40.888 | 0.025 | 0.156 | 0.092 | 1.463 |
| Performance index | **1** | **1635** | **262** | **444** | **28** |
| **Unbalanced conditions (0.5-1.0s)** | | | | | |
| CPU time taken(s) | 59.512 | 12.584 | 2.087 | 14.637 | 2.644 |
| Performance index | **1** | **5** | **28** | **4** | **22** |
| Total Simulation time | **100.40** | **12.61** | **2.24** | **14.73** | **4.12** |

# 4.6 Conclusion

In this chapter, the DP modelling technique is extended to the modelling of the PWM controlled rectifier. The developed DP model is suitable for accelerated simulations of EPS's at the functional level. The DP model of the CRU consists of two parts: an electrical converter and its control system. The DP model of the electrical converter is derived by transforming the non-switching model of the CRU into the DP domain. The DP model of the control system involves a new rotating frame, the dq frame, which is rotating at a constant speed ω. This dq frame allows a more convenient way to map the rotating voltage and current vectors into the DPs. In the dq frame, the active and reactive power currents ($i_D$ and $i_Q$) are expressed with d- and q-axis current components ($i_d$ and $i_q$). Using the DP properties, the DP forms of $i_D$ and $i_Q$ can be represented by $\langle i_d \rangle_{1,2}$ and $\langle i_q \rangle_{1,2}$. Combining the DP model of the PI controller and the electrical converter, the full DP model of the CRU can be derived.

The DP model is able to handle the unbalanced operation conditions. In the DP model, the positive sequence is viewed to be the component determining the operation point of the CRU. The negative sequence is viewed as a disturbance and its impact is included in the $2^{nd}$ order DPs in the selected dq frame. Compared with the uncontrolled rectifier, the DP model of PWM controlled rectifiers presents better accuracy under line-to-line fault conditions. The error difference of these two DP models is mainly due to the switching behaviour diffrence between the CRU and the uncontrolled rectifier. In the CRU model, the switching behaviour in the converter is modelled with modulation functions and these functions are conveniently transformed into the DPs. The control of the CRU is dependent on the current component $i_D$ and $i_Q$. The appropriate appoximation of these two components in the DP domain under both balanced and unbalanced conditions, and the well-modelled DP-domain controllers make the DP CRU model accurately model the control system of the CRU, and give accurate values of the modulation index in DPs. This makes the error of

the DP model very small. Meanwhile, the switching behaviour of the uncontrolled rectifier is exclusively dependent on the condition of the circuit. The switching behaviour is assumed to be dependent on the positive sequence of the voltage vector under both balanced and unbalanced conditions. The negative sequence is considerred as the disturbance in the DP model. Thus the accuracy of the DP model for the uncontrolled rectifier is dependent on the severity of the unbalanced condition, i.e. unbalance factor $\lambda$.

The developed DP model is validated experimentally under balanced, lightly unbalanced and open-circuit fault conditions. Due to the high current during short circuits, the validation of the DP model under line-to-line fault conditions is accomplished by comparing with the ABC model through simulations. Good agreement has been demonstrated by comparison the results from the simulations of the DP model and the experiment/simulation. Five different models, i.e. ABC model, DQ0 model, DP model, DP/int model and DQ0/int model, have been used and simulated under unbalanced and unbalanced conditions. The efficiency of the DP model has been demonstrated through simulations. Compared with DQ0 and DQ0/int models, the two DP-based models maintain a nearly constant fast simulation speed under both balanced and unbalanced conditions.

The developed CRU model has been added to the DP based modelling library for accelerated studies of future MEA EPS architectures at the functional level. This library will provide an efficient and accurate tool for system engineers to design and optimize a variety of EPS architecture candidates.

# Chapter 5

# Dynamic Phasor Models of Controlled Multi-Generator Systems

## 5.1 Introduction

Aircraft electrical systems have made significant advance over the years as aircraft have become more dependent upon electrically powered services. A typical EPS of the 1940s and 1950s was the twin 28 VDC system. This system was widely used on twin engine aircraft with each engine powering a 28VDC generator. In this system, one or two DC batteries were also fitted and an inverter was provided to supply 115 VAC to the flight instruments [7].

With the increase of electrical power loads on board, much greater power is required and the 28VDC system cannot satisfy the requirement. The advent of V-bombers introduced a new era for aircraft power system which changed the aircraft industry radically. The V-bombers were fitted with four 115VAC generators operated at 400Hz. This system has remained dominant [7].

The AC power system results in better design and allows greater use of electrical and electronic devices. Modern civil aircraft use a three-phase 115VAC, 400Hz AC power system. The primary source of the EPS is a three-phase AC generator driven by the aircraft engine. This generator comprises three separate units consisting of a Permanent Magnet Generator (PMG), an exciter generator and a main generator, as shown in Figure 5-1 [7].

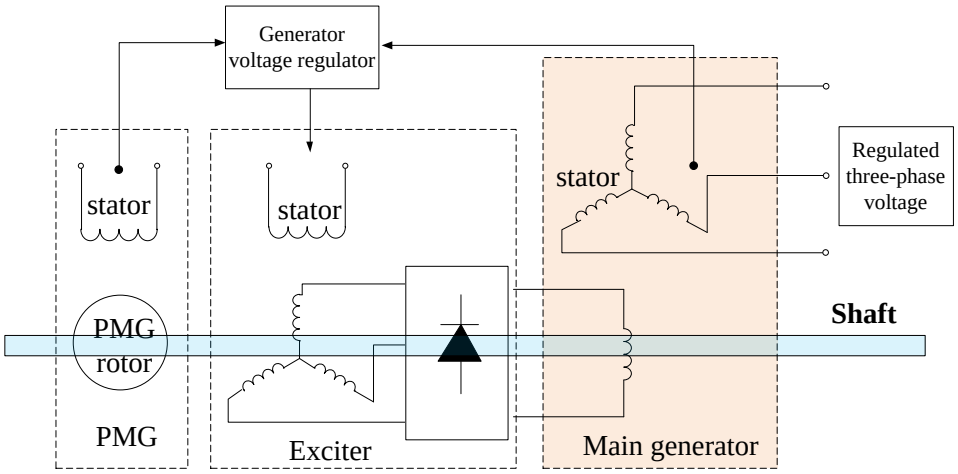


Figure 5-1 generator electrical scheme

The PMG provides the single phase, AC voltage to the voltage regulator. The voltage regulator rectifies and modulates the PMG output. This regulated output supplies power for the exciter field winding, allowing generation of AC voltages on the exciter rotor.

The main generator is a wound-field, synchronous machine. The wound rotor, when excited with DC current supplied by the exciter, establishes magnetic flux in the air gap between the rotor and the stator. This magnetic flux induces alternating voltage in the stator. The magnitude of this stator AC voltage is proportional to the DC current supplied by the exciter rotor. This DC current is in turn depends on the voltage of the exciter stator. Therefore, the main generator stator's AC voltage is determined by the magnitude of the exciter stator voltage.

In conventional aircraft, a Constant Speed Drive (CSD) is used to compensate for changes in the aircraft engine speed and fixes the generator output frequency at a nominal 400Hz. Load and fault transient limits are within 380 to 420Hz range. The CSD is a complex hydro-mechanical device and has relatively low efficiency of power conversion. In addition, this device by its nature is not highly reliable. In order to improve fuel efficiency and power system reliability, the CSD is removed from the system and the generator is directly driven by the aircraft engine in the MEA. Since the frequency of AC

power varies in proportion to the engine speed, the frequency of such a power system can vary from 360-900Hz. In the MEA, the main AC power supply is set at the high voltage 230VAC in order to allow for high power transmission [12].

Apart from the engine-driven generator, an Auxiliary Power Unit (APU) is equipped in the aircraft. The APU is used when engine-driven generators are not operating, for example during the start-up period, ground maintenance and emergency in-flight power loss conditions. The external power source also provides ground crews with electrical power for servicing, fuelling and performing maintenance actions etc.

In this thesis, the three-stage power generator is represented by the main synchronous generator with its excitation voltage controlled by a generator control unit (GCU), as shown in Figure 5-2. The mechanical behaviour and turbine model are not considered. The speed $\omega_r$ is considered to be constant or slowly varying.

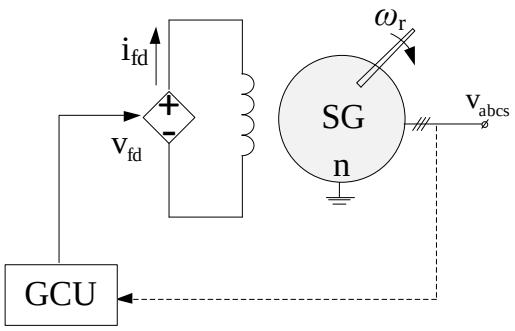


Figure 5-2 The equivalent circuit for the generating system in aircraft

Several different models for the GCU controlled SG shown in Figure 5-2 will be introduced in this chapter. These are the benchmark model (ABC model), the DQ0 model and the DPABC model. In the ABC model, the stator windings are modelled in three-phase ordinates and the rotor windings are modelled in the dq frame. The d axis is aligned with the rotor. Transforming the three-phase stator variables into the dq frame results in the DQ0 model. The DPABC model

is based on the ABC model and all the variables are transformed into DPs using the DP properties.

In an aircraft EPS, it is desirable that 'no-break' or uninterrupted power is provided in cases of engine or generator failure. A number of sensitive aircraft instruments and navigation devices which comprise some of the electrical loads may be disturbed and may need to be restarted or re-initialised following a power interruption. No-break power transfer is also important during start-up in the transition from ground power or APU generated power to aircraft main generator power (or vice versa during the shutdown) [7]. Again, this is to avoid malfunction or resetting of electrically powered equipment. In order to satisfy this requirement, two generators will need to be connected to the same bus during the transient period. We call this connection "paralleling" of generators.

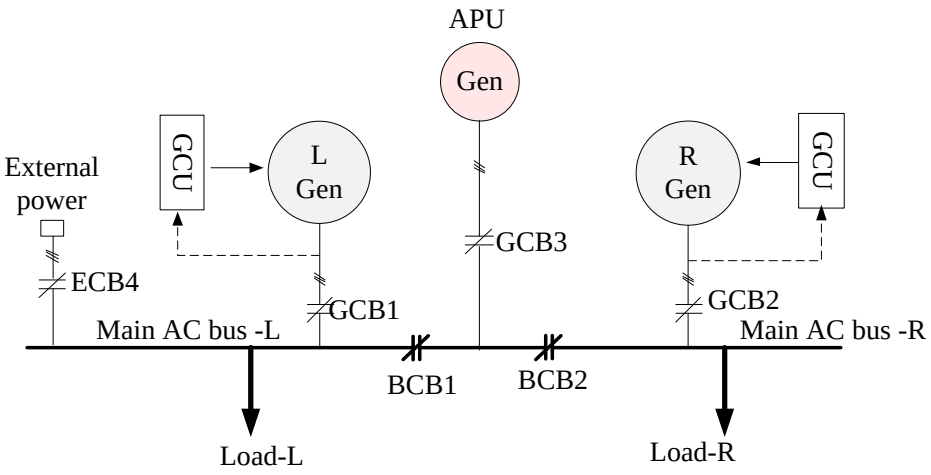


Figure 5-3 Multi-generator system in EPS of aircraft

As shown in Figure 5-3, during the L-generator start-up period, BCB1 and GCB3 are closed and the APU generator supplies electrical power to main left AC bus feeding various electrical loads during the start-up period, including the fuel control, ignition, engine starting, acceleration and monitoring etc. When the main engine ignites, the main generator is ready to feed the main bus. In order to meet the no-break requirement GCB1 will close when the output frequency of the L-generator and the APU generator are similar. The paralleling of the main generator and the APU generator exists for a short

period, e.g. 10ms, before BCB1 is opened. Then the SG starts to supply the main AC bus independently. The R-generator start-up circle is similar to that of the left generator.

It is also possible that parallel operation of multiple generators in normal conditions is a future trend for DC architecture EPS's, where the main HVDC bus is fed by multiple generators with CRUs. With the droop control, the generators, with different frequencies and load angles, can supply the HVDC bus in parallel and share the load during operation.

Modelling the parallel SG system in the DQ0 frame or DP domain is not without challenges. The main challenge is from the fact that multiple generators imply multiple dq frames in the DQ0 model and multiple sliding windows (or base frequencies) in the DP model. The parallel operation requires a common reference frame in DQ0 and DP models. Thus the relations of variables in different frames need to be developed in DQ0 and DP models.

In this chapter, we will firstly introduce the modelling of one GCU controlled SG in the ABC frame, DQ0 frame and DPs. The ABC model of the controlled SG, used as the benchmark will be developed with the stator and rotor windings modelled in their own frames respectively. Using the ABC/DQ0 transformation and aligning the d-axis with the rotor, the benchmark model is transformed to the DQ0 frame. Transforming the variables in the ABC model into DPs, the DP model for controlled SG can be derived. After that, the application of the ABC, DQ0 and DP models in multi-generator systems will be discussed in detail. The developed DQ0 and DP models will be validated by comparing with the ABC model.

# 5.2 Benchmark Model of the Controlled Wound-Field Synchronous Generator

The modelling of synchronous machines has been an important topic in power system engineering for many decades. Today there are a large number of different models used in different studies. The benchmark model, or ABC model, for the synchronous machine described in [60] will be briefly introduced in this section. The synchronous machine is represented by the voltage and flux equations. This representation is commonly used in electromagnetic transient studies as well as in transient stability studies and will be used as the benchmark model in this thesis.

In the ABC model of synchronous machines, the stator windings are modelled in three-phase coordinates and the rotor windings are modelled in dq coordinates where the d axis is aligned with the rotor.

The three-phase, wound-field salient synchronous generator has three identical armature windings symmetrically distributed around the air gap and one field windings ($f_d$ winding). One or more damper windings can also be present and, for convenience, we assume that damper windings are present in the d and q axis ($k_d$ and $k_q$ windings). The synchronous machine is shown in Figure 5-4.

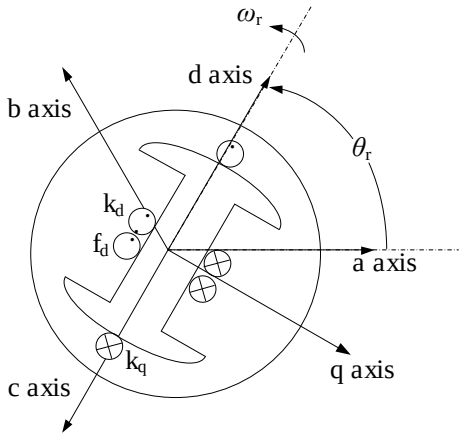


Figure 5-4 scheme of a synchronous machine

In order to derive the ABC model, the following assumptions are made:

- The direction of positive stator currents is out of the terminals.
- The rotor currents are assumed to be positive when they flow into the machine.
- All rotor windings are sinusoidally distributed.
- All the rotor variables are referred to the stator side.
- The saturation is not considered

With these assumptions, the voltage equations of the synchronous machine can be expressed in a matrix form as:

$$\begin{bmatrix} \mathbf{v}_{abcs} \\ \mathbf{v}_{dqr} \end{bmatrix} = \begin{bmatrix} \mathbf{r}_s & 0 \\ 0 & \mathbf{r}_r \end{bmatrix} \begin{bmatrix} -\mathbf{i}_{abcs} \\ \mathbf{i}_{dqr} \end{bmatrix} + \frac{d}{dt} \begin{bmatrix} \boldsymbol{\lambda}_{abcs} \\ \boldsymbol{\lambda}_{dqr} \end{bmatrix} \tag{5-1}$$

where the general vector

$$\mathbf{x}_{abcs} = \begin{bmatrix} x_{as} & x_{bs} & x_{cs} \end{bmatrix}^T \tag{5-2}$$

$$\mathbf{x}_{dqr} = \begin{bmatrix} x_{fd} & x_{kd} & x_{kq} \end{bmatrix}^T \tag{5-3}$$

In the above equations, the s and r subscripts denote variables associated with the stator and rotor windings respectively. The matrix $\mathbf{r_s}$ is the resistance of stator windings and $\mathbf{r_r}$ is the resistance of rotor windings. These matrices can be given as:

$$\mathbf{r}_{ss} = \begin{bmatrix} R_s & 0 & 0 \\ 0 & R_s & 0 \\ 0 & 0 & R_s \end{bmatrix} \tag{5-4}$$

$$\mathbf{r}_{rr} = \begin{bmatrix} R_{fd} & 0 & 0 \\ 0 & R_{kd} & 0 \\ 0 & 0 & R_{kq} \end{bmatrix} \tag{5-5}$$

In (5-1), the flux linkages can be written as:

$$\begin{bmatrix} \boldsymbol{\lambda}_{abcs} \\ \boldsymbol{\lambda}_{dqr} \end{bmatrix} = \begin{bmatrix} \mathbf{L}_{ss} & \mathbf{L}_{sr} \\ \mathbf{L}_{rs} & \mathbf{L}_{rr} \end{bmatrix} \begin{bmatrix} -\mathbf{i}_{abcs} \\ \mathbf{i}_{dqr} \end{bmatrix} \tag{5-6}$$

where $\mathbf{L}_{ss}$ denotes the stator self-inductance matrix, $\mathbf{L}_{rr}$ is the rotor self-inductance, $\mathbf{L}_{rs}$ and $\mathbf{L}_{rs}$ are the mutual inductance. These inductance matrices are given below:

$$\mathbf{L}_{ss}=\begin{bmatrix} L_{ls}+L_a\text{-}L_b\cos 2\theta_r & -0.5L_a\text{-}L_b\cos 2(\theta_r-\pi/3) & -0.5L_a\text{-}L_b\cos 2(\theta_r+\pi/3) \\ -0.5L_a\text{-}L_b\cos 2(\theta_r-\pi/3) & L_{ls}+L_a\text{-}L_b\cos 2(\theta_r-2\pi/3) & -0.5L_a\text{-}L_b\cos 2(\theta_r+\pi) \\ -0.5L_a\text{-}L_b\cos 2(\theta_r+\pi/3) & -0.5L_a\text{-}L_b\cos 2(\theta_r+\pi) & L_{ls}+L_a\text{-}L_b\cos 2(\theta_r+2\pi/3) \end{bmatrix} \tag{5-7}$$

$$\mathbf{L}_{rr}=\begin{bmatrix} L_{lfd}+L_{md} & L_{md} & 0 \\ L_{md} & L_{lkd}+L_{md} & 0 \\ 0 & 0 & L_{lkq}+L_{mq} \end{bmatrix} \tag{5-8}$$

$$\mathbf{L}_{sr}=\begin{bmatrix} L_{md}\sin\theta_r & L_{md}\sin\theta_r & L_{mq}\cos\theta_r \\ L_{md}\sin(\theta_r-2\pi/3) & L_{md}\sin(\theta_r-2\pi/3) & L_{mq}\cos(\theta_r-2\pi/3) \\ L_{md}\sin(\theta_r+2\pi/3) & L_{md}\sin(\theta_r+2\pi/3) & L_{mq}\cos(\theta_r+2\pi/3) \end{bmatrix} \tag{5-9}$$

$$\mathbf{L}_{rs}=\frac{2}{3}\mathbf{L}_{sr}^{T} \tag{5-10}$$

In (5-7), $L_a>L_b$ and $L_b$ is zero for a round rotor machine and the rotor angle $\theta_r=\int\omega_r dt+\theta_0$. In The leakage inductances are denoted with l in the subscript. The magnetizing inductances are defined as:

$$L_{md}=\frac{3}{2}(L_a+L_b) \tag{5-11}$$

$$L_{mq}=\frac{3}{2}(L_a-L_b) \tag{5-12}$$

The parameter and variable definitions for the above equations are:

$\theta_r$: rotor electrical angle;

$\mathbf{v}_{abcs}$: stator terminal voltages;

$\mathbf{i}_{abcs}$: stator terminal currents;

$\boldsymbol{\lambda}_{abcs}$: flux linked with stator windings;

$\boldsymbol{\lambda}_{dqr}$: flux linked with rotor windings;

$v_{fd}$: field winding terminal voltage ( referred to the stator side);

$i_{fd}$: field winding terminal current ( referred to the stator side);

$i_{kd}$: d-axis damping winding current ( referred to the stator side);

$i_{kq}$: q-axis damping winding current ( referred to the stator side);

$R_s$: stator phase resistance;

$R_{fd}$: field winding resistance (referred to the stator side);

$R_{kd}$: d-axis damping winding resistance (referred to the stator side);

$R_{kq}$: q-axis damping winding resistance (referred to the stator side);

$L_{md}$: d-axis coupling inductance;

$L_{mq}$: q-axis coupling inductance;

$L_{lfd}$: field winding leakage inductance (referred to the stator side);

$L_{lkd}$: d-axis damper winding leakage inductance (referred to the stator side);

$L_{lkq}$: q-axis damper winding leakage inductance (referred to the stator side)

$L_{ls}$: stator phase leakage inductance;

Equations (5-1)-(5-10) give the benchmark model of the SG. The terminal voltage of the SG is regulated by the GCU. The control block diagram and the operational principle are shown in Figure 5-5. The inner loop controls the excitation current of the exciter. The outer feedback loop provides the generator voltage regulation. The AC terminal voltages of the SG are measured and the instantaneous magnitude of the voltage vector $v_T$ is calculated. The error between the reference voltage $v_T^*$ and $v_T$ is processed by a PI controller with gains $K_{pv}$ and $K_{iv}$ to produce the excitation current demand $i_{fd}^*$.

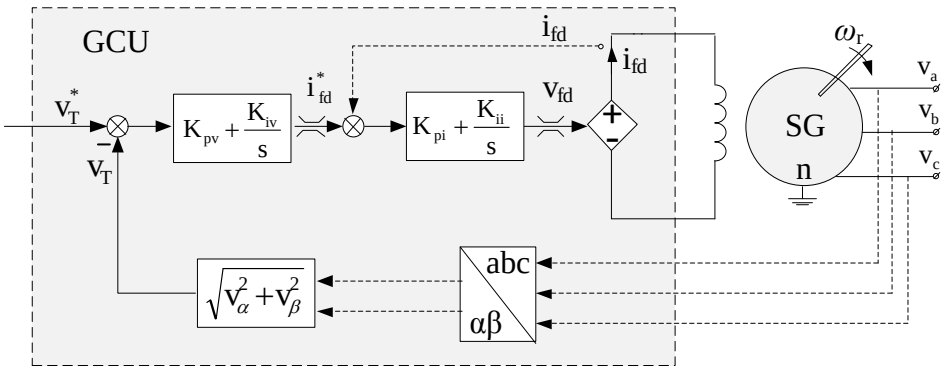


Figure 5-5 The equivalent circuit for the generating system in aircraft

The voltage regulator design is based on the no-load machine model which is given by [86]:

$$\frac{V_q(s)}{v_{fd}(s)} = \frac{\omega_r L_{md}}{R_{fd}\left(1 + sT_{d0}^{'}\right)} \tag{5-13}$$

where $T_{d0}^{'}$ is the time constant of the transient d-axis circuit under no-load conditions and is given as:

$$T_{d0} = \frac{L_{fd}}{R_{fd}} \tag{5-14}$$

where

$$L_{fd} = L_{lfd} + L_{md} \tag{5-15}$$

The equation (5-13) allows the design of the PI controller. With the required bandwidth ($\omega_n$) and the damping ratio ($\zeta$), the gains in the controller are given below:

$$K_{pv} = \frac{R_{fd}}{\omega_r L_{md}}\left(2\zeta\omega_n T_{d0}^{'} - 1\right) \tag{5-16}$$

$$K_{iv} = \frac{T_{d0}^{'} R_{fd}}{\omega_r L_{md}}\omega_n^2 \tag{5-17}$$

The current controller design is based on the transfer function as follows:

$$i_{fd}(s) = \frac{1}{R_s + L_{fd}s} v_{fd}(s) \tag{5-18}$$

With the required bandwidth ($\omega_{n1}$) and the damping ratio ($\zeta_1$), the gains in the controller are given below:

$$K_{pi} = 2\zeta_1\omega_{n1}L_{fd} - R_{fd} \tag{5-19}$$

$$K_{ii} = L_{fd}\omega_{n1}^2 \tag{5-20}$$

## 5.3 DQ0 model of the Controlled Wound-Field Synchronous Generators

In order to accelerate computation, we have seen that the AC variables can be transformed to the rotating dq frame. In the dq frame, the variables are dc-like under balanced conditions and hence the simulation speed is significantly increased. In this section, we will introduce the DQ0 modelling of the controlled wound-field SG. The developed DQ0 models will later be used in the comparative studies with ABC and DP models.

The DQ0 model of the SG has been reported in [87]. The main results will be briefly introduced in this section. The DQ0 representation of the SG model involves the ABC/DQ0 transformation of the stator winding in (5-1). With the d axis of the rotating reference frame aligned to the rotor, all the stator AC variables have been transformed to this dq frame. The DQ0 model of the generator is expressed as:

$$v_d = -R_s i_d - \omega_r \lambda_q + \frac{d}{dt}\lambda_d \tag{5-21}$$

$$v_q = -R_s i_q + \omega_r \lambda_d + \frac{d}{dt}\lambda_q \tag{5-22}$$

$$v_0 = -R_s i_0 + \frac{d}{dt}\lambda_0 \tag{5-23}$$

$$v_{fd} = R_{fd} i_{fd} + \frac{d}{dt}\lambda_{fd} \tag{5-24}$$

$$v_{kd} = 0 = R_{kd} i_{kd} + \frac{d}{dt}\lambda_{kd} \tag{5-25}$$

$$v_{kq} = 0 = R_{kq} i_{kq} + \frac{d}{dt}\lambda_{kq} \tag{5-26}$$

$$\lambda_d = -L_{ls} i_d + L_{md}(-i_d + i_{fd} + i_{kd}) \tag{5-27}$$

$$\lambda_q = -L_{ls} i_q + L_{mq}(-i_q + i_{kq}) \tag{5-28}$$

$$\lambda_0 = -L_{ls} i_0 \tag{5-29}$$

$$\lambda_{fd} = L_{lfd} i_{fd} + L_{md}(-i_d + i_{fd} + i_{kd}) \tag{5-30}$$

$$\lambda_{kd} = L_{lkd} i_{kd} + L_{md}(-i_d + i_{fd} + i_{kd}) \tag{5-31}$$

$$\lambda_{kq} = L_{lkq} i_{kq} + L_{mq}(-i_q + i_{kq}) \tag{5-32}$$

In the above equations, $\omega_r$ denotes the rotor electrical speed; $v_d$ and $v_q$ denote the stator d- and q-axis terminal voltages; $i_d$ and $i_q$ denote stator d- and q-axis terminal currents. Other parameters have been introduced in the previous section and will not be listed here.

Based on (5-21) to (5-32), the DQ0 model of the synchronous generator can be depicted by an equivalent circuit of Figure 5-6. The stator windings are magnetically coupled due to the presence of the cross-coupling terms in d and q axes. For each axis, the coupling term is equal to the product of the rotor electrical speed and the total stator flux linked with the stator winding of the other axis. If the synchronous machine has no damper winding, the equivalent circuit can be adapted by removing the corresponding branch which represents the damper winding.

In the DQ0 model, the GCU is also employed to regulate the terminal voltage of the SG. The control block diagram of the GCU is shown in Figure 5-6. The d and q axes of the terminal voltage are calculated to obtain the instantaneous magnitude of the AC voltage vector. The design process is the same as that in the ABC model and shown in (5-13)-(5-20).

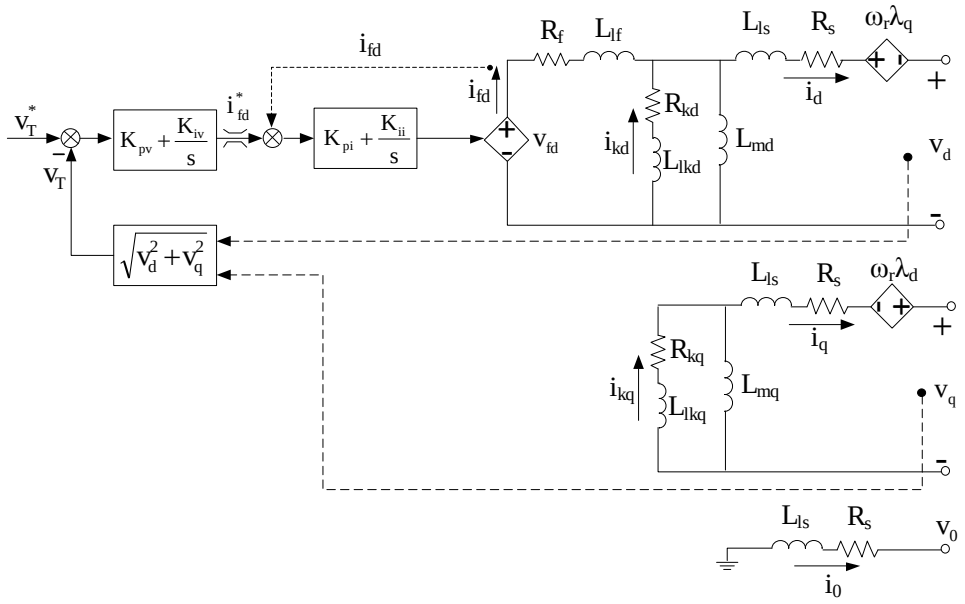


Figure 5-6 The DQ0 model of the synchronous generator with the GCU

# 5.4 Dynamic Phasor Model of Controlled Synchronous Generators

In this section, the DP model of the SG will be introduced. The DP model of the SG is based on the ABC model shown in (5-1) to (5-10) and thus denoted as the DPABC model. Using the DP transformation on both sides of these equations yields:

$$\left\langle \mathbf{v}_{\text{abcs}} \right\rangle_k = -\mathbf{r_s}\left\langle \mathbf{i}_{\text{abcs}} \right\rangle_k + \frac{\mathrm{d}\left\langle \boldsymbol{\lambda}_{\text{abcs}} \right\rangle_k}{\mathrm{dt}} + \mathrm{j}\omega\left\langle \boldsymbol{\lambda}_{\text{abcs}} \right\rangle_k \tag{5-33}$$

$$\left\langle \mathbf{v}_{\text{dqr}} \right\rangle_k = \mathbf{r_r}\left\langle \mathbf{i}_{\text{dqr}} \right\rangle_k + \frac{\mathrm{d}\left\langle \boldsymbol{\lambda}_{\text{dqr}} \right\rangle_k}{\mathrm{dt}} + \mathrm{j}\omega\left\langle \boldsymbol{\lambda}_{\text{dqr}} \right\rangle_k \tag{5-34}$$

$$\left\langle \boldsymbol{\lambda}_{\text{abcs}} \right\rangle_k = -\sum_m \left\langle \mathbf{L}_s \right\rangle_m \left\langle \mathbf{i}_{\text{abcs}} \right\rangle_{k-m} + \sum_n \left\langle \mathbf{L}_{sr} \right\rangle_n \left\langle \mathbf{i}_{\text{dqr}} \right\rangle_{k-n} \tag{5-35}$$

$$\left\langle \boldsymbol{\lambda}_{\text{dqr}} \right\rangle_k = \sum_m \left\langle \mathbf{L}_{rs} \right\rangle_m \left\langle \mathbf{i}_{\text{abcs}} \right\rangle_{k-m} + \sum_n \left\langle \mathbf{L}_r \right\rangle_n \left\langle \mathbf{i}_{\text{dqr}} \right\rangle_{k-n} \tag{5-36}$$

As mentioned before, the DP index set defines the accuracy of the DP model and has to be decided at the start of modelling. For the stator variables, we only

consider the fundamental components since the DP model is targeted at the functional level. Thus the DP index set for the stator variables is as K={1}.

The rotor-winding variables are modelled in their own frame. Under balanced conditions, these variables are dc-like. However, under unbalanced conditions, the negative sequence appears in the stator side and results in the second harmonic in the rotor-winding variables due to the coupling. Thus the DP index set for the rotor-side variables is chosen as K={0, 2}. The DP index for each particular variable is shown in Table 5-1.

Table 5-1 Dynamic phasor index used for DPABC model of the SG

| Variables | Dynamic phasor index set K={…} |
|---|---|
| $\mathbf{v}_{abcs}$, $\mathbf{i}_{abcs}$, $\boldsymbol{\lambda}_{abcs}$ | 1 |
| $\boldsymbol{\lambda}_{qdr}$,$\mathbf{v}_{qdr}$, $\mathbf{i}_{qdr}$ | 0, 2 |
| Parameters | |
| $\mathbf{L}_{ss}$ | 0, 2 |
| $\mathbf{L}_{rs}$, $\mathbf{L}_{sr}$ | 1 |
| $\mathbf{L}_{rr}$ | 0 |

The inductance matrices used in the DP formulation can be derived from (5-7)-(5-10) using the DP property and Table 2-1. These matrices are written below:

$$\left\langle \mathbf{L}_{ss} \right\rangle_0 = \begin{bmatrix} L_{ls}+L_a & -0.5L_a & -0.5L_a \\ -0.5L_a & L_{ls}+L_a & -0.5L_a \\ -0.5L_a & -0.5L_a & L_{ls}+L_a \end{bmatrix} \tag{5-37}$$

$$\left\langle \mathbf{L}_{ss} \right\rangle_2 = \begin{bmatrix} -0.5L_b e^{j2\theta_0} & -0.5L_b e^{j(2\theta_0-2/3\pi)} & -0.5L_b e^{j(2\theta_0+2/3\pi)} \\ -0.5L_b e^{j(2\theta_0-2/3\pi)} & -0.5L_b e^{j(2\theta_0+2/3\pi)} & -0.5L_b e^{j2\theta_0} \\ -0.5L_b e^{j(2\theta_0+2/3\pi)} & -0.5L_b e^{j2\theta_0} & -0.5L_b e^{j(2\theta_0-2/3\pi)} \end{bmatrix} \tag{5-38}$$

$$\left\langle \mathbf{L}_{sr} \right\rangle_1 = \begin{bmatrix} 0.5L_{mq} e^{j\theta_0} & -0.5L_{md} e^{-j\theta_0} & -0.5L_{md} e^{-j\theta_0} \\ 0.5L_{mq} e^{j(\theta_0-2/3\pi)} & -0.5L_{md} e^{-j(\theta_0-2/3\pi)} & -0.5L_{md} e^{-j(\theta_0-2/3\pi)} \\ 0.5L_{mq} e^{j(\theta_0+2/3\pi)} & -0.5L_{md} e^{-j(\theta_0+2/3\pi)} & -0.5L_{md} e^{-j(\theta_0+2/3\pi)} \end{bmatrix} \quad (5\text{-}39)$$

$$\left\langle \mathbf{L}_{rr} \right\rangle_0 = \begin{bmatrix} L_{lkq} + L_{mq} & 0 & 0 \\ 0 & L_{lfd} + L_{md} & L_{md} \\ 0 & L_{md} & L_{lkd} + L_{md} \end{bmatrix} \quad (5\text{-}40)$$

$$\mathbf{L}_{rs} = \frac{2}{3}\mathbf{L}_{sr}^{T} \quad (5\text{-}41)$$

where $\theta_0$ is the initial angle of the rotor.

The DP model of the GCU raises two issues: the PI controller and the DP expression of the magnitude of the voltage vector $|\vec{v}|$. The DP model of PI controllers has been discussed in Chapter 4. The DP value of the magnitude of voltage vectors has been illustrated in Chapter 3 but is reproduced here. The magnitude of a voltage vector is:

$$f_1(v_{d,}v_q) = |\vec{v}| = \sqrt{v_d^2 + v_q^2} \quad (5\text{-}42)$$

The dynamic phasors of voltage magnitude are derived as:

$$\left\langle |\vec{v}| \right\rangle_0 = k_0 + k_3 \left\langle v_d \right\rangle_2 \left\langle v_d \right\rangle_2^* + k_4 \left\langle v_q \right\rangle_2 \left\langle v_q \right\rangle_2^* + k_5 \left( \left\langle v_d \right\rangle_2 \left\langle v_q \right\rangle_2^* + \left\langle v_d \right\rangle_2^* \left\langle v_q \right\rangle_2 \right) \quad (5\text{-}43a)$$

$$\left\langle |\vec{v}| \right\rangle_2 = k_1 \left\langle v_d \right\rangle_2 + k_2 \left\langle v_q \right\rangle_2 \quad (5\text{-}43b)$$

where $k_i$ (i=0,1,…) is the Taylor coefficient of the expansion of (5-42). The calculation of these coefficients $k_i$ (i=0,1,…) is covered in Section 3.4.1 and Appendix II. The DP model of PI controllers is given in Section 4.2.1. The DP model of the GCU controlled SG is shown in Figure 5-7.

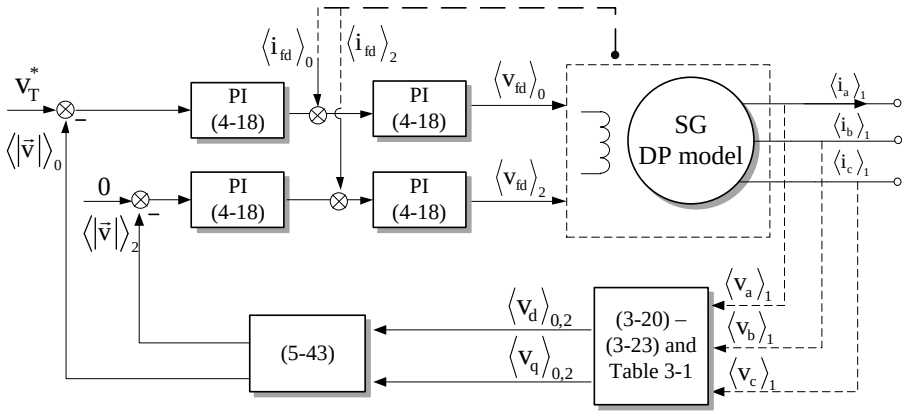


Figure 5-7 DP model of electrical power generation system

# 5.5 Modelling of Multi-generator Systems

As mentioned before, the parallel operation of generators is essential during engine start-up or shutdown. The transition of power from/to the APU generator to/from the main generator involves the parallel operation of two generators. In addition, the EPS architecture with multiple generators supplying one main HVDC bus is one option for future aircraft. In this architecture, the EPS involves multiple generators with different instantaneous frequencies operating in parallel during normal operation conditions.

In this section, the developed DQ0 model and the DPABC model will be extended to modelling multi-generator parallel-operation systems. A common reference frame, called the master frame, is chosen in the multi-generator system and all the variables in the model are referred to the master frame. As one can see later in this section, the transformation between different frames can be represented with some simple algebraic functions. This makes the application of the theory developed in this section convenient to be implemented.

### 5.5.1 Multi-generator System Modelling in DQ0 Frame

As can be seen in Section 5.3, the DQ0 model of SGs requires the rotor position. In multi-generator systems, the rotor position of each generator is independent and each generator has its own rotating dq frame. When the generator operates individually, the EPS can be divided into several subsystems with each subsystem containing one generator and its loads.

In normal operation conditions, the subsystems work separately and there is no problem if there are many dq frames in the system. However, during start-up or shutdown, the two generators are connected in parallel. In this case, a common frame, called the master frame, is needed and all the variables in different dq frames need to be referred to this master frame.

In the DQ0 model of multi-generator systems, the master dq frame is chosen to be aligned with one generator's rotor, called the master generator. Other generators are called slave generators and their dq frames are called slave frames correspondingly. In the multi-generator system, the generators are modelled in their own dq frames. However, all the loading system is modelled in the master frame. The slave generators connect with the load through an interface which transforms variables from slave frames to the master frame.

A twin generator system is shown in Figure 5-8. The whole system is divided into two subsystems. Each subsystem has one generator with its own reference frame ($d_1q_1$ frame and $d_2q_2$ frame) rotating at $\omega_1$ and $\omega_2$ separately. The output of the two SGs are denoted as $\vec{v}_1$, $\vec{i}_1$ and $\vec{v}_2$, $\vec{i}_2$ respectively. The subscript number in the variables of Figure 5-8 denotes the subsystem number or the generator number. The superscript denotes the frame number. For example, $v_{2d}^{1}$ means the d component of generator voltage vector $\vec{v}_2$ in the frame 1. Here, we assume the $d_1q_1$ frame as the master frame and the $d_2q_2$ frame as the slave frame. These two frames have an angle different $\varphi$, as shown in Figure 5-9. Correspondingly, SG1 is denoted as the master generator and SG2 as the slave generator. For simulation studies, it is reasonable to assume that the master

generator never fails since one can always choose the non-failure one to be the master generator.

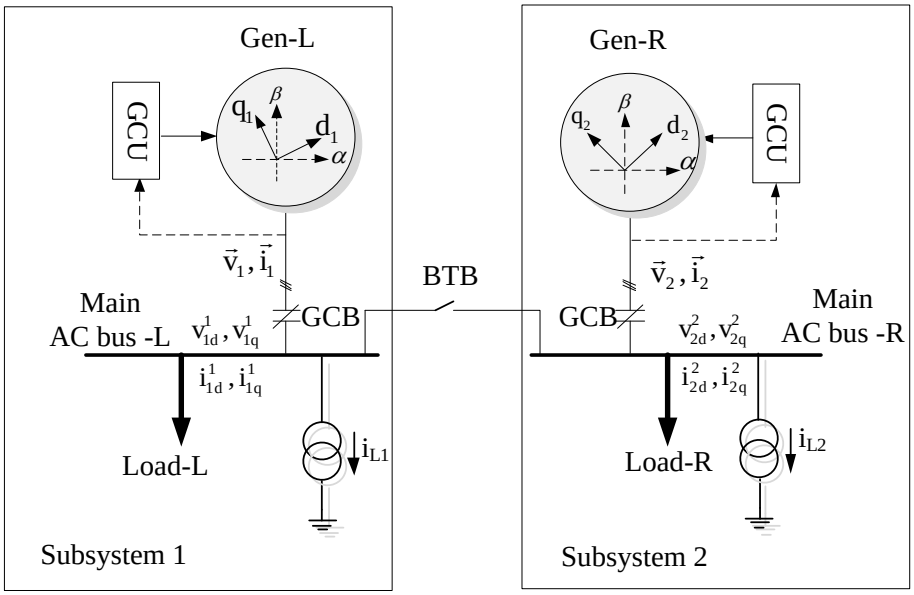


Figure 5-8 Multi-generator system configuration

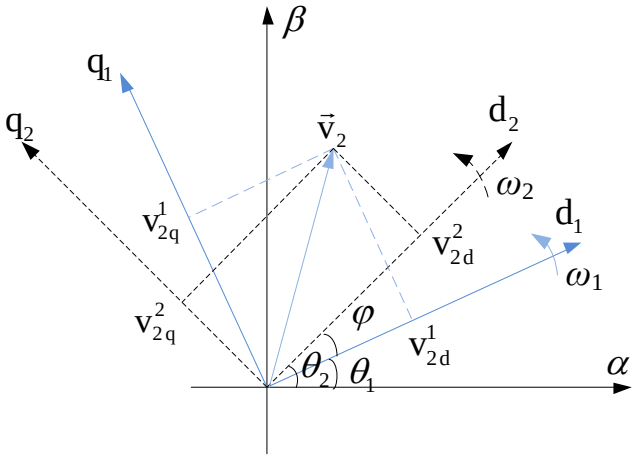


Figure 5-9 Different reference frames transformation

The components of vector $\vec{v}_2$ in the $d_2q_2$ frame are $v^2_{2d}$ and $v^2_{2q}$. However, in the master $d_1q_1$ frame, the components become $v^1_{2d}$ and $v^1_{2q}$. The relation of the components in the slave frame and the master frame can be expressed as:

$$\begin{bmatrix} v^1_{2d} \\ v^1_{2q} \end{bmatrix} = K^1_2 \begin{bmatrix} v^2_{2d} \\ v^2_{2q} \end{bmatrix} \tag{5-44}$$

where

$$\mathrm{K}_2^1 = \begin{bmatrix} \cos(\theta_2 - \theta_1) & -\sin(\theta_2 - \theta_1) \\ \sin(\theta_2 - \theta_1) & \cos(\theta_2 - \theta_1) \end{bmatrix} \tag{5-45}$$

Here, $K_2^1$ is called frame transformation matrix. The angle $\theta$ is expressed as:

$$\theta_1 = \int \omega_1 \mathrm{dt} \tag{5-46}$$

$$\theta_2 = \int \omega_2 \mathrm{dt} \tag{5-47}$$

The transformation in (5-44) is also true for the current vector of the slave generator. With (5-44), an interface can be developed to connect the slave generators with loads modelled in the master frame. For multi-generator systems, the DQ0 model thus can be developed with following procedure:

1) A master reference is selected. This means one generator is selected to be the master generator. Other generators are called slave generators and their reference frames are call slave frames correspondingly;
2) All the SGs are modelled in their own frame but the loads are directly modelled in the master reference frame;
3) The master generator supplies the load directly
4) Each slave generator supplies the load through an interface which transforms the variables from the slave frame to the master frame.

The DQ0 model of multi-generator EPS is illustrated in Figure 5-10. The master generator supplies the loading system directly and the slave generators supply the loading system with interfaces. The subsystems modelled in the master frame have been highlighted out in a green dash-lined box.

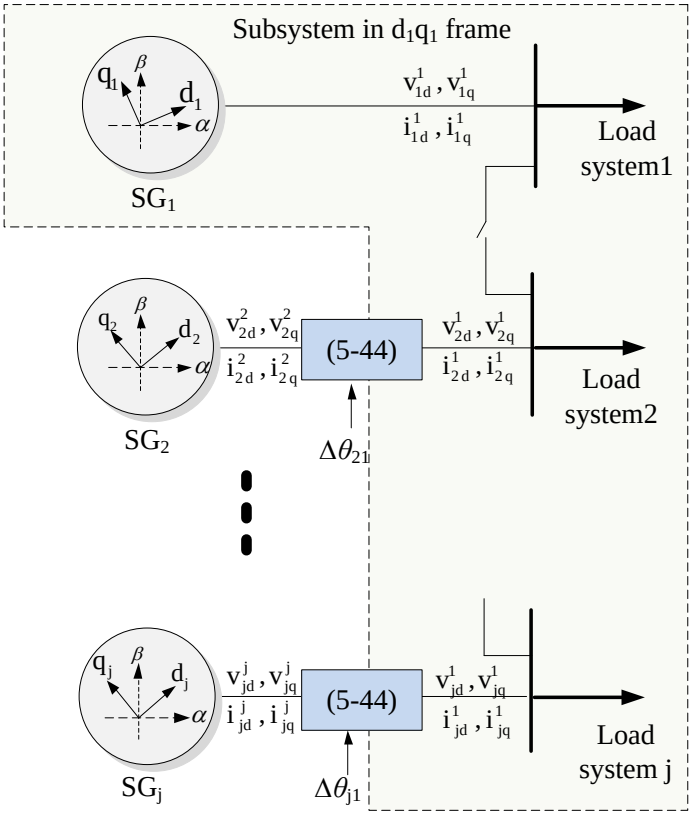


Figure 5-10 Scheme of multi-generator system in the DQ0 frame

### 5.5.2 Multi-generator System Modelling with Dynamic Phasors

In this section, the DP model will be extended to modelling multi-generator systems. The DP modelling of the multi-generator system can be achieved by two methods: the first method is using a master frame for the whole system and all the subsystem variables are referred to this master frame. This method is similar to what has been used in the DQ0 model. The second method is to model the SG of different frequencies separately in the DPs. When the SGs are working in parallel, DPs with different frequency corresponding to the generator can exist in the system and independent from each other. This method is very useful when the frequency difference is large, for example, when the high switching frequency is considered in the system. However, this method involves more variables and thus results in a higher-order system since the DP model should include all the DPs with different base frequencies. In this

thesis, we mainly focus on the first method and the transformation of DPs between different frames will be detailed in this section.

For the same time-domain waveform, the DP transformation with different base frequencies will define distinct series of DPs. Let a time-domain waveform $x_p(t)$ be associated with the $p^{th}$ generator with a frequency $\omega_p$. Then the DP of $x_p(t)$ can be written as

$$X_{pn}(t) = \frac{1}{T_p}\int_{t-T_p}^{t} x_p(\tau)e^{-jn\omega_p\tau}d\tau, \quad n = 0,1,2... \tag{5-48}$$

where $\omega_p=2\pi/T_p$. The first subscript 'p' in $X_{pn}(t)$ means the DPs are in the $\omega_p$ frame and the second subscript 'n' gives the DP index in this frame. The DPs for the same signal $x_p(t)$ in the $\omega_1$ frame can be written as

$$X_{1m}^{p}(t) = \frac{1}{T_1}\int_{t-T_1}^{t} x_p(\tau)e^{-jm\omega_1\tau}d\tau, \quad m = 0,1,2... \tag{5-49}$$

where $\omega_1=2\pi/T_1$. The first subscript number '1' in $X_{1m}^{p}(t)$ denotes the DPs are in the $\omega_1$ frame and 'm' gives the DP index in the corresponding frame. The superscript 'p' in $X_{1m}^{p}(t)$ denotes the DP corresponds to the time-domain signal associated with the $p^{th}$ generator. In this section, the $\omega_1$ frame is referred to as the master frame. The $\omega_p$ ($p\neq1$) frame is referred to as the slave frame. The generators are referred to as the master generator and the slave generator correspondingly.

Combining (5-48), (5-49) and the inverse DP transformation (2-1), the relation between the DPs in the master frame and DPs in the slave frame can be expressed as

$$X_{1m}^{p}(t) = \frac{1}{T_1}\int_{t-T_1}^{t}\left(\sum_n X_{pn}(t)e^{jn\omega_p\tau}\right)e^{-jm\omega_1\tau}d\tau, m = 0,1,2... \tag{5-50}$$

Considering that in the integration term, $X_{pn}(t)$ is a slave-frame DP at the time instant 't' and constant during the integration interval $[t-T_1,t]$, the term $X_{pn}(t)$

can be moved outside the integration. Exchanging the integration and sum calculation order yields:

$$X_{1m}^{p}(t)=\sum_{n}\left\{\left(\frac{1}{T_1}\int_{t-T1}^{t}e^{jn\omega_p\tau}e^{-jm\omega_1\tau}d\tau\right)X_{pn}(t)\right\},m=0,1,2,.... \qquad (5\text{-}51)$$

The equation (5-51) reveals that the DPs of $x_p(t)$ in the master frame $X_{1m}^{p}(t)$ can be expressed as an algebraic sum of DPs in the $\omega_p$ frame, $X_{pn}(t)$. According to the DP definition (2-2), the coefficients of $X_{pn}(t)$ in (5-51) can be viewed as the $m^{th}$ DP of $e^{jn\omega_p t}$ in the $\omega_1$ frame and denoted as $\langle e^{jn\omega_p t}\rangle_{1m}$. The coefficients are called DP frame transformation coefficients (FTCs). Therefore, (5-51) can be written as

$$X_{1m}^{p}(t)=\sum_{n}\left\{\left\langle e^{jn\omega_p t}\right\rangle_{1m}X_{pn}(t)\right\},\ m=0,1,2... \qquad (5\text{-}52)$$

Applying the DP definition in (2-2), the FTCs can be calculated as

$$\left\langle e^{jn\omega_p t}\right\rangle_{1m}=\frac{1}{T_1}\frac{1}{j(n\omega_p-m\omega_1)}e^{j(n\omega_p-m\omega_1)t}\left\{1-e^{-j(n\omega_p-m\omega_1)T_1}\right\} \qquad (5\text{-}53)$$

Defining $n\omega_p$-$m\omega_1$=$\Delta\omega_{nm}^{p}$, (5-53) can be rewritten as

$$\left\langle e^{jn\omega_p t}\right\rangle_{1m}=\frac{1}{T_1}\frac{1}{j\Delta\omega_{nm}^{p}}e^{j\Delta\omega_{nm}^{p}t}\left\{1-e^{-j\Delta\omega_{nm}^{p}T_1}\right\} \qquad (5\text{-}54)$$

Using the Euler formula, (5-54) can be written as

$$\left\langle e^{jn\omega_p t}\right\rangle_{1m}=\frac{e^{j\Delta\omega_{nm}^{p}t}}{j\Delta\omega_{nm}^{p}T_1}\left\{1-\cos(\Delta\omega_{nm}^{p}T_1)+j\sin(\Delta\omega_{nm}^{p}T_1)\right\} \qquad (5\text{-}55)$$

Considering the following sinusoidal functions:

$$1-\cos(\Delta\omega_{nm}^{p}T_1)=2\sin^2(\frac{\Delta\omega_{nm}^{p}T_1}{2}) \qquad (5\text{-}56)$$

$$\sin(\Delta\omega_{nm}^{p}T_1)=2\sin(\frac{\Delta\omega_{nm}^{p}T_1}{2})\cos(\frac{\Delta\omega_{nm}^{p}T_1}{2}) \qquad (5\text{-}57)$$

Substituting (5-56) and (5-57) into (5-55) yields:

$$\left\langle e^{jn\omega_p t}\right\rangle_{1m} = e^{j\Delta\omega_{nm}^p t}\frac{\sin(\frac{\Delta\omega_{nm}^p T_1}{2})}{(\frac{\Delta\omega_{nm}^p T_1}{2})}\left\{-j\sin(\frac{\Delta\omega_{nm}^p T_1}{2})+\cos(\frac{\Delta\omega_{nm}^p T_1}{2})\right\} \tag{5-58}$$

Using the Euler formula, (5-58) can be written as:

$$\left\langle e^{jn\omega_p t}\right\rangle_{1m} = e^{j\Delta\omega_{nm}^p t}\frac{\sin(\frac{\Delta\omega_{nm}^p T_1}{2})}{(\frac{\Delta\omega_{nm}^p T_1}{2})}e^{-j\frac{\Delta\omega_{nm}^p T_1}{2}} \tag{5-59}$$

Defining the following coefficient:

$$C_{nm}^p = \frac{\sin(\frac{\Delta\omega_{nm}^p T_1}{2})}{(\frac{\Delta\omega_{nm}^p T_1}{2})}e^{-j\frac{\Delta\omega_{nm}^p T_1}{2}} \tag{5-60}$$

Substituting (5-59) and (5-60) into (5-52) gives:

$$X_{1m}^p(t) = \sum_n C_{nm}^p e^{j\Delta\omega_{nm}^p t} X_{pn}(t), \quad m = 0,1,2... \tag{5-61}$$

With (5-61), the relation of DPs in different frames is derived and the DPs in the $\omega_p$ slave frame can be transformed into the $\omega_1$ master frame. The equation (5-61) also implies that, after the frame transformation, the DPs in the master frame spread the entire frequency axis, even if the DP in the $\omega_p$ frame includes only one single component. For example, let the DPs of $x_p(t)$ in the $\omega_p$ frame include only the n=1 component $X_{p1}(t)$. Using (5-61) and transforming the $\omega_p$-frame DPs to the master frame, the DPs will include DP components with m=0,1,2…due to the non-zero coefficients $C_{nm}^p$. Even though one can approximate the DPs $X_{1m}^p(t)$ (m=0,1,2…) by truncating higher order DPs, the system order has increased due to the increase of DP components included in the system. This makes the application of (5-61) very difficult and another method is proposed.

As only the fundamental component is considered in the DP model, we assume that the time-domain waveform $x_p(t)$ with frequency $\omega_p$ is

$$x_p(t) = A\cos(\omega_p t + \varphi) \tag{5-62}$$

Choosing the base frequency $\omega_p$, the DP $X_{pn}(t)$ can be calculated as

$$X_{pn}(t) = \begin{cases} 0.5Ae^{j\varphi}, & n = 1 \\ 0, & n \neq 1, n > 0 \end{cases} \tag{5-63}$$

From (5-63), one can see that in the $\omega_p$ frame, all the DPs except $X_{p1}(t)$ are equal to zero. With (5-61), the DPs $X_{pn}(t)$ can be transferred to the master frame with

$$X_{1m}^{p}(t) = \begin{cases} C_{11}^{p} e^{j\Delta\omega_{11}^{p} t} X_{p1}(t), & m = 1 \\ C_{1m}^{p} e^{j\Delta\omega_{1m}^{p} t} X_{p1}(t), & m \neq 1, m > 0 \end{cases} \tag{5-64}$$

where $\Delta\omega_{1m}^{p} = 1\omega_p - m\omega_1$. As shown in (5-64), the $\omega_p$-frame DP $X_{p1}(t)$ becomes a series of DPs with a wide range of frequency components in the master frame. This makes the frame transformation difficult to calculate and impractical for applications. To make progress, we note that in the slave frame, the DPs of $x_p(t)$ only include the n=1 component, as shown in (5-63). It would be convenient if the DP transformation from the $\omega_p$ frame to the $\omega_1$ frame can be accomplished with the DP index remaining the same, i.e. m=1.

According to (5-64), we define a complex variable $X_{11}^{p'}(t)$ as:

$$X_{11}^{p'}(t) = \langle x \rangle_{11}^{p'} = C_{11}^{p^{-1}} X_{11}(t) = C_{11}^{p^{-1}} \langle x \rangle_{11}^{p} \tag{5-65}$$

Combining (5-64) and (5-65) gives:

$$X_{11}^{p'}(t) = e^{j\Delta\omega_{11}^{p} t} X_{p1}(t) = e^{j\Delta\omega_{11}^{p} t} \langle x \rangle_{p1} \tag{5-66}$$

Equation (5-65) illustrates a linear relation between $X_{11}^{p'}(t)$ and the DP of $x_p(t)$ in the master frame, $X_{11}^{p}(t)$. This indicates that $X_{11}^{p'}(t)$ is still in the master frame. Equation (5-66) reveals that the DP $X_{11}^{p'}(t)$ can be derived from a rotation of transformation of the DP $X_{p1}(t)$. With the same magnitude, these two variables have a phase angle difference $\Delta\omega_{11}^{p} t = \omega_p t - \omega_1 t$. Applying (2-2), (5-65) and (5-66), the time-domain waveform $x_p(t)$ can be traced back from $X_{11}^{p'}(t)$ with

$$x_p(t) = 2\Re e\left\{X_{p1}(t)e^{j\omega_p t}\right\} = 2\Re e\left\{X_{11}^{p'}e^{-j\Delta\omega_{11}^{p}t}e^{j\omega_p t}\right\} = 2\Re e\left\{X_{11}^{p'}e^{j\omega_1 t}\right\} \tag{5-67}$$

The equations (5-65) and (5-67) illustrates that the complex variable $X_{11}^{p'}(t)$ can be used as a DP in the master frame. The DPs in the master frame and the DPs in the slave frame are related with a rotating function $e^{j\Delta\omega_{11}^{p}t}$, as shown in (5-66). The introduction of this extra complex variable makes the frame transformation more convenient and mathematically easier for application.

An interface can be developed based on (5-67). The interface allows subsystems modelled in different DP frames to be connected and is written as:

$$\begin{bmatrix} \langle v \rangle_{11}^{p'} \\ \langle i \rangle_{11}^{p'} \end{bmatrix} = e^{j\Delta\omega_{11}^{p}t}\begin{bmatrix} \langle v \rangle_{p1} \\ \langle i \rangle_{p1} \end{bmatrix} \tag{5-68}$$

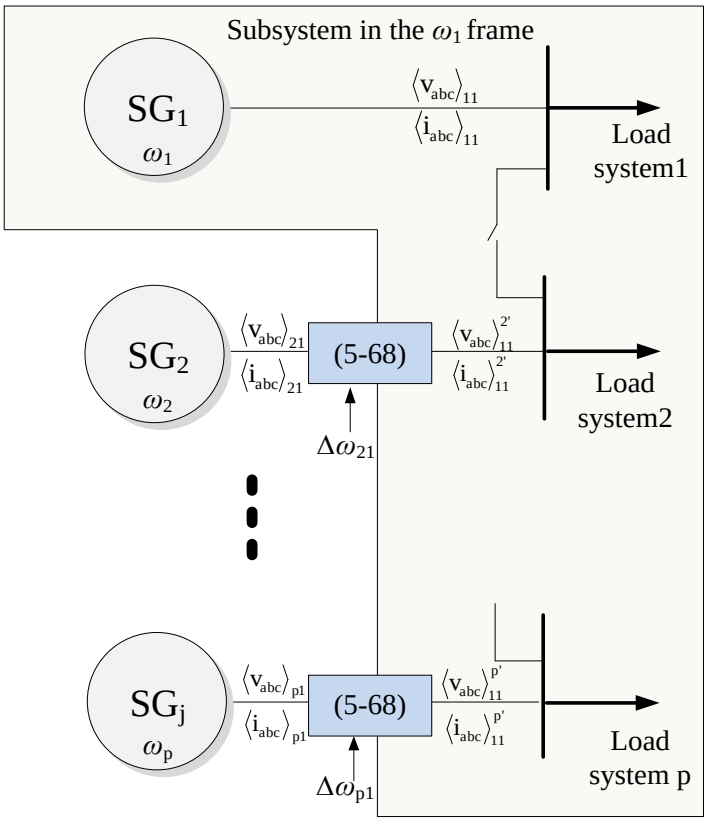


Figure 5-11 DP modelling of multi-generator systems

The multi-generator system in DP domain can be represented in Figure 5-11. As can be seen, the master generator connects to the load system directly. The slave generators connect to the load system using an interface based on (5-68). All the load system is modelled in the master frame, $\omega_1$ frame.

# 5.6 Model Validation

In this section, two test cases have been simulated to illustrate the efficiency and accuracy of the DP model. The first case is simpler and consists of two unsynchronized generators and some RL loads. The second case studies a twin-generator system with ATRU supplying the main DC bus to show that the proposed method is also valid for nonlinear systems.

In both cases, the two generators work separately in the beginning, then connect in parallel for a short period, 100ms, and work separately again. Three modelling techniques are compared in this section, i.e. the DP model (denoted as DPABC), models in the ABC and DQ0 frames (denoted as ABC and DQ0 respectively). The ABC model can be conveniently applied to model the multi-generator system. The multi-generator system is built based on the model discussed in Section 5.5. All the models and simulations have been done in Dymola 2012.

## 5.6.1 Twin-Generator System with RL Loads

In this case, two synchronous generators with different frequencies are used to supply identical load systems, as shown in Figure 5-12. The transmission lines are modelled as an RLC circuit. The parameters for the system are shown in Table 5-2. In the DP and DQ0 models, the frame relating to SG1 is chosen to be the master frame.

Table 5-2 The set of parameters of the basic generator-load system

| **Parameters** | **Values** | **Description** |
|---|---|---|
| **Synchronous Generator 120kVA rated with GCU** | | |
| $R_s$ | 0.0044Ω | Stator resistance |
| $L_{ls}$ | 19.8μH | Stator leakage inductance |
| $L_{md}$ | 0.221mH | Stator d-axis magnetizing inductance |
| $L_{mq}$ | 0.162mH | Stator q-axis magnetizing inductance |
| $R_f$ | 68.9mΩ | Field resistance |
| $L_{lf}$ | 32.8μH | Field leakage inductance |
| $R_{kd}$ | 0.0142 Ω | d-axis resistance |
| $L_{lkd}$ | 34.1μH | d-axis leakage inductance |
| $R_{kq}$ | 0.0031 Ω | q-axis resistance |
| $L_{lkq}$ | 0.144mH | q-axis leakage inductance |
| P | 2 | Pole pairs of the generator |
| $V^*_T$ | 230Vrms | Voltage command of GCU |
| $\omega_{n,voltage}$ | 10Hz ($K_{pv}$=1.38, $K_{iv}$=188.4) | Natural frequency of voltage loop in GCU |
| $\omega_{n,current}$ | 100Hz ($K_{pi}$=0.05, $K_{ii}$=100.4) | Natural frequency of current loop in GCU |
| $R_{Line}$ | 0.02 Ω | Transmission line resistance |
| $L_{line}$ | 24uH | Transmission line inductance |
| $C_{line}$ | 20nF | Transmission line capacitance |
| R | 10 Ω | Load resistance |
| L | 1mH | Load inductance |

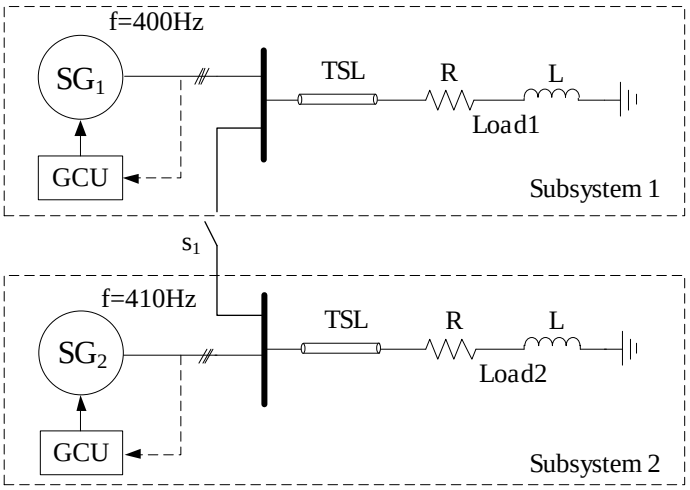


Figure 5-12 Simulation scheme of a simple twin-generator system

The fundamental frequency of SG1 is set at 400Hz and SG2 is set at 410Hz. The initial rotor angle of SG1 is set at $\theta_0=0^o$ and SG2 set at $\theta_0=90^o$. Initially these two generators supply their loads respectively. At t=0.2s, $s_1$ is closed and the two generators are connected in parallel. At t=0.4s, $s_1$ opens and the two subsystems are separated. At t=0.5s, the simulation is terminated.

The load currents in phase A from different models are shown in Figure 5-13. Before t=0.2s, the two generators work separately. Due to the GCU control of the generator terminal voltages, the magnitude of the currents through load1 and load2 are constant during this period. When the two generators are connected, the currents in both load1 and load2 start beating due to the frequency difference of the two generators. After 0.1s, the two generators work separately and the currents become constant again. During all the simulation period, the results from three modelling techniques are well matched as shown in Figure 5-13.

The DPs of phase A currents of load1 and load2 are shown in Figure 5-14. When the two subsystems operate separately, the load currents in subsystem1 are dc-like since the frequency of SG1 (400Hz) has been chosen as the master frame. However the load currents in subsystem2 exhibit a 10Hz fluctuation due

to the frame transformation. When the two generators are connected in parallel, the load currents in both subsystems fluctuate at 10Hz.

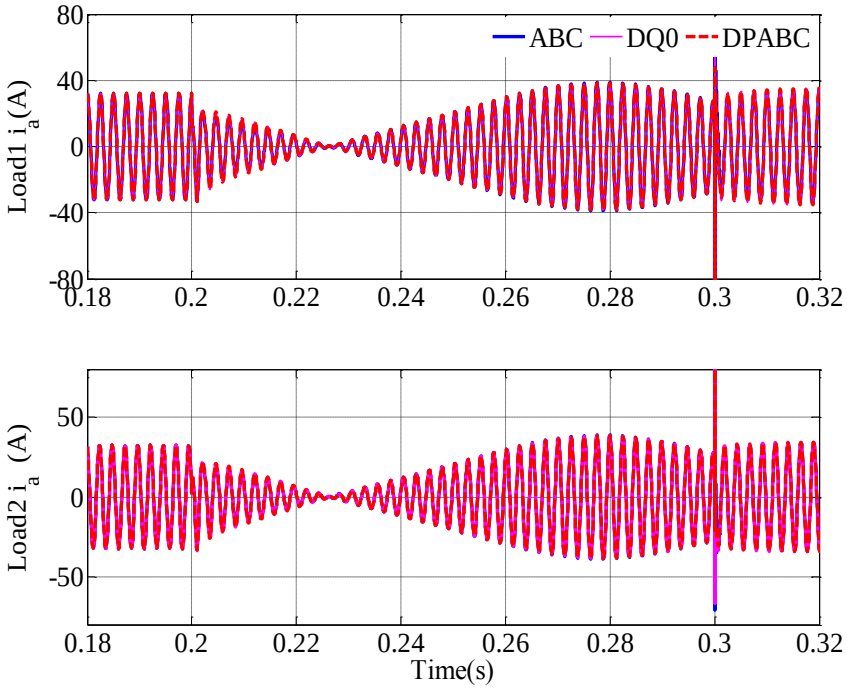


Figure 5-13 Load currents comparison between different DP model and ABC model

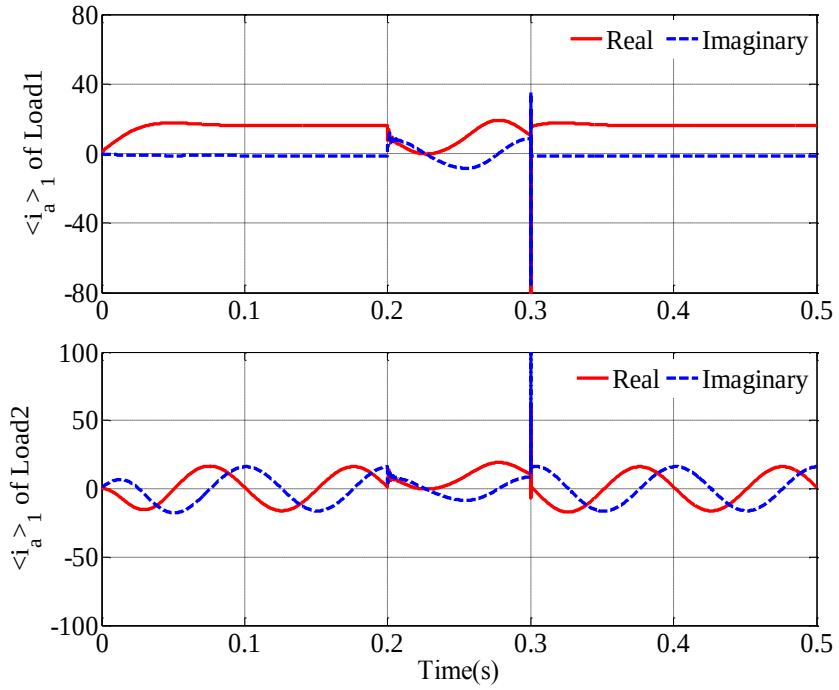


Figure 5-14 Load currents $\langle i_a \rangle_1$ in the DP models

## 5.6.2 Twin-Generator System with ATRUs

In this section, a more complex multi-generator system is simulated and the generators supply nonlinear loads as shown in Figure 5-15. The two generators are feeding two resistive loads through an 18-pulse ATRU. The generator parameters are the same as those given in Table 5-2. Other additional parameters are shown in Table 5-3.

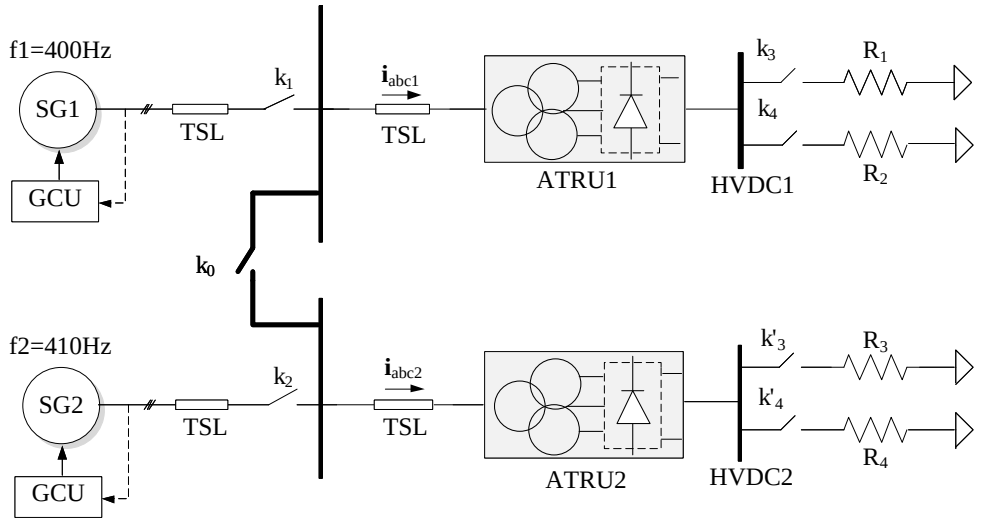


Figure 5-15 Twin-generator system with 18-pulse ATRUs feeding resistive loads through HVDC buses

Table 5-3 Parameter for ATRU system simulation

| **ATRU** | |
|---|---|
| Power rate | 150kW |
| **DC-link** | |
| Capacitors $C_{f1}$ | 45uF |
| Resistor $R_1$ and $R_3$ | 10Ω |
| Resistor $R_2$ and $R_4$ | 12.5Ω |

The fundamental frequency of SG1 is set at 400Hz and SG2 is set at 410Hz. The initial rotor angle of SG1 is set at $\theta_0=0^o$ and SG2 at $\theta_0=90^o$. The events for the simulation are shown in Table 5-4.

Table 5-4 Simulation events in EPS shown in Figure 5-16

| **Time** | **Event** |
|---|---|
| t=0s | Two SGs start from zero initialization |
| t=0.1s | $k_1$,$k_2$, $k_3$ and $k'_3$ are closed; SGs start to supply their loads separately |
| t=0.12s | $k_4$, $k'_4$ are closed; loads change at ATRU DC-link side |
| t=0.2s | $k_0$ is closed; SGs connect and work in parallel |
| t=0.25s | $k_0$ opens; SGs separate |
| T=0.35s | Simulation ends |

The phase A current flowing into the two ATRUs have been shown in Figure 5-16 and Figure 5-17. Before t=0.1s, there is no load connected and the AC currents are equal to zero. When the load is on at t=0.1s, the SGs start to supply power to the load and a step of current can be seen in Figure 5-16 and Figure 5-17. Another step of current can also be noticed at t=0.12s, when there is a load step change at the DC-link. At t=0.2s, the two generators are connected and the currents start beating until t=0.25s when the two generators are separated. The currents from DP and DQ0 models are transformed to the time-domain three-phase signals in order to compare with the ABC model. It can be seen from the zoomed results that three different modelling techniques give well matched results during all the simulation period.

The DC-link voltage from different models is shown in Figure 5-18. Before t=0.1s, the DC-link voltage remains at 0V as there is no current to charge the capacitor. When $k_1$ is closed at t=0.1s, the DC-link voltage goes from 0V to 540V. A step change can also be noticed when the load becomes larger at t=0.12s. This is because the voltage drop in the transmission lines becomes larger with the heavier load. When the two generators are connected at t=0.2s, the DC-link voltage starts to fluctuate due to the beating current at the AC

terminals. In all the simulation period, the results from three different models are well-matched.

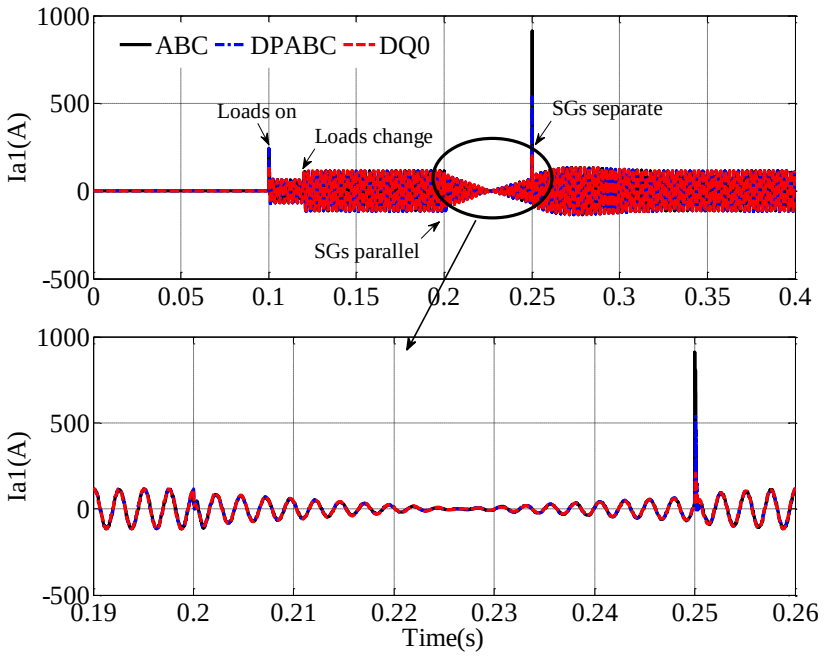


Figure 5-16 Phase A current flowing into ATRU1 comparison between different models

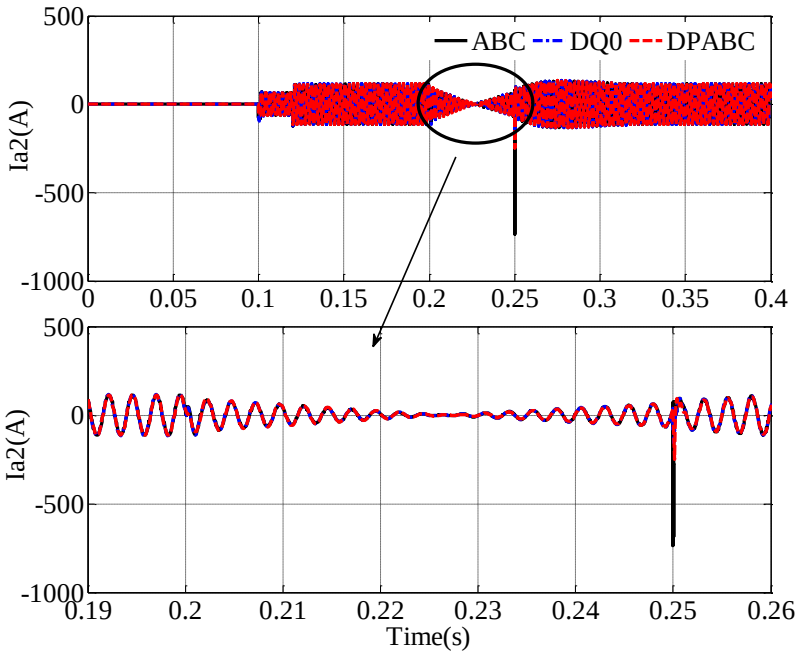


Figure 5-17 Phase A current flowing into ATRU2 comparison between different models

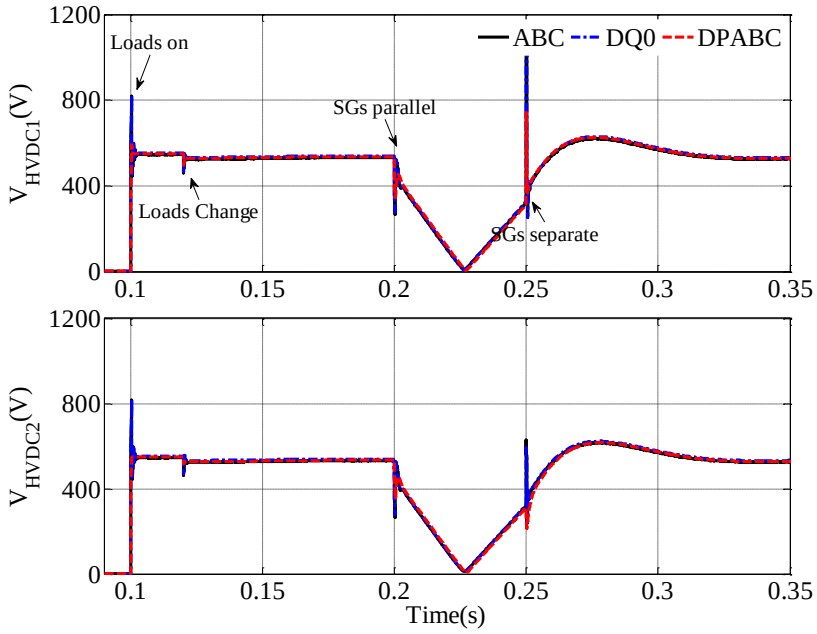


Figure 5-18 DC-link voltage in the ATRU comparison between different models

The currents flowing into ATRUs for the DP and DQ0 models are shown in Figure 5-19. When the SGs work separately, the DP and dq components of the SG1 current, $\langle i_a \rangle_{11}$ , $i_{1d}^{1}$ and $i_{1q}^{1}$ , are dc-like. However, after the frame transformation, the DPs and dq components of the SG2 current, $\langle i_a \rangle_{11}^{2'}$, $i_{2d}^{1}$ and $i_{2q}^{1}$ , present slowly fluctuating behaviour at f=10Hz. During the period of connection, the DPs in two subsystems become equal and fluctuate at f=10Hz. This is also true in the DQ0 model; the dq components in the two subsystems fluctuate at f=10Hz during the connected SG period.

The computation time for the three modelling techniques is shown in Figure 5-20. It can be seen that the DQ0 and DP model are significantly faster than the ABC model. The computation efficiency of the DQ0 and DP models arises due to the dc-like or slowly time-varying variables (10Hz) in the model. The DQ0 model is faster than the DP model. This is due to the system order of the DP model being higher than that of the DQ0 model.

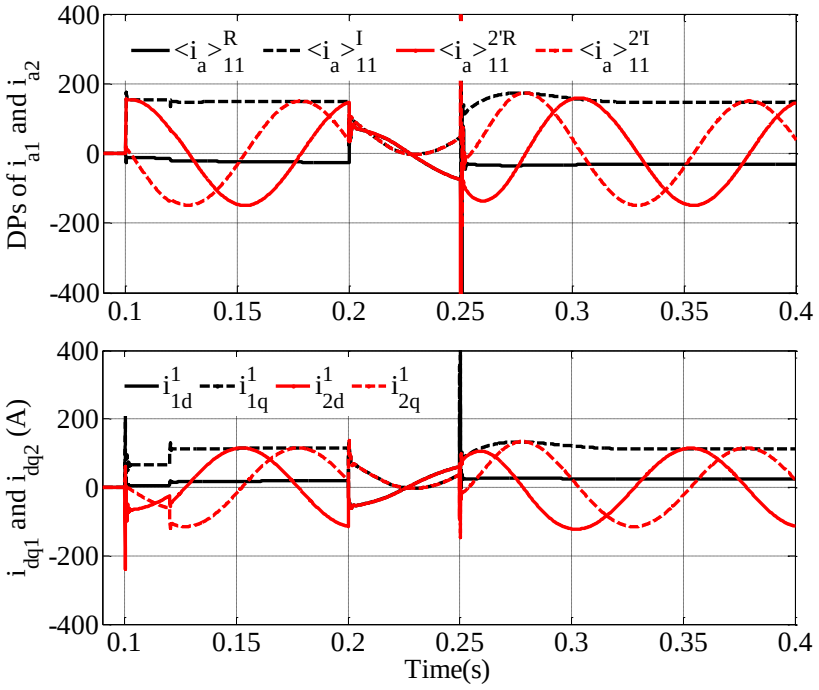


Figure 5-19 The current flowing into the ATRUs. Above: The phase A current in DP model; below: currents in DQ0 model

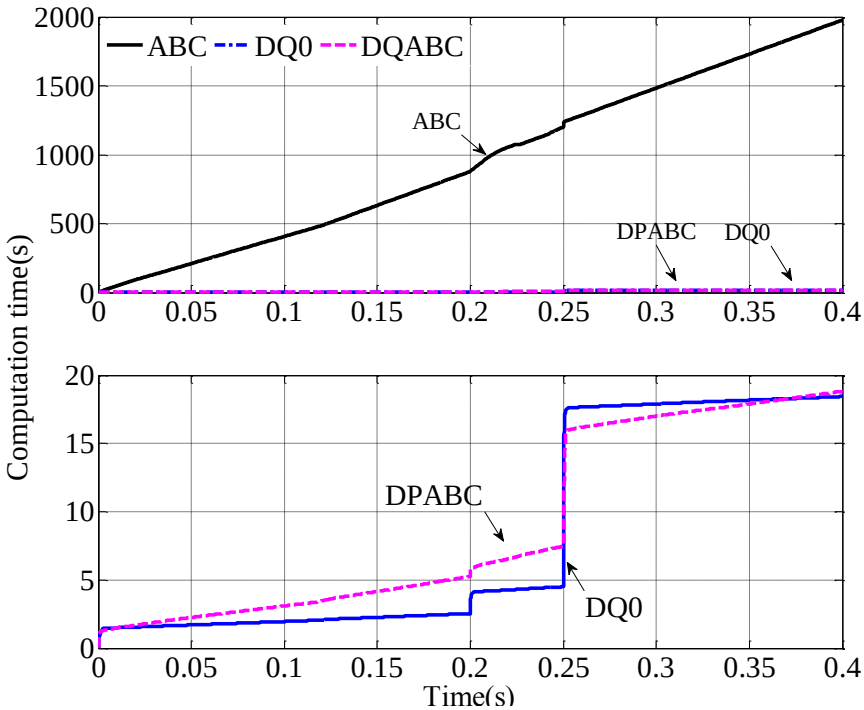


Figure 5-20 The computation time comparison between different models. Above: computation time of ABC, DQ0 and DP models; below: computation time of DQ0 and DP models.

## 5.7 Conclusion

In this chapter, three modelling techniques, ABC, DQ0 and DPABC models, have been implemented for modelling the controlled wound-field SG. In the ABC model, the stator is modelled in three-phase coordinates and the rotor is model modelled in the dq frame. Transforming the three-phase stator model into the dq frame with the d axis aligned to the rotor, yields the DQ0 model. The DPABC model is based on the ABC model and all the variables are transformed to DPs.

Based on the developed models of the single wound-field SG, the three modelling techniques have been extended to modelling multi-frequency multi-generator systems. The modelling of multi-generator system in the ABC frame is straight forward and each subsystem can be modelled independently. The developed ABC model is used as the benchmark model in this chapter. The modelling of such system in the DQ0 frame and with DPs requires a common reference frame, or master frame. All the variables are transformed into the master frame. The DQ0 model is used for efficiency comparison studies with the DP model.

During the generator start-up and shutdown, the transition of power from/to the APU generator to/from the main generator involves the parallel operation of two generators. In addition, the multi-generator system is also a future trend for the aircraft EPS with DC structures, where the main HVDC bus is fed by multiple connected generators with CRUs.

With the multi-frame transformation theory presented, the DP model and the DQ0 model can be extended to studying the parallel operation multi-generator systems without the assumption of single frequency in the EPS.

When modelling a multi-generator system in the DQ0 frame, the master dq frame is chosen to be aligned with the rotor of any of the generators in the

system. The whole loading system is modelled in the master frame. The slave generators are connected to the system through an interface which transforms the variables from the slave frame to the master frame.

The same idea can be used in the DP model. When modelling a multi-generator system in DPs, the frequency of one generator is chosen as the master frame and all the loading system is modelled in this master frame. The slave generators connect to the loading system with an interface which transforms the DPs from the slave frame to the master frame. After transformation, the DPs in the subsystems exhibit time-varying behaviour at a frequency $\Delta\omega$, which depends on the difference between the master frame and the slave frame. In general, the frequency difference will be small which means that the subsystems will have slowly varying DPs. This still allows larger simulation steps and accelerated simulations. Comparing with ABC model simulation results, the efficiency and accuracy of DP models have been revealed in this chapter.

The performance of the multi-frame DP model is executed through comparison of simulation results from different modelling techniques: ABC, DQ0 and DPABC models. Simulations of the twin-generator system for two different loading cases are compared and the results are well-matched with each other.

In this chapter, the different fundamental frequencies of the generators are still constant. For the time-varying frequencies, the time-varying DPs introduced in Section 2.5 can be used.

# Chapter 6

# Twin-Generator Aircraft Power System Studies Using Dynamic Phasors

## 6.1 Introduction

As future commercial aircraft incorporates more EMAs, the aircraft electrical power system architecture will become a complex electrical distribution system with increased number of PECs and electrical loads. The overall system performance and the power management for on board electrical loads are therefore key issues that need to be addressed. In order to understand these issues and identify high pay-off technologies that would enable a major improvement of the overall system performance, it is necessary to study the aircraft EPS at the system level, in contrast to looking at the system behaviour at individual subsystem or the small-scale system level.

From the work of previous chapters, the DP model library of the main element for aircraft EPS simulations has been established. The simulation comparison of ABC, DQ0 and DP models has demonstrated the efficiency and accuracy of the DP modelling technique with a small-scale EPS level. In this chapter, the three modelling techniques will be compared with a more complex system. A twin-generator aircraft EPS based on the MOET large aircraft EPS architecture will be used for simulation and comparison studies. The system will be simulated under both balanced and unbalanced conditions. The efficiency and accuracy of the functional DP model for integrative simulation studies of the

future aircraft will be demonstrated.

## 6.2 Description of MOET Aircraft Electrical Power System

In this chapter, the EPS structure based on the MOET large aircraft EPS architecture from Airbus France (document WP3.11 architecture V0 [12]). This architecture has been briefly introduced in Chapter 1 and redrawn in Figure 6-1. In this architecture, the EPS is organized in several main sections: the power generation section, the power distribution and conversion section, and the on-board electrical load section. The primary sources for this system come from two gas turbine engines (ENG1/ENG2). Each aircraft engine drives two 250kVA starter/generators (SG1-SG4). Each generator is controlled by its GCU to maintain 230/400Vrms at the terminals. Since the generator is directly driven by the aircraft engine, the power system is frequency-wild (360-900Hz) reflecting the recent industry trend in moving away from constant frequency 400Hz power. The electrical power is distributed in AC form through four high-voltage AC distribution buses (HVAC1-1, HVAC1-2, HVAC2-3 and HVAC2-4). In Figure 6-1, there are three Primary Electrical Power Distribution Centres (PEPDC1-PEPDC3) and two Emergency Electrical Power Distribution Centres (EEPDC1 and EEPDC2). The PEPDC is used to supply the primary electrical loads such as the Wing Icing Protection System (WIPS), the ECS, Back-up Batteries (BAT) and other loads. The EEPDC is assigned to supply the essential electrical loads for the function of the flight surface control. These essential electrical loads require no loss of power for supplying the vital electrical loads under emergency. When an emergency occurs, the electrical power supply to loads within the PEPDC can be interrupted, given the priority to the vital electrical loads for the flight surface control.

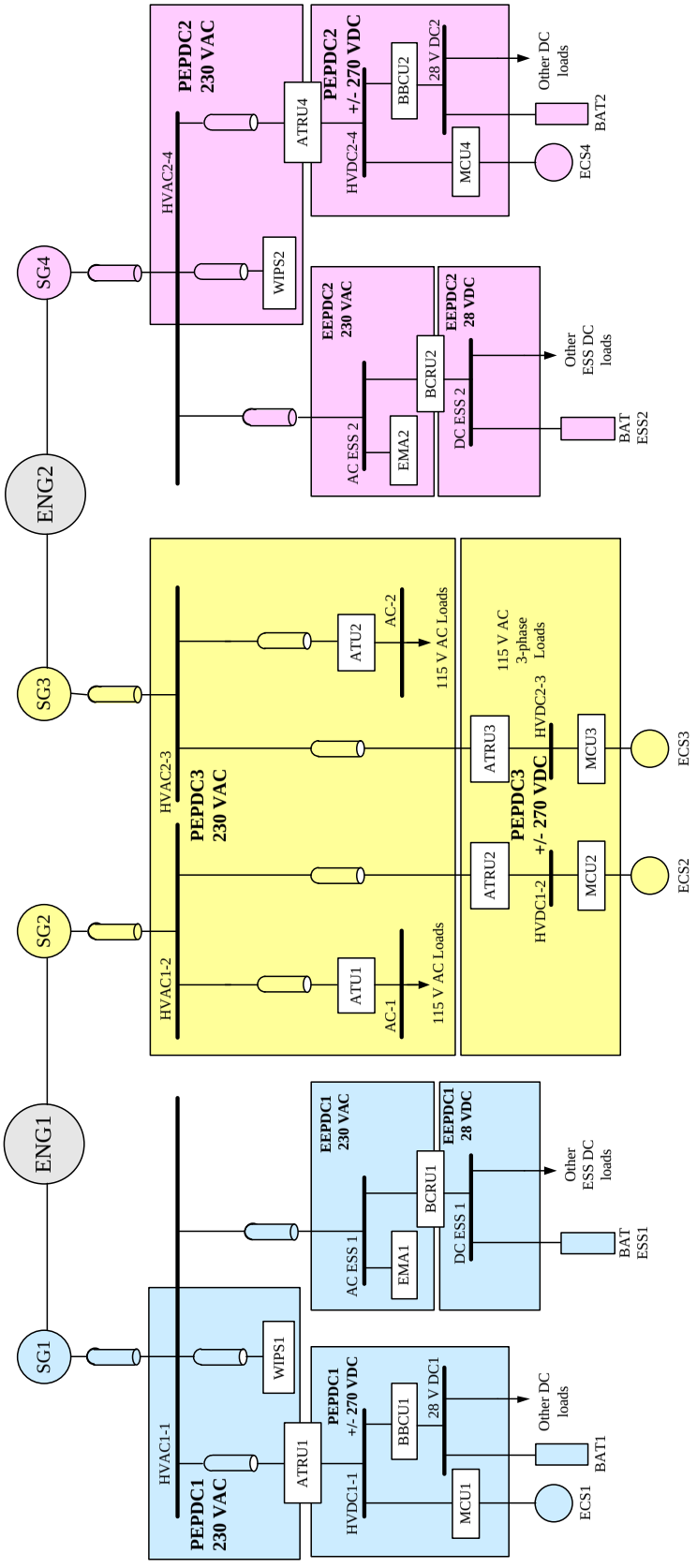


Figure 6-1 MOET aircraft electrical power system architecture

As shown in Figure 6-1, for the primary electrical distribution centres, the PEPDC1 is a multiple-bus electrical system, which consists of a 230VAC bus (HVAC1-1), a +/-270VDC bus (HVDC1-1) produced by the ATRU1, and a 28VDC bus (DC1) fed from a buck-boost converter unit (BBCU1). Similarly, the PEPDC2 consists of a 230VAC bus (HVAC2-4), a +/-270VDC bus (HVDC2-4) supplied by the ATRU4, and a 28VDC bus (DC2) fed from BBCU2. The PEPDC3 consists of two 230VAC buses (HVAC1-2, HVAC2-3), two +/-270VDC buses (HVDC1-2, HVDC2-3) produced by ATRU2 and ATRU3, and 115VAC buses (AC1, AC2) fed from auto-transformer units (ATU1, ATU2).

For the emergency electrical power distribution centres, the EEPDC1 contains a 230V AC essential bus (AC ESS1) and a 28V DC essential bus (DC ESS1) fed from a battery charge rectifier unit (BCRU), while the EEPDC2 contains 230VAC essential bus (AC ESS2), and 28VDC essential bus (DC ESS2) fed from BCRU2.

The system is generally symmetrical in which each component is operated in parallel with an identical component or is used as a back-up by having redundant secondary devices for the situation when the primary device fails. The subsystem including SG1, SG2, PEPDC1, EEPDC1 and half of PEPDC3 embodies half of aircraft electrical power system. During normal operation, SG1 supplies the power to PEPDC1, EEPDC1, the electrical wing ice protection system (WIPS1), and the environmental control system (ECS1) controlled by a Motor Control Unit (MCU1). Similarly, SG4 feeds the PEPDC2, EEPDC2, WIPS2 and ECS4. The generators SG2 and SG3 supply the power to PEPDC3 of which the electrical loads are the ECS2, ECS3 and other 115 AC loads. Four batteries (BAT1, BAT ESS1, BAT2 and BAT ESS2) are charged during the normal operation conditions and supply power to the essential loads through bi-directional converters during loss of main power supply.

Considering symmetry of the MOET aircraft EPS architecture, this chapter will focus on studies of a twin-generator aircraft power system shown in Figure 6-2. Such a twin-generator aircraft EPS actually represents half of the system of Figure 6-1 and has a reduced component count. However, it contains all the component types and is considered of sufficient complexity to illustrate the increase in computational efficiency resulting from the DP representations. The twin-generator system is divided into two subsystems with each containing one generator. These two subsystems are connected by the switch $S_{HVB}$. The battery and other DC loads connected to the 28V DC bus in the PEPDC1 are represented by a resistive load fed by the +/-270 DC bus (HVDC1). Two identical AC-fed EMAs are supplied from the AC essential bus to represent the essential electrical loads for performing actuation functions. The battery and other DC loads connected to the 28V DC bus in the EEPDC1 are ignored since they consume a small amount of power and do not significantly affect the power system behaviour. The 115V AC loads in the PEPDC3 are represented as resistors.

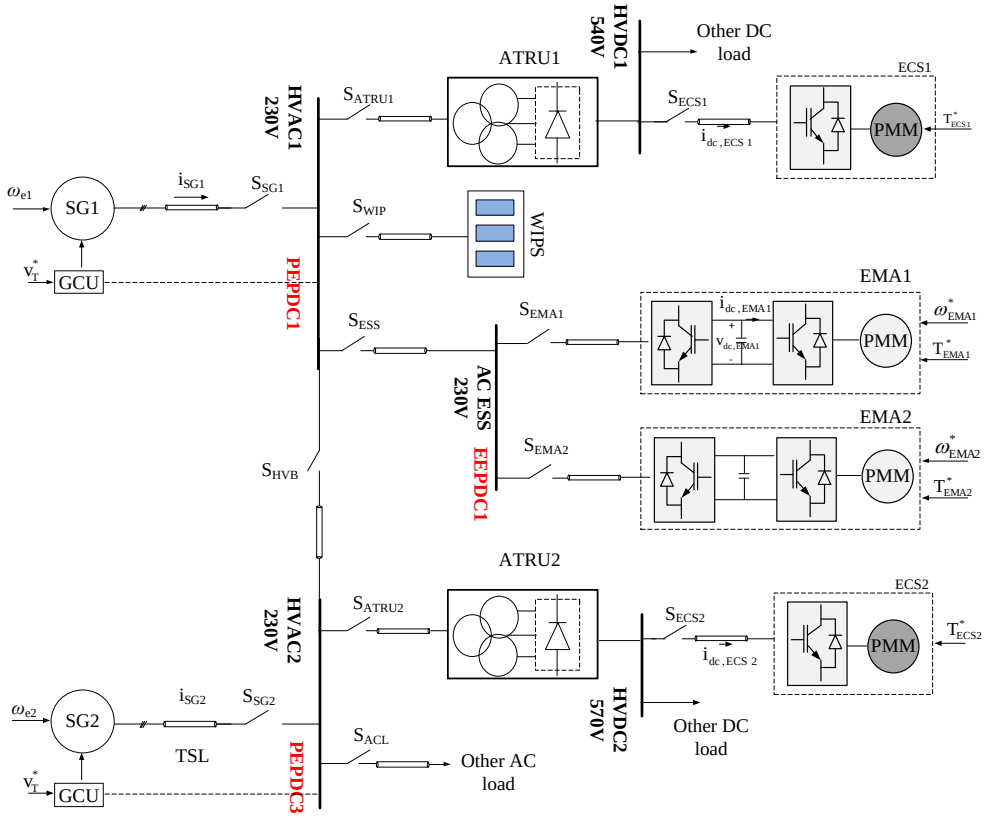


Figure 6-2 The EPS of the twin-generator aircraft

# 6.3 Models of Electromechanical Actuator Drives

Before simulating the EPS shown in Figure 6-2, the libraries of ABC, DQ0 and DP models still need the model for EMAs. The EMAs will potentially be widely used in the future aircraft as the aircraft moves toward the more-electric architecture. Depending on the aircraft EPS architecture, the EMA can be fed either from a DC or AC bus, as shown in Figure 6-3.

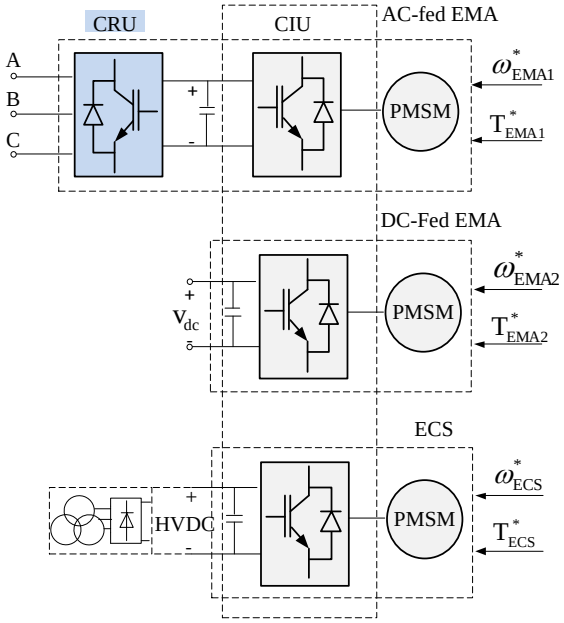


Figure 6-3 the structure of DC-fed EMA, AC-fed EMA and ECS

The AC-fed EMA comprises of a controlled rectifier unit (CRU), a Controlled Inverter Unit (CIU) and a Permanent Magnet Synchronous Machine (PMSM). The DC-fed EMA is basically a part of the AC-fed EMA without the CRU.

As shown in Figure 6-2, the ECS is essentially a DC-fed PMSM drive system. The ECS is one of the largest consumers of electrical power in future aircraft. Since there is no engine bleed air available, the ambient air will be pressurized via electrical compressors. These compressors are fed by the HVDC buses as shown in Figure 6-3.

The model of AC-fed EMAs, DC-fed EMAs and ECS's involves the modelling of CRUs and the DC-fed PMSM drive system. The modelling of CRU has been

introduced in Chapter 3. This section will focus on the modelling of the DC-fed PMSM drive system, which consists of the CIU and the PMSM.

In the DC-fed PMSM drive system, the vector control is selected since it allows independent control of flux and torque and has been widely used in the motor drive system. The control structure is shown in Figure 6-4. It can be seen that the control of machine flux and torque is decoupled. The q-axis stator current is used to generate electromechanical torque. The d-axis current is used to build up machine flux. Since the rotor of the PMSM is a permanent magnet itself, the reference for the d-axis stator current can be set to zero. At this stage, we assume that no field-weakening is applied in the PMSM vector control system.

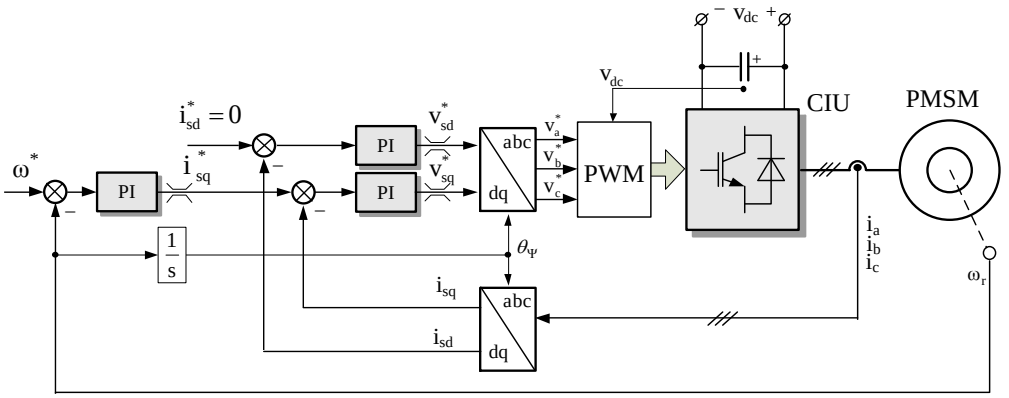


Figure 6-4 Vector control structure for the PMSM

Three techniques will be considered in modelling the PMSM drive system shown in Figure 6-4, i.e. the ABC model, the DQ0 model and the DP model. In the ABC model, the PMSM stator and rotor windings are modelled in the static *αβ* frame but transformed to the ABC frame at the terminals using the *αβ/ABC* transformation. The PWM converter in the ABC frame is modelled with or without switching behaviour, called a switching ABC model or a non-switching ABC model respectively. The switching ABC model means that the PWM power converter is modelled using real or ideal switches such that the switching behaviour is taken into account. The non-switching ABC model means the power converter is modelled by a set of voltage and current

equations without the consideration of switching behaviour. In the DQ0 model, the $\alpha\beta$-frame PMSM model and the non-switching ABC model of PWM converters are transformed into the DQ frame with the d-axis fixed on the rotor of the PMSM. The DP model of the DC-fed PMSM drive system stays the same as that in the DQ0 model. This is due to the fact that in DP models, only the DC component is considered at the DC side of the ATRUs and CRUs. With the DP definition, these DPs are essentially equal to their time-domain values, i.e. $\langle x \rangle_0 = x$. Thus the DC-fed PMSM models in the DQ0 frame can interface with the DP ATRU and CRU models directly.

Since the CIU in reality is the same as the CRU, there is no necessity to develop an extra model for the CIU in the libraries. The non-switching ABC model and DQ0 model can refer to Chapter 4 and will not be detailed here. In this section, the PMSM and the switching model of the CIU will be briefly introduced.

### 6.3.1 Permanent Magnet Synchronous Machine

The PMSM can be either a salient (interior magnet) or non-salient (surface mount) PM machine. In general a non-salient machine is assumed, i.e. $L_d \neq L_q$ [27].

#### 1) ABC model

The ABC model of PMSM is based on the $\alpha\beta$-frame model. The voltage equations of the stator circuit in the $\alpha\beta$ reference frame can be given by

$$v_\alpha = r_s i_\alpha + \frac{d\lambda_\alpha}{dt} \tag{6-1}$$

$$v_\beta = r_s i_\beta + \frac{d\lambda_\beta}{dt} \tag{6-2}$$

where $r_s$ is the stator resistance. The flux linkage of the stator circuit can be given by

$$\lambda_\alpha = \left( L_{ls} + \frac{3}{2} L_m \right) i_\alpha + \lambda_m \cos\theta_r \tag{6-3}$$

$$\lambda_\beta = \left( L_{ls} + \frac{3}{2} L_m \right) i_\beta + \lambda_m \cos\left( \theta_r - \frac{\pi}{2} \right) \tag{6-4}$$

where $L_m$ is the magnetizing inductance; $L_{ls}$ is the leakage inductance; $\lambda_m$ is the peak magnitude of the flux produced by the rotor magnet; $\theta_r$ is the position angle of the rotor. The electromechanical torque is written as

$$T_e = \frac{3}{2}\frac{P}{2} \lambda_m \left( \lambda_\alpha i_\beta - \lambda_\beta i_\alpha \right) \tag{6-5}$$

where P is the number of poles. The electromagnetic torque and the rotor mechanical speed is related by

$$\omega_{rm} = \frac{1}{J} \int \left( T_e - T_L - B_m \omega_{rm} \right) dt \tag{6-6}$$

where J is the rotor inertia; $T_L$ is the load torque and $B_m$ is the coefficient of friction. The ABC model of the PMSM can be developed based on the equations (6-1)-(6-6) using the *αβ/ABC* transformation as:

$$\begin{bmatrix} x_a & x_b & x_c \end{bmatrix}^T = \begin{bmatrix} 1 & -0.5 & -0.5 \\ 0 & \sqrt{3}/2 & -\sqrt{3}/2 \end{bmatrix}^T \begin{bmatrix} x_\alpha & x_\beta \end{bmatrix}^T \tag{6-7}$$

**2) DQ0 model**

The DQ0 model of PMSM machine has been well-developed in [27]. The voltage equations in machine variables are:

$$v_d = -R_s i_d - \omega_r \lambda_q + \frac{d}{dt} \lambda_d \tag{6-8}$$

$$v_q = -R_s i_q + \omega_r \lambda_d + \frac{d}{dt} \lambda_q \tag{6-9}$$

$$v_0 = -R_s i_0 + \frac{d}{dt} \lambda_0 \tag{6-10}$$

where the positive current is assumed to be flowing into the PMSM. The flux linkages can be written as:

$$\lambda_d = L_d i_d + \lambda_m \tag{6-11}$$

$$\lambda_q = L_q i_q \tag{6-12}$$

$$\lambda_0 = L_{ls} i_0 \tag{6-13}$$

where $\lambda_m$ is the flux linkages established by the permanent magnet. The inductance $L_d$ and $L_q$ are

$$L_d = L_{ls} + L_{md} \tag{6-14}$$

$$L_q = L_{ls} + L_{mq} \tag{6-15}$$

The electromagnetic torque in the DQ0 model is

$$T_e = \frac{3}{2}\frac{P}{2}\left\{\lambda_m i_q + (L_d - L_q) i_d i_q\right\} \tag{6-16}$$

## 6.3.2 Switching ABC Models of PWM Converters

Though the switching model of PWM converters is not used when simulating the EPS of Figure 6-2 due to convergence issues, it is still an essential element in the library for small-scale system simulations. In the switching model, the IGBT or MOSFET in the converter is modelled using ideal switches in Dymola. The PWM control scheme is shown in Figure 6-4. The switching function for switches in each leg is complementary and the delay time in the logic component is neglected.

In the switching model, the voltage references $v_a^*$, $v_b^*$ and $v_c^*$ are fed into the PWM block, which generates the modulation index $m_a$, $m_b$ and $m_c$ using the scheme shown in Figure 6-5. The magnitude of the modulation index is constrained to less than 1 using a saturation block.

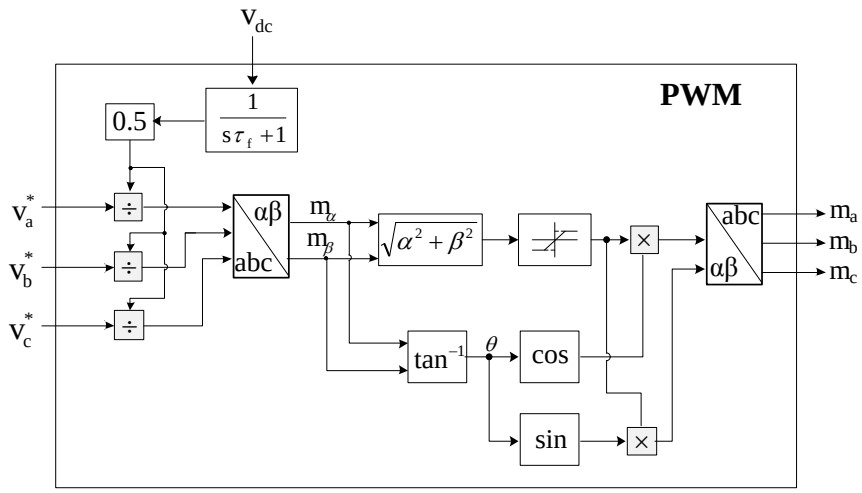


Figure 6-5 Diagram of the PWM block

The final switching signal is generated through comparison of $m_a$, $m_b$ and $m_c$ with a triangle carrier (frequency $f_c$), as shown in Figure 6-6. The generated pulse train is used to control the on and off state of switches in the converter.

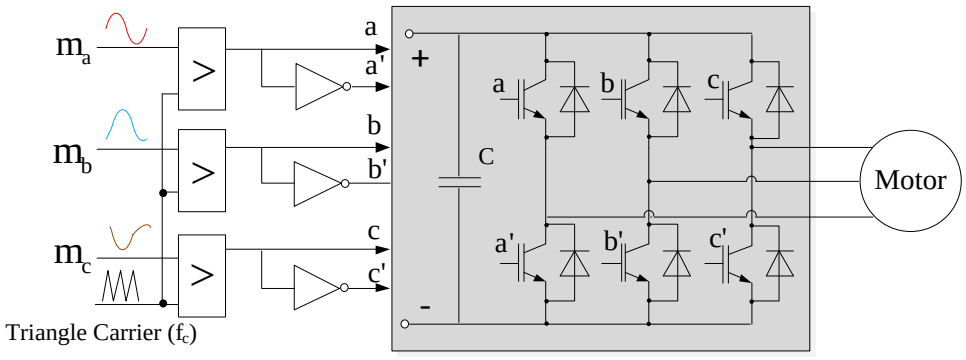


Figure 6-6 Three-phase PWM generator

## 6.3.3 Non-switching Model of PWM Converters

As mentioned before, due to simulation convergence issues, non-switching models of PWM converters are used in the ABC model when simulating the EPS shown in Figure 6-2. The development of the non-switching model of the CRU is detailed in [76]. The AC terminal voltages of the converter are determined by the product of the dc-link voltage and the modulation index. Similarly, the dc-link current is a function of the three-phase currents flowing

into the converter and the modulation index. The non-switching model of the PWM converter is shown in Figure 6-7.

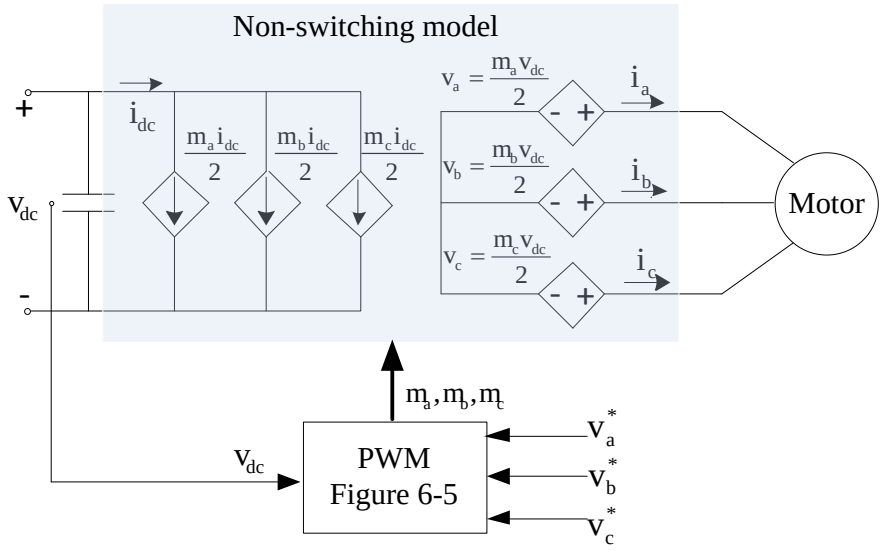


Figure 6-7 The non-switching model of PWM converters

## 6.4 Simulation Studies of a Twin-Generator Electrical Power System

This section will deal with the simulation study of the twin-generator EPS shown in Figure 6-2. In order to demonstrate the performance of the DP functional model, simulation comparison between the ABC model (the model as a benchmark, in the ABC frame with switching behaviour), the DQ0 model (the model in the DQ0 frame) and the DPABC model of such a complex system is carried out under both normal and abnormal conditions. The library of the three modelling techniques was developed using the software Dymola. When developing the benchmark model of this twin-generator EPS, the initial choice of the benchmark model is to include all the switching behaviour in the power electronic devices. Specifically, the IGBTs, MOSFETs, diodes in power converters are modelled with ideal controlled switches. Although many trial solutions in terms of Dymola solver settings are made, such a switching

benchmark model suffers from numerical stability problems and numerical convergence is not possible. In order to obtain a benchmark model which can be successfully simulated, all PWM controlled power converters are replaced by their corresponding non-switching models. The only switching behaviour retained in the benchmark model results from the ATRU. So the benchmark model of the individual components with this power system can be summarized as:

- The synchronous generator with GCU control as shown in Figure 5-5.
- The benchmark model of the three-phase transmission line as shown in Figure 2-8.
- The benchmark model of the ATRU as shown in Figure 3-19.
- The benchmark model of the CRU as shown in Figure 4-1. The non-switching ABC model is used for the benchmark due to the convergence issues when using switching CRU models.
- Both the ECS and the EMA are PMSM-based drive systems. The configuration of their benchmark models is shown in Figure 6-3 in which a full-order vector control is implemented. Again, the PWM converter is represented by the non-switching model due to the convergence issues.

### 6.4.1 Power System Start-up and Normal Operation Studies

This section presents simulation studies of the power system in Figure 6-2 under start-up and normal conditions. During the start-up process, the two subsystems operate independently. It is assumed that the generators have reached the rated speed before the electrical system starts operation. At the same time, the generators SG1 and SG2 are set with different speeds and phase angles. The asynchronism is due to the fact that the generators are driven by different engines whose speeds are not synchronized. Switches $S_{SG1}$ and $S_{SG2}$ are closed at the start of the simulation. This allows GCU1 and GCU2 to regulate the voltages on the HVAC1 and HVAC2 buses at 230Vrms. After the HVAC bus voltages reach steady state, a series of events occurs. The ECS's and EMAs speed up and loads applied as illustrated in Table 6-3.

Though the application of DP concept in modelling multi-generator and multi-frequency system has been demonstrated in Chapter 5 with some simple EPS, the developed theory is further tested using the EPS in Figure 6-2. The test is implemented by closing $S_{HVB}$ when the two subsystems are fully loaded. The two subsystems operate in parallel for a short period and then separate by opening $S_{HVB}$. It is important to point out that this parallel operation is a completely artificial case. It is, however, very useful to further validate the theory developed in Chapter 5 and to demonstrate the application of DP theory in parallel generator case studies in other EPS potential architectures. The switches used during the simulation are modelled in Figure 6-8. As can be seen a small resistance is used in the "on" state to represent to conduction loss. The "off" state of switch is modelled using a large resistance to avoid numerical ill conditioning.

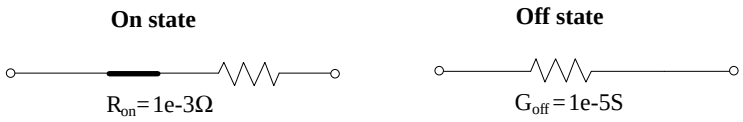


Figure 6-8 Modelling of switches

In Figure 6-2, the generators SG1 and SG2 have identical GCU structures. The parameters of the generator and its control unit are listed in Table 5-2. The transmission line parameters within this system are assumed to be the same as those listed in Table 5-2. The ATRU parameters are listed in Table 3-2. The parameters of the ECS and the EMA are given in Table 6-1. The power rating of elements is shown in Table 6-2

Table 6-1 The parameters of PMSM-based ECS's and EMAs

| Parameters | Values | Description |
|---|---|---|
| **PMSM-based ECS 30kW rated** | | |
| $R_s$ | 0.0052Ω | Stator resistance |
| $L_d$ | 0.207mH | d-axis inductance |
| $L_q$ | 0.207mH | q-axis inductance |
| $\varphi_m$ | 0.3T | The flux of the magnet |
| P | 2 | Pole pairs of the generator |
| J | 0.156Kgm$^2$ | Moment of inertia |
| $\tau_f$ | 0.01sec | Filter time constant |
| $\omega_{n,speed}$ | 20Hz ($K_{p\omega}$=52.24, $K_{i\omega}$=2050) | Natural frequency of speed loop |
| $\omega_{n,current}$ | 200Hz ($K_{pi}$=0.514, $K_{iv}$=326.54) | Natural frequency of current loop |
| $\omega_n^*$ | 3000rpm | Rated speed reference |
| $T_L$ | 95Nm | Rated load torque |
| **PMSM-based EMA 5kW rated** | | |
| $R_s$ | 0.042Ω | Stator resistance |
| $L_d$ | 0.54mH | d-axis inductance |
| $L_q$ | 0.54mH | q-axis inductance |
| $\varphi_m$ | 0.4T | The flux of the magnet |
| P | 3 | Pole pairs of the generator |
| J | 0.05Kgm$^2$ | Moment of inertia |
| $\tau_f$ | 0.01sec | Filter time constant |
| $\omega_{n,speed}$ | 20Hz ($K_{p\omega}$=11.18, $K_{i\omega}$=1752) | Natural frequency of speed loop |
| $\omega_{n,current}$ | 200Hz ($K_{pi}$=2.18, $K_{iv}$=3407) | Natural frequency of current loop |
| $\omega_n^*$ | 900rpm | Rated speed reference |
| $T_L$ | 54Nm | Rated load torque |

Table 6-2 Rated power of equipment in the example EPS

| Equipment | Power rating |
|---|---|
| ATRU | 150kW |
| WIPS | 60kW |
| ECS | 30kW |
| EMA | 5kW |
| AC essential bus fed CRU | 10kW |
| HVAC2 bus fed resistance | 9kW |
| HVDC bus fed resistance | 5kW |

Table 6-3 Simulation scenarios of twin-generator aircraft EPS under normal operation conditions

| Time (s) | Events |
|---|---|
| 0.00 | Simulation starts. $S_{SG1}$ and $S_{SG2}$ closed; GCUs starts to regulate $v_{HVAC1}$ and $v_{HVAC2}$ to 230Vrms |
| 0.15 | Switches $S_{ATRU1}$ and $S_{ATRU2}$ are closed<br>DC loads on HVDC buses are connected |
| 0.20 | ESC1 and ECS2 start to accelerate to the rated speed (3000rpm) |
| 0.50 | Rated load torques applied to ECS1 and ECS2 (95Nm) |
| 0.70 | Rated WIPS applied (60kW) |
| 0.75 | WIPS changes from 60kW to 6kW |
| 0.80 | EMA1 and EMA2 start to accelerate to the rated speed (900rpm) |
| 0.90 | Rated load torque applied to EMA1 and EMA2 (54Nm) |
| 1.00 | SG1 and SG2 connected |
| 1.02 | $S_{HVB}$ opens; SG1 and SG2 disconnected |
| 1.20 | Simulation ends |

In this simulation study, the electrical frequency of SG1 is fixed at 400Hz and SG2 fixed at 405Hz. This asynchronism represents the real situation which the two generators are driven by different engine shafts. The HVAC bus voltages are controlled at 230Vrms. The speed reference and the load torque for the ECS and the EMA are set to be zero in the initial conditions. The event sequence of start-up of the twin-generator aircraft EPS is also shown in Table 6-3.

The simulation starts at t=0s. The GCU starts to regulate the HVAC bus phase voltage to 230Vrms. After the HVAC bus voltage reaches the steady state, the switches $S_{ATRU1}$ and $S_{ATRU2}$ are closed at t=0.15s. The SG1 starts to supply ATRU1 through HVAC1 bus. At the same time, the SG2 starts to supply ATRU2 through HVAC2 bus. At t=0.2s, the speed reference for two ECS drive system is set at 3000rpm and the rated load torque 95Nm applied to these ECS systems at t=0.5s. At t=0.7s, the de-icing system starts to run at rated power and the WIPS is set at 60kW. After 50ms second, the de-icing process finishes and the power requirement of WIPS is reduced to 6kW to maintain the temperature of the aircraft wings. The DC-link voltage reference of EMA is set to 800V at t=0.6s. The speed reference of the EMA is set to rated speed 900rpm at t=0.8s with rated load applied at t=0.9s. In order to demonstrate parallel operation of the two generators, $S_{HVB}$ is closed at t=1.0s. The two generators start to work in parallel for a short period, 20ms, then $S_{HVB}$ opens and the two generators work separately again.

Results from the ABC, DQ0 and DPABC models are compared in the following figures. The dynamic responses of HVDC bus voltages, $v_{HVDC1}$ and $v_{HVDC2}$ are shown in Figure 6-9. It can be seen that the voltage $v_{HVDC1}$ and $v_{HVDC2}$ from 18-pulse ATRUs have very small AC ripple. In most graphs, the traces from the three methods override each other. The initial values of $v_{HVDC1}$ and $v_{HVDC2}$ are set at zero. At t=0.15s, the HAVC bus voltages $v_{HVAC1}$ and $v_{HVAC2}$ are in steady state and controlled at 230Vrms as shown in Figure 6-12. The switches $S_{ATRU1}$ and $S_{ATRU2}$ are closed, $v_{HVDC1}$ and $v_{HVDC2}$ jump from 0V to around 800V. This is due to the inrush current charging the zero-initialized

capacitor. The inrush current can be seen in Figure 6-10 and Figure 6-11. This large inrush current must be avoided in the real system and a protection mechanism is required. Possible ways are either pre-charging the capacitor or using a current limiter. From t=0.2s, the ECS starts to speed up and draws power from the generator. A ramped voltage drop at HVDC bus can be noticed from this point. This is because the PMSM in the ECS draws a linearly increasing power from the generator as shown in Figure 6-10 and Figure 6-11. The linearly increasing AC currents result in a corresponding ramped voltage drop in the transmission lines and hence at the AC terminals of ATRUs. This results in a linear decrease of the DC voltages $v_{HVDC1}$ and $v_{HVDC2}$. When the rated loads of ECS1 and ECS2 are applied, a slight voltage drop can also be seen in $v_{HVDC1}$ and $v_{HVDC2}$. A voltage drop can also be noticed when the WIPS is applied to the system at t=0.7s. The reduction of the WIPS power requirement at t=0.75s results in an increase of $v_{HVDC1}$ and $v_{HVDC2}$. When SG1 and SG2 are connected, $v_{HVDC1}$ and $v_{HVDC2}$ drops due to the difference between $v_{HVAC1}$ and $v_{HVAC2}$. When the two generators disconnect at t=1.02s, the two subsystems return to the previous steady state before parallel operation. SG2 starts to supply the whole load system and the system comes to the steady state after a short transient period.

Again, it is important to notice that the parallel operation of AC generators here is to test the DP theory developed in Chapter 5. The parallel operation of AC generators in a real application is much more complex than just connecting the two generators using one switch. The active power and reactive load vectors have to be synchronised for effective load sharing. As can be seen, the direct connection of the two generators actually degrades the system power quality. The paralleling of AC generators feeding and controlling a DC bus is, however, a possible arrangement having future potential. In that case, several generators will supply and share the control of the main HVDC bus through bi-directional AC/DC converters. This has the advantage of enabling power management between generators and integrating energy storage in the system on a continual basis.

The $v_{HVDC1}$ and $v_{HVDC2}$ from three different modelling techniques are well-matched as shown in Figure 6-9.

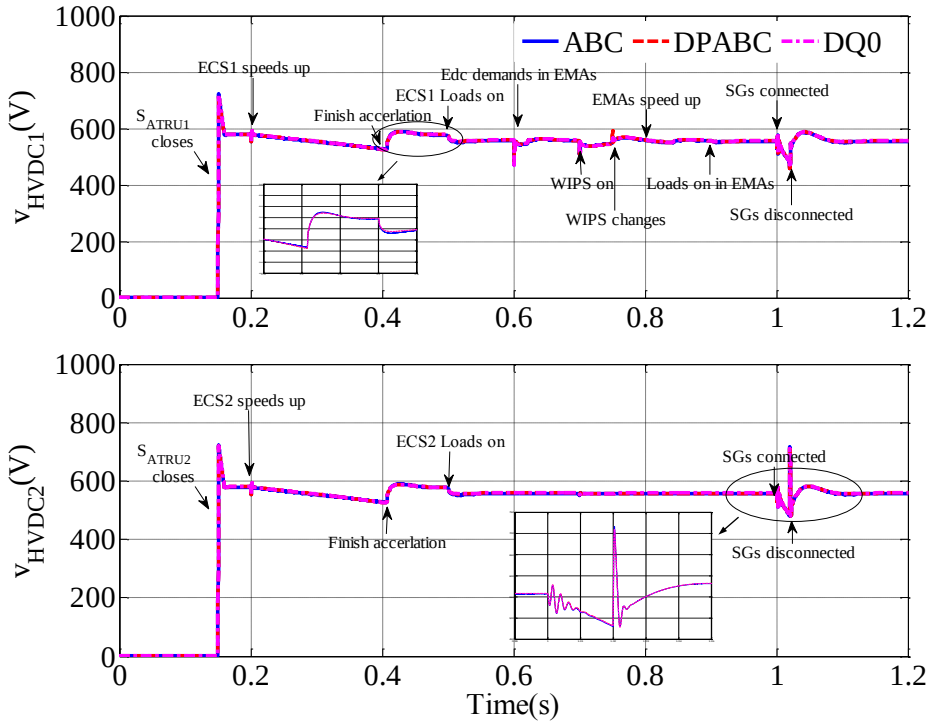


Figure 6-9 The dynamic response of $v_{HVDC1}$ and $v_{HVDC2}$. Above: response of $v_{HVDC1}$; below: response of $v_{HVDC2}$

Since the system is assumed to be balanced, the currents flowing into the ATRUs $i_{ATRU1}$ and $i_{ATRU2}$ are represented by the phase A current only. For comparison studies, the variables in the DQ0 and DP models are transformed to the time domain in the ABC frame as shown in Figure 6-10 and Figure 6-11. The magnitude of DPs is also shown in these two figures. The currents $i_{ATRU1}$ and $i_{ATRU2}$ remain at zero until the load is connected to the HVDC buses. The acceleration of PMSMs in the ECS increases the current $i_{ATRU1}$ and $i_{ATRU2}$ from t=0.2s. The application of rated ECS load causes steps of $i_{ATRU1}$ and $i_{ATRU2}$. Again, it can be seen that the results from ABC, DQ0 and DPABC models are well matched during the whole simulation process. The use of an 18-pulse ATRU makes the harmonics on the AC current very small as shown in the zoomed area in Figure 6-10. The magnitude of DPs $\langle i_{ATRU1} \rangle_1$ and $\langle i_{ATRU2} \rangle_1$ are also shown in Figure 6-10 and Figure 6-11. From these two figures, it can be

seen that the magnitudes of $\langle i_{ATRU1} \rangle_1$ and $\langle i_{ATRU2} \rangle_1$ give the envelope of the sinusoidal quantities from the DPABC and DQ0 models.

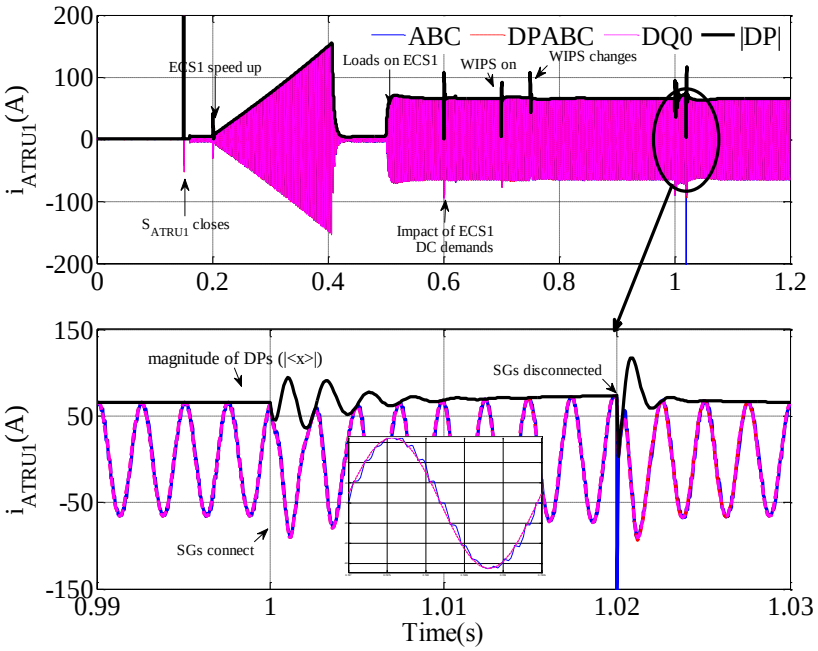


Figure 6-10 The dynamic response of $i_{HVAC1}$, phase A current flowing into ATRU1. Above: $i_{HVAC1}$; below: zoom-in area of $i_{HVAC1}$

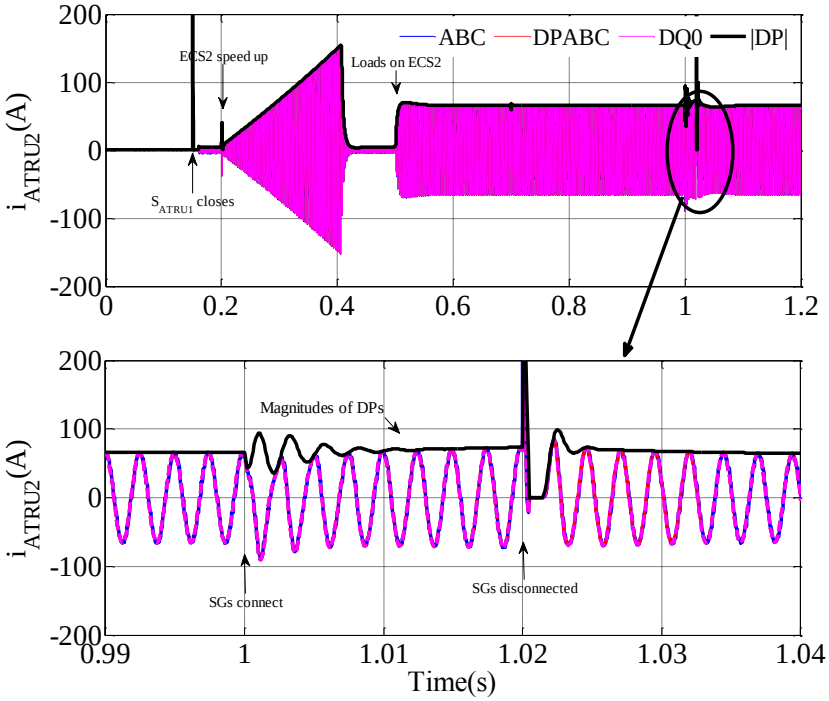


Figure 6-11 The dynamic response of $i_{HVAC2}$, phase A current flowing into ATRU2 Above: $i_{HVAC2}$; below: zoom-in area of $i_{HVAC2}$

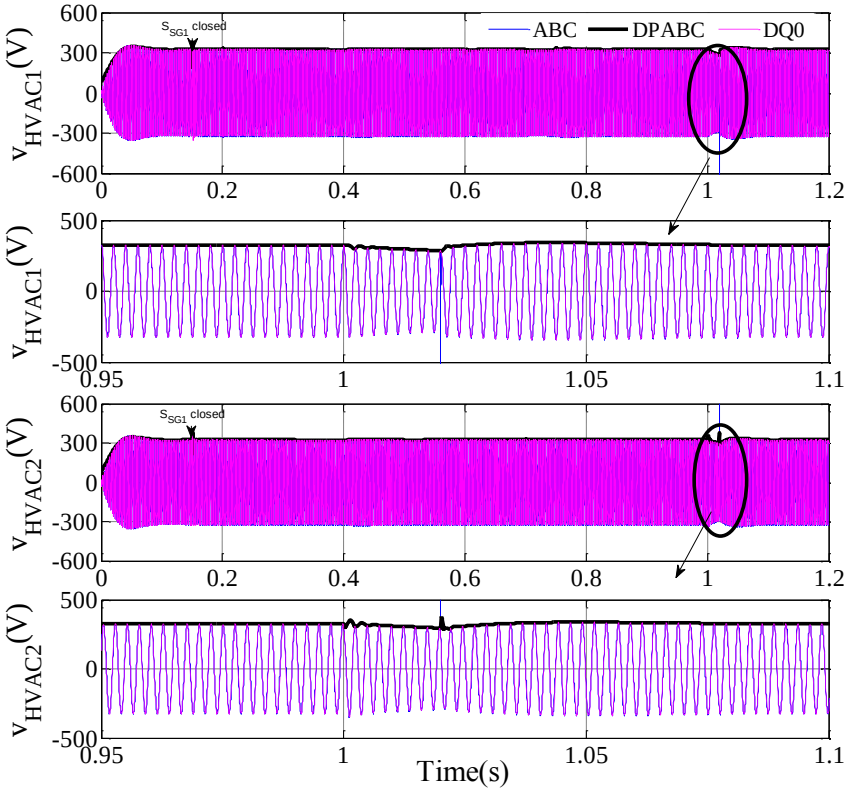


Figure 6-12 Phase A voltage of HVAC buses, (a) $v_{HAVC1}$ phase A of HVAC1 bus; (b) zoomed area of $v_{HAVC1}$; (c) $v_{HAVC2}$ phase A of HVAC2 bus; (d) zoomed $v_{HAVC2}$

The simulation results of HVAC bus voltages $v_{HVAC1}$, $v_{HVAC2}$ from ABC, DQ0 and DPABC models are shown in Figure 6-12. The results from DQ0 and DPABC models are transformed into the time-domain ABC frame for comparison studies. The zoomed-in area shows a good agreement of results during the generator parallel period. The magnitudes of the DPs $\langle v_{HVAC1} \rangle_1$ and $\langle v_{HVAC2} \rangle_1$ are shown in the figure. The magnitudes of DPs show the envelope of results in the ABC frame.

The speed of PMSMs of ECS1, ECS2, EMA1 and EMA2 is shown in Figure 6-13. The PMSMs are well controlled by their speed controllers and once more agreement between the three modelling techniques is good.

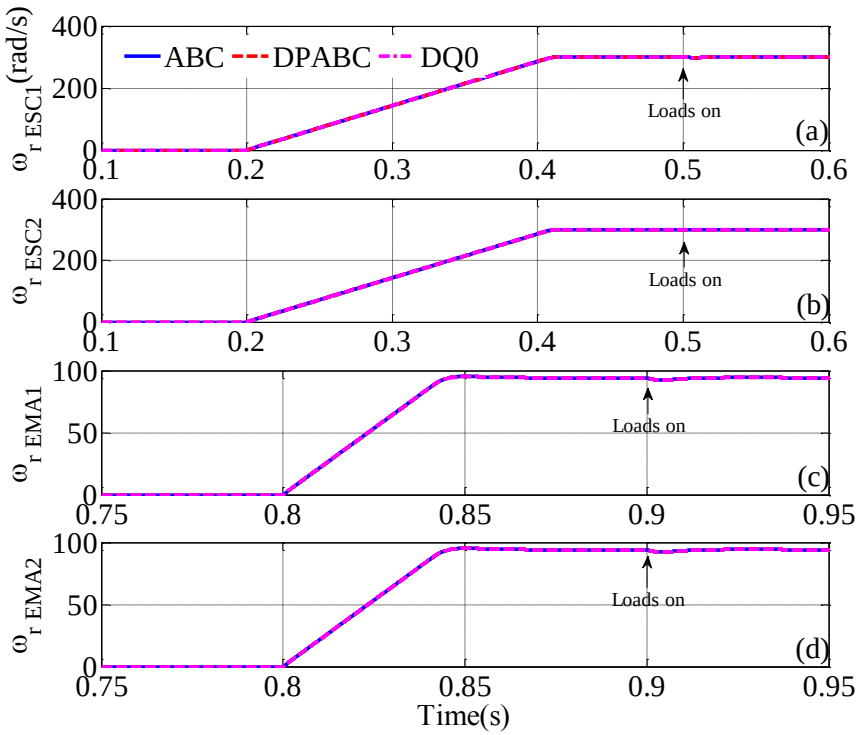


Figure 6-13 Dynamic response of drive loads, (a) $\omega_{r\_ECS1}$ speed of PMSM of ECS1; (b) $\omega_{r\_ECS2}$ speed of PMSM of ECS2; (c) $\omega_{r\_EMA1}$ speed of PMSM of EMA1; (d) $\omega_{r\_EMA2}$ speed of PMSM of EMA2

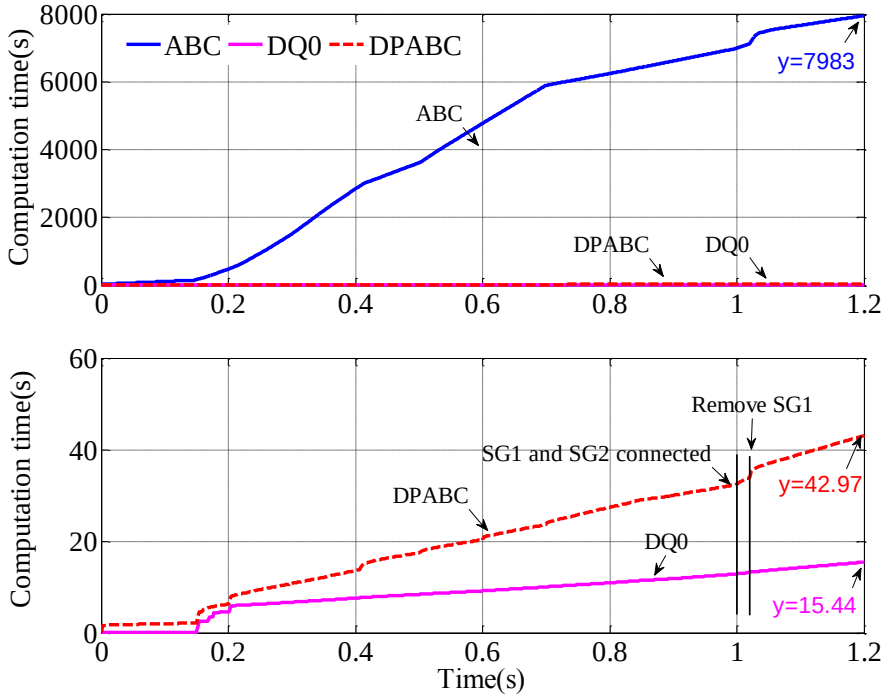


Figure 6-14 Comparison of the computation time between three different models

Table 6-4 Comparison of the computation time between three different models

| Model | ABC | DQ0 | DP |
|---|---|---|---|
| Simulation time (s) | 7983.00 | 15.44 | 42.97 |
| Acceleration | **1** | **517** | **185** |

The computation time consumed by the three models is compared in Figure 6-14 and in Table 6-4. It can be seen that the DQ0 is 517 times faster than the ABC model. The DPABC model is 185 times faster than the ABC model. The simulation time of ABC model is counted in hours compared with that of the DQ0 and DPABC model in seconds. The DQ0 model is about three times faster than the DPABC model. This is due to the complexity and the order of the DPABC model being higher than that of the DQ0 model.

### 6.4.2 Fault Condition Studies with SG1 Loss

This section will discuss one possible scenario in which the electrical power on the HVAC1 bus is interrupted due to the loss of SG1, and the subsequent power recovery of the HVAC1 bus after reconfiguration of the aircraft EPS.

Table 6-5 Simulation scenarios of twin-generator aircraft EPS under abnormal operation conditions

| Time (s) | Events |
|---|---|
| 0.00 | Simulation starts; EPS starts up |
| ... | Same as session 6.4.1 |
| **1.00** | **SG1 loss, $S_{SG1}$ open** |
| **1.01** | **$S_{HVB}$ closes and SG2 starts to supply the whole system** |
| 1.20 | Simulation ends |

In order to study the impact of the loss of SG1 on the power system behaviour under the worst-case scenario, it is assumed that all ECS's and EMAs are operated under full power conditions before the fault occurs. The event sequence is shown in Table 6-5. The system goes through the same events as those in Section 6.4.1 until t=1.0s. Prior to the loss of SG1 at t=1.0s, the system events keep the same as those in the previous session. Once SG1 is lost due to an internal fault associated with the generator itself, the switches ($S_{SG1}$ and $S_{HVB}$) will act to allow the transfer of power delivery from SG1 to SG2. All electrical loads originally supplied by SG1 will be powered by SG2 to ensure non-interrupted power of the EPS. Since automatic fault sensing is not yet implemented in the model, the switches are pre-programmed to change their states according to the prescribed scenario. Prior to losing SG1, the $S_{SG1}$ and $S_{SG2}$ are closed and $S_{HVB}$ is open. In order to mimic the fault scenario regarding the loss of the SG1 at t=1.0s, the switch $S_{SG1}$ is open at t=1.0s. The switch $S_{HVB}$ is closed after 10ms (around four cycles of the fundamental frequency).

The HVDC bus voltages are shown in Figure 6-15. The HVAC bus voltages are shown in Figure 6-16 and the input currents of ATRUs are shown in Figure 6-17. The current flowing into EMA1 and the currents of SG1 and SG2 are shown in Figure 6-18. The DC-link currents feeding inverters of ECS's and EMA1 are shown in Figure 6-19. The rotor speeds of EMAs and ECS's are shown in Figure 6-20. There is a very small discrepancy (note scales) between the DQ0/DPABC models and the ABC model.

The loss of SG1 results in a decrease of HVDC1 bus voltage, $v_{HVDC1}$. This is due to the fact that after the SG1 loss, there is no power supply to the HVDC1 bus; however, the ECS1 is still drawing power from it. In Figure 6-19, the positive current $i_{dc,ECS1}$ represents the power delivered from the DC link to the PMSM. The decrease of $v_{HVDC1}$ also results in a short period of an increase of current $i_{dc,ECS1}$. This is because the ECS1 behaves as constant power load and more current is required with a reduced DC-link voltage. After the loss of SG1, the current flowing into the HVDC1 bus $i_{ATRU1}$ and the current flowing out of SG1 $i_{SG1}$ drops to 0A. This implies the power interruption of the power supply

from SG1 and the power to the HVDC1 bus. After reconfiguration of the EPS at t=1.01s, the HVDC1 bus starts to gain power from SG2 and $v_{HVDC1}$ recovers to around 540V after 40ms. An inrush current flowing into ATRU1 can be identified in $i_{ATRU1}$ as shown Figure 6-17 when the SG2 starts to supply subsystem1 at t=1.01s. This inrush current is due to the $v_{HVDC1}$ reducing to around 300V and is much lower than its rated voltage 540V. The reconfiguration of the system results in the increase of $i_{ATRU1}$ charging the DC-link capacitor and an increased $i_{SG2}$, as shown Figure 6-18. This increased current $i_{SG2}$ results in an increase of voltage drop in the transmission lines and thus a decrease of $v_{ATRU2}$, as shown in Figure 6-15. The current $i_{dc,ECS2}$, in turn, increases with a reduced $v_{ATRU2}$ as shown in Figure 6-19. After a short transient period, both $v_{HVDC1}$ and $v_{HVDC2}$ settle at around 540V.

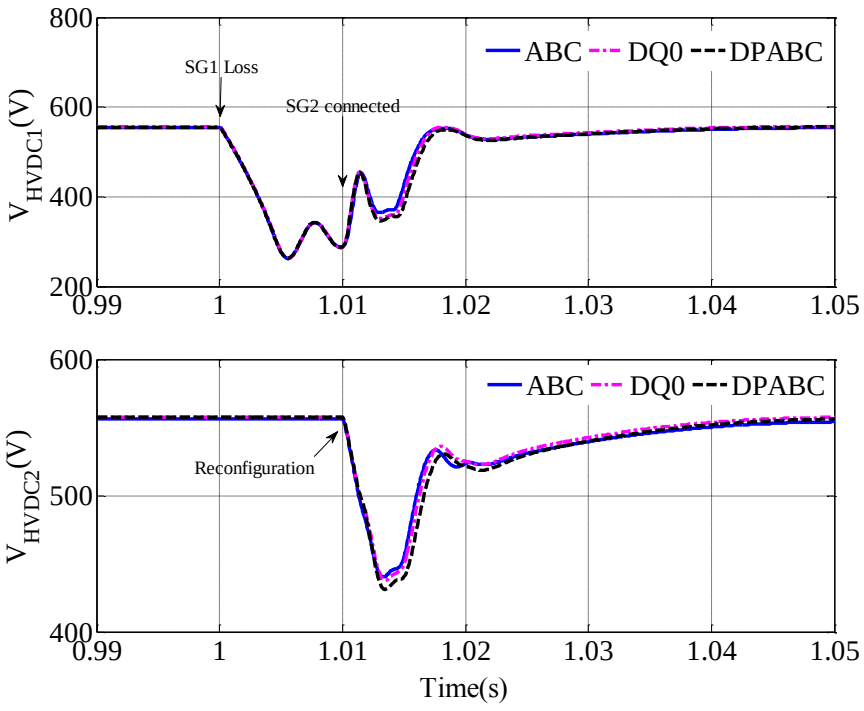


Figure 6-15 The dynamic response of HVDC bus voltages, $v_{HVDC1}$ and $v_{HVDC2}$, with SG1 loss at t=1.0s

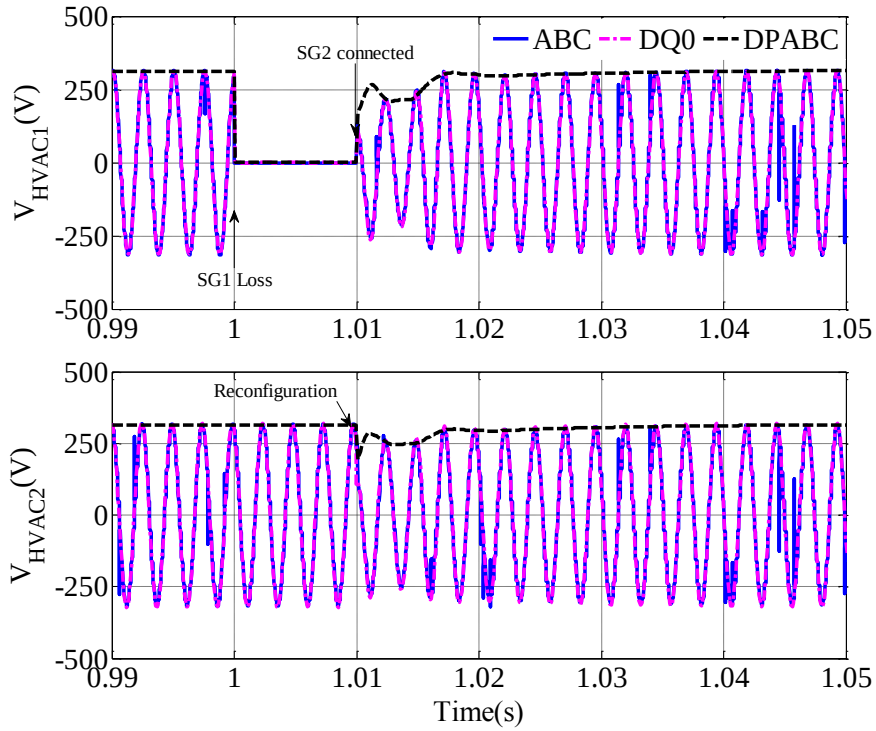


Figure 6-16 The dynamic response of ATRU terminal voltages, $v_{HVAC1}$ and $v_{HVAC2}$, with SG1 loss at t=1.0s

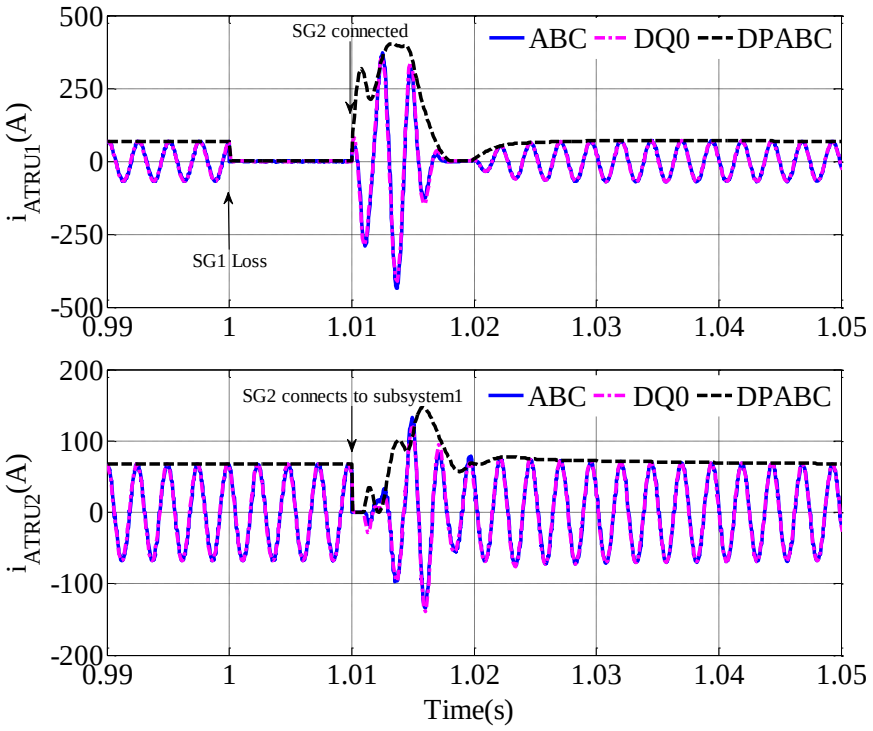


Figure 6-17 The dynamic response of currents flowing into ATRUs, $i_{HVAC1}$ and $i_{HVAC2}$, with SG1 loss at t=1.0s

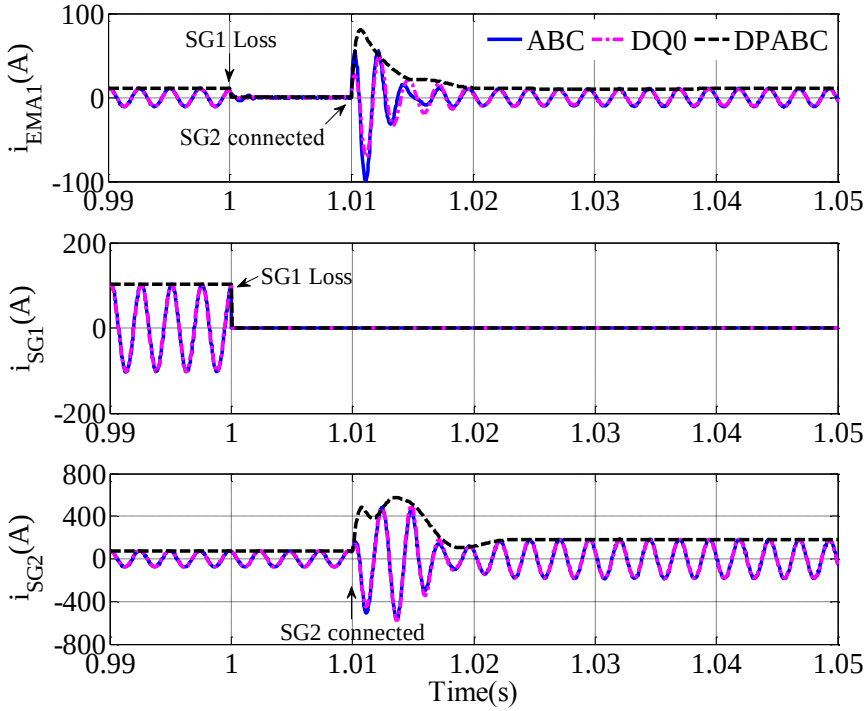


Figure 6-18 The dynamic response of currents with SG1 loss at t=1.0s: $i_{EMA1}$ is the current flowing into the CRU; $i_{SG1}$ and $i_{SG2}$ are the SG currents

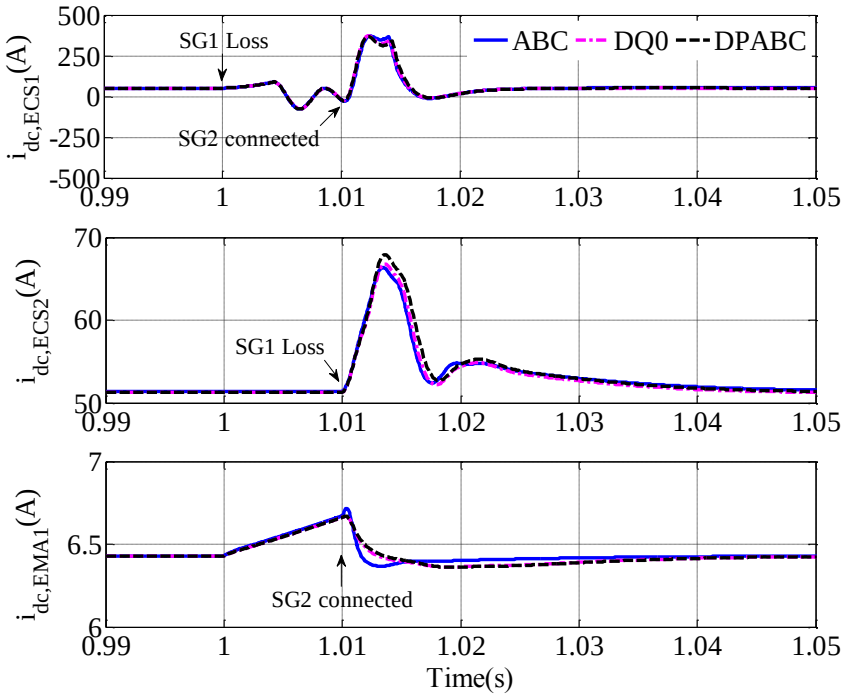


Figure 6-19 The dynamic response of dc-link currents with SG1 loss at t=1.0s: $i_{dc,ECS1}$ and $i_{dc,ECS2}$ are the current flowing into the ECS1 and ECS2; $i_{dc,EMA1}$ is the current flowing into CIU of EMA1

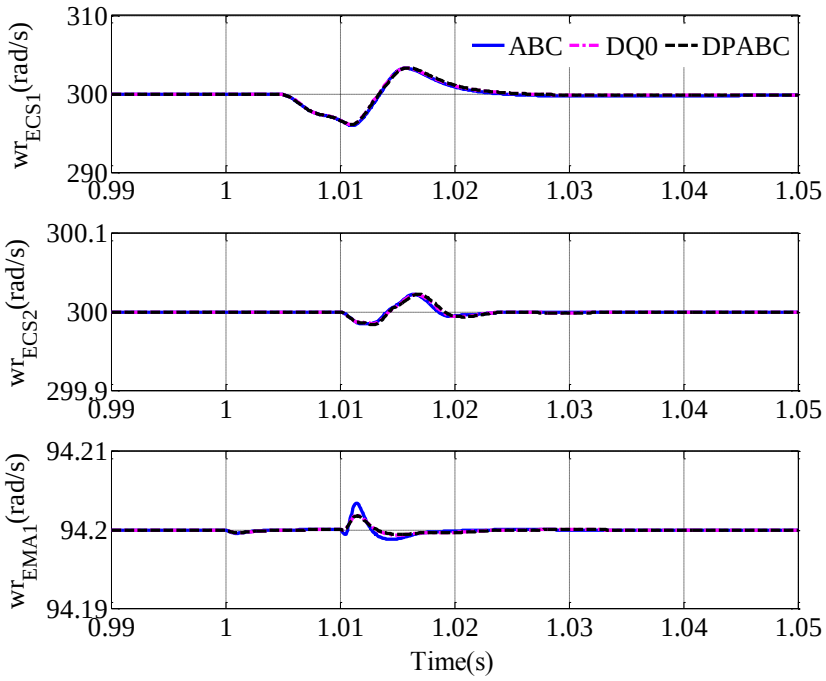


Figure 6-20 The dynamic response of drive speeds with SG1 loss at t=1.0s: $\omega_{rECS1}$ is the speed of ECS1; $\omega_{rECS2}$ is the speed of ECS2; $\omega_{rEMA1}$ is the speed of EMA1

Figure 6-20 shows the PMSM speed in ECS1, ECS2 and EMA1 from different modelling techniques. The speed of ECS1 stays at 300 rad/s until the HVDC1 bus voltage $v_{HVDC1}$ is lower than the PMSM terminal line-to-line voltage. From that point, the power cannot be transferred from the converter to the PMSM and the speed of rotor in ECS1 starts to decrease. The reconfiguration of the system allows ECS1 to recover to the normal condition and the speed returns to 300 rad/s in less than 30ms. The power loss of SG1 has very little impact on ECS2 and EMA1. As shown in Figure 6-20, the speed ripple is less than 0.1% of the rated speed.

The computation time of three different models is shown in Table 6-6. As can be seen, both the DQ0 model and the DPABC model are more than two hundred times faster than the ABC model in this case. This is because the dc-like variables in these two models allow larger simulation steps. Specifically, the DQ0 model is the fastest model and is 251 times faster than the ABC model. The DPABC model, which is 209 times faster than the ABC model, is slightly

slower than the DQ0 model. This is due to the higher order of the DPABC model.

Table 6-6 Comparison of the computation time between three different models

| Model | ABC | DQ0 | DP |
|---|---|---|---|
| Simulation time (s) | 8693.76 | 34.54 | 41.57 |
| Acceleration | **1** | **251** | **209** |

### 6.4.3 Line-to-Line Fault Conditions

The twin-generator aircraft power system is redrawn in Figure 6-21 for convenience.

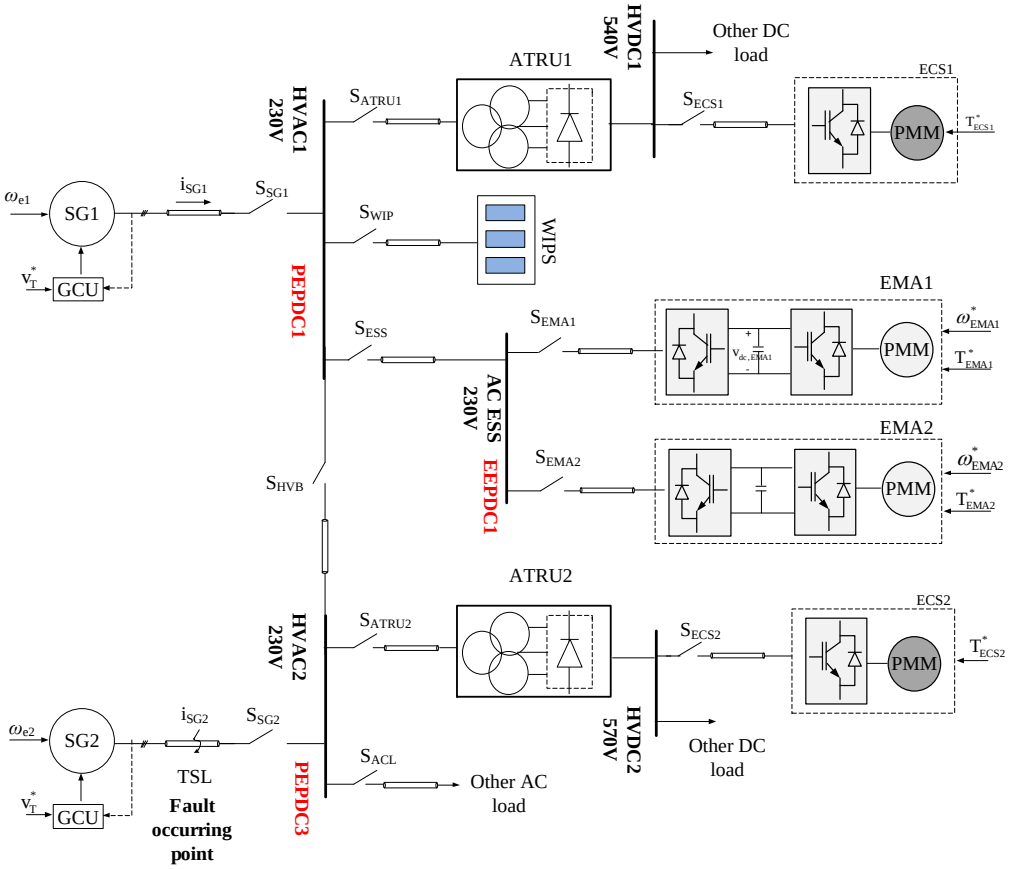


Figure 6-21 The EPS of the twin-generator aircraft with line-to-line fault occurring at t=1.2s

In the previous section, the generator SG2 takes over the entire electrical loads, including the loads originally driven by SG1, after the power loss of SG1 and system reconfiguration. In such a case, the system is still under balanced conditions. It is of interest to study the behaviour of such an EPS under unbalanced line fault conditions. In this section, the system behaviour under line-to-line fault conditions will be studied. The line-to-line fault is imposed between the phase A and the phase B at the transmission line connecting the SG2 and the HVAC1 bus. This is the worst fault scenario. Since the fault happens at the main AC supplying cables and all the elements in the EPS will be fed by severely distorted power. The fault is implemented by using a 0.1mΩ resistor across the phases.

The simulation scenario is shown in Table 6-7. The system goes through a series of events the same in Section 6.4.2 prior to the line-to-line fault occurred at t=1.2s. Before the fault occurs, the SG2 is supplying power for the entire EPS.

Table 6-7 Simulation scenarios of twin-generator aircraft EPS under abnormal operation conditions

| Time (s) | Events |
|---|---|
| 0.00 | Simulation starts; EPS starts up |
| .... | Same as in Section 6.4.2 |
| **1.20** | **A line-to-line fault occurs between the SG2 and the HVDC2 bus** |
| 1.30 | Simulation ends |

Figure 6-22 shows the transient response of the three-phase terminal voltages of SG2, $v_{SG2}$. All the results from three different modelling methods are transformed to the time-domain ABC frame for comparison studies. It can be seen that the voltage of phase A and phase B are identical after the line-to-line fault occurs. It can also identify that the harmonics appearing in $v_{SG2}$ is due to the line-to-line fault. Figure 6-23 shows the dc-link voltages of ATRU1,

ATRU2 and EMA1. After the fault occurs, $v_{HVDC1}$ and $v_{HVDC2}$ reduce to a new steady state. The current $i_{dc,ECS1}$ and $i_{dc,ECS2}$ increase to new steady values correspondingly, as shown in Figure 6-24. A short period transient of the DC-link voltage $v_{EMA1}$ can be noticed after the fault occurs. The CRU can still regulate $v_{EMA1}$ to 800V; however, some small ripples can be identified under fault conditions. The three-phase currents flowing into ATRUs are shown in Figure 6-25 and Figure 6-26. Before the fault occurs, these currents are balanced. However, after the fault occurs, harmonics start to appear in the system. As can be seen, results from three modelling techniques are well matched before and after the fault occurs. The current flowing into EMA1 $i_{EMA1}$ is shown in Figure 6-27. Some discrepancies can be noticed between the DPABC model and the other two models. This is mainly due to the error of the approximation of the distorted voltage vector angle and its nonlinear sinusoidal function values in the DP model of the CRU. The discrepancy of $i_{EMA1}$ also results in the error of $v_{dc,EMA}$ in the DP model as shown in Figure 6-23. However, considering the line-to-line fault is the worst scenario for the EPS conditions, the accuracy of the DPABC model is still tolerable.

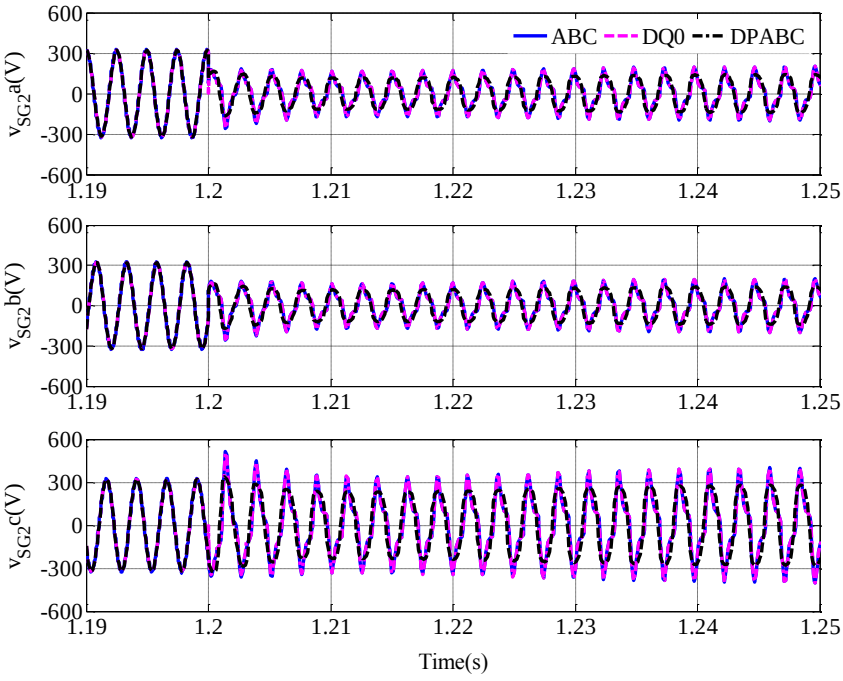


Figure 6-22 The dynamic response of SG2 terminal voltages with a line-to-line fault occurring at t=1.2s

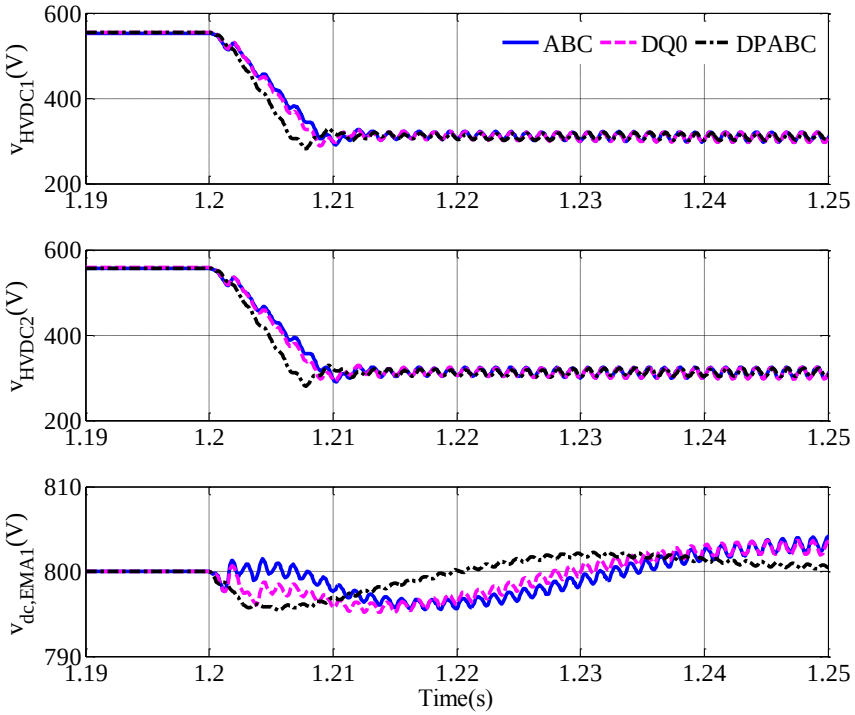


Figure 6-23 The dynamic response of HVDC bus voltages, $v_{HVDC1}$ and $v_{HVDC2}$, with Line-to-line fault occurring at t=1.2s.

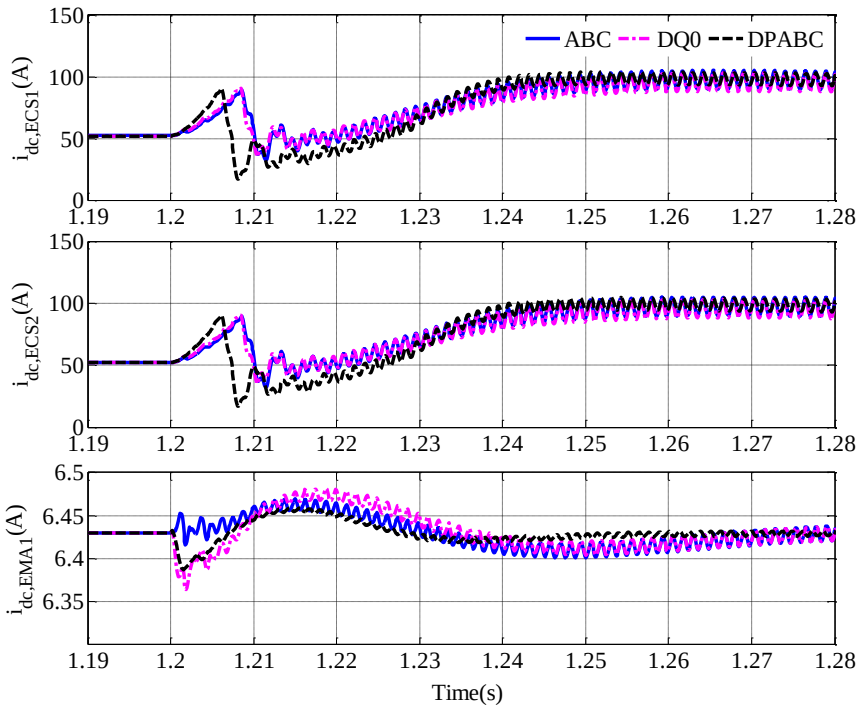


Figure 6-24 The dynamic response of dc-link currents with line-to-line fault occurring at t=1.2s: $i_{dc,ECS1}$ and $i_{dc,ECS2}$ are the current flowing into the ECS1 and ECS2; $i_{dc,EMA1}$ is the current flowing into CIU of EMA1

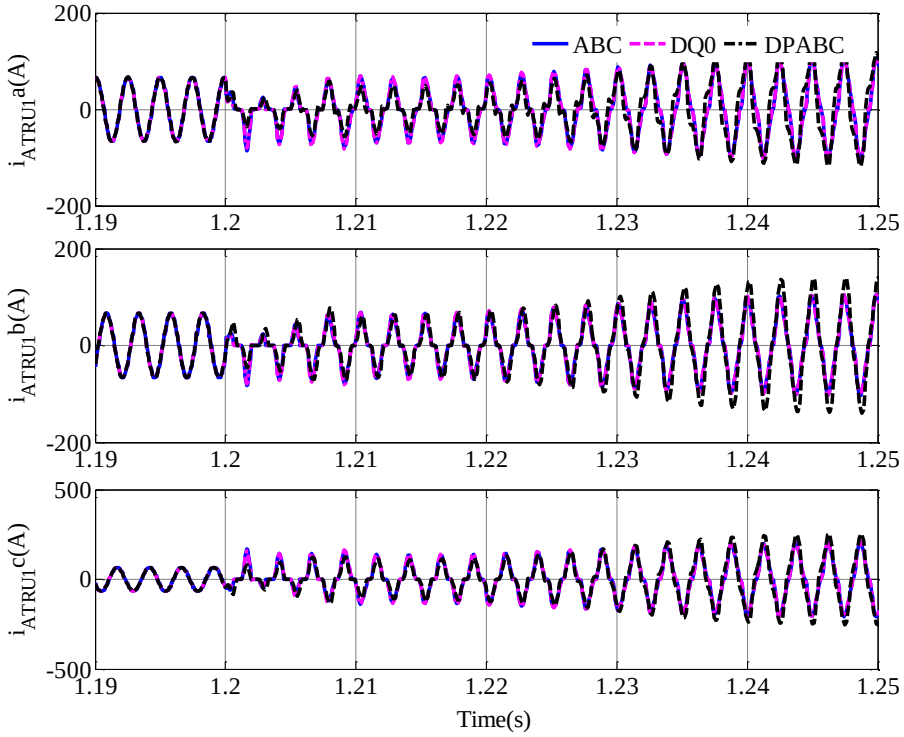


Figure 6-25 The dynamic response of currents flowing into the ATRU1 with a line-to-line fault occurring at t=1.2s

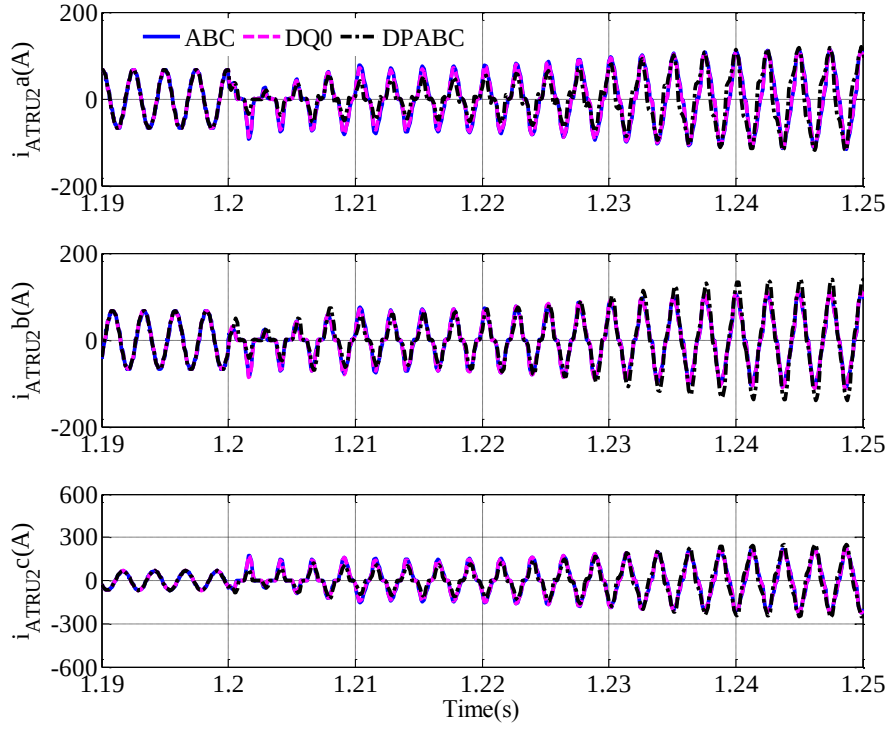


Figure 6-26 The dynamic response of currents flowing into the ATRU2 with a line-to-line fault occurring at t=1.2s

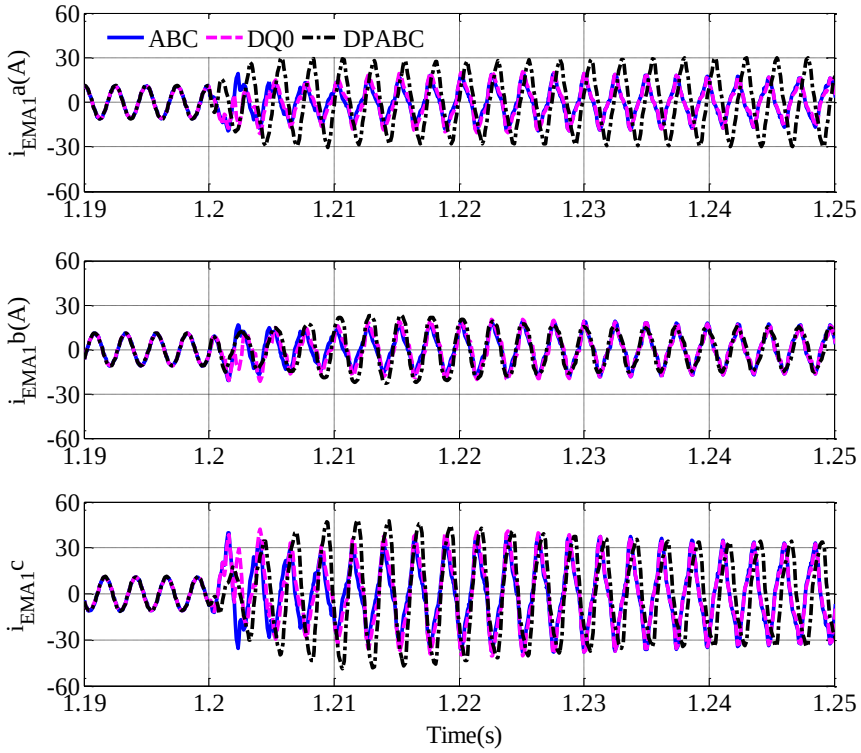


Figure 6-27 The dynamic response of currents flowing into EMA1, $i_{EMA1}$, with a line-to-line fault occurring at t=1.2s

The computation time of three different models is shown in Table 6-8. During fault conditions, the efficiency of the DQ0 model decreases dramatically. It is only 2.66 times faster than the ABC model. On the other hand, the DP model can still run very fast with good accuracy. The DPABC model in this case is 40 times faster than the DQ0 model.

Table 6-8 Comparison of the computation time between three different models (for 0.1s fault conditions only)

| Model | ABC | DQ0 | DPABC |
|---|---|---|---|
| Simulation time (s) | 724.5 | 272.6 | 8.066 |
| Acceleration | **1** | **2.66** | **89.7** |

## 6.5 Chapter Summary

This chapter aims at demonstrating the application of the DP concept in modelling a large-scale EPS including generators, PECs and motor drives etc. A twin-generator EPS under the MOET aircraft power system architecture is studied. The main contribution of this chapter is to demonstrate the performance of the DP models under both balanced and unbalanced conditions. In this chapter, the EPS is simulated under normal operation conditions, abnormal conditions with SG1 loss and line-to-line fault conditions. The comparison between three different modelling techniques, ABC, DQ0 and DPABC models, has been studied. Under balanced conditions, the DQ0 model is the most efficient model. However, under line-to-line fault conditions, the DPABC model is much faster than the DQ0 model with acceptable errors. This merit gives the DP model great potential in studying a large-scale EPS such as the EPS in the aircraft, ships, vehicles etc. The DP library developed in this thesis allows simulations with different architectures since the EPS element are independently developed and can be reused conveniently.

# Chapter 7

# Conclusion

## 7.1 Summary

The More-electric aircraft (MEA) has been identified as a future trend for commercial aircraft. Many functions that used to be driven by pneumatic, mechanical and hydraulic power will be replaced with electrical power subsystems. As a result, a large number of new electrical loads will appear in aircraft, for example the ECS, EHAs and EMAs for the flight control and the wing anti-icing systems. The increase of the electrical power on board the MEA will push the evolution of electrical power system architecture at the same time. The development and finalization of future EPS's will require extensive simulation studies, under both normal and abnormal conditions, to assess overall system performance, the impact of the line faults on the system, and system stability and availability issues. Since a large number of power electronic converters will be used in the future aircraft EPS, simulations based on the switching power converter models will result in large and perhaps impractical computation time as well as showing some convergence problems. The average model in the DQ frame (DQ0 models) is a very effective way to model the EPS under balanced conditions. However, the performance of DQ0 models decreased severely when the EPS is subject to an AC fault or unbalanced condition. This research aims to solve the problem.

In this research, the DP concept is extended to modelling time-varying frequency systems as well as multi-generator multi-frequency systems. The DP

technique is applied to model the aircraft EPS for the first time. In the DP model, the DC, fundamental and higher harmonic components all become dc-like variables under steady-state conditions. This merit of DP enables bigger time steps during simulations under both balanced and unbalanced conditions.

In this thesis, the DP concept has been discussed with different phasors being introduced in Chapter 2. The practical way of using DP modelling in the time-varying frequency system has been discussed and revealed for the first time. The move from a constant frequency (CF) system to a variable frequency (VF) system has been identified as the future trend. The theory developed in Chapter 2 allows the DP concept to model VF EPS in the future aircraft.

In Chapter 3**,** the DP model of uncontrolled rectifiers has been developed. Together with the Taylor expansion and the vector theory, the developed DP model conveniently embraces higher harmonics ($2^{nd}$ and $6^{th}$ order) for the three-phase diode bridge. The developed model demonstrates good performance under both balanced and unbalanced conditions. Based on that model, the DP model for multi-pulse rectifier units has been derived and an 18-pulse ATRU is used to demonstrate the DP modelling procedure. The transformer rectifier unit is currently and probably remains an essential element in aircraft EPS feeding the main DC bus. The developed DP model is able to model the aircraft EPS which uses the TRU feeding the HVDC bus.

In Chapter 4, the DP concept has been extended to modelling of the controlled PWM rectifier. It is the first time the PWM converter as well as its controller has been modelled in DPs. This type of rectifiers will be widely used in the future aircraft due to its bi-directional power flow capability and flexibility. For example in the aircraft with DC distribution systems, the PWM converter will be used to transform the VF AC power to the DC power. The DP model of this converter is an essential part in DP modelling of EPS for future aircraft.

In Chapter 5, the DP technique has been used in modelling a multi-generator system. The DP theory is for the first time extended to multi-generator and

multi-frequency system. The developed theory allows the study of multi-generator parallel operations. The parallel operation will be potentially used in aircraft with DC distribution systems in which multiple generators or power sources may supply a common HVDC bus at the same time.

In Chapter 6, a twin-generator aircraft EPS under MOET architecture has been studied. It mainly aims to demonstrate the application of the DP library as the result of this research. Simulation comparison between the ABC, DQ0 and DP models demonstrates the accuracy and efficiency of the DP model under both balanced and unbalanced conditions.

## 7.2 Future work

The possible future work that can be developed from this research is listed below：

- Further development of DP models could cover higher harmonics. In this thesis, only the fundamental component is considered in the DP model. The higher harmonics, which cause substantial power losses in the system, is of great interest for power system studies and can be covered in s future DP model library. The DP representation entails assigning DP variables to each (dominant) harmonics. Each of the DP variables will be dc-like in steady state. Therefore such a DC model is able to model multi-frequency transient behaviour very effectively. Since the switching functions are dependent on the topology and control of the converters, different topologies of converters may result different DP models. The DP model with higher harmonics will allow the calculation of power losses in the system level and thus optimise the system during the design period. The optimized control structure for active rectifiers based on DP models is also of great interest.

- The DP model for different types of machines also needs to be further developed in the library, including the permanent magnet machine and the switched reluctance machine. The saturation of machines can also be considered in the DP models. In this thesis, the main generator is considered to be a controlled wound-field synchronous generator. The permanent magnet machine, which has high torque and high power density, will be widely used as a starter/generator in future aircraft. The development of high speed induction machine also makes this type of machine a candidate for starter/generator applications.

- The optimised control structure design for active filters based on DP models is also of great interest. The DP model is fundamentally a frequency domain model and different harmonics are separated in these models. This enables non-linear control theories to be implemented in the system. The main function of the active filter is to dissipate the harmonics introduced by the distorting load and provide clean line currents. Since the energy in different harmonics can be conveniently calculated in DP models, the passivity based control can be implemented in the active filter with desired harmonics being dissipated.

## 7.3 Publications

The research work given in this thesis has resulted in the following conference papers:

[1] S. Bozhko, T. Yang, and G. Asher, "Application of Dynamic Phasors for Modeling of Active Front-end Converter for More-Electric Aircraft," presented at the Aerospace Electronics and Avionics systems Conference, Pheonix, AZ, 2012.

[2] S. V. Bozhko, T. Wu, T. Yang, and G. M. Asher, "More-electric aircraft electrical power system accelerated functional modeling," in

Power Electronics and Motion Control Conference (EPE/PEMC), 2010 14th International, 2010, pp. T9-7-T9-14.

[3] T. Yang, S. Bozhko, and G. Asher, "Assessment of dynamic phasors modelling technique for accelerated electric power system simulations," in Power Electronics and Applications (EPE 2011), Proceedings of the 2011-14th European Conference on, 2011, pp. 1-9.

[4] T. Yang, S. Bozhko, and G. Asher, "Modeling of active front-end rectifiers using dynamic phasors," in Industrial Electronics (ISIE), 2012 IEEE International Symposium on, 2012, pp. 387-392.

[5] T. Yang, S. Bozhko, and G. Asher, "Modeling of An 18-pulse Autotransformer Rectifier Unit with Dynamic Phasors," SAE 2012, 2012.

[6] T. Yang, S. Bozhko, and G. Asher, "Dynamic phasor modeling of autotransformer rectifier units for more-electric aircraft," in Power Electronics and Motion Control Conference (IPEMC), 2012 7th International, 2012, pp. 1566-1572.

[7] T. Yang, S. V. Bozhko, and G. M. Asher, "Modeling of uncontrolled rectifiers using dynamic phasors," in Electrical Systems for Aircraft, Railway and Ship Propulsion (ESARS), 2012, 2012, pp. 1-6.

[8] T. Yang, S. V. Bozhko, and G. M. Asher, "Fast functional modelling for 18-pulse autotransformer rectifier units in more-electric aircraft," in Power Electronics, Machines and Drives (PEMD 2012), 6th IET International Conference on, 2012, pp. 1-6.

[9] T. Yang, S. V. Bozhko, and G. M. Asher, "Multi-Generator System Modelling Based on Dynamic Phasor Concept", EPE 2013, accepted.

[10] T. Yang, S. V. Bozhko, and G. M. Asher, "Application of Dynamic Phasor Concept in Modeling Aircraft Electrical Power systems", SAE AeroTech 2013, accepted.

Currently, there are several journal papers are in draft now.

[1] T. Yang, S. V. Bozhko, and G. M. Asher, "Analysis of Controlled Rectifiers Using the Dynamic phasor Approach "

[2] T. Yang, S. V. Bozhko, and G. M. Asher, " Modelling of Uncontrolled Rectifiers Using the Dynamic phasor Approach "

[3] T. Yang, S. V. Bozhko, and G. M. Asher, "Analysis of Electrical Power Systems Using the Dynamic phasor Approach"

# APPENDIX I

For a time-varying frequency signal with $\omega = \omega(t)$, The phase-based DP is written as:

$$\langle x \rangle_k = \frac{1}{2\pi} \int_{\theta-2\pi}^{\theta} x(t(\theta)) e^{-jk\theta} d\theta \qquad k = 0,1,2,... \tag{A1- 1}$$

The time interval T(t) define as follows:

$$\theta_1 = \theta(t_1) \tag{A1- 2}$$

$$\theta_1 - 2\pi = \theta\{t_1 - T(t)\} \tag{A1- 3}$$

With the definition (A1-1), the phase-based DP of the derivative dx/dt becomes:

$$\begin{aligned} \left\langle \frac{dx}{dt} \right\rangle_k &= \frac{1}{2\pi} \int_{t-T(t)}^{t} \left( \frac{dx}{dt} \right) e^{-jk\theta(t)} \omega(t) dt = \frac{1}{2\pi} \int_{t-T(t)}^{t} e^{-jk\theta(t)} \omega(t) dx \\ &= \frac{1}{2\pi} x e^{-jk\theta(t)} \omega(t) \Big|_{t-T(t)}^{t} - \frac{1}{2\pi} \int_{t-T(t)}^{t} x d\left\{ e^{-jk\theta(t)} \omega(t) \right\} \end{aligned} \tag{A1-4}$$

The integration operation in the second term of (A1-4) can be expanded as:

$$\begin{aligned} \int_{t-T(t)}^{t} x d\left[ e^{-jk\theta(t)} \omega(t) \right] &= \int_{t-T(t)}^{t} x e^{-jk\theta(t)} \dot{\omega}(t) dt + \int_{t-T(t)}^{t} x \omega(t) e^{-jk\theta(t)} \{ -jk\omega(t) \} dt \\ &= \int_{t-T(t)}^{t} x e^{-jk\theta(t)} \omega(t) \left\{ \frac{\dot{\omega}(t)}{\omega(t)} - jk\omega(t) \right\} dt \end{aligned} \tag{A1-5}$$

Substituting (A1-5) to (A1-4) yields:

$$\left\langle \frac{dx}{dt} \right\rangle_k = \frac{1}{2\pi} \left\{ x e^{-jk\theta(t)} \omega(t) \Big|_{t-T(t)}^{t} - \int_{t-T(t)}^{t} x e^{-jk\theta(t)} \omega(t) \left\{ \frac{\dot{\omega}(t)}{\omega(t)} - jk\omega(t) \right\} dt \right\} \tag{A1-6}$$

In the meantime, the differential of the DP $\langle x \rangle_k$ is written as:

$$\frac{d\langle x\rangle_k}{dt} = \frac{d\frac{1}{2\pi}\int_{\theta-2\pi}^{\theta} x(t(\theta))e^{-jk\theta}d\theta}{dt}$$
$$= \frac{1}{2\pi}xe^{-jk\theta(t)}\omega(t) - \frac{1}{2\pi}x\{t-T(t)\}e^{-jk\theta[t-T(t)]}\omega\{t-T(t)\}\{1-\dot{T}(t)\} \quad \text{(A1-7)}$$
$$= \frac{1}{2\pi}\left\{xe^{-jk\theta(t)}\omega(t)|_{t-T(t)}^{t} + x\{t-T(t)\}e^{-jk\theta[t-T(t)]}\omega\{t-T(t)\}\dot{T}(t)\right\}$$

Combing (A1-6) and (A1-7) gives:

$$\left\langle\frac{dx}{dt}\right\rangle_k =$$
$$= \frac{d\langle x\rangle_k}{dt} - \frac{1}{2\pi}x\{t-T(t)\}e^{-jk\theta[t-T(t)]}\omega\{t-T(t)\}\dot{T}(t) - \frac{1}{2\pi}\int_{t-T(t)}^{t} xe^{-jk\theta(t)}\omega(t)\left\{\frac{\dot{\omega}(t)}{\omega(t)} - jk\omega(t)\right\}dt$$
$$= \frac{d\langle x\rangle_k}{dt} - \frac{1}{2\pi}x\{t-T(t)\}e^{-jk\theta[t-T(t)]}\omega\{t-T(t)\}\dot{T}(t) - \frac{1}{2\pi}\left\{\int_{t-T(t)}^{t} xe^{-jk\theta(t)}\dot{\omega}(t)dt - \int_{t-T(t)}^{t} jkxe^{-jk\theta(t)}\omega^2(t)dt\right\}$$
(A1-8)

# APPENDIX II

The Taylor expansion of the DC-link voltage in (3-27) is written as:

$$f_1(v_{d,}v_q) = v_{dc} = \frac{3\sqrt{3}}{\pi}\sqrt{v_d^2 + v_q^2} \tag{A2-1}$$

The Taylor expansion of (A2-1) is

$$\begin{aligned} v_{dc} = k_0 + \frac{k_1}{1!}(v_d - V_{d0}) + \frac{k_2}{1!}(v_q - V_{q0}) + \frac{k_3}{2!}(v_d - V_{d0})^2 + \frac{k_4}{2!}(v_q - V_{q0})^2 \\ + \frac{k_5}{2!}(v_d - V_{d0})(v_q - V_{q0}) + \ldots \end{aligned} \tag{A2- 2}$$

where the Taylor coefficients are:

$$k_0 = f_1(V_{d0}, V_{q0}) \tag{A2-3}$$

$$k_1 = \frac{\partial f_1(V_{d0}, V_{q0})}{\partial v_d} \tag{A2-4}$$

$$k_2 = \frac{\partial f_1(V_{d0}, V_{q0})}{\partial v_q} \tag{A2-5}$$

$$k_3 = \frac{\partial^2 f_1(V_{d0}, V_{q0})}{\partial v_d^2} \tag{A2-6}$$

$$k_4 = \frac{\partial^2 f_1(V_{d0}, V_{q0})}{\partial v_q^2} \tag{A2-7}$$

$$k_5 = 2\frac{\partial^2 f_1(V_{d0}, V_{q0})}{\partial v_d \partial v_q} \tag{A2-8}$$

The sinusoidal functions of the voltage vector angle (3-38a) and (3-38b) are rewritten as:

$$\cos\varphi = f_2(v_d, v_q) = \frac{v_d}{\sqrt{v_d^2 + v_q^2}} \tag{A2- 9}$$

$$\sin\varphi = f_3(v_d, v_q) = \frac{v_q}{\sqrt{v_d^2 + v_q^2}} \quad \text{(A2-10)}$$

The Taylor coefficients in equation (3-39a) and (3-39b) are given below:

$$h_0 = f_2(V_{d0}, V_{q0}) \quad \text{(A2-11)}$$

$$h_1 = \frac{\partial f_2(V_{d0}, V_{q0})}{\partial v_d} \quad \text{(A2-12)}$$

$$h_2 = \frac{\partial f_2(V_{d0}, V_{q0})}{\partial v_q} \quad \text{(A2-13)}$$

$$h_3 = \frac{\partial^2 f_2(V_{d0}, V_{q0})}{\partial v_d^2} \quad \text{(A2-14)}$$

$$h_4 = \frac{\partial^2 f_2(V_{d0}, V_{q0})}{\partial v_q^2} \quad \text{(A2-15)}$$

$$h_5 = 2\frac{\partial^2 f_2(V_{d0}, V_{q0})}{\partial v_d \partial v_q} \quad \text{(A2-16)}$$

The Taylor coefficients of (3-39c) and (3-39d) are given as

$$g_0 = f_3(V_{d0}, V_{q0}) \quad \text{(A2-17)}$$

$$g_1 = \frac{\partial f_3(V_{d0}, V_{q0})}{\partial v_d} \quad \text{(A2-18)}$$

$$g_2 = \frac{\partial f_3(V_{d0}, V_{q0})}{\partial v_q} \quad \text{(A2-19)}$$

$$g_3 = \frac{\partial^2 f_3(V_{d0}, V_{q0})}{\partial v_d^2} \quad \text{(A2-20)}$$

$$g_4 = \frac{\partial^2 f_3(V_{d0}, V_{q0})}{\partial v_q^2} \quad \text{(A2-21)}$$

$$g_5 = 2\frac{\partial^2 f_3(V_{d0}, V_{q0})}{\partial v_d \partial v_q} \quad \text{(A2-22)}$$

# APPENDIX III

A general three-phase fault can be represented by a conductance matrix [88]

$$Y_f = \begin{bmatrix} \frac{1}{R_{aa}} + \frac{1}{R_{ab}} + \frac{1}{R_{ac}} & -\frac{1}{R_{ab}} & -\frac{1}{R_{ac}} \\ -\frac{1}{R_{ab}} & \frac{1}{R_{ab}} + \frac{1}{R_{bb}} + \frac{1}{R_{bc}} & -\frac{1}{R_{bc}} \\ -\frac{1}{R_{ac}} & \frac{1}{R_{bc}} & \frac{1}{R_{ac}} + \frac{1}{R_{bc}} + \frac{1}{R_{cc}} \end{bmatrix} \quad \text{(A3-1)}$$

The three-phase fault currents associated with the general fault can be given by

$$i_{abcf} = Y_f v_{abcf} \quad \text{(A3-2)}$$

The above equation can be expressed in the DQ0 frame as

$$i_{dq0\,f} = K_s Y_f K_s^{-1} v_{dq0\,f} \quad \text{(A3-3)}$$

# REFERENCES

[1] A. Srimoolanatha, "Aircraft Electrical Power Systems – Charged with Opportunities," 2008.

[2] K. Rypdal, "Aircraft Emission," Good Practice Guidance and Uncertainty Management in National Greenhouse Gas Inventories.

[3] IATA. (2012). Fact Sheet: Environment. Available: **http://www.iata.org/pressroom/facts_figures/fact_sheets/pages/environment.aspx**

[4] R. E. J. Quigley, "More Electric Aircraft," in Applied Power Electronics Conference and Exposition, 1993. APEC '93. Conference Proceedings 1993., Eighth Annual, 1993, pp. 906-911.

[5] K.J.Karimi, "The role of power electronics in more-electric airplanes (MEA)," presented at the Workshop on Computers in Power Electronics, 2006.

[6] E. Q. Richard, Jr., "More Electric Aircraft," 1993.

[7] I. Moir and A. Seabridge, Aircraft Systems: mechanical, electrical, and avionics subsystems integration 3rd ed.: John Wiley & Sons, 2008.

[8] J. A. Rosero, J. A. Ortega, E. Aldabas, and L. Romeral, "Moving towards a more electric aircraft," Aerospace and Electronic Systems Magazine, IEEE, vol. 22, pp. 3-9, 2007.

[9] T. Wu, "Integrative System Modelling of Aircraft Electrical Power Systems," Doctor of Philosophy, University of Nottingham, 2010.

[10] L. Faleiro, "Summary of The European Powre Optimised Aircraft (POA) Project," presented at the 25th International Congress of the Aeronautical Science, 2006.

[11] More Open Electrical Technologies. Available: **http://www.eurtd.com/moet/**

[12] T. Jomier. (2009). More Open Electrical Technologies Techincal Report. Available: **http://www.eurtd.com/moet/**

[13] Innovating togehter, flying greener. Available: **http://www.cleansky.eu/**

[14] "Boeing 787."

[15] T. Jomier, "More Open Electrical Technologies (MOET) technical report," pp. 164-165, 2009.

[16] P. Rakhra, P. J. Norman, S. J. Galloway, and G. M. Burt, "Modelling and Simulation of a MEA Twin Generator UAV Electrical Power System," in Universities' Power Engineering Conference (UPEC), Proceedings of 2011 46th International, 2011, pp. 1-5.

[17] P. J. Norman, S. J. Galloway, G. M. Burt, D. R. Trainer, and M. Hirst, "Transient analysis of the more-electric engine electrical power distribution network," in Power Electronics, Machines and Drives, 2008. PEMD 2008. 4th IET Conference on, 2008, pp. 681-685.

[18] G. M. Raimondi, T. Sawata, M. Holme, A. Barton, G. White, J. Coles, P. H. Mellor, and N. Sidell, "Aircraft embedded generation systems," in Power Electronics, Machines and Drives, 2002. International Conference on (Conf. Publ. No. 487), 2002, pp. 217-222.

[19] S. D. A. Fletcher, P. J. Norman, S. J. Galloway, and G. M. Burt, "Determination of protection system requirements for dc unmanned aerial vehicle electrical power networks for enhanced capability and survivability," Electrical Systems in Transportation, IET, vol. 1, pp. 137-147, 2011.

[20] L. K, "MODELING AND ANALYSIS OF A DC POWER DISTRIBUTION SYSTEM IN 21ST CENTURY AIRLIFTERS," Virginia Polytechnic Institute and State University, Virginia, 1999.

[21] N. Mohan, W. P. Robbins, T. M. Undeland, R. Nilssen, and O. Mo, "Simulation of power electronic and motion control systems-an overview," Proceedings of the IEEE, vol. 82, pp. 1287-1302, 1994.

[22] S. V. Bozhko, T. Wu, C. I. Hill, and G. M. Asher, "Accelerated simulation of complex aircraft electrical power system under normal and faulty operational scenarios," in IECON 2010 - 36th Annual Conference on IEEE Industrial Electronics Society, 2010, pp. 333-338.

[23] M. O. Martin R. Kuhn, Loic Raulin, "A Mulit Level Approach for Aircraft Electrical System Design," presented at the International Modelica Conference, 2008.

[24] S. Chiniforoosh, J. Jatskevich, A. Yazdani, V. Sood, V. Dinavahi, J. A. Martinez, and A. Ramirez, "Definitions and Applications of Dynamic Average Models for Analysis of Power Systems," Power Delivery, IEEE Transactions on, vol. 25, pp. 2655-2669, 2010.

[25] S. Jian, "Unified averaged switch models for stability analysis of large distributed power systems," in Applied Power Electronics Conference and Exposition, 2000. APEC 2000. Fifteenth Annual IEEE, 2000, pp. 249-255 vol.1.

[26] B. Lehman and R. M. Bass, "Switching frequency dependent averaged models for PWM DC-DC converters," Power Electronics, IEEE Transactions on, vol. 11, pp. 89-98, 1996.

[27] P. C.Krause, O. Wasynczuk, and S. D. Sudhoff, Analysis of electric machinery and dirve systems: Wiley-interscience, 2002.

[28] S. V. Bozhko, T. Wu, T. Yang, and G. M. Asher, "More-electric aircraft electrical power system accelerated functional modeling," in Power Electronics and Motion Control Conference (EPE/PEMC), 2010 14th International, 2010, pp. T9-7-T9-14.

[29] T. Wu, S. Bozhko, G. Asher, and P. Wheeler, "Fast Reduced Functional Models of Electromechanical Actuators for More-Electric Aircraft Power System Study," SAE Technical Paper 2008-01-2859, 2008.

[30] T. Wu, S. V. Bozhko, G. M. Asher, and D. W. P. Thomas, "Accelerated functional modeling of aircraft electrical power systems including fault scenarios," in Industrial Electronics, 2009. IECON '09. 35th Annual Conference of IEEE, 2009, pp. 2537-2544.

[31] S. R. Sanders, J. M. Noworolski, X. Z. Liu, and G. C. Verghese, "Generalized averaging method for power conversion circuits," IEEE Transactions on Power Electronics, vol. 6, pp. 251-259, 1991.

[32] D. S. AB, Dymola User Manual, 2011.

[33] M. R. Kuhn, A. Griffo, W. Jiabin, and J. Bals, "A components library for simulation and analysis of aircraft electrical power systems using

Modelica," in Power Electronics and Applications, 2009. EPE '09. 13th European Conference on, 2009, pp. 1-10.

[34] B. C. L. Aleksandar. M Stankovic, Timur Aydin, "Applications of Generalized Averaging to Synchronous and Induction Machine," 28th North American Power Symposium, 1996.

[35] A. M. Stankovic and T. Aydin, "Analysis of asymmetrical faults in power systems using dynamic phasors," Power Systems, IEEE Transactions on, vol. 15, pp. 1062-1068, 2000.

[36] A. M. Stanković, S. R. Sanders, and T. Aydin, "Dynamic phasors in modeling and analysis of unbalanced polyphase AC machines," IEEE Transactions on Energy Conversion, vol. 17, pp. 107-113, 2002.

[37] T. Yang, S. Bozhko, and G. Asher, "Assessment of dynamic phasors modelling technique for accelerated electric power system simulations," in Power Electronics and Applications (EPE 2011), Proceedings of the 2011-14th European Conference on, 2011, pp. 1-9.

[38] T. Demiray, F. Milano, and G. Andersson, "Dynamic Phasor Modeling of the Doubly-fed Induction Generator under Unbalanced Conditions," in Power Tech, 2007 IEEE Lausanne, 2007, pp. 1049-1054.

[39] B. C. L. Aleksandar. M Stankovic, Timur Aydin, "Applications of Generalized Averaging to Synchronous and Induction Machines," 28th North American Power Symposium, 1996.

[40] P. C. Stefanov and A. M. Stankovic, "Modeling of UPFC operation under unbalanced conditions with dynamic phasors," Power Systems, IEEE Transactions on, vol. 17, pp. 395-403, 2002.

[41] P. Mattavelli and A. M. Stankovic, "Dynamical phasors in modeling and control of active filters," in Circuits and Systems, 1999. ISCAS '99. Proceedings of the 1999 IEEE International Symposium on, 1999, pp. 278-282 vol.5.

[42] M. A. Hannan, A. Mohamed, and A. Hussain, "Modeling and power quality analysis of STATCOM using phasor dynamics," in Sustainable Energy Technologies, 2008. ICSET 2008. IEEE International Conference on, 2008, pp. 1013-1018.

[43] Q. Qingru, Y. Chang, W. Chan Ka, and N. Yixin, "Modeling and simulation of a STATCOM system based on 3-level NPC inverter using dynamic phasors," in Power Engineering Society General Meeting, 2004. IEEE, 2004, pp. 1559-1564 Vol.2.

[44] H. Zhu, Z. Cai, H. Liu, Q. Qi, and Y. Ni, "Hybrid-model transient stability simulation using dynamic phasors based HVDC system model," Electric Power Systems Research, vol. 76, pp. 582-591, 2006.

[45] Q. Qingru, C. Shousun, V. Ni, and F. F. Wu, "Application of the dynamic phasors in modeling and simulation of HVDC," in Advances in Power System Control, Operation and Management, 2003. ASDCOM 2003. Sixth International Conference on (Conf. Publ. No. 497), 2003, pp. 185-190.

[46] A. M. Stankovic, P. Mattavelli, V. Caliskan, and G. C. Verghese, "Modeling and analysis of FACTS devices with dynamic phasors," in Power Engineering Society Winter Meeting, 2000. IEEE, 2000, pp. 1440-1446 vol.2.

[47] H. Ruiwen and C. Zexiang, "Modeling and Harmonic Analysis of TCSC with Dynamic Phasors," in Transmission and Distribution Conference and Exhibition: Asia and Pacific, 2005 IEEE/PES, 2005, pp. 1-5.

[48] P. Mattavelli, G. C. Verghese, and A. M. Stankovic, "Phasor dynamics of thyristor-controlled series capacitor systems," Power Systems, IEEE Transactions on, vol. 12, pp. 1259-1267, 1997.

[49] V. A. Caliskan, O. C. Verghese, and A. M. Stankovic, "Multifrequency averaging of DC/DC converters," Power Electronics, IEEE Transactions on, vol. 14, pp. 124-133, 1999.

[50] A. M. M A Hanna, "Dynamic phasor modeliang and EMT simulation of USSC," Proceeding of World congress on Engineering and Computer Science, 2009.

[51] S. Chiniforoosh, H. Atighechi, A. Davoudi, J. Jatskevich, A. Yazdani, S. Filizadeh, M. Saeedifard, J. A. Martinez, V. Sood, K. Strunz, J. Mahseredjian, and V. Dinavahi, "Dynamic Average Modeling of Front-End Diode Rectifier Loads Considering Discontinuous Conduction

Mode and Unbalanced Operation," Power Delivery, IEEE Transactions on, vol. 27, pp. 421-429, 2012.

[52] A. Griffo and W. Jiabin, "State-space average modelling of synchronous generator fed 18-pulse diode rectifier," in Power Electronics and Applications, 2009. EPE '09. 13th European Conference on, 2009, pp. 1-10.

[53] P. Norman, "Parametric Average-Value Converter Modelling for Aerospace Applications," SAE International, 10.22 2012.

[54] V. Venkatasubramanian, H. Schattler, and J. Zaborszky, "Fast time-varying phasor analysis in the balanced three-phase large electric power system," IEEE Transactions on Automatic Control, vol. 40, pp. 1975-1982, 1995.

[55] P. Fang Zheng and L. Jih-Sheng, "Generalized instantaneous reactive power theory for three-phase power systems," Instrumentation and Measurement, IEEE Transactions on, vol. 45, pp. 293-297, 1996.

[56] Z. Peng, J. R. Marti, and H. W. Dommel, "Synchronous Machine Modeling Based on Shifted Frequency Analysis," Power Systems, IEEE Transactions on, vol. 22, pp. 1139-1147, 2007.

[57] Z. Peng, J. R. Marti, and H. W. Dommel, "Induction Machine Modeling Based on Shifted Frequency Analysis," Power Systems, IEEE Transactions on, vol. 24, pp. 157-164, 2009.

[58] N. Mohan, T. M. Undeland, and W. P. Robbins, Power Electronics: Converters, Applications and Design: John wiley&Sons, INC, 2003.

[59] S. Jian, B. Zhonghui, and K. J. Karimi, "Input Impedance Modeling of Multipulse Rectifiers by Harmonic Linearization," Power Electronics, IEEE Transactions on, vol. 24, pp. 2812-2820, 2009.

[60] P. C. Krause and T. A. Asipo, "Analysis and Simplified Representations of Rectifier - Inverter Reluctance-Synchronous Motor Drives," Power Apparatus and Systems, IEEE Transactions on, vol. PAS-88, pp. 962-970, 1969.

[61] S. D. Sudhoff, K. A. Corzine, H. J. Hegner, and D. E. Delisle, "Transient and dynamic average-value modeling of synchronous

machine fed load-commutated converters," Energy Conversion, IEEE Transactions on, vol. 11, pp. 508-514, 1996.

[62] S. D. Sudhoff and O. Wasynczuk, "Analysis and average-value modeling of line-commutated converter-synchronous machine systems," Energy Conversion, IEEE Transactions on, vol. 8, pp. 92-99, 1993.

[63] S. Jian and K. J. Karimi, "Small-signal input impedance modeling of line-frequency rectifiers," Aerospace and Electronic Systems, IEEE Transactions on, vol. 44, pp. 1489-1497, 2008.

[64] J. Wang, A. Griffo, L. Han, and D. Howe, "Input Admittance Characteristics of Permanent Magnet Brushless AC Motor Drive Systems," in Vehicle Power and Propulsion Conference, 2007. VPPC 2007. IEEE, 2007, pp. 191-196.

[65] T. Wu, S. V. Bozhko, G. M. Asher, and D. W. P. Thomas, "A fast dynamic phasor model of autotransformer rectifier unit for more electric aircraft," in Industrial Electronics, 2009. IECON '09. 35th Annual Conference of IEEE, 2009, pp. 2531-2536.

[66] H. Zhu, "New Multi-pulse diode rectifier average models for AC and DC power system studies," CPES, Virginia Polytech Inst State University, VA, Blacksburg, 2005.

[67] S. D. P. Juri Jatskevich, "Six-phase synchronous generator-rectifier parametric average value modeling considering operational modes," HAIT Journal of Science and Engineering B, vol. 2, pp. 365-385, 2005.

[68] C. T. Rim, D. Y. Hu, and G. H. Cho, "Transformers as equivalent circuits for switches: general proofs and transformation-based analyses," Industry Applications, IEEE Transactions on, vol. 26, pp. 777-785, 1990.

[69] K. Erwin, Advanced Engineering Mathematics: John Wiley & Sons, 2006.

[70] C. C. Marouchos, The Switching Function Analysis of Power Electronic Circuits: The Institution of Engineering and Technology, 2008.

[71] D. A.Paice, "Power Electronic Converter Harmonics: Multipulse Methods for clean Power," IEEE Industry Application Society, IEEE press.

[72] R. Gabriel, W. Leonhard, and C. J. Nordby, "Field-Oriented Control of a Standard AC Motor Using Microprocessors," Industry Applications, IEEE Transactions on, vol. IA-16, pp. 186-192, 1980.

[73] R. Wu, S. B. Dewan, and G. R. Slemon, "Analysis of an AC to DC voltage source converter using PWM with phase and amplitude control," in Industry Applications Society Annual Meeting, 1989., Conference Record of the 1989 IEEE, 1989, pp. 1156-1163 vol.1.

[74] S. Fukuda, Y. Iwaji, and T. Aoyama, "Modelling and control of sinusoidal PWM rectifiers," in Power Electronics and Applications, 1993., Fifth European Conference on, 1993, pp. 115-120 vol.4.

[75] R. Pena, J. C. Clare, and G. M. Asher, "A doubly fed induction generator using back-to-back PWM converters supplying an isolated load from a variable speed wind turbine," Electric Power Applications, IEE Proceedings -, vol. 143, pp. 380-387, 1996.

[76] T. Wu, S. Bozhko, G. Asher, P. Wheeler, and D. W. Thomas, "Fast Reduced Functional Models of Electromechanical Actuators for More-Electric Aircraft Power System Study," SAE International, 2008.

[77] G. Venkataramanan and W. Bingsen, "Dynamic modeling and control of three phase pulse width modulated power converters using phasors," in Power Electronics Specialists Conference, 2004. PESC 04. 2004 IEEE 35th Annual, 2004, pp. 2822-2828 Vol.4.

[78] H. Akagi, "Active Harmonic Filters," Proceedings of the IEEE, vol. 93, pp. 2128-2141, 2005.

[79] L. R. Limongi, R. Bojoi, C. Pica, F. Profumo, and A. Tenconi, "Analysis and Comparison of Phase Locked Loop Techniques for Grid Utility Applications," in Power Conversion Conference - Nagoya, 2007. PCC '07, 2007, pp. 674-681.

[80] V. Kaura and V. Blasko, "Operation of a phase locked loop system under distorted utility conditions," Industry Applications, IEEE Transactions on, vol. 33, pp. 58-63, 1997.

[81] C. Se-Kyo, "A phase tracking system for three phase utility interface inverters," Power Electronics, IEEE Transactions on, vol. 15, pp. 431-438, 2000.

[82] P. Rodriguez, J. Pou, J. Bergas, J. I. Candela, R. P. Burgos, and D. Boroyevich, "Decoupled Double Synchronous Reference Frame PLL for Power Converters Control," Power Electronics, IEEE Transactions on, vol. 22, pp. 584-592, 2007.

[83] P. Rodriguez, R. Teodorescu, I. Candela, A. V. Timbus, M. Liserre, and F. Blaabjerg, "New Positive-sequence Voltage Detector for Grid Synchronization of Power Converters under Faulty Grid Conditions," in Power Electronics Specialists Conference, 2006. PESC '06. 37th IEEE, 2006, pp. 1-7.

[84] Y. Xiaoming, W. Merk, H. Stemmler, and J. Allmeling, "Stationary-frame generalized integrators for current control of active power filters with zero steady-state error for current harmonics of concern under unbalanced and distorted operating conditions," Industry Applications, IEEE Transactions on, vol. 38, pp. 523-532, 2002.

[85] Z. Keliang and W. Danwei, "Relationship between space-vector modulation and three-phase carrier-based PWM: a comprehensive analysis [three-phase inverters]," Industrial Electronics, IEEE Transactions on, vol. 49, pp. 186-196, 2002.

[86] S. Rosado, M. Xiangfei, G. Francis, W. Fei, and D. Boroyevich, "Model-Based Digital Generator Control Unit for a Variable Frequency Synchronous Generator With Brushless Exciter," Energy Conversion, IEEE Transactions on, vol. 23, pp. 42-52, 2008.

[87] T. Wu, S. V. Bozhko, G. M. Asher, and D. W. Thomas, "Fast functional modelling of the aircraft power system including line fault scenarios," in Power Electronics, Machines and Drives (PEMD 2010), 5th IET International Conference on, pp. 1-7.

[88] D. W. P. Thomas, "Protection of major transmission lines using travelling waves," Ph.D thesis,University of Nottingham, Uk, 1990.